Characterising Star forming and Luminous Infrared Galaxies with the Southern African Large Telescope (SALT)

Rajin Anand Ramphul

February 2018

A thesis submitted in fulfilment of the requirements
for the degree of Doctor of Philosophy
in the Department of Astronomy
UNIVERSITY OF CAPE TOWN

Supervisors: Prof. Petri Väisänen (SAAO)[1]
A/Prof. Kurt Van der Heyden (UCT)[2]

[1]South African Astronomical Observatory
[2]Astronomy Department, University of Cape Town

Abstract

Context: Stellar population modelling is a popular technique that has been extensively applied to main sequence galaxies. Yet starburst galaxies and Luminous InfraRed Galaxies (LIRGs) have, so far, not been studied as much using the method. LIRGs in the local universe are known to be highly interacting galaxies with strong star formation in obscured environments. Still, LIRGs also have diversity in terms of morphology and mode and location of star formation.

Aim: This thesis investigates the stellar population properties of a group of 52 starbursts and luminous infrared galaxies (LIRGs) in the local universe that forms part of the SUper-Novae and starBurst in the InfraReD (SUNBIRD) survey. The galaxies in a distance range of $3.5 < D_l < 280$ Mpc and infrared luminosity of $10.30 < L_{IR} < 11.91$ $L_{\odot}$ were observed with the Southern African Large Telescope in long-slit spectroscopy mode.

Method: The stellar populations of the galaxies are derived by fitting Bruzual & Charlot (2003) templates to the reduced spectra using STARLIGHT software with a Monte Carlo method implemented to recover uncertainties on age, metallicity and extinction. The derived stellar population models are then subtracted from the observed spectra to produce emission spectra from which emission line fluxes are measured. Both integrated spectra and spatially resolved apertures are extracted to be analysed in this work.

Results: The light-weighted and mass weighted age of the sample is found to be 160 Myr and 7.2 Gyr respectively. The star formation history of the sample shows a rise of activity in the past ~ 50 Myr and with a jump of an order of magnitude in the past 3 Myr. Analysis of the stellar metallicity hints at inflow of pristine gas, which decreases the observed metallicity content as well as ignites SF-activity. Analysis of the oxygen abundances shows that while LIRGs and SF galaxies are under abundant, their under-abundance may have previously been over-estimated as compared to main sequence galaxies.

The radial age profile of the sample is flat, similar to that of late-type Sd galaxies. Interaction is found to cause a drop in the age of apertures although the post-merging stages shows con-

tinued star forming activity in the nuclear region. The stellar metallicity gradient is found to be -0.029 ± 0.018 dex/kpc, comparable to Sb or Sbc galaxies favouring an inside-out formation scenario for the galaxies. As interaction stage increases, both age and metallicity gradients are seen to get flatter, eventually getting slightly positive. The more active interaction stages are HII driven, while isolated and post merging stages shows higher AGN activity.

The current work offers an update on the abundances of IR dominated galaxies from the previous work done by Rupke et al. (2008). The formation scenario of our LIRGs in the local universe is shown to be in line with the scenario put forward by Hopkins et al. (2008). Future works with medium resolution spectra acquired during the course of this thesis should allow for detection of gas inflows and better constrain the different ionising mechanisms involved at different interaction stages.

Declaration

I, Rajin Anand Ramphul, know the meaning of plagiarism and declare that all of the work in the document, save for that which is properly acknowledged, is my own. It has not been submitted before, either in the same or different form, for any degree or examination in any other University. The thesis has been submitted to the Turnitin module and I confirm that my supervisor has seen my report and any concerns revealed by such have been resolved with my supervisor.

Signed: Signed by candidate

Date: 19/02/2018

Acknowledgements

A PhD thesis is by no means an easy endeavour, and there are people without whom I would never have crossed the finished line. I would firstly like to thank Petri Väisänen, my supervisor, for being understanding in whatever situation I was, and, whose advice always made a difference. He allowed me the freedom to explore and steer the project in whichever direction I was more passionate about. This ultimately allowed me to fully experience the life of an independent researcher - an invaluable experience that I will always hold on to. I would also like to thank Kurt van der Heyden for being a very understanding co-supervisor as well as providing funding for most part of the project. He was always ready to help both on the academic side and the administrative side.

Likewise, I will use this opportunity to thank the University of Cape Town and the South African Astronomical Observatory, for providing funding for this work as well as travelling grants to attend conferences. Being a foreigner, it meant a lot to be given the same opportunities as locals with the various resources allocated to us. The NASSP programme will always be dear to me, for it being the reason I was able to come to South Africa and providing me with the foundation knowledge in Astronomy. Nicky Walker who was the NASSP administrator at the time made sure the programme ran smoothly and encouraged all the students to persevere. A few other academics that I interacted with during the course of my PhD and who provided a helping hand are: Steve Crawford, David Gilbank, Sudanshu Barway, Alexei Kniazev, Kaustubh Vaghmare and Andre Luiz de Amorim.

My friends in South Africa were part of the family I had here. Their roles varied immensely depending on their different personalities. These includes but are not limited to: Iniyan Natarajan, Eli Kasai, Rocco and Deanne Coppejans, Moses Mogotsi, Nikhita Madhanpall, Susan Wilson, Vinesh Rajpaul, Riona Ramraj, Mpati Ramatsoku, Zara Randriamanakoto and Abiy Tekola. A lot of my path up to here was moulded by those mentioned. A special thanks to Iniyan and Sheean who helped in proof reading this thesis. My gratitude goes also to the OAD crowd, especially to Kevin Govender, Nuhaah Solomon and J.C. Mauduit who provided me with first hand experience in outreach. It was a much needed break from the academic focus of a doctoral

student's life.

The Mauritian Astro community played an enjoyable part in my life as a PhD student. Here I am referring to Nadeem Oozeer, Rajeev Manick, Vinand Prayag, Sheean Jolicoeur, Suraj Chumroo, Harry Mootoovaloo, Zafiirah Hosenee and Ridhima Nunhokee. Their presence allowed me to have a feeling of home away from home here in Cape Town as well as providing a helping hand whenever and wherever needed. Most of them are part of the JEDI community that we built over the years. JEDI workshop is a concept created by Bruce Bassett to whom I am also very grateful, for organising workshops around Africa and inspiring a lot of young graduates to join the science research bandwagon.

A thank you to Patrick Paya and Serge Florens of the College du Saint Esprit, who firstly as my high school teachers sparked my curiosity for physics. Then later on, as my colleagues, were pivotal in transferring their love of teaching to me as well as helped me in my basic understanding of some physical concepts. Serge, as an avid, amateur astronomer, rubbed off some of his passion for the Universe on to everyone around him, including me. Dinesh Somanah, King Kis-Sion and Shailendra Oree are the lecturers from University of Mauritius who helped to shape my journey up to here.

I will end by thanking the most important people of my life - my family for their unconditional love and support. My father, Anand, has throughout his life been an example of selflessness and dedication. My mother, Purnima is the one who continuously sparked my curiosity as a child leading me to enjoy and value science. My two elder brothers, Nitin and Ashvin, who throughout my childhood and until now provide incredible support. Dyuksha, my little sister, who always looks up to me, inspires me to be a better version of myself. My Dadi (paternal grandmother) who shared half of the burden of my upbringing in my early years, is an example of modesty and placed a priceless value on the education of her kids and grandchildren. My partner in life, Diksha Rumjeet, who like a rock, was reliable in both the good and bad times along this long journey, always ready to be supportive and adding a touch of sweetness to everything. Two of my long time friends, Shaan Ramchurn and Faizal Sheik Chan, whom I consider as my siblings, are people I can always open up to and share my struggles with at any time. Two of my maternal uncles, Dan and Baboo, who both sadly passed away during the course of this endeavour, were people I looked up to when I was a kid - the second being a person who had a keen interest in sciences and always challenged me with tough questions about the physics of the universe...

"Look at the stars
Look how they shine for you ... "

List of papers relevant to this thesis.

Ramphul, R.; Väisänen, P.
Characterising (U)LIRGs using SALT/RSS.
Proceedings of the SALT Science Conference 2015 (SSC2015).
1-5 June 2015. Stellenbosch Institute of Advanced Study, South Africa

Väisänen, P.; **Ramphul, R.**; Randriamanakoto, Z.; Tekola, A.
SALT and SUNBIRD: Young massive star clusters and superwinds in strongly star-forming galaxies.
Proceedings of the SALT Science Conference 2015 (SSC2015).
1-5 June 2015. Stellenbosch Institute of Advanced Study, South Africa

Väisänen, Petri; Reunanen, Juha; Kotilainen, Jari; Mattila, Seppo; Johansson, Peter H.; **Ramphul, Rajin**; Romero-Cañizales, Cristina; Kuncarayakti, Hanindyo
Shutting down or powering up a (U)LIRG? Merger components in distinctly different evolutionary states in IRAS 19115-2124 (the Bird).
Monthly Notices of the Royal Astronomical Society, Volume 471, Issue 2, p.2059-2076

Contents

List of Figures

List of Tables

Chapter 1

Literature Review

1.1 Overview

This chapter gives a condensed overview of our current understanding of galaxy formation and evolution. It further focuses on star formation and chemical evolution of galaxies in the context of Luminous Infrared Galaxies (LIRGs).

1.2 Galaxies in the universe

When Galileo Galilei, invented the telescope, it revolutionised our ability to study the stars and universe around us. For the next couple of centuries since, the exciting and important discoveries were first about the solar system and then the stars in our galaxies. With the ever increasing abilities of newer generation telescopes, scientists of the late eighteenth century had catalogued a large number of extended objects they called 'nebulae' that were different from the normal point-like sources stars. For a long time after their discovery, the nebulae were contentious due to two emerging school of thoughts. On the one side, Thomas Wright and Immanuel Kant were in favour of the idea that the nebulae were 'island universes' i.e. objects similar to our own Milky Way that are outside of the latter. On the other side, many astronomers still believed that the observed nebulae were residing inside our own galaxy which at the time was thought to make up the entire universe.

This disagreement culminated in 1920, in what is known as the 'Great Debate' where Heber Curtis and Harlow Shapley presented papers to support each school of thought. Curtis was in favour of the 'island universe' theory with other galaxies outside our own, populating the universe. On the other hand, Shapley argued that if the disk observed in M31 (Andromeda galaxy) was the same size as that of the Milky Way, then it would imply a huge distance of the order of 10^8 light years to account for the observed angular size of the disk. Such distances were

unknown of at the time.

In 1922, the great astronomer Edwin Hubble, through the use of Cepheid variable stars as distance indicators, finally proved the existence of other galaxies outside the realm of our own Milky Way. This in turn sparked a new branch of astronomy; extragalactic astronomy. We now know that galaxies are gravitationally bound objects which contain stars, gas, dark matter, stellar remnant and dust. While stellar astrophysics mainly centres around the study of stars and other objects in our Milky Way, and cosmology models the universe in its grandest scale, extragalactic astronomy is the study of the complex evolution of the different types of galaxies in the universe. Extragalactic astronomy is hence the link between the other two main branches of astronomy and requires input from both branches to paint a scientifically accurate picture.

In the early days of the study of galaxies, Hubble mainly focused on classifying them based on the morphology shown on photographic plates (Hubble, 1926). Galaxies were found to have two main classes: ellipticals and spirals. Moreover, among the spirals two main sub-classes emerged: Normal and Barred. Hubble also observed few irregular galaxies which did not fit into the classification scheme. A visual representation of the scheme developed by Hubble is shown in Figure 1.1. At the time it was believed, that the ellipticals on the left were young galaxies which evolved to the older spirals, hence being referred to "Early" and "Late" type galaxies respectively. Even though this picture is no longer thought to be accurate in present time the tuning fork diagram is still an indication for the age of galaxies. Usually spirals on the extreme right are the youngest and ellipticals on the extreme left shows older properties with a general age gradient for the different subclasses in the middle.

As more data were acquired, and with better telescope technology, more complex classification schemes have been devised by astronomers. For example, de Vaucouleurs (1959) added features such as bars, rings or the structure of the spiral arms as additional parameters to consider. Another strategy to classify galaxies is to use the stellar population of the galaxies as described by the Yerkes System (Morgan, 1958). This scheme linked the luminosity profile to stellar population, along with shape and inclination to distinguish between different classes. van den Bergh (1976) came up with a system where lenticulars were not the transition stage between ellipticals and spirals, as proposed originally by Hubble. The author placed lenticulars on a separate parallel branch to spirals while using the bulge to disk ratio as a discriminator among different types of lenticulars. In more recent years, grouping galaxies by different parameters makes use of the vast amount of data available in both photometry and spectroscopy (Cappellari et al., 2011; Kormendy & Bender, 2012) or even multi-wavelength datasets (Buta et al., 2015). Emsellem et al. (2007) showed for example that early-type galaxies could be classified into slow

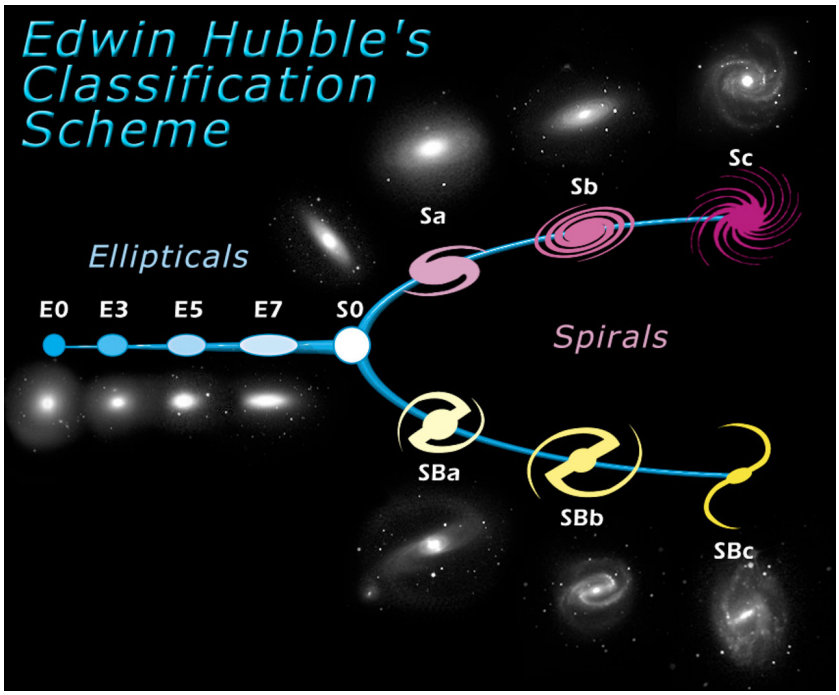

Figure 1.1: A modern representation of the Hubble's tuning fork diagram. Elliptical galaxies are classified by ellipticity with E0 being the spheres while E7 are flattened. Spirals are classified depending on the presence (SB) or absence (S) of bars. The two branches are then grouped by how tightly wounded the spiral arms are. Lenticular (S0) galaxies lies at the intersection of the Elliptical and Spiral branches. Image credit: https://www.spacetelescope.org/images/heic9902o.

and fast rotators where slow rotators show brighter luminosity than their faster counterparts. In the case of late-type galaxies, internal secular evolution can lead to bulge-like features from the disks that often are referred to as pseudobulges (for an extensive review see Kormendy & Kennicutt (2004a)). While newer schemes have brought in improvement to our understanding of galaxy formation and evolution, the different classes identified by Hubble are still relevant and widely used. A brief review of those main groups is given in following sections (1.3.1-1.3.4).

1.3 Galaxies Classification

1.3.1 Elliptical (E) galaxies

Elliptical galaxies are rugby-ball shaped objects which possess very smooth and round surface brightness profiles. The luminosity profile of those galaxies follows the de Vaucouleurs profile (de Vaucouleurs, 1948) which is a special case of the Sersic profile (Sersic, 1968). Most of ellipticals are deprived from cold gas or dust which explain their low current star formation rate. The lack

of raw materials for newer generation of stars means that the general population of stars present in ellipticals is an ageing one (Mo et al., 2010). Consequently, the light is dominated by G,K or M stars, which gives ellipticals a redder photometric colour. Previously it was thought that ellipticals were very old and relaxed system, but this view has changed. Since relaxation time to properly get random motions of stars around the centre is much greater than the age of the universe, the original momentum of stars from the time of the formation of these galaxies is still dominant (Sparke & Gallagher, 2007). The implications are that the kinematics of ellipticals are complex with some having fast motions and others having slow stellar motions. Variations in ellipticity are also noted with some cases showing near spheroidal (E0) shape while others are extremely elongated (E7). In the local universe, ellipticals account for around $\sim 12\%$ of total number of galaxies (Wilman & Erwin, 2012).

1.3.2 Spiral (S) galaxies

The structure of spiral galaxies is more complex than the typical elliptical case. Spirals usually have a bulge at their centres surrounded by a flat rotating disk. Both components (bulge and disk) are surrounded by a spherical halo where globular clusters usually reside. The bulge shares similarities with an elliptical galaxy but on a smaller scale, while the thin rotationally supported disk contains stars, gas and dust. Tidal waves in the disk usually give rise to new generation of stars which is why spirals are bluer in colour than ellipticals. The surface brightness of spirals also follows the Sersic profile but with the galaxy concentration index, n, set to 1, i.e. the profile is exponential. The Hubble classification groups spirals based on the presence of bars, bulge to disk ratio, the spread of the spiral arms and separation of the bulge with the arms (Sandage et al., 1975). A key difference is that of regular (S) versus those presenting a bar structure along their major axis (SB). The scheme defines spirals 'a' as those with arms very near to a relatively large bulge and as we move towards 'c' galaxies the bulge becomes smaller while the arms are more defined and stretched outwards. Spirals dominate the local universe where their populations have been estimated to be around $\sim 67\%$ of all galaxies (Wilman & Erwin, 2012).

1.3.3 Lenticular (S0) galaxies

Lenticulars (S0) possess characteristics of both spirals and ellipticals. Usually they have a bulge component along with a disk-like structure which in most cases does not display arms or gas. There is a significant amount of dust present in lenticulars (van Dokkum & Franx, 1995; Ferrari et al., 1999), but on average it is expected to be less than in spirals for example. The central bulge is more dominant than in the case of spirals (Mo et al., 2010). To add to the complexity of this class, presence of bars can sometimes be observed (Sparke & Gallagher, 2007). As mentioned earlier, van den Bergh (1976), realising that there are important bulge to disk ratio variations, decided to create a separate branch of lenticulars. The variation of bulge to disk ratio implies

that lenticulars could have fundamental differences in how they are formed depending on their environment. For full reviews on lenticulars see Kormendy & Kennicutt (2004b); Kormendy & Ho (2013). The fraction of lenticulars in the local universe is approximately 20% of the total population of galaxies (Wilman & Erwin, 2012).

1.3.4 Irregular (Irr) galaxies

Irregular galaxies as the name suggests, have no real symmetry with no dominant forces from the bulge or disk (Mo et al., 2010) which is why they were left out of the Hubble classification system. The motion of the stars in Irregulars is highly stochastic with no rotational motion (Sparke & Gallagher, 2007). They usually contain the highest amount of gas which drives current star formation. As a result their stellar population is very young and their photometric colour are very blue. Irregulars are usually smaller in size than standard galaxies with masses in the range of $10^8 - 10^{10} M_\odot$. They are sub-classified into three types namely type I and type II. Type I are gas-rich with low metallicity that are very close to spirals but do not show enough pronounced structures to be classified as such. Type II are high in dust content and often the most chaotic ones which in principle is the result of recent interactions or collisions.

1.4 Observational constraints to galaxy evolution

The process of galaxy formation and evolution is a hot topic in modern astrophysics. To be able to understand the birth and subsequent evolution of complicated objects, requires the mastery of a high number of parameters. The formation of galaxies is mostly governed by the large scale structure of dark matter in the early Universe (White & Frenk, 1991; Sheth et al., 2001). On the other hand, their evolution depends on smaller scale processes like feedback and its impact on triggering or quenching star formation (Hopkins et al., 2014). The problem becomes more complicated because most of the time in astrophysics we cannot run experiments to confirm or reject any hypothesis. Fortunately the universe is vast and offers a huge sample of galaxies at different stages and environments to study. But even then, observations are limited by the resolution and collecting power of telescopes. Ground based telescopes are limited by the earth's atmosphere, while space telescopes are limited by the size of the payload that can be sent in orbit. Simulations offer the closest approach to running experiments, and while in the past decades our ability to do intensive computing has risen exponentially, the simulations are still dependent on parameters collected from observational surveys.

1.4.1 Bimodal distribution of colours

To paint an accurate picture of galaxy evolution, we first look at some of the observational evidence of the behaviours of galaxies. As explained in Section 1.3.1, colour, after correcting for

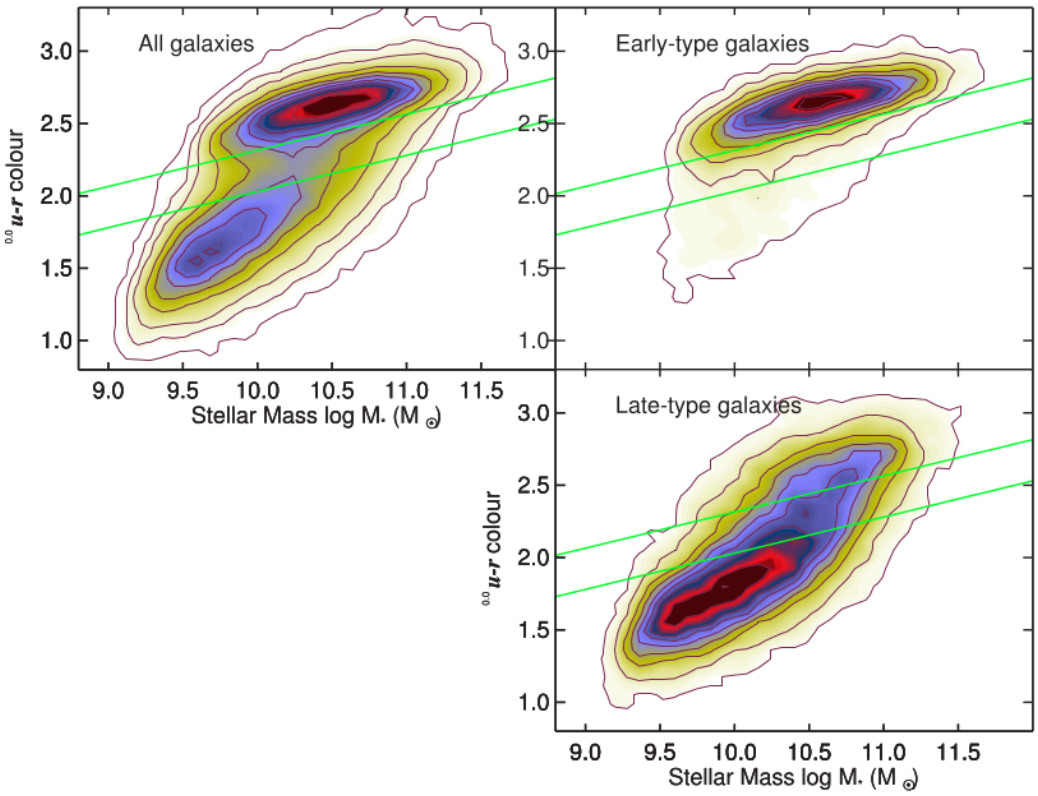

Figure 1.2: u-r colour vs stellar mass plot from Schawinski et al. (2014) shows the bimodal distribution of galaxies in the left panel. The right panels show the breakdown of the contribution of each classes of galaxies. The "green valley" is the depleted region occupied by galaxies falling between the two green lines. Above the green valley lies the "red sequence" which mostly consists of ellipticals. The main constituents of the "blue cloud", which is the region below the green valley, are the late type galaxies.

extinction effect due to dust, is a good indicator of the age of the stellar population of galaxies. There is solid evidence showing a bimodal distribution in galaxy colours (Strateva et al., 2001; Baldry et al., 2004; Salimbeni et al., 2008; Schawinski et al., 2014). Figure 1.2 shows a plot of colour vs stellar mass from Schawinski et al. (2014) where we can clearly see a high galaxy density in the "red sequence" (top portion) and slightly lower density in the second maximum representing the "blue cloud". It is important to note that the red and blue colours in Figure 1.2 are generally related to the morphological classification of ellipticals and spirals. The bimodal distribution was observed to $z \sim 1.5$ by Cirasuolo et al. (2007) and was extended to $z \sim 3$ by Whitaker et al. (2011). It is also apparent in UV photometry up to a redshift in the range of $z \sim 3 - 3.5$ (Salimbeni et al., 2008). Even though the number of red sequence galaxies is lower at higher redshifts (Kriek et al., 2008), their mere presence put constraints on models of galaxy

evolution. Any consistent model, must be able to account for the quenching of star formation at a young age of the universe.

The region between the two main populations of early and late type galaxies is known as the "green valley" (found between the two green lines of Figure 1.2). Previously it was expected that the green valley was a transition phase through which a galaxy would move quickly from the blue cloud to the red sequence, after star formation has been quenched (Bell et al., 2004; Faber et al., 2007; Salim et al., 2007). One of the reasons suggested for the quenching of star formation is the presence of active galactic nuclei (AGN). Schawinski et al. (2014) suggested that the green valley galaxies mainly consists of two different populations (early and late type galaxies) that overlap each other in the colour-mass diagram. Moreover they also argued that the transition phase is different for each type of galaxy with distinct quenching mechanism at play on different time-scales. On the other hand, Casado et al. (2015), showed that if the green valley galaxies are treated as a single group of indeterminate morphology which can possibly evolve in towards both the "red sequence" and "blue cloud". More recently, Oemler et al. (2017) by using specific star formation (sSFR) rates showed that there is a continuous transition between red and blue galaxies with no clear-cut region for the "green valley".

1.4.2 Mass assembly

Galaxies are factories that convert hydrogen gas into stars. While massive stars send enriched gas back into the interstellar medium (ISM) and are lives for millions or tens of millions of years, while smaller stars have lifetimes reaching the tens of billions of years. This has the consequence of 'locking' gas into those stars. We can therefore expect an increase in the overall stellar mass with the evolution of the universe. Measurement of this phenomenon helps us to constrain models about how stellar mass is assembled over time. This quantification is usually done in two ways: either directly measure the stellar mass density at different redshift bins or determine the star formation rate at different epochs.

The first studies of star formation rate as a function of cosmological time-scales was carried out by Lilly et al. (1996) followed by Madau et al. (1996). Both observed that as we go back in time, star formation activity increases, and peaks at around $z \sim 2$, and then slowly decreases again. The observed peak is an order of magnitude greater than the current star formation activity in the local universe. This result has since been corroborated by multiple studies (Steidel et al., 1999; Hopkins & Beacom, 2006; Bauer et al., 2011; Madau & Dickinson, 2014). Some recent results, however, show lower activity at high redshift ($z > 2$) (Behroozi et al., 2013). A plot of the evolution of star formation density with redshift is shown in Figure 1.3. The best fit function of the star formation history of the universe is given by the following equation (Madau

& Dickinson, 2014):

$$\psi(z) = 0.015(1+z)^{2.7}\left[1+\left(\frac{1+z}{2.9}\right)^{5.6}\right]^{-1} \quad \mathrm{M}_{\odot}\ \mathrm{yr}^{-1}\ \mathrm{Mpc}^{-1}\ . \tag{1.1}$$

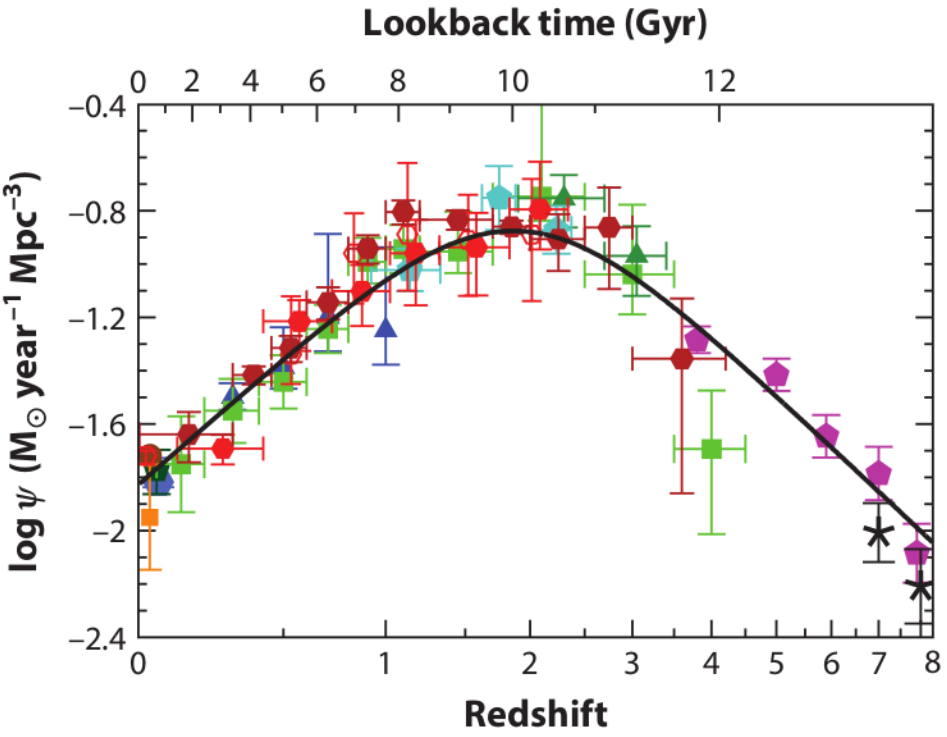

Figure 1.3: Cosmic star formation history up to redshift $z \sim 8$ using a combination of FUV (green, blue, purple and black symbols)and IR (red, orange and brown symbols) data assuming a Salpeter IMF. Equation 1.1 gives the best-fit curve shown in black in the plot. Image Credit: Madau & Dickinson (2014).

Direct measurements of the stellar mass assembly process has been done since the year 2000, after researchers started using stellar population modelling to estimate stellar mass (Madau & Dickinson, 2014). The approach used is the fitting of the galactic Spectral Energy Distribution (SED) from photometric intensities of different filters (Pérez-González et al., 2008; Smith et al., 2012). Once the mass of a particular galaxy is estimated, one can then estimate for a particular redshift bin the mass function, which is the number of galaxies in a mass interval. Figure 1.4 shows the evolution of the stellar mass with redshift based on the simulations of Behroozi et al. (2013). In this case the simulated data was constrained by observed data in all the redshift bins currently accessible. A clear progression of the growth of stellar mass can be seen in Figure 1.4, the number density of high mass galaxies is higher at lower redshifts which is a consequence of 'downsizing' (see Section 1.5.3 for a broader perspective.)

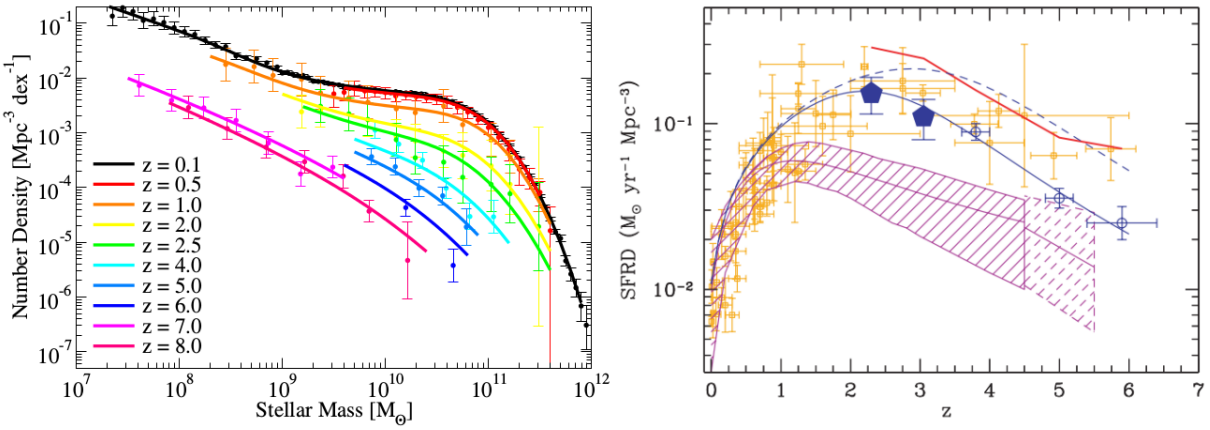

Figure 1.4: *Left Panel*: Galaxy stellar mass as a function of redshift from simulation constrained by observational data. It is clear that there has been a constant progression of galactic stellar mass over the history of the universe as the number density of each mass bins has gradually increased. Image Credit: Behroozi et al. (2013). *Right Panel*: Cosmic Star formation as a function of redshift with the purple hatched region representing star formation calculated from stellar mass by (Wilkins et al., 2008). Stellar mass build-up is a relatively good proxy for star formation rate calculated from more 'traditional' indicators (UV or IR data). Image Credit: Reddy & Steidel (2009).

1.5 Galaxy formation models

We now explore some of the models of galaxy formation and will then combine observational evidence put forward in the Sections 1.4.1-1.4.2 to give a brief assessment of each one of them. For extensive reviews on galaxy formation see for example Baugh (2006); Benson (2010); Somerville & Davé (2015).

1.5.1 Monolithic formation

One of the early galaxy formation models proposed, was the monolithic collapse by Eggen et al. (1962), now commonly known as the Top-Down theory. The model proposed that galaxies formed from the direct gravitational collapse of a huge amount of primordial gas. During this massive collapse the gas also fragments into smaller chunks which are then virialised around the same time to form the stellar population of the galaxy with virtually uniform age. After the initial star-formation burst the stellar population slowly evolves without much change. To try to explain the different morphologies of galaxies, it was suggested that in the case of ellipticals, most of the gas is converted to stars and the radial collapse of the gas is then translated to the random motion of the stars. In the case of spirals, the collapse is not as effective into fragmenting into the smaller pieces which could then become stars. Hence the gas cloud flattens into a rotationally supported disk (Mo et al., 2010). This scenario of galaxy formation is less supported now due

to lack of observational evidence and because a more complicated picture having emerged . In a revised form, the monolithic collapse model appears to fit some observational evidences such as stellar population of early-type galaxies (ETG) (Ogando et al., 2005; Kampakoglou et al., 2008; Chiosi et al., 2014).

1.5.2 Hierarchical merging

Hierarchical merging, or Bottom-up theories, is a set of theories which postulates that galaxy evolution is driven by merging of smaller objects at higher redshift (White & Rees, 1978; Cole et al., 1994; Steinmetz & Navarro, 2002). Galaxies build up in size in the universe as a consequence of merging of smaller galaxies, which is analogous to the cosmological structure formation in a Lambda Cold Dark Matter (ΛCDM) model (Ogando et al., 2005). It is known that the small scale perturbations of the young universe translated to over-dense regions, where dark matter agglomerated, which in turn created big potential wells where baryonic matter was 'funnelled' to form clusters. While in the monolithic model, the bulk of star formation is expected to have happened at the early stage of the universe, in hierarchical merging, star formation is a more continuous process, which in fact is consistent with the observation of the star formation history of the universe described in section 1.4.2. As smaller sized galaxies are naturally attracted towards the big potential wells of dark matter halos, they merge to create the big Early-type galaxies. It was already apparent from the canonical work of Toomre (1977) that mergers can create spheroidal galaxies through the merging of spirals of equal sizes. This natural progression of Late-type galaxies evolving towards Early-type ones through ubiquitous merging is in line with the hierarchical ΛCDM (Blumenthal et al., 1984) framework (Somerville & Davé, 2015). However there are still some unanswered questions that need to be addressed; why the number of low mass dwarf galaxies predicted by simulations seems higher by at least a magnitude than what is being observed, why the bulk of star formation post $z \sim 1$ has been in intermediate mass galaxies - known as downsizing. The latter is addressed in the next section.

1.5.3 Downsizing

An important aspect of galaxy formation that was mentioned earlier is that massive elliptical galaxies have very old stellar population as compared to spirals, which show younger stellar populations. It appears to be counter-intuitive to the hierarchical formation scenario that ellipticals formed a lot of their stars (and hence mass) at an early stage of the universe in a short time span (Juneau et al., 2005). Cowie et al. (1996) noticed that the K-band rest-frame luminosities of star forming galaxies decline with redshift over an interval of $0.2 < z < 1.7$. This phenomena was named as 'downsizing'. Over the years many observational parameters such as star formation rate, mass assembly and stellar ages of nearby galaxies have all been associated with downsizing, creating some confusion over its implications towards galaxy evolution (Fontanot et al., 2009).

Archaeological downsizing refers to observational evidence of stars in early type galaxies being formed much quicker than those in bluer galaxies (Heavens et al., 2004; Thomas et al., 2005; Neistein et al., 2006; Thomas et al., 2010). This is illustrated in Figure 1.5 where we see the ranges of time for star formation activity in galaxies of different masses. This effect is in line with the observed galaxy colour bi-modality covered in a Section 1.4.1. One of the plausible explanations of how downsizing is not in conflict with the hierarchical model, is by implying feedback processes such as AGN, which quench star forming activity in the early type galaxies after they have reached a certain critical mass (Cattaneo et al., 2008). Another aspect to downsizing is the case of specific star formation rate, where more actively star forming galaxies are more massive as a function of redshift (Cowie et al., 1996; Brinchmann & Ellis, 2000; Juneau et al., 2005). This latter version of downsizing is less related to mass as it focuses mainly on delayed star formation a lower redshift ($z \leq 1$) (Neistein et al., 2006).

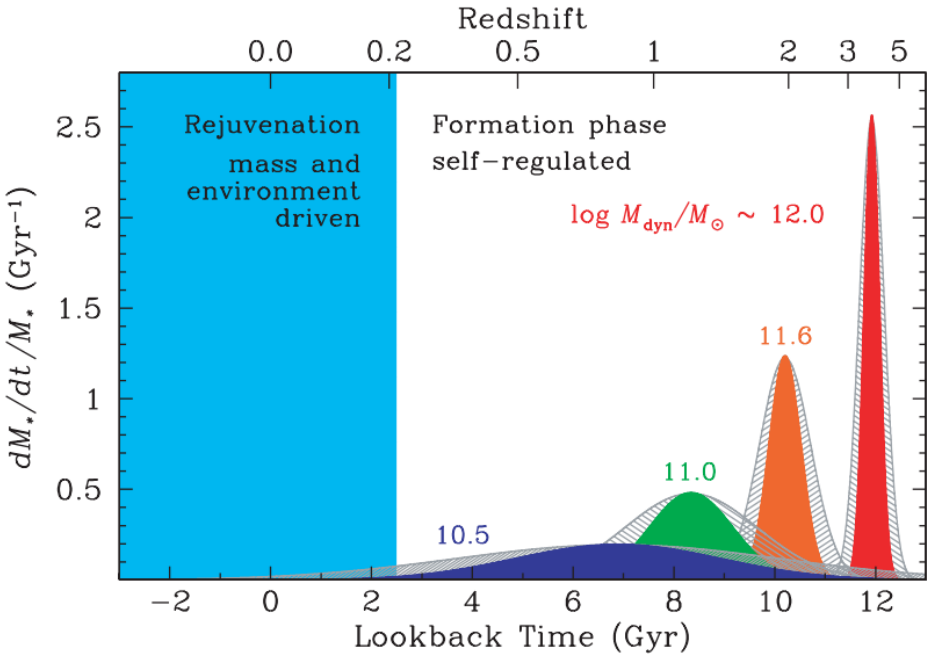

Figure 1.5: Specific star formation rate (SFR/M_*) as a function of lookback time or redshift. The different peaks illustrate the expected average star formation history for different galaxy masses with grey hatched areas the expected uncertainty regions around the central peaks. The figure illustrates how archaeological downsizing has happened over the history of the universe with massive galaxies forming quickly over short period of time, while the lower the mass of the galaxies, the more diffuse and continuous the star formation process is. Image Credit: Thomas et al. (2010).

1.6 Star formation

Star formation (SF) is the transformation of gas (mainly hydrogen) from the interstellar medium (ISM) into stars after gravitational collapse has happened and stellar nucleosynthesis has been ignited. Surprisingly, even though the topic is of great importance to astronomy in general, the details of SF is still relatively poorly understood due to several reasons. On one hand, understanding SF relies on a good physical modelling of supersonic non-ideal magnetohydrodynamics turbulence, which is still currently lacking (Krumholz, 2014). On the observational side, it is only over the last few years, owing especially to the advent of telescopes such as ALMA, that astronomers have had access to deep high-resolution images of the deeply obscured regions of SF (for example see Ohashi et al. (2014)). Prior to that, directly probing the details of the different mechanisms involved was difficult.

SF mainly happens in dense gaseous regions of the ISM called giant molecular clouds (GMC) (Lada & Lada, 2003), which have masses in the range of $10^5 - 10^6 M_\odot$, and sizes in the range of a few tens of parsecs, and have lifetimes of $\sim 10^7$yr (Mo et al., 2010). The GMC are highly dense regions where molecular hydrogen H_2 is formed from neutral atomic gas (HI). When some of the regions exceed the Jean's mass (Tohline, 1980), the regions will collapse under their gravity forming protostars - the first stage of stellar evolution. This system will continue to gain mass through accretion until nuclear reactions are sparked to give birth to new stars. Protostars, sometimes referred as cores, are subset to larger regions of star-forming clusters known as clumps, which themselves are subset to the GMC, vaster regions containing all these elements of different scales (McKee & Ostriker, 2007).

Once a first generation of stars is formed from the GMC, feedback processes self-regulate the global star formation process. Strong winds from the massive young stars such as OB stars will ionise and sweep away the remaining surrounding gas (Bastian & Goodwin, 2006) and dust. During their lifetimes OB stars are strong emitters of UV radiation, which ionise the surrounding gas. At the end of their short lives, the OB stars die in supernova explosions which are responsible for removing gas in neighbouring regions (Iffrig & Hennebelle, 2015).

As GMCs are an essential component in active star formation, their presence indicates and traces the amount of star formation happening inside a specific galaxy. It can then be deducted that, GMC are more and more prevalent moving along the Hubble sequence towards the later type of galaxies. Usually GMCs are found in the spiral arms, where the tidal waves going through the plane of the arms help to compress the gas present fostering the formation of clouds.

1.7 Tracers of star formation

Star formation involves many processes happening simultaneously, as well as a range of different stellar/interstellar objects. Therefore various tracers can be used as probes to quantify the amount of star formation happening in different galaxies. Several of the relevant SF indicators are introduced below.

1.7.1 Ultraviolet

Young populations of stars ($< 10^8$ yr) usually contain significant amounts of massive OB stars which are are short lived ($10^5 - 10^7$ yr) and have high surface temperatures (10,000 - 60,000 K). At these sort of temperatures, black-body radiation peaks in the UV, which is why young stellar populations emit a considerable amount of their radiation in the UV. Since the advent of balloons, rockets and satellites telescopes, many observations in the UV have been to measure and quantify star formation (Israel & Koornneef, 1979; Lequeux et al., 1981; Meurer et al., 1995; Leitherer et al., 1995; Salim et al., 2007). The advantage of UV is that it is a direct measurement of the light emitted by the young stars themselves, but unfortunately it is also highly affected by obscuration by dust in those regions generally. In addition, any conversion of UV flux to an actual SF value will be IMF (Initial Mass Function see section 3.3.1) dependent, because the fraction of massive stars is different in each IMF. Nevertheless, Kennicutt (1998a), using a Salpeter (1955) IMF, introduced the following relationship:

$$\text{SFR } (M_\odot \text{ yr}^{-1}) = 1.4 \times 10^{-28} L_\nu \text{ (ergs s}^{-1} \text{ Hz}^{-1}), \tag{1.2}$$

where L_ν for the wavelength range $1500 - 2800\,\mathring{A}$ valid for time-scales longer that $t > 10^8\,yr$. The relation is applicable for a wide range of redshift because it is based on the light emitted by young stellar populations. But this equation requires accurate extinction correction and is dependent on the assumed IMF (Kennicutt, 1998a). The equation 1.2 was updated in Kennicutt et al. (2009) by taking into account a more realist Kroupa IMF (Kroupa, 2002) and is described by:

$$\text{SFR } (M_\odot \text{ yr}^{-1}) = 8.8 \times 10^{-29} L_\nu \text{ (ergs s}^{-1} \text{ Hz}^{-1}), \tag{1.3}$$

1.7.2 Optical

Since OB stars are short lived, their presence indicates, for a particular cloud, that star formation was triggered in the very recent history. The strong winds they blow contain highly ionised particles which in turn ionise the interstellar medium in the neighbouring region of the young stars. Free electrons of this ionised gas will then recombine with the atoms, jumping from

highly excited states to lower excited states. Through this process, photons corresponding to the quantum leaps from one excited state to another are emitted. This follows from basic quantum mechanics of the Bohr's model and the wavelength of emitted photon is given by Rydberg's formula. In the case of hydrogen gas, several possible transitions are possible, such as the Lyman, Balmer, Paschen and Brackett series. The Balmer series is visible in the optical, with Hα at 6562.8 nm being the strongest of the emitted recombination lines. It is a very good indicator of current star formation ($<$ 20 Myr). By using evolutionary synthesis modelling, $H\alpha$ can be converted to SFR, after work done to calibrate the relationship (see for example Kennicutt (1983); Leitherer & Heckman (1995)). The following equation given by Kennicutt (1998a):

$$\text{SFR } (M_\odot \text{ yr}^{-1}) = 7.9 \times 10^{-42}\ L_{H\alpha} \text{ (ergs } s^{-1}) = 1.08 \times 10^{-53}\ Q(H^0)\ (s^{-1}), \tag{1.4}$$

where Case B recombination at T_e= 10,000 K is assumed for $H\alpha$ and $Q(H^0)$ is the ionising photon luminosity. This relation was updated in Kennicutt et al. (2009) by using the Kroupa IMF, taking into consideration extinction and take the form:

$$\text{SFR } (M_\odot \text{ yr}^{-1}) = 5.5 \times 10^{-42}\ [L(H\alpha)_{obs}\ + a_\lambda L_\lambda](\text{ergs } s^{-1}), \tag{1.5}$$

where the term a_λ takes care for internal dust extinction.

The presence of heavier metals in the interstellar medium in addition to hydrogen means that it is highly likely there are emissions from those heavier elements when the cloud of gas is ionised. Due to the low densities of gas ($n_e \leq 10^4$ cm^{-3}), forbidden lines, which are lines that cannot be reproduced in the laboratory on earth, are very commonly observed. The [OII]λ3727 doublet is one of the lines in the blue part of the spectrum that can be empirically calibrated and be used as a star formation rate (SFR) tracer Kennicutt (1998a). In the cases of surveys of redshift, z $>$ 0.4, $H\alpha$ is redshifted beyond the optical window (Aragón-Salamanca et al., 2003). [OII]λ3727 is then chosen instead to measure the amount of star formation since it is observable in the optical until $z \sim 1.15$, although it is highly dependent on variations of chemical abundance, ionisation and dust extinction (Moustakas et al., 2006). By using the calibration of several surveys (e.g. Gallagher et al. (1989); Kennicutt (1992b)) and making similar assumptions (Case B recombination) as described earlier, Kennicutt (1998a) introduced the following conversion:

$$\text{SFR } (M_\odot \text{ yr}^{-1}) = (1.4 \pm 0.4) \times 10^{-41}\ \text{L[OII] (ergs } s^{-1}), \tag{1.6}$$

where the lower limit value is applicable for bluer galaxies while the upper limit is valid for the spirals and irregulars. Extinction correction must be done at the Hα line in this case because of the method used to calibrate the relation. This relation was then updated to:

$$\text{SFR } (M_\odot \text{ yr}^{-1}) = 5.6 \times 10^{-42} \text{ [L([OII])}_{obs} + a'_\lambda L_\lambda](\text{ergs } s^{-1}), \tag{1.7}$$

by Kennicutt et al. (2009) similarly to Equation 1.2 and 1.4 by assuming a Kroupa IMF where a'_λ is a different dust extinction coefficient to that of a_λ.

1.7.3 Infrared

It was brought forward earlier that star forming region emit a lot of light in the UV due to the presence of OB stars. It is known that star forming regions are high in dust content and thus have high extinction. Interstellar dust reprocesses light by first absorbing the UV emission of hot OB stars, then heating up like a black-body in the process and re-emitting the light isotropically in the far infrared regime. There are other processes, that in principle can be responsible for dust to get heated and then emit in the IR, such as any very strong interstellar radiation fields or Active Galactic Nucleus (AGN) activity, but their contributions are negligible when young stellar populations are dominant, as is the case in starburst galaxies. By using similar assumptions as explained in the sections above, Kennicutt (1998a), derived the correlation between FIR luminosity and SFR as follows:

$$\text{SFR } (M_\odot \text{ yr}^{-1}) = 4.5 \times 10^{-44} L_{FIR} \text{ (ergs s}^{-1}). \tag{1.8}$$

The infrared luminosity in this case is a fully integrated luminosity from 8 to 1000 μm and the assumption is that the relation applies for regions of age $< 10^8$ years. Since there are different possible strong sources of light in the IR, for different types of galaxies, a universal calibration for all galaxies cannot be applied with the above equation.

1.7.4 Radio

Atomic hydrogen is detected at 21 cm wavelength (radio) due to its spin-flip transition, molecular hydrogen on the other hand has no dipole moment and therefore no rotational transitions. Since the molecule is unlikely to be excited by the temperature of the gas, the only option to probe for its presence is to use carbon monoxide (^{12}C ^{16}O, CO), which is the second most abundant molecule in GMCs. Loren et al. (1973) were the first to observe CO molecules using radio waves in Nebular environment near young stars, which was then followed by other authors to show the association of CO with star formation in the galaxy (Woodward, 1976; Knapp & Morris, 1976; Gordon & Burton, 1976). Since the relationship between CO and H_2 was found, much work has been focused on the calibration of the conversion ratio, which is now known to be around 1 CO molecule for every 10,000 H_2 molecules (Magnani & Onello, 1995; Neininger et al., 1998; Bolatto et al., 2013; Clark & Glover, 2015).

Murphy et al. (2012) using the work from Kennicutt (1998a) and their updated work in Kennicutt et al. (2009), found a conversion for radio luminosity to SFR similar to the other wavelengths (UV, Optical and IR). The relation in this case uses Kroupa (2001) IMF and Starburst99 (Leitherer et al., 1999) to derive an equation which has a factor of ∼1.5 difference compared to equations derived with Salpeter IMF. The equation assumes high radio frequencies and links thermal spectral luminosity, L_ν^T, with electron temperature, T_e, with a SFR as follows:

$$\mathrm{SFR}_\nu^{\mathrm{T}}\ (M_\odot\ \mathrm{yr}^{-1}) = 4.6 \times 10^{-28} \left(\frac{T_e}{10^4\ \mathrm{K}}\right)^{-0.45} \left(\frac{\nu}{\mathrm{GHz}}\right)^{0.1} \times \left(\frac{L_\nu^{\mathrm{T}}}{\mathrm{ergs\ s^{-1}}}\right). \tag{1.9}$$

By assuming standard calibrations between the supernova rate and non-thermal synchrotron radiation, the equation can be generalised to all frequencies as follows:

$$\mathrm{SFR}_\nu\ (M_\odot\ \mathrm{yr}^{-1}) = 10^{-27} \left[2.18 \left(\frac{T_e}{10^4\ \mathrm{K}}\right)^{0.45} \left(\frac{\nu}{\mathrm{GHz}}\right)^{-0.1} + 15.1 \left(\frac{\nu}{\mathrm{GHz}}\right)^{-\alpha^{NT}}\right]^{-1} \left(\frac{L_\nu}{\mathrm{ergs\ s^{-1}\ Hz^{-1}}}\right), \tag{1.10}$$

where the radio emission has both free-free and synchrotron components, and α^{NT} is the non-thermal radio spectral index (Condon & Yin, 1990).

1.7.5 Empirical law

Schmidt (1959) was the first to empirically derive a formula between star formation rate and local gas density through a power-law. The equation takes the form of

$$\sum_{SFR} = A\ \sum_{gas}^{N}, \tag{1.11}$$

where $\sum_{SFR}$ is the SF surface density and $\sum_{gas}$ is the gas (both molecular or atomic, or the sum of both) surface density and the constant A, is the star formation efficiency. In the 1990s, when large surveys became possible, astronomers were able to gather enough data on normal galaxies to confirm the relationship. By studying 61 normal galaxies and starburst galaxies Kennicutt (1998b) generalised the empirical function. It was done using photometric measurements of Hα as an indicator of absolute star formation rate, along with data of HI and CO. The derived correlation from the Schmidt law had an index N = 1.4 ± 0.15.

We now introduce the gas depletion time as being the ratio of total gas in a galaxy to the rate at which stars are being formed (SFR), which leads to: $t_{dep} = M_{gas}/\dot{M_{gas}}$. This parameter is in fact a measure of star formation efficiency, i.e how much stars are being formed from the total mass of gas available. In the case of starburst galaxies, t_{dep} is in the range of $10^7 - 10^8$ yr,

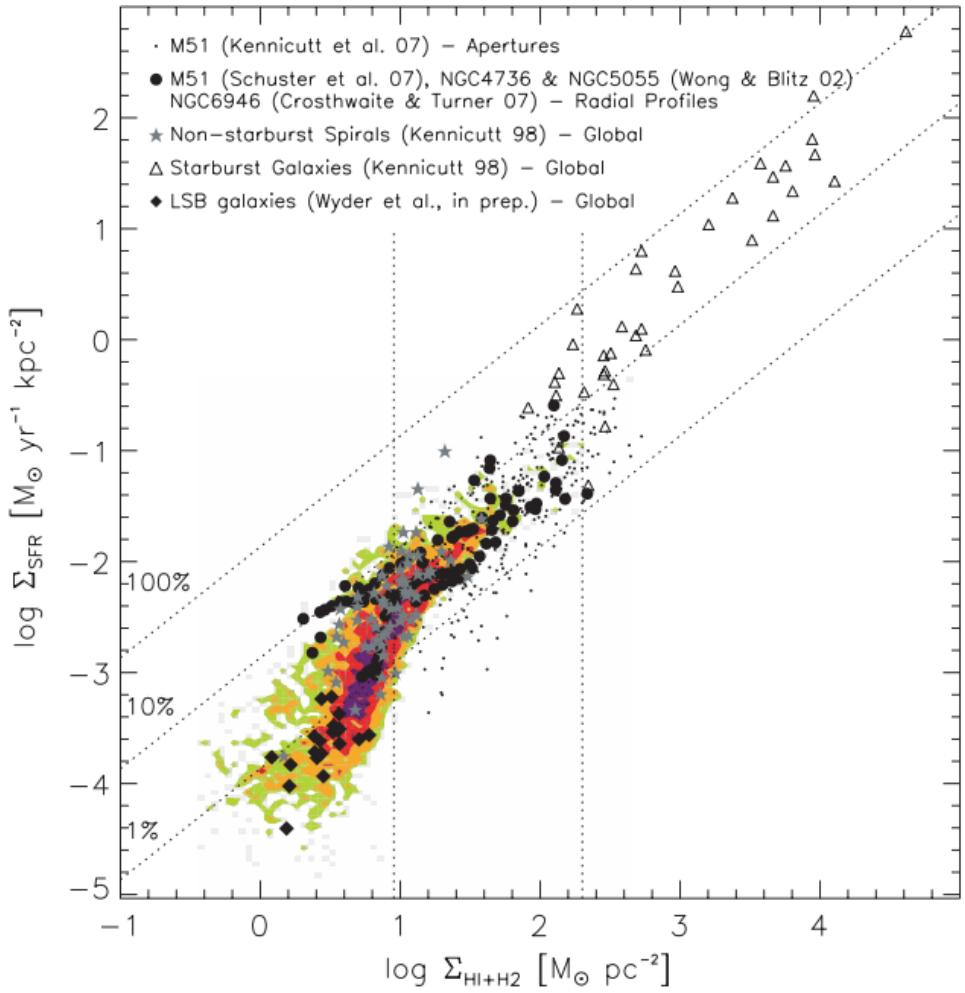

Figure 1.6: The correlation between surface density of gas, $\sum_{HI+H_2} = \sum_{gas}$ and surface density of star formation, $\sum_{SFR}$. The data used are from various surveys/papers listed in the plot along with data gathered from sub kiloparsecs surveys (The HI Nearby Galaxy Survey, THINGS, (Walter et al., 2008), the BIMA Survey of Nearby Galaxy, (Regan et al., 2001) and HERA Extragalactic CO Line Extragalactic Survey, (Leroy et al., 2009)). The diagonal lines indicates loci of constant star formation efficiency or gas depletion times from top to bottom, 10^8, 10^9, 10^{10} yr. Image credit: Bigiel et al. (2008).

while for normal galaxies the value extends to an order of magnitude higher (Mo et al., 2010). Figure 1.6 shows the Kennicutt-Schmidt law as observed in nearby galaxies from a study done by Bigiel et al. (2008). Above a surface density of gas of, $\log(\sum_{HI+H2}) > 1$ M$_\odot$ pc^{-2}, the relation between $\log \sum_{gas}$ and $\log \sum_{SFR}$ is linear and follows a more or less constant depletion time. Figure 1.7 on the other hand displays the relationship of only molecular gas with star formation surface density. This time the data is purely linear, following closely a single depletion rate, across the range of values available. The variation seen in Figure 1.6 is due to the ISM being

dominated by molecular hydrogen at large surface densities while at lower surface densities, it is the atomic hydrogen which is the driving force in the gas (Krumholz, 2014). Star formation hence follows more closely the presence of H_2 than it follows HI. Bigiel et al. (2008) also found that molecular hydrogen has a constant SF efficiency for all types of spirals, with an average gas depletion time of $\sim 2 \times 10^9$ yr. For full reviews on star formation see McKee & Ostriker (2007) and Krumholz (2014).

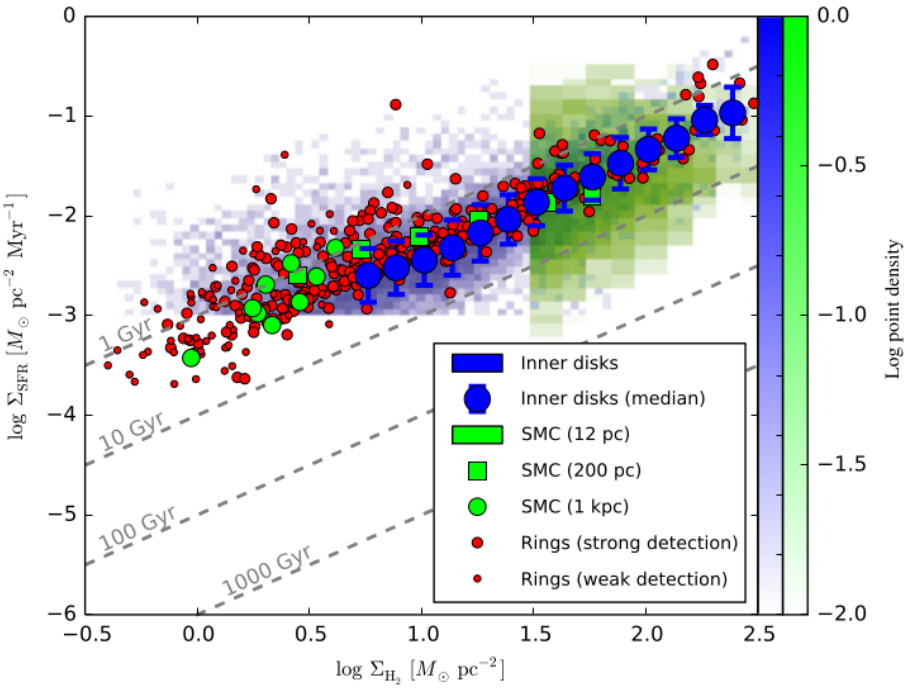

Figure 1.7: Three datasets (Blue pixels and Blue Circles (Leroy et al., 2013; Bigiel et al., 2008), Green pixels (Bolatto et al., 2011), Red points (Schruba et al., 2011)) overplotted on each other showing relationship of molecular gas $\sum_{H_2}$ with SF surface density $\sum_{SFR}$. Image credit: Krumholz (2014).

1.8 Scaling relations

Large sample of galaxies display many relationships between their many observable properties. The underlying reasons for such connections is that that there are fundamental physical processes driving the galaxy formation and subsequent evolution which are then seen in the correlations of the observable parameters of the galaxies. Scaling relations are usually correlations between two parameters with small scatter (Somerville & Davé, 2015). By studying those tight correlations, astrophysicists hope in essence to reverse engineer, the underlying processes driving extragalactic astronomy. Scaling relations are various: some link luminosity with rotation speed of disk

galaxies (Tully & Fisher, 1977) or size, velocity dispersion and surface brightness for ellipticals (Djorgovski & Davis, 1987) or the mass of super massive black holes (SMBH) with many different galaxy properties (see Kormendy & Ho (2013)). There are many scaling relations, in fact even the Kennicutt-Schmidt law described in the previous section is one of them. We explore only two very relevant scaling relations in the sections below.

1.8.1 Mass-Metallicity relation

Metallicity is a crucial parameter in understanding the evolution of galaxies as it is a by product of stellar evolution. Galaxies are characterised by their stellar mass, which is the amount of gas locked up in stars, and since their metallicity usually derives from how much gas has been processed into heavier elements, a link between the two parameters is natural. However, galaxies are very dynamical objects with gas inflows and outflows, which alters the observed metallicity. Metallicity is therefore not purely a proxy of the stellar evolution happening in situ, but instead a more complex parameter. However, it is still a powerful parameter and while there were early studies of it (Lequeux et al., 1979), it is only through large scale surveys such as the Sloan Digital Sky Survey (SDSS, York et al. (2000)) that the relationship between mass and metallicity (MZ) became evident.

Figure 1.8 shows the observed variation of metallicity at different mass bins for a sample of $>$ 53,000 star forming galaxies. The more massive, early-type galaxies are more chemically evolved galaxies with lower scatter than the younger, late-type galaxies. The flattening of the metallicity at higher mass could be explained in several ways. Firstly, higher mass galaxies have deeper potential well which makes it more difficult for enriched gas to leave the galaxy through galactic winds (outflows) (Tremonti et al., 2004; Kobayashi et al., 2007; Ma et al., 2016). The second reason that could explain this feature is gas inflows that mixes with the enriched gas of galaxies to lower their observed metallicity. However, this model is unlikely because of the lower mass galaxies usually have high gas mass fractions(Tremonti et al., 2004; Finlator & Davé, 2008). Another possibility is the variation of stellar IMF at different epochs (low vs high) of star formation could lead to the observed relationship (Köppen et al., 2007; Recchi & Kroupa, 2015). The MZ relation has been confirmed to exist at different epochs of the universe (Savaglio et al., 2005; Erb et al., 2006; Zahid et al., 2011; Izotov et al., 2015; Ma et al., 2016) though possibly some evolution of the function has been suggested (Zahid et al., 2014).

1.8.2 SFR-mass relation

Star formation rate is another parameter that is closely linked to mass as was discovered with the era of large surveys starting from the SDSS onwards. Since star formation is the process of converting gas into stars over time, it is intuitive to see how it is linked to stellar mass of

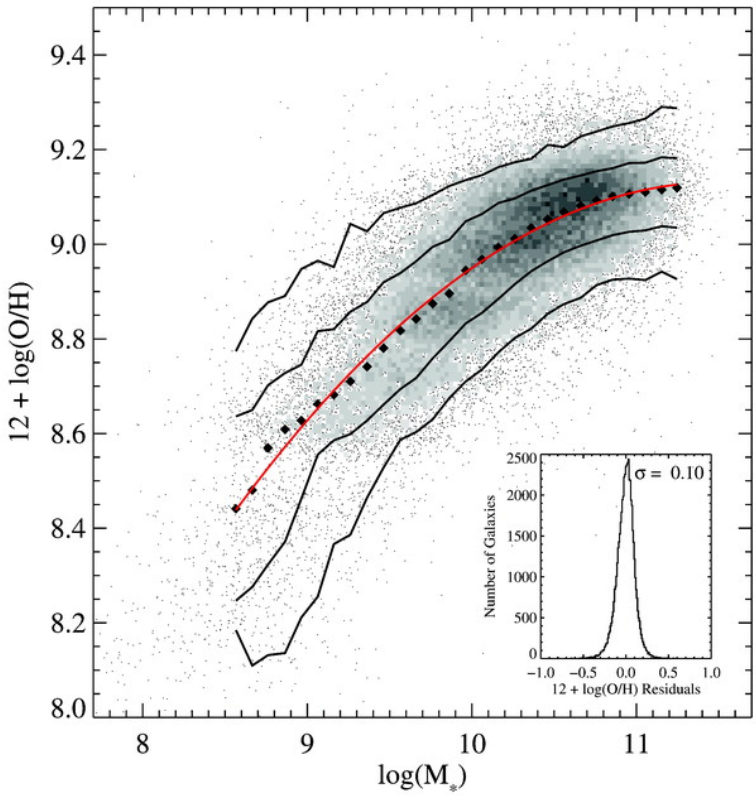

Figure 1.8: Stellar mass vs. gas-phase oxygen abundances in the SDSS survey for $\sim$ 53400 star-forming galaxies. Large black points are the median for the bins of 0.1 dex of mass. Red line is a polynomial best fit line to the median value, with the 2 sets of contours showing the 1-σ and 2-σ confidence level for the fitting. A residual plot is shown in the embedded window. Image credit: Tremonti et al. (2004).

galaxies through a tight correlation. Galaxies forming the tight relation are known as main sequence (MS) galaxies. and as one goes up the main sequence an increasing amount of dust extinction is also observed (Wuyts et al., 2011; Whitaker et al., 2012). This picture is illustrated by the left panel of Figure 1.9, where the coloured arrow shows the position of the main sequence of galaxies and the observed increase in dust, with stellar mass of galaxies (Reddy et al., 2006; Wuyts et al., 2011). The right panel of the same figure shows the observed trend from separately for different redshifts (Elbaz et al., 2007; Noeske et al., 2007; Daddi et al., 2007). Daddi et al. (2010), using CO as a proxy for molecular mass and L_{IR} as a tracer for SFR, suggested that the mode of star formation for MS galaxies is different to that of starbursts. The authors favours a scenario where mergers or dense nuclear regions are the triggers for the extreme SF observed in the starbursts, as opposed to e.g. top-heavy IMF. From a hierarchical perspective, therefore, galaxies are expected to grow upwards along the MS sequence through mergers until their star formation is quenched (discussed in Section 1.9) and the galaxies then moving vertically down-

ward in the diagram.

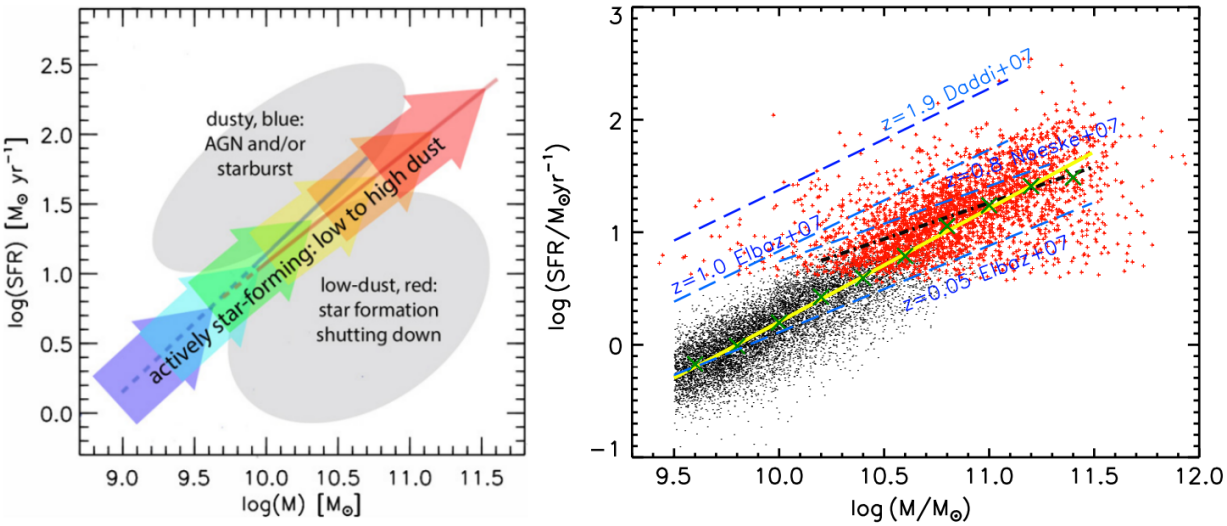

Figure 1.9: SFR as a function of Mass. *Left Panel* : A schematic diagram showing the expected position of the main sequence along the diagonal line with Starburst galaxies higher above than the main sequence. Green valley galaxies and red galaxies are expected to slowly fade away lower than the main sequence. Image credit: Whitaker et al. (2012). *Right Panel*: A comparison of the evolution of the main sequence with redshift from different observational studies (Elbaz et al., 2007; Noeske et al., 2007; Daddi et al., 2007) Image credit: (Guo et al., 2013).

Finally, Mannucci et al. (2010) and Lara-López et al. (2010) showed that in fact all three parameters, namely, mass, metallicity and SFR, can be mapped onto a plane for galaxies up to a redshift of $z = 3.5$, within uncertainties. Mannucci et al. (2010) named the relationship the fundamental metallicity relation (FMR) and went on to argue that such a plane can be explained by the balance between the inflow of low metallicity gas and the removal of enriched gas through outflows.

1.9 Galaxy interactions

In a hierarchical universe, galaxies are constantly interacting and merging with each other to form larger, more massive galaxies. It was the seminal work of Toomre & Toomre (1972), with rudimentary yet effective N-body simulations, that set up the landscape to study interactions of galaxies. They showed that major mergers results in the creation of tidal tails, and the process also randomises stellar orbits. Further investigations lead to the hypothesis, that mergers could be responsible for the conversion of spiral galaxies to bulge dominated galaxies (Toomre, 1977). Interactions play a key role the transformation process of galaxies from late-type to early-types,

and the growth of stellar mass (Kormendy & Sanders, 1992; Tran et al., 2005; Lotz et al., 2008). Furthermore, the gravitational forces can impact the life of galaxies by triggering of star formation (Hernquist & Mihos, 1995; Hopkins et al., 2013), by forming and regenerating bars (Friedli, 1999; Berentzen et al., 2004; Martinez-Valpuesta et al., 2017) and by sparking AGN activity (Hernquist, 1989; Chiaberge et al., 2015).

1.9.1 Major mergers

Major mergers describe the interaction of gravitationally bound galaxies of comparable masses (mass ratios up to 3:1), which would have significant impact on their separate structures and the subsequent product (Benson, 2010). Bournaud et al. (2005) showed that interactions in the mass range of major mergers usually leads to elliptical type remnants. When the mass difference is too large - like in the case of minor mergers - structures such as spiral disks are not dramatically affected. Mihos & Hernquist (1996) showed through simulations that the remnant of a major merger will drive a considerable gas fraction towards the central regions of the remnant that will spark a short burst of intense star formation often called a starburst. Mihos & Hernquist (1996) also showed a distinction between disk galaxy collisions and collisions involving at least one bulge dominant galaxy. In the first case SF activity occurs mainly during the first passage, while in the second case SF activity is delayed until the last stages of merging.

1.9.2 Minor mergers

Minor mergers usually happens when bigger galaxies (above a mass ratio of 4:1) 'eat' smaller ones by absorbing all the stars of the secondary galaxy, while not destroying their own disk. While studies focus mainly on major mergers, which have a major impact on the galaxies involved, minor mergers are thought to be much more common (Ostriker & Tremaine, 1975; Mihos & Hernquist, 1994) in a hierarchical universe as smaller galaxies provide the small building blocks to form bigger ones. In fact, their contribution to the star formation budget of the local universe is thought to be around 40% (Kaviraj, 2014). Minor merging has been proposed as the trigger that enables the fuelling of nuclear activity seen in Seyfert galaxies (Taniguchi, 1999; González Delgado et al., 2002), analogous to how major mergers are linked to Quasar activity (Sanders et al., 1988; Hopkins & Hernquist, 2009).

1.9.3 Evolution scenario

Hopkins et al. (2008) describes the different steps that take spirals to ellipticals through the major merger process as shown in Figure 1.10. A typical expected time-line of the model is also

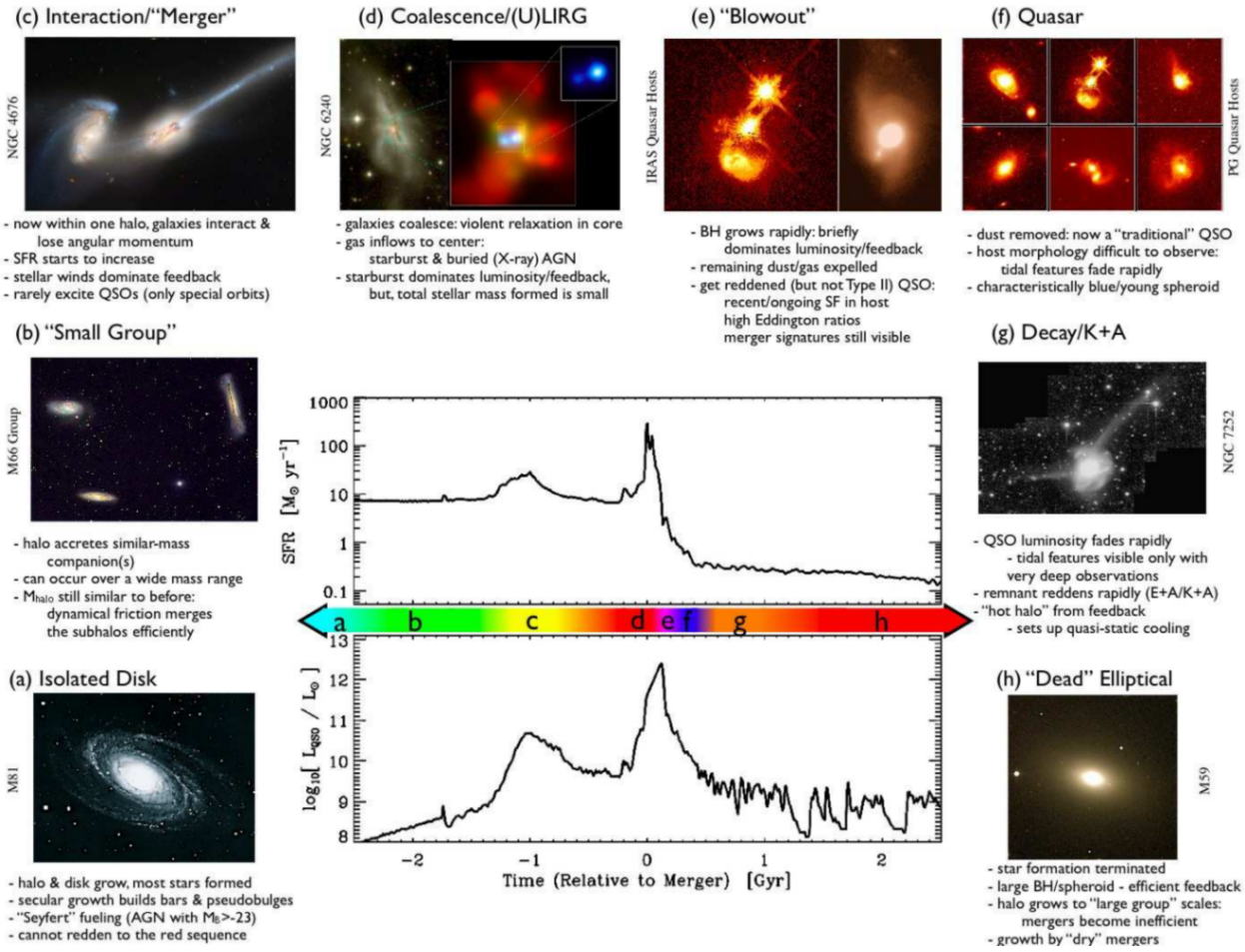

Figure 1.10: The 8 steps that a typical late-type galaxy undergo during a gas-rich major merger. The middle plot is a typical time-line of when the different stages occur and their overall impact on SF and AGN activity. Image credit Hopkins et al. (2008)

given in the diagram, showing the different time-scales involved. A summary of the different stages involved is given below. The first stage is the formation of an isolated galaxy that has a rotationally supported disk with arms, bars and a halo, which is then attracted into the potential well of small galaxy clusters (stage a & b). At this stage, low level AGN activity such as Seyfert nucleus may be active at the core of the galaxy. As the galaxies approach the pericenter and intersect each other (stage c) there is a rise in SF activity due to the tidal interactions while AGN activity is still at the original level, unless there is a special angle of collision. At the next stage (d), the galaxies coalesce together, which funnels gas inflows. In turn this will spark starburst activity, possibly taking the infrared luminosity to LIRGs or ULIRGs level, and will also increase the activity of the AGN at the centre. While during the first three stages stellar winds were the main feedback, at fourth and fifth stages (d & e), starburst feedback (mixture

of both stellar winds and supernova explosions), along with AGN feedback will drive gas and dust outwards in a 'blowout' phase. This will in turn decrease the available hydrogen to sustain the starburst or AGN activity, keeping the rise in activity to a minimum. The latter stages are the slow 'death' of the merged galaxy. The highly extincted QSO (due to dust) slowly moves to an optical QSO as dust is removed through feedback. The signatures of the merger are slowly erased with the formation of a blue spheroid. Finally, since gas is either used up in the formation of stars or removed through feedback, the stellar population grows older and the motion of the stars relaxes to mimic an elliptical.

1.9.4 Impact on stellar population

Mergers have a huge impact on the host galaxies as was previously described. With the funnelling of gas through inflows which then spark massive amount of star formation, which can even lead to starburst periods, the properties of the stellar populations present in the host and of the eventual merger remnant are expected to be permanently changed. Recently, Cook et al. (2016) found from the ILLUSTRIS galaxy simulations that the stellar population gradients in the stellar halo ($2 - 4\ R_e$) are good tracers of galactic accretion histories. Simulations also showed that the star formation due to merging is strongly correlated with the mass ratio of the two progenitors with major mergers being stronger (Cox et al., 2008). Observationally, metallicities of major mergers have been known to be non-existent or very shallow (Kewley et al., 2006; Miralles-Caballero et al., 2012). Bekki & Shioya (1999) demonstrated using simulations that the central areas of galaxies will end up younger and more metal rich that the outer regions for disk galaxies of gas rich major mergers.

In the case of minor mergers, which have been under-studied, Mihos & Hernquist (1994) showed that they can also experience strong starbursts but mostly at higher redshifts where they were devoid of bulges, which have the effect of suppressing gas inflows. Krabbe et al. (2011), studied a minor merger, and showed that it had a very flat oxygen abundance profile, deducing that tidal gas flows due to the interaction were the main reason for this lack of a gradient.

1.10 LIRGs

1.10.1 Background

The InfraRed Astronomical Satellite (IRAS) (Neugebauer et al., 1984) was a telescope of 60cm diameter developed within a consortium consisting of the US, the UK and the Netherlands, that was sent to space in 1983. It surveyed 96% of the whole sky, in four bands centred around 12, 25, 60 and 100 μm detecting around 20,000 new galaxies in the Point Source Catalogue (1988). Before the IRAS era, it was already known that some galaxies could emit more light in the IR

domain than in the optical regime (Low & Kleinmann, 1968; Kleinmann & Low, 1970; Rieke & Low, 1972) and in some extreme cases even 99% of the bolometric luminosity was in the IR (Soifer et al., 1984).

These objects were characterised much more fully in the post-IRAS era. Luminous InfraRed Galaxies (LIRG) was designated to galaxies having luminosities ranging $10^{11}L_{\odot} \leq L_{IR} < 10^{12}L_{\odot}$ and their more energetic counterparts, the ULIRGs, were classified having $10^{12}L_{\odot} \leq L_{IR} < 10^{13}L_{\odot}$ (Sanders & Mirabel, 1996). In the extreme cases where the $L_{IR} > 10^{13}L_{\odot}$ the galaxy is referred to as a hyper-LIRG but these are quite rare and sometimes even included in the ULIRG group. It is important the understand, however, that these limits were chosen out of a mere mathematical convenience of classification, without any physical meaning (though there are differences in the galaxies as the L_{IR} grows as is discussed below).

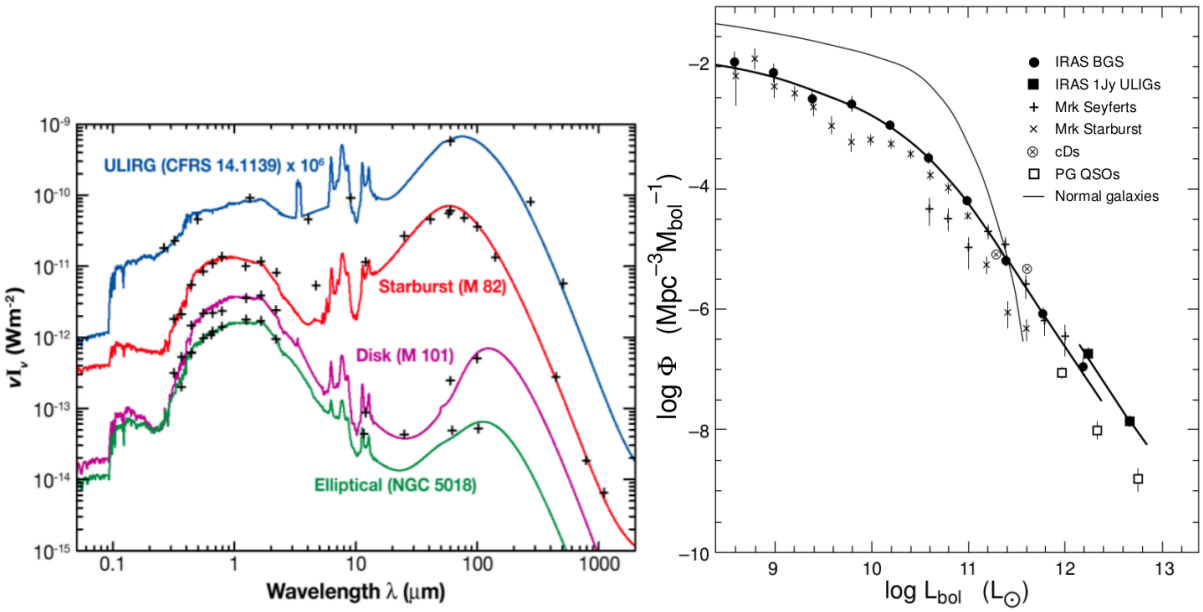

Figure 1.11: *Left Panel*: The comparison of the SED of Elliptical (NGC5018), Spiral (M101) , Starburst (M82) and ULIRG (at redshift 0.66). While SED will vary from galaxy to galaxy, this gives a view of the difference in of the IR emission of ULIRGs and Starburst galaxies as compared to main sequence galaxies. Image credit Lagache et al. (2005). *Right Panel*: The comparison of the luminosity function between infrared galaxies and other extragalactic objects taken from Sanders & Mirabel (1996). The darker line is a fit through the data points of IRAS Bright Galaxy Sample (BGS). The other thick line at the bottom right uses data from IRAS 1Jy catalog. The thin line illustrates the luminosity functions of normal galaxies

The cause of such high emission in the IR is due to dust enshrouded star formation, a strong AGN activity (usually QSO), or a combination of both. The main explanation for the amount of IR

light emitted is the reprocessing of light, from shorter wavelengths to the longer IR wavelengths, by the dust around star formation regions or AGN. The definition of L_{IR} from Sanders & Mirabel (1996) is as follows:

$$L_{IR} = L(8 - 1000\ \mu m) = 4\pi \mathrm{D}_L^2\ F_{IR}\ \ [L_\odot], \tag{1.12}$$

where the total flux, $\mathrm{F_{IR}} = 1.8 \times 10^{-14}\{13.48 f_{12} + 5.16 f_{25} + 2.58 f_{60} + f_{100}\}$ $[Wm^{-}2]$ with f_{12}, f_{25}, f_{60} and f_{100} being the fluxes in the 4 different IRAS bands. D_L is the luminosity distance with any assumed set of standard cosmological parameters. Similarly, F_{FIR} is calculated to be:

$$L_{FIR} = L(40 - 500\mu m) = 4\pi D_L^2 C F_{FIR}\ \ [L_\odot], \tag{1.13}$$

where C is a scale factor correcting for extrapolated flux in the IRAS Survey and F_{FIR} is set to be $1.26 \times 10^{-14}\ \{2.58 f_{60} + f_{100}\}$ $[Wm^{-}2]$.

Since the IRAS days, much progress has been accomplished in getting a better understanding of those objects with the advent of more sophisticated surveys, like ISO (Kessler et al., 1996), Spitzer (Werner et al., 2004), AKARI (Matsuhara et al., 2006) and the Herschel Space Observatory (Pilbratt et al., 2010). In the next sections we give a summarised description on some of the relevant features of (U)LIRGs. For a full review on the subject see e.g. Lonsdale et al. (2006).

1.10.2 Properties of (U)LIRGs

The high amount of infrared emission is due to the amount of dust present inside a galaxy, which will absorb radiation to re-emit in the infrared. This is illustrated in the left panel of Figure 1.11, where there is a huge boost particularly in the infrared, in the spectral energy distribution (SED) of LIRGs as compared to standard types of galaxies. Older galaxies tends to have more flux in the near- and mid-infrared regime than the far-infrared regime (FIR). As the galaxy becomes more starburst or AGN dominated, the FIR flux becomes stronger, and the peak of the FIR emission also tends to move towards shorter wavelengths suggesting warmer dust.

From the evolutionary scenario painted in section 1.9.3, it is evident that galaxy interactions play an essential role in triggering either starburst or AGN activity inside most LIRGs and ULIRGs. The differences are further explored in the right panel of Figure 1.11, where the luminosity functions of different objects are compared. The shape of the luminosity function of starbursts and Seyferts are more closely related to ULIRGs (called ULIGs in the diagram) than normal galaxies. For normal galaxies, the standard Schechter function (Schechter, 1976) is usually used to model the Luminosity function. It is essentially a Gamma function i.e. a combination of an

exponential law which regulates the shape at higher luminosities and a power law which operates at the lower luminosity regimes. In the cases of IR galaxies, a double power law with slope $\lesssim -1$ for low luminosities and slope ~ -2.35 for $L_{bol} \gtrsim 10^{10.3} L_{\odot}$ is a better fit to the overall shape of luminosity function instead of the standard Schechter function (Sanders & Mirabel, 1996).

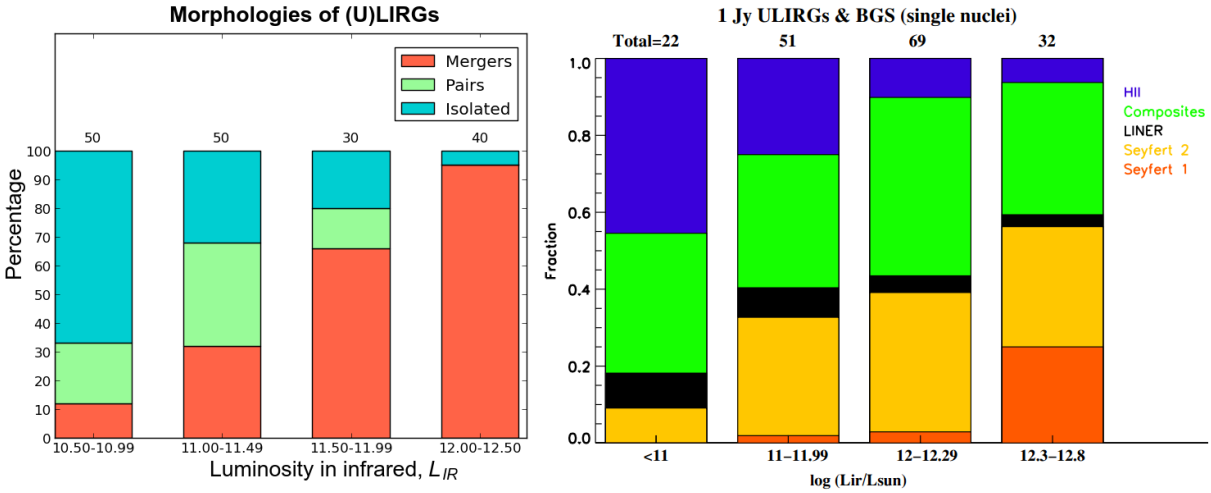

Figure 1.12: *Left Panel*: The Morphology/Interaction stage of (U)LIRGs as a function of IR luminosity. It clearly demonstrates that as we move from the LIRGs to the ULIRGs regime there is a higher rate of merging and lower probability of isolated galaxies. At the top of each bar sits the number of galaxies used to compute the percentage. Image adapted from data of Sanders & Mirabel (1996). *Right Panel*: The spectral classification of the 1 Jy sample from Veilleux et al. (1999) as a function of IR luminosity. AGN activity gradually becomes more dominant while starburst becomes less dominant. Image credit Yuan et al. (2010).

Figure 1.12 shows statistics collected about the various mechanisms present in IR dominated galaxies as a function of luminosity. In the left panel of the figure, is a histogram made from data shown in Table 3 of Sanders & Mirabel (1996). The influence of galaxy interactions/merging is strongly correlated with the IR luminosity and similar trends have been observed more recently with higher resolution data (Larson et al., 2016). The right panel of Figure 1.12 (taken from Yuan et al. (2010)) shows the AGN contribution of different bins of IR luminosity from the same 1 Jy ULIRG sample out of which Veilleux et al. (1999) did an earlier similar study. Using the SDSS classification scheme developed by Kewley et al. (2006) the different subclasses are identified. As we move from LIRGs to the ULIRGs regime, the contribution of AGN grows dominant in the emission of the galaxies, on the expense of SF contribution.

Figure 1.13 shows the total IR luminosity density (red) of the universe as a function of redshift with the contribution of LIRGs and ULIRGs are shown in blue and yellow (Caputi et al., 2007).

Since we know that IR is a direct tracer of SF (from section 1.7), the plot is a rough estimate of the SF history of the universe. While the contribution of LIRGs or ULIRGs is minimal in the local universe, at $z > 1$ they dominate galaxy formation. At $z \sim 2$, LIRGs and ULIRGs amount to 90% of the SF happening in the universe, highlighting the importance of why they are such an important class of objects.

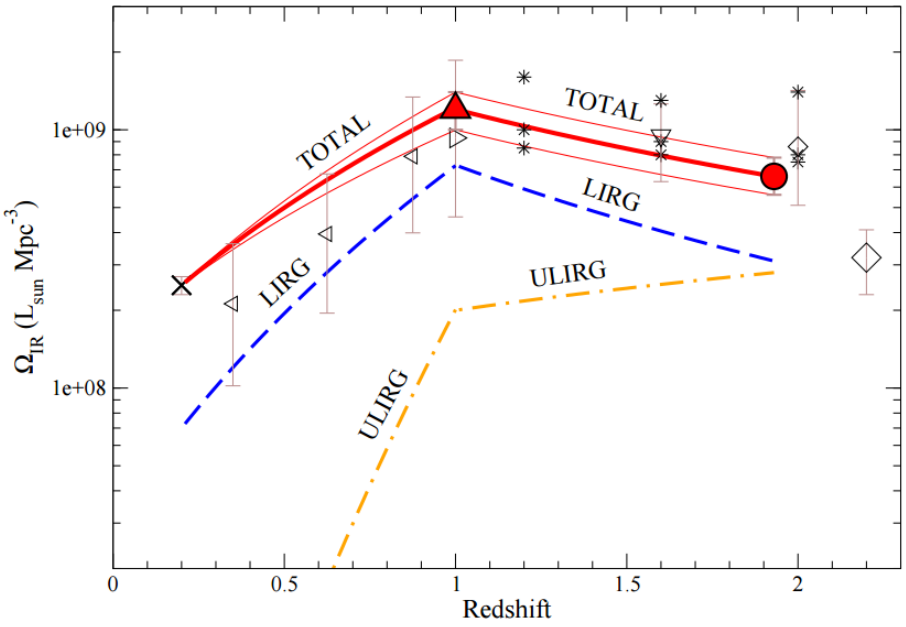

Figure 1.13: Co-moving bolometric IR luminosity density as a function of redshift. The red line is the total for all galaxies in the universe at the different epochs, while the blue and yellow dashed line are the contribution due to LIRGS and ULIRGs respectively. Image credit Caputi et al. (2007).

From CO observations in the radio end of the spectrum, and using a standard conversion factor, it was found that (U)LIRGs have an expected high concentration of molecular hydrogen (Sanders & Mirabel, 1996). Knowing that H_2 is a key ingredient for star formation, the high content of H_2 is one of the main reasons for the observed high rate of star formation in those galaxies.

1.10.3 Super Star Clusters

It has been known for a long time that there are two kinds of star clusters that populates the Milky way: Open Clusters - which contain $10^2 - 10^3$ stars of young ($10^6 - 10^9$ yr) age and with a relative combined low mass ($< 10^4$ $M_\odot$), and Globular Clusters - which have $10^4 - 10^5$ stars of older age (10^{10} yr) and with a higher total mass ($10^4 - 10^6$ $M_\odot$). It was suggested that star clusters are the product of the collapse of giant molecular clouds (GMC) (Lada & Lada, 2003).

With the advent of the Hubble Telescope a new type of cluster was discovered in the central galaxy of the Perseus Cluster - Super Star Clusters (SSCs), also referred to as Young Massive Clusters (YMCs) (Holtzman et al., 1992). These clusters have masses similar to GCs, while their ages are closer to OCs. SSCs are mainly found in galaxies, which are undergoing strong star formation episodes, usually triggered by merging events. SSCs are found in particularly large quantities in (U)LIRGs (Whitmore, 2000; Randriamanakoto et al., 2013a,b). It is assumed that SSCs are formed in a burst (coeval) of star formation in a giant molecular cloud, meaning that the resulting stellar population, which has a mass range of $10^3 - 10^7$ $M_\odot$, is of singular age and metallicity (Whitmore, 2000). The mass range and high stellar density that has been observed in those SSCs has drawn inevitable comparison to globular clusters (Gilbert & Graham, 2007), while there are still discrepancies over the age and metallicity, where SSCs appear more closely related to open clusters. The close link between SF-activity and SSCs has sparked interest in studying these objects extensively since SSCs may well be progenitors of modern-day GCs, being born in LIRGs and merging galaxies.

Figure 1.14 shows the link between the photometric magnitude of the brightest cluster in a galaxy with the overall SFR of the galaxy (Randriamanakoto et al., 2013a). The left panel shows the relation purely in the infrared regime as derived by Randriamanakoto et al. (2013a) for the SUNBIRD sample. In the right panel a comparison is made between what was previously previously known in the optical, and the newer data in the IR. The cause for such a relationship is still debated, with some pointing to a statistical effect, where brighter clusters are more likely to be sampled from a luminosity function and observed than less luminous ones (Larsen, 2002). Others believes the relation is due to physical implication such as mass (Weidner et al., 2004) or age - youngest clusters being the brightest links to the current episode of star formation (Bastian, 2008). The work of Randriamanakoto et al. (2013a), due to the small scatter of points around the observed relation, seems to favour that physical interpretation plays a role.

1.10.4 Starburst galaxies

Starburst is the term coined in the 70s-80s, to refer to highly luminous infrared sources, whose SF was thought to be unsustainable to be maintained over the duration of the galaxy's life (Harwit & Pacini, 1975; Rieke & Low, 1975; Weedman et al., 1981). The term can be used loosely to refer to two different cases; in one of them it is the localised intense SF activity in a specific region of a galaxy, that defines a starburst, in the other case the overall amount of SF activity of the entire galaxy is orders of magnitude above a standard galaxy, and hence the entire galaxy is classified as a starburst galaxy.

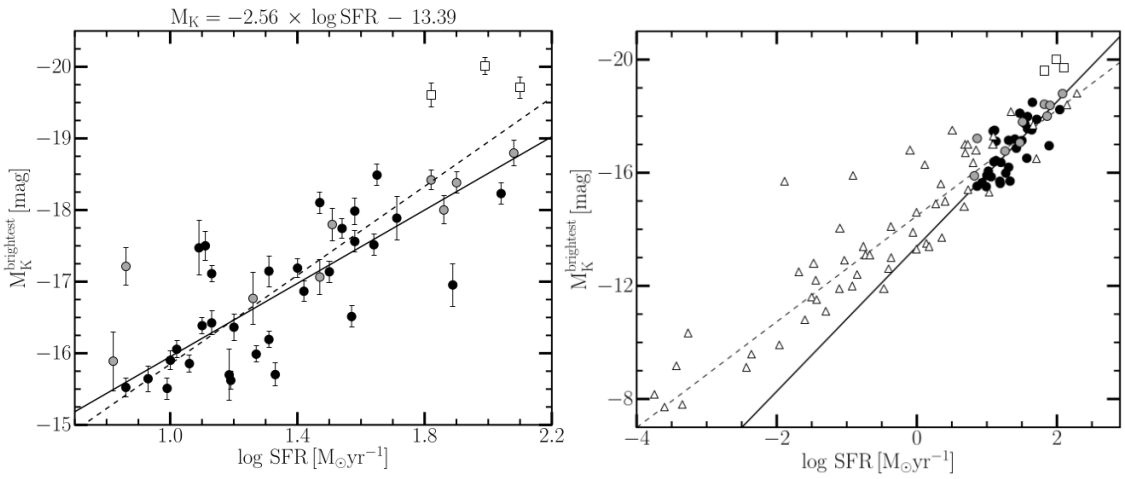

Figure 1.14: The observed relation between Near Infrared magnitude of brightest cluster and SFR. *Left Panel*: The relation derived for SSC in the SUNBIRD galaxies in NIR. *Right Panel*: The NIR data of Randriamanakoto et al. (2013a) (black filled circle) plotted along optical data (white triangles) (Weidner et al., 2004; Adamo et al., 2011). The NIR best-fit is shown in with the black line while the dashed line is the best-fit for the optical. Image credit Randriamanakoto et al. (2013a).

In the case of starburst galaxies, since the intensity of SF activity is so high, there is a quick depletion of available gas to form newer stars. Added to that the effect of feedback such as strong winds from young OB stars and supernova explosions, which drives raw material outwards, the speed of depletion is accelerated. The burst of SF is hence limited to a short span of time as compared to the Hubble time, usually around $\sim 10^8$ yr. Starburst galaxies can have various processes and characteristics, such as starburst rings (Wilson et al., 1991; Downes & Solomon, 1998), AGN jets (García-Burillo et al., 2014), interaction tidal tails (Hibbard & Yun, 1999; Elmegreen et al., 2007) and their morphology can range from the low luminosity Blue Compact Dwarf Galaxies (BCDGs) to ULIRGs (Moorwood, 1996). The correlation derived by Kennicutt (1998a) (refer to equation 1.8) shows that $SFR \propto L_{IR}$, if any AGN contribution to the IR luminosity is corrected out. This direct proportionality means that since LIRGs and ULIRGs are at least $1-2$ orders of magnitude brighter in the IR than typical galaxies, they are by the same orders of magnitude more active in terms of SFR than normal galaxies. Their SFR is typically in the range $\sim 20-200$ $M_\odot$ yr^{-1} as compared to single digit numbers for the standard cases.

1.10.5 AGN activity

Active galactic nuclei, AGN, is a very large topic of interest in extragalactic astronomy. It refers to processes that happens right at the core of galaxies around their super-massive black holes

(SMBH). One of the major breakthroughs over the past two decades was the discovery that all galaxies host SMBH at their centre (Ferrarese & Merritt, 2000; Gebhardt et al., 2000) making the study of AGN even more crucial for galaxy evolution. AGN exhibits very different properties from the usual stellar mechanism that affects most areas of a galaxy that are not near the very core. AGN usually consists of a central massive core around which matter (gas and dusts) agglomerates in an accretion disk. Due to the viscosity of the matter that accretes, and strong tidal forces involved, the accretion disk is heated up and emits enormous amounts of energy that can outshine the host galaxy by a few orders of magnitude.

Sanders et al. (1988) originally derived a link between ULIRGs and quasars and suggested an evolutionary sequence that takes gas-rich mergers to ULIRGs and then to optical quasars. By extending this work, Hopkins et al. (2008) developed a comprehensive merging scenario which describes in details the different stages of merging and how ULIRGs are linked to AGN activity as shown in Figure 1.10. Statistically, the link between increasing IR luminosity and AGN activity has also been shown to exists (Veilleux et al., 2009; Yuan et al., 2010) (shown in Figure 1.12).

AGN activity in IR dominated galaxies are usually classified into Seyferts (I and II) and Low Ionisation Narrow Line Regions (LINERS). To be able to distinguish which power source is dominant, between the different AGN types, SF and/or a combination of both, Baldwin et al. (1981) devised what is now commonly referred as the BPT diagram, where spectral line ratios are compared and distinctions can be made between the different sources. While the concept has remained the same over the years, updates on the demarcation line between the different sources has been made (e.g. Kauffmann et al. (2003b); Kewley et al. (2006); Cid Fernandes et al. (2010))

1.10.6 Feedback

Feedback, when it comes to galaxy evolution, is an umbrella term which regroups many processes, that usually transfers energy or momentum to gas, and set it into motion. Feedback can both fuel or quench star formation by either funnelling gas towards nuclear regions or cutting out the supply of gas, respectively. Over the years the presence of outflows in galaxies has been shown to correlate with the strong star formation rate (Martin, 2005; Veilleux et al., 2005; Rupke et al., 2005; Väisänen et al., 2008; Weiner et al., 2009; Cicone et al., 2014). The link was strong enough for Martin (2005) to derive a correlation between SFR and speed of outflows in the case of ULIRGs. Similarly, Cicone et al. (2014), using CO data, found a correlation between SFR and mass loss rate due to outflows. However, observationally it is known that SF itself is self regulating because the short lived OB stars drive flows of gas outside the host, through galactic winds or supernova explosions at the end of their lives, which shut down SF (Rupke et al., 2005;

Cazzoli et al., 2014). These two pictures are not contradictory, since only very recent SF will drive the outflows, which in turn will shut down even newer SF, hence an ability to time-stamp the different processes is crucial to understanding of their impact (Väisänen et al., 2017).

AGN is a key driver of the feedback mechanism, and has been shown to have two main modes of operation, namely "superwind-mode" and "radio-mode". Figure 1.15 illustrates the two modes in a schematic diagram (Alexander & Hickox, 2012). In the superwind-mode, the AGN through radiative output will drive gas out of the galaxy at sub-relativistic speeds, which then shuts down SF. Such negative feedback outflows have been estimated to carry up to ~ 1200 $M_{\odot}$ yr^{-1} of molecular mass out of ULIRGs (Sturm et al., 2011). Radio-mode, on the other hand, operates at relativistic speeds by narrow jets which continuously heats the gas preventing cooling, which is essential for star formation.

Feedback can also be positive i.e. it may enhance the overall SF of its host. Merger induced inflows of metal-poor gas are known to trigger SF (Bournaud, 2011). More surprisingly, even outflows, in specific conditions have been shown to induce SF-activity (Cresci et al., 2015; Maiolino et al., 2017). An AGN powered outflow, will drive gas outside of the galaxy through an outflow cavity, but molecular gas on the edge of the cavity, will get compressed and start forming stars.

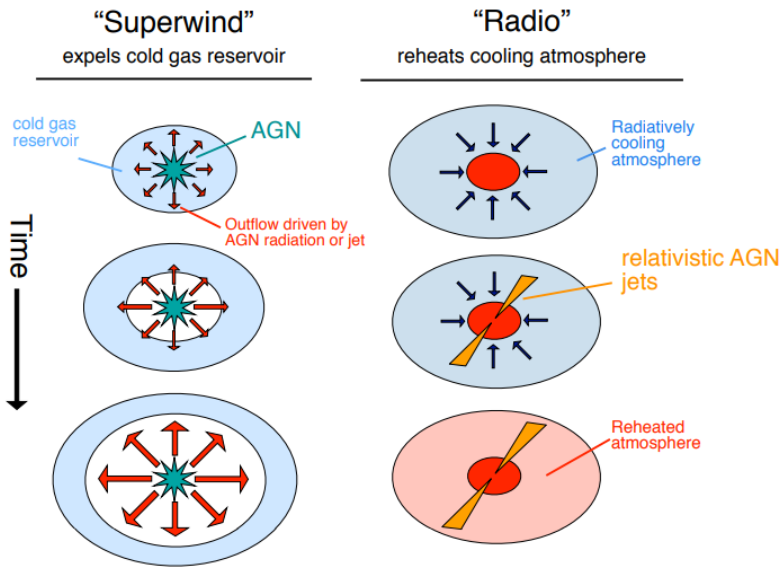

Figure 1.15: The difference between "superwind-mode" and "radio-mode" as a negative feedback process. Image credit Alexander & Hickox (2012).

1.10.7 Stellar populations of infrared dominated galaxies

Stellar population studies have become a standard tool in the past decade to study evolution of galaxies especially in the local universe, where the quality of the data observed is high in signal-to-noise, and spatial resolution is good as well. Since the advent of large surveys such as SDSS, galaxies from ellipticals to dwarfs have been extensively studied (Trager et al., 2000; Kauffmann et al., 2003a; Cid Fernandes, 2007; Salim et al., 2007; González Delgado et al., 2014). On the other hand, the amount of studies done for starburst and Infrared dominant galaxies are still few, one of the reasons being that they are less prevalent in the local universe. The other main difficulty is that stellar population modelling is complex even with relaxed and older galaxies, while LIRGs are known to host both actively SF regions, and AGN in the nuclear region - which are highly disruptive regions. Nonetheless, a few studies have been done in the past decade to fill the knowledge gap and we look at a few relevant ones below.

Marcillac et al. (2006) studied the star formation histories (SFH) of distant LIRGs ($z \sim 0.7$) through a Bayesian approach. First they used the Bruzual & Charlot (2003) model to create a large library of 200,000 possible Monte Carlo realisations of SFH, from which the $H\delta_A$ and H8 absorption lines and the 4000 $\mathring{A}$ were measured. Figure 1.16 shows the evolution of $D_n(4000)$ and $H\delta_A$ for different cases where different values of extinctions, velocity dispersion and metallicity are considered. The number '3' in the diagram indicates the start of SF around 3 Gyr either in burst mode or continuous mode. By comparing the same indices on real galaxies, they deduced that distant LIRGs and local ones are similar in their starburst phase, although local LIRGs showed that they were older than their distant counterparts. One of the limitations of such a method is that it reduces the dimensionality of spectral information so much that it becomes difficult to disentangle effects such as metallicity variations or extinction.

Following a different approach to the one above, the stellar population of 36 ULIRGs were studied using long-slit data in Rodríguez Zaurín et al. (2009) and Rodríguez Zaurín et al. (2010). Along the slit position, several apertures were extracted depending on the available signal-to-noise ratio in their data. Their fitting method allowed for only 2 stellar components to be fitted along with a power law (to account for AGN), in their minimisation procedure. To partially overcome this difficulty, they attempted multiple combination fits. Younger stellar populations were found in the nuclear regions, along with higher reddening. Their modelling also revealed that ULIRGs have known at least two epochs of star formation activity.

Another interesting study of the stellar population of LIRGs was published in Alonso-Herrero et al. (2009) and Alonso-Herrero et al. (2010). Their approach is a more complete one, studying different aspects of their sample with integral field spectroscopic (IFS) data, though with a

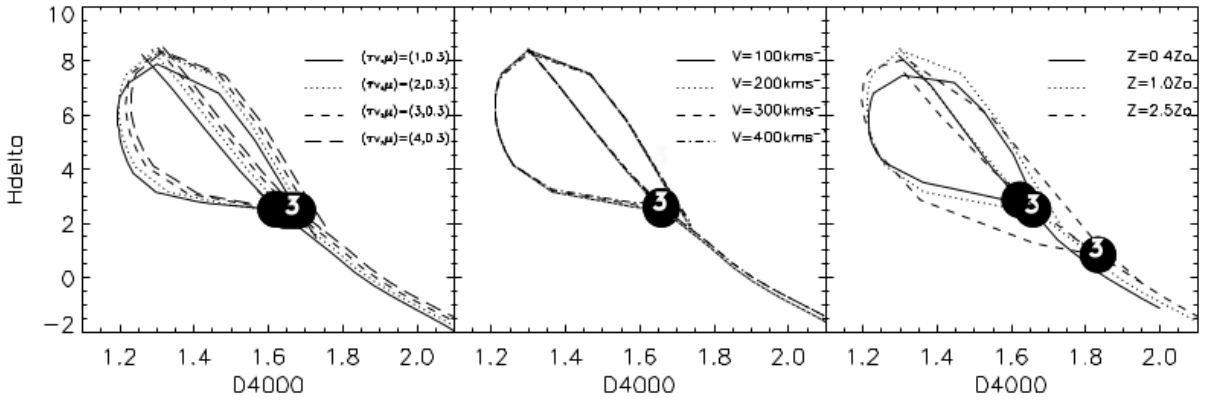

Figure 1.16: The different possible evolution of the $D_n(4000)$ and $H\delta_A$ indices. In effect, the different loops indicate different star formation histories that LIRGs can have with the *left panel* showing extinction effect, the *middle panel* the effects of velocity dispersion and the *right panel* showing metallicity variations. Image credit Marcillac et al. (2006).

limited sample of 11 local LIRGs. They also found that the stellar population of LIRGs are well fitted by a mixture of evolved and very young ($1 - 20$ Myr) populations, with more extinction in the younger population, as expected. Figure 1.17 shows the $D_n(4000)$ and $H\delta_A$ indices of the 11 LIRGs from Alonso-Herrero et al. (2010), with the black line indicating the locus galaxies would follow as their age increases at a single metallicity values. The plot mainly shows that to get the indices for LIRGs, one need a combination of a very young population and an evolved one.

More recently, Cortijo-Ferrero et al. (2017) examined in great detail two LIRGs (one of which is a merging pair of individual galaxies) using IFU data from the Calar Alto Legacy Integral Field Area (CALIFA). After performing stellar population modelling with the software STARLIGHT, the main findings of the study, shows a young population ($50 - 80$ Myr), which contributes to most of the light emitted by the galaxy. They also find that the mergers had lower oxygen abundances and flatter gradients than non-interacting galaxies. The SFR of the mergers were found to be $6 - 9$ times higher than main sequence star forming galaxies, while the specific SFR was calculated to be of the order of $5 - 6$ higher than their control sample. To explain their observations, they suggest that an enhanced SF is seen early in the merging stage of LIRGs, during the first contact between both galaxies. At this stage, the SF is concentrated in the nuclear regions and is not expected to be extended to outer regions.

1.11 Thesis structure

This chapter has been a condensed review of many topics touching our current understanding of galaxy evolution. The subject is extremely complex and requires an approach from a large

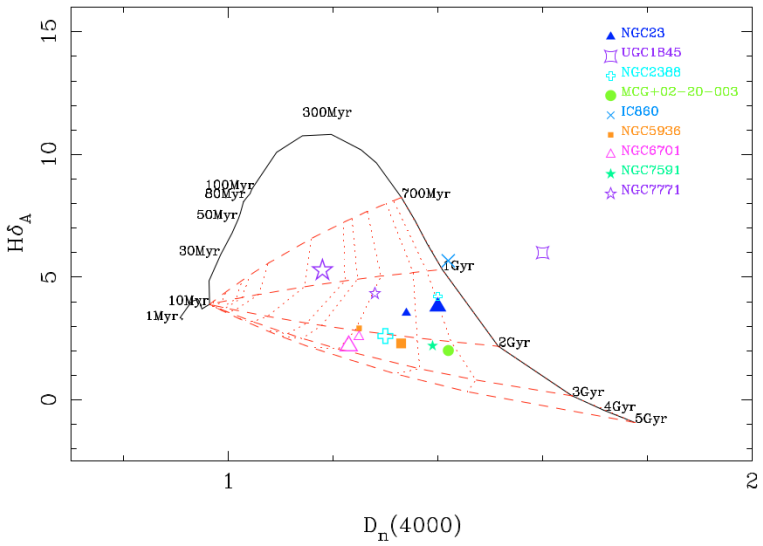

Figure 1.17: The $D_n(4000)$ and $H\delta_A$ diagram roughly gives an idea of the combination of stellar populations for galaxies. Here the galaxies are LIRGs plotted along with the locus of the two indices as age increases for population with a single metallicity. Image credit Alonso-Herrero et al. (2010).

range of angles, from the cosmological scales studying cosmic star formation throughout the history of the universe, to the smaller scale of understanding the impacts of disk instabilities on star formation, to performing simulations that gives insight to properties that cannot be observed with the current generation of instruments. Studying starbursts and LIRGs is part of the puzzle regarding the formation and evolution of galaxies. By using the discussion of this chapter as background, this work tackles the properties of star forming and LIRGs on different fronts, namely stellar populations ages, metallicities, extinction and dust, oxygen abundances, impact of morphology and radial gradients.

Below is a structure of the work to follow from this thesis:

- In Chapter 2, our aims and objectives are laid out along with how data were acquired and treated to give science grade spectra for analysis.
- A review of spectral synthesis modelling along with its implementation for our dataset is shown in Chapter 3.
- In Chapter 4, a multi-faceted study of different integrated properties of our sample is presented.
- A radial analysis of the properties of LIRGs and star forming galaxies is shown in Chapter 5.

- A full summary and conclusion of the current work is given in Chapter 6.

Chapter 2

Thesis outline and Data handling

2.1 Introduction

The focus of this chapter is to present the main scientific objectives of this thesis, followed by the sample of galaxy considered to achieve the objectives stated. Furthermore, the instruments used along with the observational set-up that were chosen are explained. The last section is dedicated to how the data collected was processed to extract scientific information as well to the treatment of uncertainties.

2.2 Scientific goals

The background for this thesis work is an international collaboration studying galaxy evolution in the context of strongly star-forming galaxies, mainly (U)LIRGs. We make use of multi-wavelength data available from many different facilities. The Super Star Clusters (SSCs) for the same sample of galaxies were studied with NIR adaptive optics imaging from NaCo on Very Large Telescope (VLT) and ALTAIR/NIRI on the Gemini-North telescopes. The results have been extensively reported in Randriamanakoto et al. (2013a,b). Our study focuses mainly on the long-slit spectroscopic follow-up from the Southern African Large Telescope (SALT). The main objectives of the overall work are:

1. The stellar population properties - age, metallicities and extinction in both nuclear and other areas of the galaxies.

2. Understanding the ionized gas by studying the oxygen abundances as well as gas ionization mechanism and line ratios.

3. Measurement of the gas and stellar kinematics and velocity dispersion where possible. Rotation curves of the gas and stellar populations will be derived and a more in-depth

study will be conducted of the features like the NaD line.

4. Deriving the stellar mass and dust content of the galaxies via SED fitting. This is achieved by getting the colours from UV to far-IR where possible.

In this thesis, our work will mainly be centred on the first two objectives listed above. The remaining two goals are beyond the scope of this thesis and will be published in follow up studies. The main motivation for this thesis is an understanding of how SF happens and the influence of interaction on SF, in LIRGs and starburst galaxies. This can be achieved by doing a thorough characterisation of the different properties of these galaxies in their various stages, and at different radial locations. A study of metallicity, will give us an understanding on the chemical enrichment process of the observed sample. On the other hand, by deriving the ionisation of the gas, we hope to understand the dominant mechanisms driving the line emission observed. Standard Cosmology is used throughout the calculations of this thesis: this means that $H_o = 73\,\mathrm{km\ s^{-1}\ Mpc^{-1}}$, $\Omega_m = 0.27$, and $\Omega_\lambda = 0.73$.

2.3 The Sample

We set to investigate the different physical properties of IR-dominated galaxies, including Starbursts galaxies and LIRGs in this work. The galaxies that were chosen are a major sub-sample of the SUperNovae and starBursts in the InfraReD (SUNBIRD) sample (see Väisänen et al. (2014)) taken from the IRAS galaxies from the Revised Bright Galaxy Sample (RBGS) (Sanders et al., 2003). Our sample consists mainly of southern galaxies in the local universe in a distance range of $40 \leq D_L \leq 350$ Mpc. Their IR luminosities coverage is in the range $10^{10.6} L_\odot \leq L_{IR} \leq 10^{11.9} L_\odot$ which from Sanders & Mirabel (1996) means they vary from just under the LIRG limit to just below the ULIRG category. The sample of galaxy chosen is listed in Table 2.1 and some key statistical properties are plotted in Figure 2.1.

The sample contains a wide variety of interaction stages as shown by the middle panel of Figure 2.1. The classification scheme follows from a simplification of the scheme devised by Veilleux et al. (2002) and later adapted by Miralles-Caballero et al. (2011). The scheme consists of five main classes/stages: 0, I, II, III and IV. Class I are cases prior to the end of the first passage. During that stage disks are still stable and not disrupted. Formation of bars or tidals have not yet arisen. Class II is where the two nuclei and the two disks are still very well distinguishable, but features such as tidal tails or bridges are observed. This stage happens around $200-400$ Myr after the first stage (Bournaud et al., 2008; Miralles-Caballero et al., 2011). Class III describes the merging stage where the two nuclei are close to each other (< 1.5 kpc) as well as disks that can no longer be associated with their original nuclei. Shell structures and tails are present

at this stage which occurs $500 - 700$ Myr after the first approach started. Class IV is that of the post Merging phase, where the nucleus has totally merged into one and a more relaxed galaxy starts to emerge as artefacts of merging (tails and bridges) slowly fades away. Isolated galaxies that have no obvious pair, or interacting pairs, are classified as Class 0 in this scheme to distinguish them from the rest.

We derive K-band luminosity for the SUNBIRD sample by getting K_s band magnitudes from the Two Micron All Sky Survey (2MASS) (Skrutskie et al., 2006). The vast majority of photometric values along with their associated uncertainties were obtained using NED[1]. For cases that were entangled due to interactions, the on-line photometric tool of 2MASS was enough to derive the required magnitude. The K_s band magnitude was then converted to mass using standard equation in the form of equation (5) of Masters et al. (2003), doing K-correction, galactic extinction and accounting for luminosity distance. The corrected K-band has a strong correlation with stellar mass, as was shown in the work of Bell et al. (2003). Salpeter (1955) is the standard mass that is derived for our sample, but changing to another mass function only requires a conversion factor.

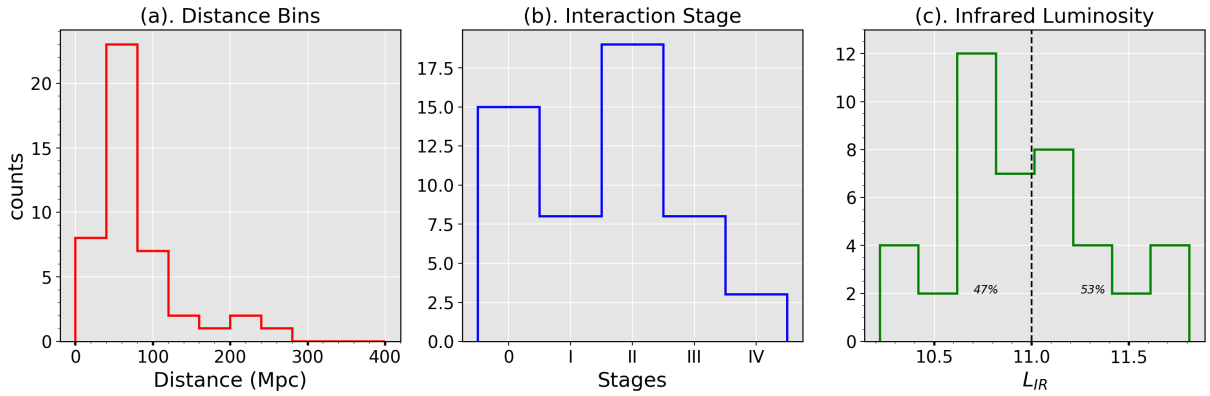

Figure 2.1: An overview of the SUNBIRD sub-sample studied in this thesis. *Panel (a)*: Histograms of the Distance modulus of the different targets. *Panel (b)*: Histogram of the different interaction stages present in the SUNBIRD sample according the the Veilleux et al. (2002) and Miralles-Caballero et al. (2011) updated scheme. *Panel (c)*: Histogram of the IR luminosity of our galaxies. The dashed line is the cut-off at $10^{11} L_{\odot}$ between Non-LIRGs and LIRGs. Although almost half (47%) of the sample are below the nominal LIRG limit, there is a continuous distribution of luminosities shared by starbursts and L1RGs.

[1]The NASA/IPAC Extragalactic Database (NED) is operated by the Jet Propulsion Laboratory, California Institute of Technology, under contract with the National Aeronautics and Space Administration.

Table 2.1: Properties of the SUNBIRD sub-sample. Targets are listed in alphabetical order. Column 1: Name; Column 2 & 3: Equatorial coordinates; Column 4 & 5: The radial velocity and its associated redshift; Column 6: Galaxy Types; Column 7: The K_s-band magnitude from 2MASS; Column 8: The stellar mass assuming Salpeter IMF - derived from K_s band; Column 9: The Infrared Luminosity from RBGS catalogue data; Column 10: Interaction Stage; Column 11: The Log of the Star formation Rate derived from IR luminosity (Column 9). Column 12: These indicates different photometric imaging samples (refer to Randriamanakoto et al. (2013a)) where 'VLT' stands for VLT/NACO data, 'GEMINI' is short-form of GEMINI/ALTAIR/NIRI data, 'La Palma' is a lower IR luminosity sample of galaxies done at the La Palma telescope and SALT means that this data has only spectroscopic data from SALT/RSS). Columns 2-6 are taken from NED online database.

Target	RA	DEC	Vel (km s^{-1})	z	Type	K_s Mag.	Log(Mass) ($M_\odot$)	Log(L_{IR}) ($L_\odot$)	Stg	Log(SFR) ($M_\odot yr^{-1}$)	Sample
(1)	(2)	(3)	(4)	(5)	(6)	(7)	(8)	(9)	(10)	(11)	(12)
CGCG049-057	15 13 13.1	+07 13 32.0	3897	0.0130	Irr	11.13	10.37	11.27	0	1.50	Gemini
ESO154-G010	02 45 08.7	-55 44 26.0	5586	0.0186	(R')SB(r)a	9.02	11.53	11.05	I	1.28	SALT
ESO221-IG008	13 50 27.6	-48 16 38.5	3153	0.0105	pec	11.21	10.16	10.76	II	0.99	VLT
ESO221-IG010	13 50 57.3	-49 03 25.0	3099	0.0103	pair	9.25	10.93	11.17	II	1.40	VLT
ESO264-G036	10 43 07.6	-46 12 44.6	6315	0.0211	SB	9.54	11.45	11.35	I	1.58	VLT
ESO264-G057	10 59 00.9	-43 26 29.0	5156	0.0172	SA(rs)cd	9.99	11.10	11.08	II	1.31	VLT
ESO267-G030	12 14 12.6	-47 13 37.0	5543	0.0185	SA(rs)b pec	9.72	11.25	11.19	II	1.42	VLT
ESO319-G022	11 27 54.0	-41 36 52.5	4902	0.0164	(R')SB(r)a	10.37	10.89	11.04	0	1.27	VLT
ESO320-G030	11 53 12.0	-39 07 54.0	3232	0.0108	(R')SAB(r)a	9.22	10.98	11.10	0	1.33	VLT
ESO428-G023	07 22 09.7	-29 14 04.9	3026	0.0101	(R')SB(rs)ab	8.90	11.07	10.76	0	0.99	VLT
ESO440-IG058-N	12 06 51.7	-31 56 47.0	6956	0.0232	pair	10.91	10.97	10.79	II	1.02	VLT
ESO440-IG058-S	12 06 51.7	-31 56 47.0	6956	0.0232	pair	12.52	10.34	11.22	II	1.45	VLT
ESO491-G020	07 09 47.5	-27 34 14.0	2965	0.0099	SB(rs)b/pec	10.84	10.26	10.86	II	1.09	VLT
ESO550-IG025-N	04 21 20.0	-18 48 48.0	9652	0.0322	Pair/triple	11.21	11.15	11.24	II	1.47	VLT
ESO550-IG025-S	04 21 20.0	-18 48 48.0	9652	0.0322	Pair/triple	11.87	10.89	11.03	II	1.26	VLT
IC2522	09 55 08.9	-33 08 14.0	3019	0.0101	SB(s)c/pec	9.32	10.87	10.63	I	0.86	VLT
IRAS06164+0311	06 19 02.5	+03 09 52.9	2902	0.0097	-	8.06	11.42	10.79	0	1.02	VLT
IRAS12116-5615	12 14 22.0	-56 32 34.0	8125	0.0271	-	10.89	11.18	11.59	IV	1.82	VLT
IRAS13052-5711	13 08 18.7	-57 27 30.9	6364	0.0212	-	10.40	11.14	11.34	IV	1.57	VLT
IRAS18293-3413	18 32 41.1	-34 11 27.0	5449	0.0182	-	9.39	11.37	11.81	II	2.04	VLT
IRAS19115-2124	19 14 30.9	-21 19 07.0	14608	0.0487	Pair	11.01	11.62	11.87	III	23.10	VLT

Table 2.1 – continued from previous page

Target	RA	DEC	Vel (km s^{-1})	z	Type	K_s Mag.	Log(Mass) ($M_\odot$)	Log(L_{IR}) ($L_\odot$)	Stg	Log(SFR) ($M_\odot yr^{-1}$)	Sample
(1)	(2)	(3)	(4)	(5)	(6)	(7)	(8)	(9)	(10)	(11)	(12)
IRAS19254-7245	19 31 21.5	-72 39 21.0	18500	0.0617	Pair	11.28	11.73	11.91	III	2.14	SALT
IRASF01364-1042	01 38 52.9	-10 27 11.1	14464	0.0482	-	12.79	10.89	11.76	III	1.99	VLT
IRASF06076-2139	06 09 45.1	21 40 22.0	11226	0.0374	-	11.78	11.06	11.59	III	1.82	VLT
IRASF16516-0948	16 54 24.0	-09 53 21.0	6807	0.0227	-	10.37	11.26	11.24	IV	1.47	Gemini
IRASF17138-1017	17 16 35.8	-10 20 39.0	5197	0.0173	-	10.15	11.10	11.42	0	1.65	VLT
IRASF17578-0400	18 00 31.9	-04 00 53.0	4210	0.0140	-	10.80	10.74	11.35	II	1.58	Gemini
MCG-02-01-051	00 18 50.8	-10 22 36.9	8125	0.0271	SB(s)b/pec	12.09	10.65	11.41	II	1.64	VLT
MCG-02-01-052	00 18 50.1	-10 21 42.0	8193	0.0273	SB(s)c/pec	11.39	10.92	10.72	II	0.95	VLT
MCG-02-33-098	13 02 20.5	-15 46 05.0	4773	0.0159	Sc/pec		10.15	10.89	III	1.12	VLT
NGC1022	02 38 32.7	-06 40 39.0	1453	0.0048	(R')SB(s)a	8.50	10.55	10.35	0	0.58	La Palma
NGC1068	02 42 40.7	-00 00 48.0	1137	0.0038	(R)SA(rs)b	5.81	11.41	11.27	0	1.50	La Palma
NGC1204	03 04 39.9	-12 20 28.7	4610	0.0154	S0/a	9.95	11.00	10.88	0	1.11	VLT
NGC1222	03 08 56.7	-02 57 19.0	2448	0.0082	S0/pec	9.92	10.44	10.60	0	0.83	La Palma
NGC1819	05 11 46.1	+05 12 02.0	4470	0.0149	SB0	9.23	11.26	10.90	0	1.13	VLT
NGC253	00 47 33.1	-25 17 18.0	243	0.0008	SAB(s)c	3.82	10.87	10.44	0	0.67	La Palma
NGC3110	10 04 02.7	-06 28 35.0	5054	0.0169	SB(rs)b/pec	9.53	11.24	11.31	II	1.54	VLT
NGC3508	11 02 59.6	-16 17 19.1	3899	0.0130	SA(r)b/pec	9.83	10.89	10.90	0	1.13	VLT
NGC4433	12 27 37.5	-08 16 35.0	3000	0.0100	SAB(s)ab	9.51	10.85	10.87	II	1.10	VLT
NGC4575	12 37 52.1	-40 32 20.0	2967	0.0099	SB(s)bc/pec	9.35	10.85	10.96	I	1.19	VLT
NGC470	01 19 44.8	+03 24 36.0	2374	0.0079	SA(rs)b	8.84	10.85	10.37	I	0.60	La Palma
NGC520	01 24 35.1	+03 47 33.0	2281	0.0076	pec	8.54	10.93	10.91	III	1.14	La Palma
NGC6000	15 49 49.5	-29 23 13.0	2193	0.0073	SB(s)bc	8.20	11.05	10.97	I	1.20	VLT
NGC6835	19 54 32.9	-12 34 03.0	1611	0.0054	SB(s)a	9.19	10.38	10.32	I	0.55	La Palma
NGC7714	23 36 14.1	+02 09 19.0	2798	0.0093	SB(s)b:pec	9.76	10.63	10.72	II	0.95	La Palma

2.4 SALT

Figure 2.2: The Southern African Large Telescope. On the right a view at the 10m wide mirror

Our sample data were gathered through the SALT (Buckley et al., 2006; O'Donoghue et al., 2006), which is a 10 m class telescope with the possibility of doing both imaging via SALTICAM and spectroscopy with the Robert Stobie Spectrograph (RSS; (Burgh et al., 2003; Kobulnicky et al., 2003)) and the High Resolution Spectrograph Crause et al. (2014); Miszalski et al. (2018). The SALT main design is based on the Texan telescope Hobby-Eberly Telescope (HET). It consists of an array of 91 identical hexagonal mirrors which are all spherical and a Spherical Abberation Corrector (SAC) is used before any instruments. The mirrors are kept aligned by an active mirror alignment system. The SALT primary mirror has a fixed tilt of 37^o from the vertical and therefore the mirror itself cannot track an object during observation. For tracking, the payload which is 13 m from the primary at the top of the dome, will move according to the target while the primary remains fixed (in azimuth) during the whole observation. The payload in fact houses the SAC along with the two actual science instruments SALTICAM and RSS.

2.5 Observations

RSS consists of three combined CCD chips each having 2048×4102 pixels. Since each of those CCDs have 2 amplifiers, the readnoise and gain across the CCD varies and needs to be corrected for (during pre-reduction process). Even though the three CCDs are close together, two gaps are still present and can be seen on any data recorded. It is therefore crucial to plan one's observation so that critical data do not fall in the gap areas. This can be achieved with the RSS

simulator in the PIPT tool[1].

The observations were done from the commissioning period of June-July, 2011 following the upgrade in the design of the SAC, until 2015 under different programs. Long-slit spectra were acquired for all the galaxies with the Position Angle (PA) aligned to the orientation of the major axis of the respective galaxy. In some cases, we had more than one observation per galaxy and therefore another PA was chosen according to interesting features that are visible from photometry. Position angle is measured East from North (counter-clockwise) therefore negative values indicates PA measured in the other direction (clockwise).

There were two main volume phase holographic (VPH) gratings used for this survey: PG0900 and PG1800. PG0900 is a low resolution grating which allows for a dispersion of 0.91 $\mathring{A}$. The wavelength range depends on the grating angle setting used, and in this work it was chosen to roughly result in a range between $3640-6740\,\mathring{A}$. This is wide enough to get lines such as [OII] at $3727\,\mathring{A}$ and the [NII] line at $6584\mathring{A}$ which falls just after the Hα line at $6563\,\mathring{A}$. This is the main grating for our Stellar Population modelling work and line ratio analysis and the data from this set-up is presented in Table 2.2. PG1800 offers higher resolution data over a general range of $5590-6926\,\mathring{A}$ with dispersion of $0.421\,\mathring{A}$. With PG1800, we are able to get the two [SII] lines at $6716.47\,\mathring{A}, 6730.85\,\mathring{A}$. We intend to use PG1800 data for the modelling of the kinematics of gas and stars inside galaxies for future work, hence the data from this grating shall not be presented here. Figure 2.3 shows the two slit positions (at position angle 283^o and 315^o) that were chosen for galaxy ESO-221IG008 with SALT. Figure 2.3 is shown as an example, for the slit positions of all the other targets please consult Appendix A.

Table 2.2: SALT/RSS - PG0900 observation log for SUNBIRD sub-sample.

Target	Grating Angle (°)	PA (°)	wavelength range ($\mathring{A}$)	Date observed	Airmass	Slit Width (")	Exposure Time (s)
CGCG049-057	14.00	199.0	3775 - 6859	21/05/2014	1.300	1.25	2 x 1200
	13.63	200.0	3625 - 6726	25/02/2012	1.328	1.25	1 x 1000
	13.25	234.0	3488 - 6588	27/02/2012	1.313	1.50	1 x 1000
ESO154-G010	14.00	24.5	3773 - 6858	01/08/2014	1.280	1.25	1 x 1100
ESO221-IG008	13.63	315.0	3612 - 6726	12/02/2013	1.351	1.50	1 x 1400
	13.63	283.0	3609 - 6726	12/02/2013	1.254	1.50	1 x 1400
ESO221-IG010	13.63	150.0	3622 - 6735	11/07/2013	1.245	1.25	2 x 1400
ESO264-G036	14.00	294.0	3755 - 6865	12/01/2013	1.275	1.50	2 x 1200
	14.00	294.0	3755 - 6865	12/02/2013	1.261	1.50	2 x 1200
ESO264-G057	14.00	276.6	3756 - 6865	07/01/2013	1.251	1.50	2 x 1200

[1]PIPT means Principal Investigator Proposal Tool and is available at: *http://www.salt.ac.za/observing/proposing-for-salt-observations/pipt/*

Table 2.2 – continued from previous page

Target	Grating Angle (°)	PA (°)	wavelength range (Å)	Date observed	Airmass	Slit Width (")	Exposure Time (s)
ESO267-G030	14.00	135.0	3767 - 6872	05/06/2013	1.290	1.25	2 x 1400
ESO319-G022	13.63	295.0	3632 - 6722	31/12/2013	1.262	1.50	1 x 1200
ESO320-G030	13.63	315.0	3611 - 6730	13/01/2013	1.187	1.50	3 x 870
ESO428-G023	13.63	261.0	3612 - 6728	15/11/2012	1.232	1.50	2 x 1400
ESO440-IG058	13.63	65.5	3630 - 6718	27/06/2014	1.303	1.25	2 x 1100
	13.63	237.8	3615 - 6728	19/12/2012	1.228	1.50	2 x 1000
ESO491-G020	13.63	18.0	3618 - 6728	22/01/2013	1.259	1.50	2 x 1200
ESO550-IG025	13.25	175.0	3459 - 6588	30/11/2011	1.199	1.25	1 x 1153
	13.25	175.0	3481 - 6584	21/12/2011	1.231	1.25	1 x 1153
IC2522	13.63	31.0	3632 - 6720	28/06/2014	1.332	1.25	3 x 767
	13.63	7.0	3613 - 6730	20/11/2012	1.265	-	2 x 1200
	15.88	211.0	4477 - 7542	27/12/2013	1.252	1.50	2 x 900
IRAS06164+0311	13.63	87.0	3624 - 6731	18/03/2012	1.381	1.50	1 x 1021
IRAS12116-5615	13.25	231.0	3465 - 6586	02/01/2012	1.294	1.25	1 x 1154
IRAS13052-5711	14.00	270.0	3755 - 6869	09/03/2013	1.217	1.50	2 x 1400
IRAS17578-0400	14.00	110.0	3757 - 6868	18/08/2012	1.328	1.50	2 x 1200
	13.62	106.8	3611 - 6721	07/09/2013	1.286	1.50	2 x 1200
IRAS18293-3413	14.00	127.0	3759 - 6867	14/10/2012	1.322	1.50	2 x 835
IRAS19115-2124	14.00	190.0	3758 - 6865	01/04/2012	1.197	1.25	3 x 600
	15.88	-170.0	4474 - 7548	30/07/2011	1.211	1.25	2 x 600
IRAS19254-7245	14.38	347.0	3920 - 6998	28/06/2014	1.325	1.25	1 x 1200
IRASF01364-1042	14.00	222.0	3763 - 6870	24/09/2013	1.262	1.50	2 x 1200
	14.00	222.0	3764 - 6874	06/09/2013	1.311	1.50	1 x 522
IRASF06076-2139	14.00	158.2	3767 - 6874	07/09/2013	1.257	1.50	2 x 1200
IRASF16516-0948	14.00	86.0	3763 - 6863	17/05/2012	1.341	1.50	2 x 1200
IRASF17138-1017	13.62	-170.0	3628 - 6729	22/06/2011	1.277	1.00	2 x 600
	13.63	190.0	3629 - 6730	03/03/2012	1.176	-	1 x 1400
IRASF18293-3413	14.00	308.0	3756 - 6866	12/05/2013	1.237	1.50	2 x 1200
MCG-02-01-052	14.00	170.0	3753 - 6865	18/08/2012	1.188	1.50	2 x 1200
MCG-02-33-098	13.63	245.9	3627 - 6720	06/03/2014	1.261	1.50	2 x 1200
NGC1022	13.63	-38.0	3627 - 6727	15/07/2011	1.219	1.50	3 x 300
NGC1068	13.63	-148.0	3620 - 6720	30/07/2011	1.312	1.25	3 x 300
NGC1204	13.63	73.0	3610 - 6726	12/11/2012	1.241	1.50	2 x 1200
NGC1222	13.63	-132.0	3619 - 6725	30/07/2011	1.216	1.25	3 x 600
NGC1819	13.63	135.0	3565 - 6718	29/11/2011	1.280	1.25	3 x 860
	13.63	231.0	3618 - 6722	21/12/2011	1.265	1.25	1 x 2500
NGC253	13.63	-40.0	3613 - 6711	09/07/2011	1.293	1.00	3 x 300
NGC253	13.63	-130.0	3604 - 6705	09/07/2011	1.174	1.00	2 x 250
NGC3110	13.63	111.0	3632 - 6724	02/05/2014	1.263	1.25	2 x 1100
	13.63	185.0	3621 - 6729	06/03/2013	1.230	1.50	2 x 1200
NGC3508	13.62	194.5	3617 - 6727	06/03/2013	1.218	1.50	2 x 1200
NGC4433	13.63	187.7	3620 - 6729	11/04/2013	1.275	1.50	2 x 1100
NGC4575	13.63	280.0	3613 - 6726	10/03/2013	1.241	1.50	2 x 1200

Table 2.2 – continued from previous page

Target	Grating Angle (°)	PA (°)	wavelength range (Å)	Date observed	Airmass	Slit Width (")	Exposure Time (s)
NGC470	13.63	-160.0	3622 - 6723	01/08/2011	1.316	1.25	3 x 300
	13.63	-160.0	3621 - 6726	22/07/2011	1.301	1.25	2 x 501
NGC520	13.63	132.0	3621 - 6724	23/07/2011	1.240	1.25	3 x 600
NGC6000	13.62	170.0	3621 - 6725	27/07/2011	1.222	1.25	2 x 600
	13.63	174.0	3617 - 6731	05/04/2013	1.246	1.50	2 x 1200
NGC6835	13.63	-110.0	3620 - 6722	09/07/2011	1.274	1.00	3 x 600
NGC7714	13.63	-90.0	3613 - 6717	08/07/2011	1.241	1.00	2 x 600
	13.63	180.0	3620 - 6720	08/07/2011	1.215	1.00	2 x 600
	13.63	-105.0	3615 - 6716	08/07/2011	1.230	1.00	2 x 600

To be able to flux calibrate our targets, various spectrophotometric standard stars were observed during the period of our programmes. We note that it is non-trivial to perform absolute flux calibration due to the particular mode of operation of the telescope. Since SALT has a moving pupil which is illuminated by different mirrors during an observation, the exact same set up of mirrors are not use to observed the standard stars. Hence, standard stars are usually observed only to calibrate the relative shape of the spectrum. P.Is are sent a list of standard stars that were observed matching the settings of their observational set up. We have compiled a list of the standard stars that we used for our programme in Table 2.3. The standard stars are observed using exposures of ranging from 30 s to 120 s depending on the grating settings and the luminosity of the specific star chosen.

Table 2.3: Observation log of Standard Stars in chronological order.

Star	Grating	Grating angle	Date and time
G93-48	PG0900	13.625	22/06/2011 03:25:45
LTT4364	PG0900	13.250	22/12/2011 02:37:54
LTT4364	PG0900	13.250	02/01/2012 02:16:26
LTT7379	PG0900	13.625	19/03/2012 02:09:06
Feige110	PG0900	14.000	17/05/2012 04:08:26
LTT4364	PG0900	13.625	13/01/2013 01:54:46
LTT7379	PG0900	13.625	07/03/2013 02:59:45
HILT600	PG0900	14.005	10/03/2013 18:04:12
G93-48	PG0900	14.000	06/06/2013 03:58:47
EG21	PG0900	15.875	28/12/2013 18:55:42
LTT4364	PG0900	13.250	02/05/2014 17:09:42
G93-48	PG0900	14.000	23/06/2014 02:16:09
LTT7379	PG0900	13.625	28/06/2014 19:53:13

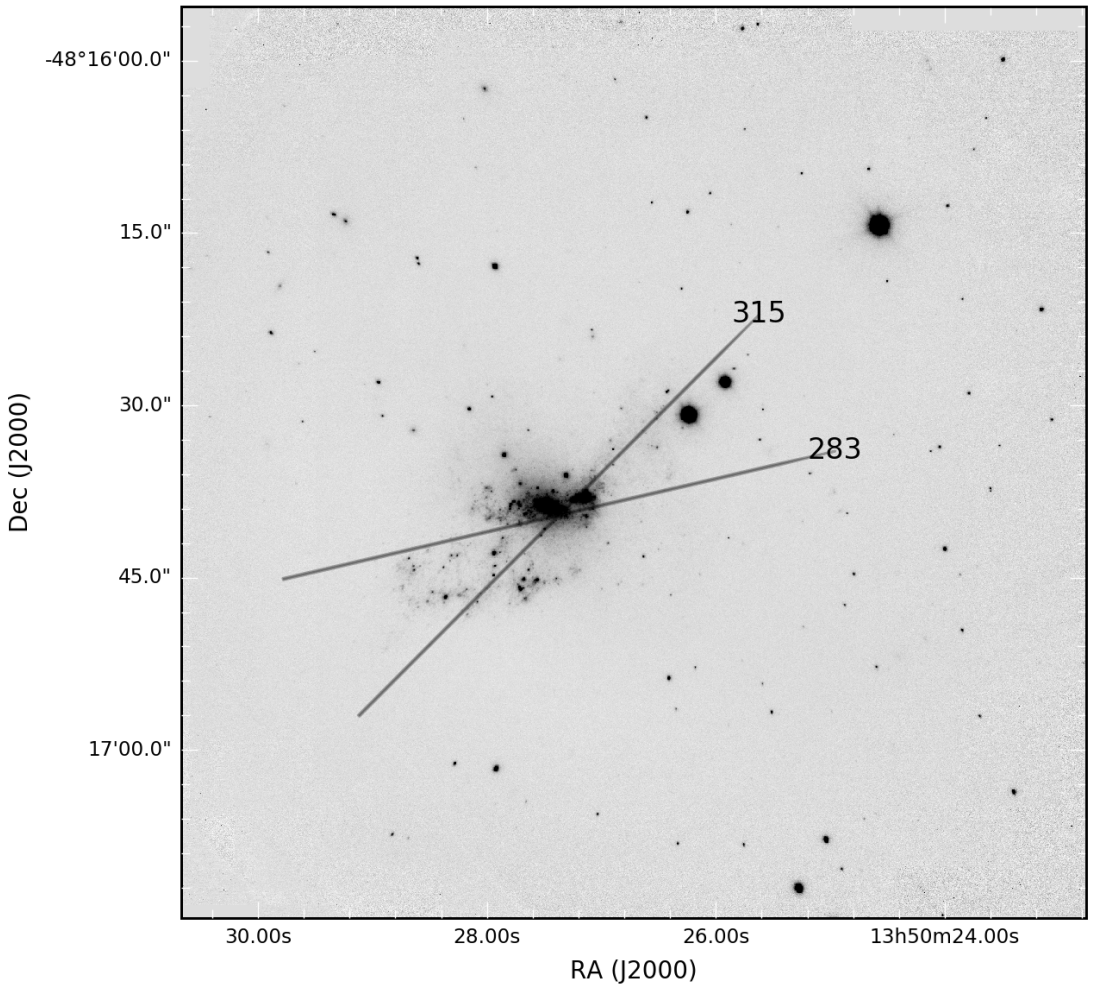

Figure 2.3: The observation of ESO221IG008 with SALT at position angles 283^o and 315^o respectively.

2.6 Data Reduction

SALT data are available in two forms for any Principal Investigator of an observation run: Raw images from the telescope and a set of pre-reduced images. For spectroscopic data, the SALT pre-reduction procedure applies the following steps: bias subtraction, overscan correction, trimming, gain correction, correction for amplifiers cross-talk. Since the pre-reduced data are stable (Crawford et al., 2010) and has yielded stable and reliable results for years to other astronomers, we decided to make use of them.

2.6.1 Reduction pipeline

To be able to cope with the amount of data collected and to be reduced in this project, as well as for consistency across all datasets, we wrote a reduction pipeline in IRAF[1], PyRaf and Python. We follow standard procedures of long-slit spectroscopic reduction similar to those in Valdes (1986)[2] and to some extent the online guideline given by Kevin Hainline[3] The main steps are given in flowchart shown in Figure 2.4. We give some explanations of each of the steps below, but to get the exact settings of each step consult github link[4] to the pipeline.

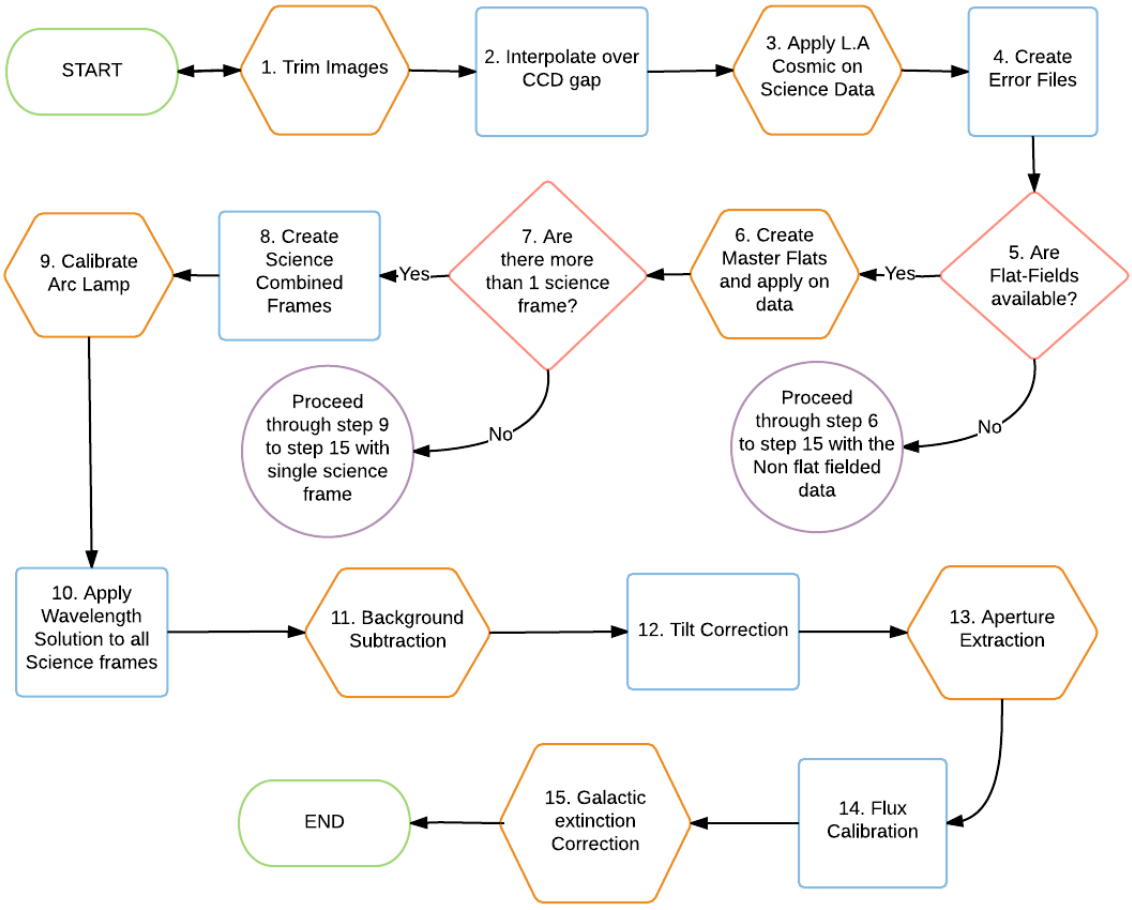

Figure 2.4: An outline of the flow of the reduction pipeline with the different key steps required for successful science quality data output.

[1]IRAF: the Image Reduction and Analysis Facility is distributed by the National Optical Astronomy Observatory.

[2]http://iraf.noao.edu/iraf/docs/lslit.ps.Z

[3]http://mips.as.arizona.edu/~khainline/salt_redux.html

[4]https://github.com/rajin/rajin_code

2.6.1.1 Trim Image

First step is to get rid of the portion of the images that do not contain any valuable information. The edges at the top and bottom of frames are sometimes partially blocked by the RSS guide probe. Trimming images also allows to decrease file sizes of the subsequent images, for a survey of this scale, it is essential to use hard disk space optimally. Trimming also ensures better results for the wavelength calibration of the two-dimensional frames. When there are low signal-to-noise ratios (SNR) near the edges of the CCD, it was noted that the task RE-IDENTIFY in IRAF cannot properly trace the arc lamp emission lines which leads to incorrect curvature corrections.

2.6.1.2 CCD Gap interpolation

This is a quick step which interpolates the two CCD gaps with a linear function by fitting a straight line to 5 pixel columns on each sides of each gap. The interpolation helps to get as much usable data as possible, near the gaps after background subtraction (Step 11). It is also an important step that helps the Flat-Fielding of the images. Creating master flats requires some smoothing to correct for the changing illumination across the field. Performing illumination corrections with CCD gaps in the middle of the frame will lead to incorrect averaging in areas around the gaps. This effect arises because smoothing uses a moving box to calculate the median value of pixels in a region. Around the edges the box will fall in areas with zero flux and will therefore not only affect the gaps but also the surrounding regions. The interpolation is therefore applied to all science frames and flats but is not applied to the arc lamps. The gap interpolation does not affect the science results, as masking of the relevant regions is applied in later stages when fitting for the stellar populations. The masking covers a slightly wider window than the actual physical size of the CCD gap as a precaution against any residual artefact that might be present in that area.

2.6.1.3 Cosmic Ray Removal

Since our science frames are exposed for extended amount of time, Cosmic Rays (CR) strike the CCD at several random location. To remove CR from the science frames we apply the widely used L.A. Cosmic (van Dokkum, 2001) in Python. The package makes use of Laplacian edge detection to get rid of contaminated areas and is faster in python than in IRAF. The laplacian algorithm is used to detect boundaries in images regardless of shape. Since cosmic rays strikes the detector at random angles it leads to irregular and random patterns. Therefore properly detecting their boundaries (hence their shapes) allows better removal of these data artefacts (van Dokkum, 2001). L.A. Cosmic was allowed to iterate a maximum of five times on each frames and the gain setting was set to one, since gain corrections were already carried out by SALT pre-reduction pipeline. A value of 4.5 for the sigma clipping value was adopted as it was

low enough to remove the cosmic rays but high enough to prevent removal of regions exposed with strong Balmer emission lines. Figure 2.5 shows the removal of cosmic rays on the data frame of IC2522 as an example.

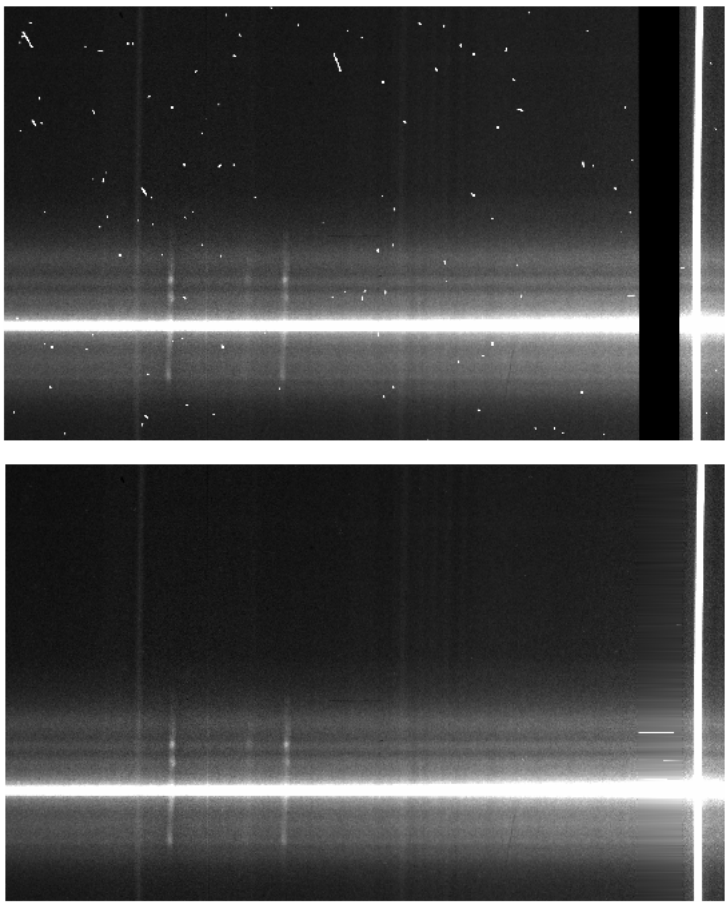

Figure 2.5: Removal of cosmic rays by L.A Cosmic on IC2522 spectrum. The panel on the top shows the image before the treatment and the panel on the bottom shows the image after. Note also that the big vertical strip is one of the CCD gap which is filled in by an interpolation value on the right panel.

For each science frame where this procedure was applied, masks containing only the detected cosmic rays were created and inspected to check if the algorithm properly removed the artefacts without removing spectral features. In the few rare cases where the algorithm failed, the settings were tweaked to get the optimal removal of cosmic rays while conserving all the signal from the objects.

2.6.1.4 Error Frames

One of the focus of the reduction process was to propagate the noise from the observation through the different reduction process. The main assumptions that we made at the beginning was that noise followed Poisson statistics even though it went through a couple of steps in the SALT pipeline during pre-reduction. Since there are very little change to the data during the bias subtraction and the gain correction, the assumption is sensible. From there on, the Poisson noise was calculated for each pixel of each of the science frames and this array was saved in another FITS file so that it could be manipulated as the reduction process was being carried out. We saved all the files at each step to be able to back track mistakes in case there was suspicion. Since the read noise was different but nearly the same for all the amplifiers of the CCD, an average value of the read-noise of the entire CCD was calculated and this average value was added to the noise using the standard method i.e.

$$\text{Original poissonian noise} = \sqrt{\text{science frame values} + \text{average read noise}^2}. \tag{2.1}$$

2.6.1.5 Flat Fielding

Flat Fielding is not carried out on SALT images by default. Since SALT's pupil varies across the mirrors during the observation, Flat-Fielding is not necessarily as straight forward as with a conventional telescope. For the commissioning period of SALT, flat fields were not available but for the rest of the dataset, in most cases flats were taken on the night of observation with the same setting as the our science data. We chose to do two sets of data reduction for each data block: a flat fielded set (if flats were available) and a non flat fielded set. We decided to leave it to the end of the reduction procedure to decide which set of data provided the best quality on a case by case basis. Flat fielded science images had their associated error frames as well.

SALT usually provides five flat fields for each observation block. We use IRAF's IMCOMBINE task to median average the five flats into one frame. Since the illumination of the flats are not constant across the field, the combine frame is corrected for that using MKILLUMFLAT with small box size settings. The illuminated corrected frame is then normalised to create our Master Flat field with which science frames are divided.

2.6.1.6 Combine Science frames

In most cases, exposures for our targets were broken into two or three shorter exposures. This is done for a couple of reasons; (a) to be able get at least one good frame in case weather changes or that the other exposures are aborted during observation due to technical issues, (b) to reduce the number of cosmic rays that strike the CCD. Longer exposures, lead to more cosmic rays and

makes it harder for software to treat this issue.

To combine science frames, alignment of the different frames are required. The science frame taken nearest to the arc frame is considered as the reference frame, and all other frames are aligned to the latter. Since the difference in position of the other frames as compared to the reference frame is usually small (sub pixel) we apply interpolation on the frames to make the array sizes bigger. Interpolation is done using the ZOOM task in the SCIPY package in python and the image sizes are increased four times in x and y direction, hence the accuracy of our alignment is to a quarter of a pixel. The huge sizes of the interpolated image frames (12600×8200 pixels) means that the the task is computationally expensive. To speed up the process, we select strips in the x and y direction of the images to calculate the shifts required to perfectly align the frames instead of using the entire frames. By constantly shifting in the x or y direction and multiplying the flux in the reference frame's strip and the equivalent strip in the other science frame (i.e we are cross-correlating the two signals) we try to find the place where the signal is maximised. This procedure gives us the shift that needs to be applied in the two dimensions of image. The shift is then applied to create a new science frame which is aligned to the reference frame. The aligned images are then combined by adding the signal in all the frames to create a master science frame. The shifting procedure is also applied to the propagated error frames. The signal for the error frames are added in quadrature.

2.6.1.7 Wavelength Calibration

Wavelength calibration is performed on Arc Lamp frames that are generally recorded just after an observation (though in some cases they were recorded before). The task IDENTIFY is used for the calibration by fitting emission lines of the middle row of the Arc frame. The model which is used in the fitting is that of the SALT's longlist line atlas[1]. A second order cubic spline is used for the fitting function with a minimum of 20 identified lines over the entire wavelength range for accurate results. Figure 2.6 shows the line identification of an Argon arc lamp in IRAF.
RSS like other spectrographs has curved distortion in the spacial dimension and this is corrected in the data by running the REIDENTIFY task. The latter uses the results of the IDENTIFY task as a reference and searches for the same set of identified lines along the spatial dimension of the Arc frame. FITCOORDS is then run interactively to produce a 2-Dimensional wavelength and distortion correction of the CCD array. Figure 2.7 shows how FITCOORDS was run on the dataset. A 6^{th} order Chebyshev function was used for FITCOORDS fitting in both x and y direction. Outliers were removed to produced more accurate fits with lower r.m.s value. The solution derived is then applied to all the science frames (and error frames) via the task TRANSFORM. (**Note:** All the tasks mentioned above are in the IRAF sub-package

[1] http://pysalt.salt.ac.za/lineatlas/lineatlas.html

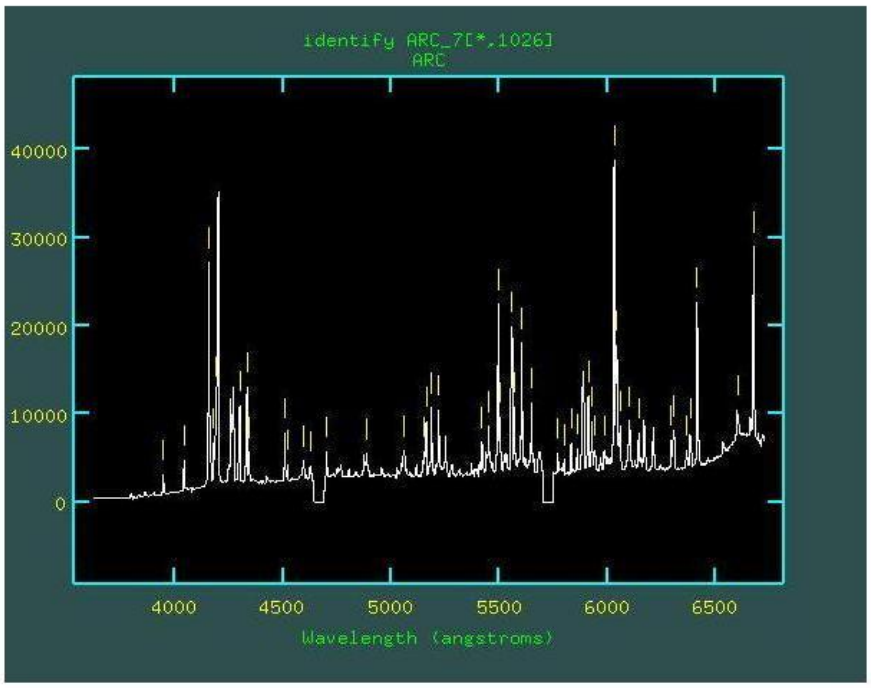

Figure 2.6: Identification of lines in a Argon arc lamp for PG0900 data with the task IDENTIFY in IRAF.

NOAO.TWODSPEC.LONGSLIT)

2.6.1.8 Background Subtraction

Now that the science images have been straightened and wavelength calibrated we can proceed to removing the sky background in each of them. The task BACKGROUND is run interactively and a low order Chebyshev function is fitting along each column of the image. The regions which are illuminated by the galaxy light and some buffer regions around the galaxy, are flagged and not taken into consideration for this fit. In case the spectrum contains stars, other galaxies or some residual of bad cosmic ray removal, those are also masked.
For the error calculation of this step, we first create a frame with pure sky emission. We use the science frame before background subtraction and subtract it with the science frame with has been background subtracted to get a sky image.

$$\text{Sky frame} = \text{Science frame with sky} - \text{Background subtracted science frame}, \tag{2.2}$$

$$\text{Sky frame error} = \sqrt{\text{Sky frame}}. \tag{2.3}$$

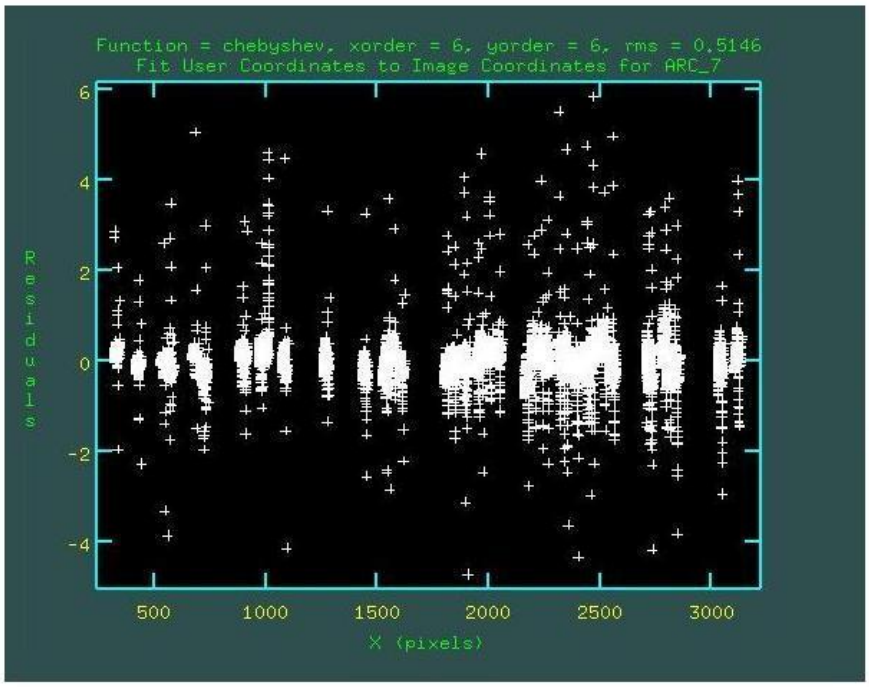

Figure 2.7: Using FITCOORDS from the IRAF package interactively on the data to correct for distortion.

We then add in quadrature the sky frame error and wavelength calibrated error frame for the previous step.

$$\text{Background subtracted error frame} = \sqrt{(\text{Sky Frame error})^2 + (\text{Wavelength Calibrated error frame})^2}. \tag{2.4}$$

Figure 2.8 displays an example of background subtraction for both a science frame (left) and the error frame (right) following the procedures described above.

2.6.1.9 Tilt Correction

Since the spectrograph and its CCD are not perfectly aligned to each other, spectra tend to be slightly tilted. The tilt can be become more prominent with different angle of the instrument in the payload, because of flexure due to gravity. This means that a spectrum never appears perfectly horizontal on the CCD image. We correct for this by running the task APALL which traces the signal of the spectrum. APALL allows us to self-define a window centred around a peak. The tracing is done by APALL trying to find the same peak at different columns of the data. By fitting a cubic spline of second order to the location of the peaks at different columns,

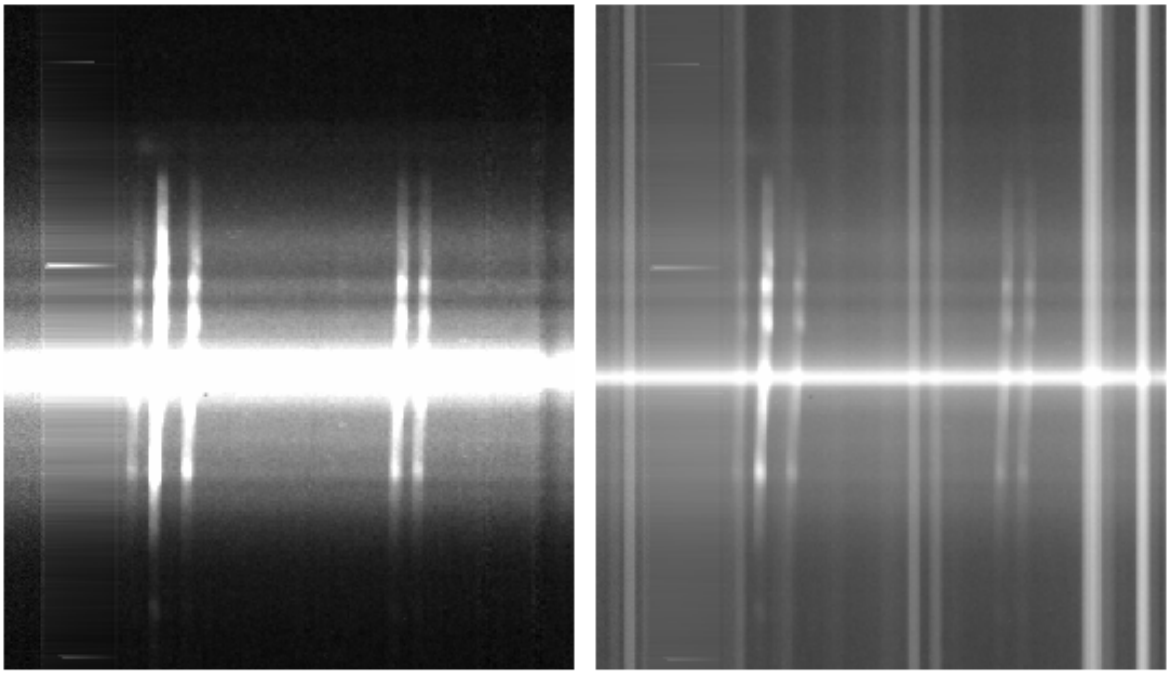

Figure 2.8: *Left Panel*: Background subtracted image of IC2522 showing the Hα line surrounded by the two [NII] lines as well as the two [SII] lines. *Right Panel*: The error frame of the same background subtracted portion. The strong presence of the sky lines are due to their added noise at the specific wavelength.

the signal is traced along the entire x-axis of the data. Using the signal of galaxy with lower surface brightness or with varying nuclear activities for the tracing can sometimes be tricky and lead to incorrect results. In such cases, if foreground stars appeared in the field, they can be used to give better results. Stars have very narrow spatial dimension and strong signal, which makes them very good candidate.

2.6.1.10 Aperture Extraction

Tilt correction and Aperture Extraction are two different process that work hand in hand in APALL. Both tasks can be carried out during the same run. The Aperture selected for extraction are usually wide enough to contain all the galaxy signals in the data. The solution from the tilt correction and aperture extraction of one frame can then be saved and applied it on all other frames for that observation block. For each frame we usually extract one Strip aperture which contains all the interesting features in that frame. APALL then outputs a two dimensional spectrum which is corrected for tilt. Error frames are also extracted with the same solution as their science image counterparts.

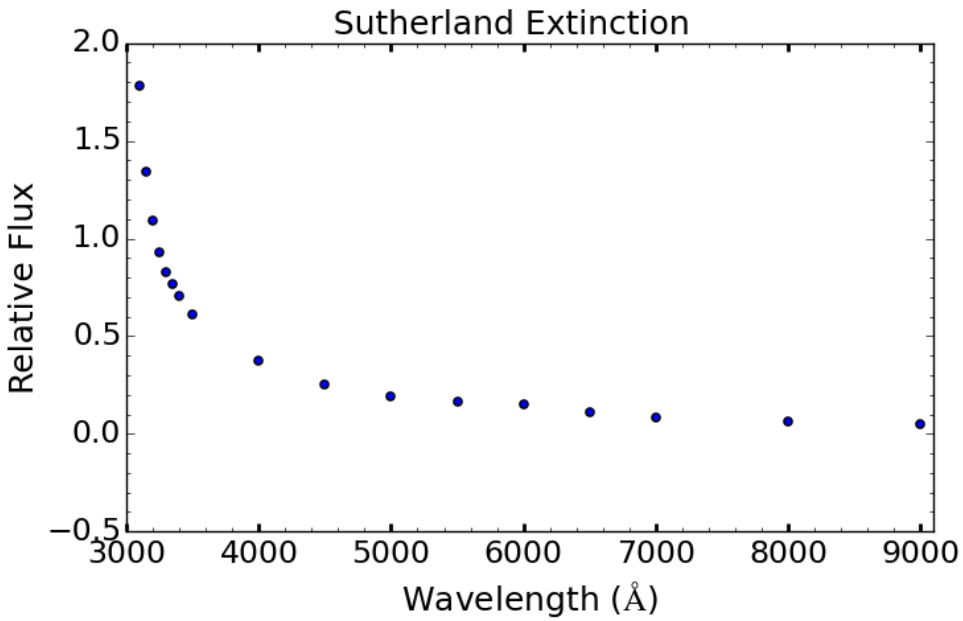

Figure 2.9: The Sutherland extinction curve that is an input parameter for the IRAF task STANDARD.

2.6.1.11 Flux Calibration

Spectrophotometric standard stars are observed by the telescope with the same settings as our different observation blocks. Usually the standard stars could be observed on the same night or a few days apart. The standard stars go through the same reduction process described above. Reaching the step of aperture extraction, a 1-Dimensional spectrum is extracted instead of a strip. The 1-D spectrum of the same star from the ESO database website[1] is downloaded. By comparing the spectrum of the star from SALT observation, and that from the ESO database along with the atmospheric extinction curve from Sutherland (see Figure 2.9, we use of the task STANDARD and SENSFUNC to create a sensitivity curve for that particular grating setting. This sensitivity curve is then applied to all galaxy spectra observed with the same setting around the same dates. Figure 2.10 demonstrates an example of a sensitivity curve that was derived for the standard stars LTT4364 using grating PG0900 along with grating angle 13.625^o.

2.6.1.12 Galactic Extinction Correction

The last step in our reduction pipeline is to correct for the foreground extinction effect of the Milky Way. We use the NED database to acquire V band extinction values for the entire sam-

[1] https://www.eso.org/sci/observing/tools/standards/spectra.html

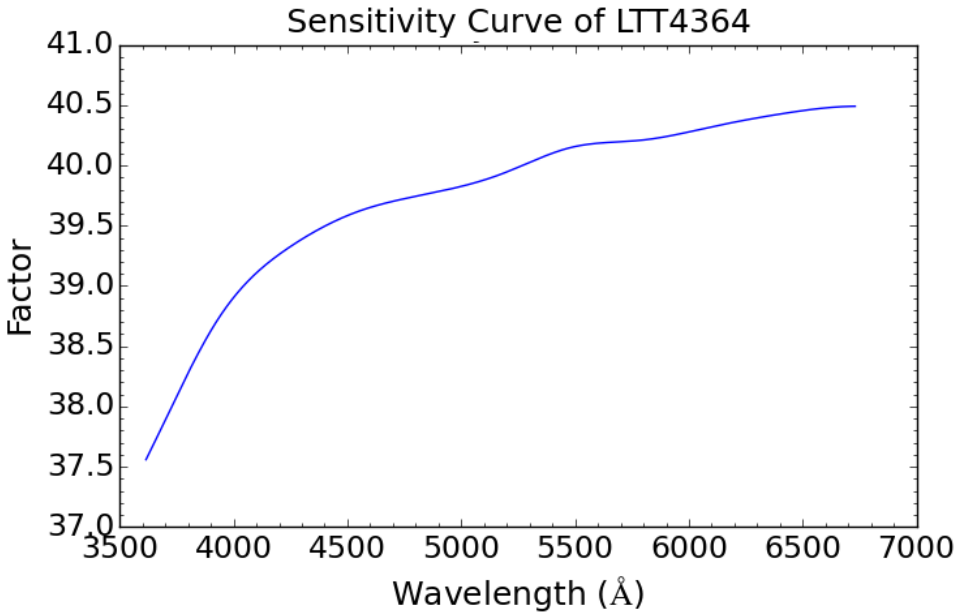

Figure 2.10: The derived sensitivity curve of the standard star LTT4364.

ple. The NED values are based on the work done by Schlafly & Finkbeiner (2011) which is a recalibration of the maps derived by the more popular work of Schlegel et al. (1998) presented in the DIRBE dust map. We assume a reddening law which follows the work of Fitzpatrick (1999) with an $R_v = 3.1$. To do the flux correction following the parameters stated above we make use of the task DEREDDEN in IRAF and apply the corresponding V band extinction for each of the galaxies.

After all the corrective measures described above has been properly applied and cross-checked, the spectra are now ready to be used for data analysis. As an example of a finished product, a plot of the spectrum of ESO 221-IG008 is available in Figure 2.11.

2.7 Summary

Observations of the SUNBIRD sub-sample galaxies were performed over the course of a three-year period, collecting long-slit spectroscopic data from SALT. The data collected consisted of southern Infrared Luminous Galaxies in the local universe. A relatively diverse population of galaxies was observed in terms of interaction stages. In turn this allows for the current work to be a good representation of the behaviour of LIRGs at low redshift ranges. To properly tackle

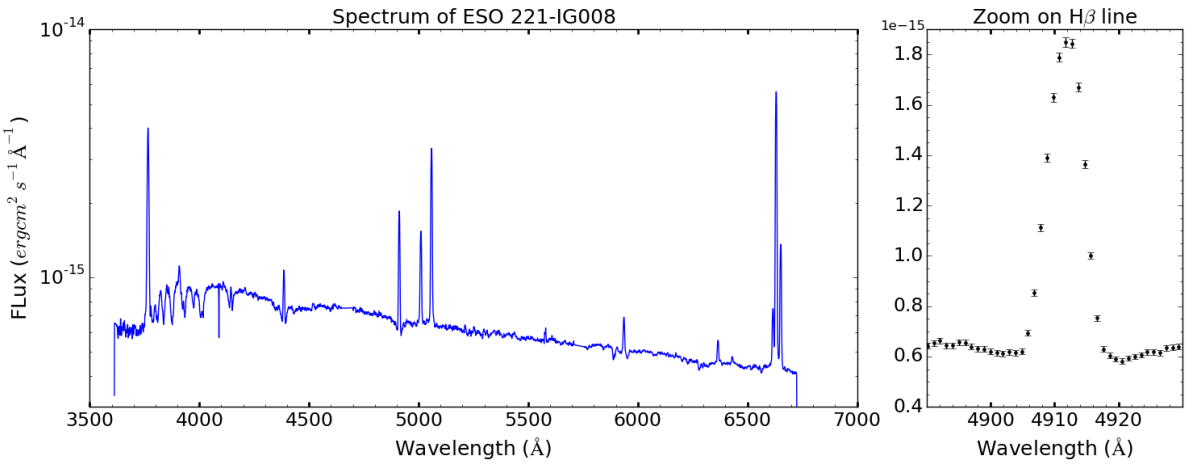

Figure 2.11: *Left Panel*: The spectrum of ESO 221-IG008 after data reduction. *Right Panel*: A zoom on the Hβ line with the errorbars. (**Note:** On the left we use a logarithmic scale for the y-axis to be able to plot the emission line as well as the continuum. The right panel is a linear scale)

the size of the dataset, a reduction pipeline was written, tested and then applied to produce high quality science frames maximising the signal-to-noise ratio for each observation.

Chapter 3

Spectroscopic Analysis Techniques

3.1 Introduction

In this chapter, we review the different techniques that we will apply to the data assembled. Our aim is to give an overview of all the different scientific information that can be extracted from spectral data. First, an in-depth review on some of the topics that were introduced in the literature review is made. Then the focus is placed on the specific techniques that were developed and fine-tuned for this thesis. Stellar Population Modelling will comprise the majority of this chapter, but other topics, such as oxygen abundances, ionisation, extinction and mass estimation will also be explored.

3.2 Spectral Fitting

The spectrum of any astronomical object carry a lot of valuable information. Over the years, different techniques have been developed to extract the physical parameters of stars and galaxies from their spectra. Information about stellar population usually resides in the absorption features of galaxies which is a combination of all the atmospheres of the stars constituting the particular galaxy. There are three main categories of spectral fitting: absorption indices, full spectrum fitting and spectral energy distribution (SED) fitting. While we explore the first two methods in the next sections, SED fitting is beyond the scope of this thesis.

3.2.1 LICK Indices

One method to extract information from a galaxy spectrum is to measure a single or a series of absorption indices, where the indices is a quantitative measure of the different absorption lines. Before the advent of full spectrum fitting, astronomers were limited to mostly using spectral indices to measure the age and metallicity of stellar populations. The most common spectral

index system is the LICK/IDS system which makes use of 21 indices in the wavelength region of 4000-6500$\AA$ (Burstein et al., 1984; Faber et al., 1985; Worthey et al., 1994). LICK indices are measured around absorption lines according to the following procedure: the absorption line is defined in a central region; two pseudo-continuum regions on each side of the absorption feature are then defined; a line joining the midpoints of the 2 pseudo-continuum regions is then drawn and used as the reference to calculate the flux of the absorption line (Worthey et al., 1994) (see figure 3.1).

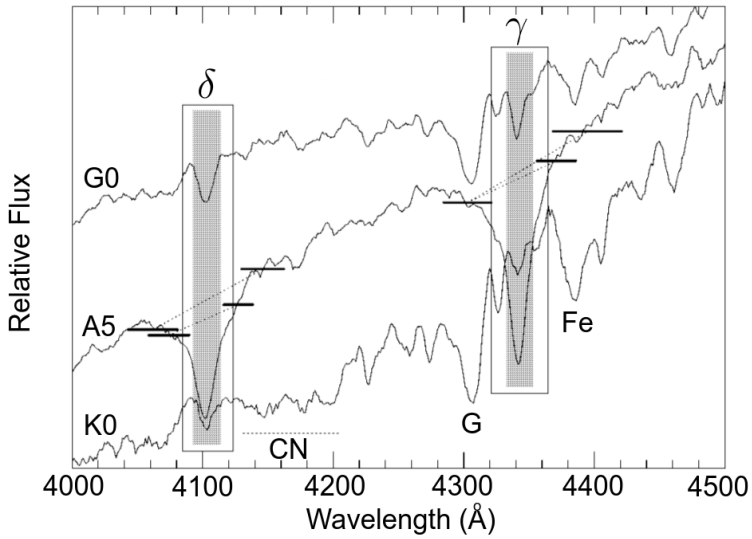

Figure 3.1: An overview of how LICK indices are measured, here the cases of $H\delta$ at 4101$\AA$ and $H\gamma$ at 4340$\AA$ are demonstrated. The grey region denotes F-definition of the index while the larger empty boxes shows the A-definition. The dashed horizontal lines represent the sideband regions selected for the pseudo-continuum. The pseudo-continuum level is represent in the dashed lines linking the side-bands. (Figure taken from Worthey & Ottaviani (1997))

Spectrophotometric indices have traditionally been used in an era where only low resolution data were available and hence many of the features that were selected were a mixture of several lines (Koleva et al., 2008). Therefore, calibrating the subtle influences of each of the indices with respect to abundances or age of stellar populations, it requires very precise and careful modelling (see for example: Korn et al. (2005)). Ultimately, indices are only localised snapshots of an entire spectrum. While they may have good indications of the age and metallicity of a galaxy they can easily be affected by poor data quality in their region. The disadvantage of the method is the loss of valuable information stored in the entire spectrum, that the indices cannot make use of.

3.2.2 Full Spectrum Fitting

Full spectrum fitting fits the entire wavelength range observed in one go and derives different parameters such as age and metallicity by weighing on the different important absorption features as well as the overall shape of the continuum. For the past ten years, this technique has become very popular because we have a better understanding of the different ingredients involved. In essence, full spectrum fitting tries to match an observed spectrum with a series of template spectra through a chi-squared minimisation technique. It then outputs the best set of templates that match the observation, from which the physical parameters can be recovered. The templates are created by assuming different models of stellar formation and evolution based on the ingredients discussed below in Section 3.3. Several codes such as ULySS (Koleva et al., 2009), STECMAP (Ocvirk et al., 2006b), STARLIGHT (Cid Fernandes et al., 2004, 2005), FIREFLY (Wilkinson et al., 2017), are now available to do full spectrum fitting.

3.3 Ingredients of spectral fitting

3.3.1 The Initial Mass Function

The Initial Mass Function (IMF) is a distribution of stars in different mass bins at the time of their birth in a given location, a nebula or cluster or galaxy. It is a description of the distribution of masses of the stars prior to any stellar evolution and is a key ingredient to understanding stellar populations. Stars of different masses exhibit a range of properties, hence a function which models the masses properly will be able to inform us of the expected properties of the population. Salpeter (1955) was the first to introduce the concept of IMF through a simple power-law in the form:

$$\phi(m)\mathrm{d}m \propto m^{-\alpha}\mathrm{d}m, \quad \text{where} \quad \alpha = 2.35, \tag{3.1}$$

for the mass range of $0.4M_{\odot}$ to $10M_{\odot}$. Over the years, more complex functions were used to model the IMF from newer observations. Log-normal shape was used by Miller & Scalo (1979) following observations of field stars, and later a segmented power law was used by Kroupa et al. (1993) to match the shape of distribution at the lower mass range up to $0.08M_{\odot}$, and was further extended to $0.01M_{\odot}$ in Kroupa (2002):

$$\phi(m) \propto \begin{cases} m^{-2.7} & (1.0M_{\odot} < m < 100M_{\odot}) \\ m^{-2.3} & (0.5M_{\odot} < m < 1.0M_{\odot}) \\ m^{-1.3} & (0.08M_{\odot} < m < 0.5M_{\odot}) \\ m^{-0.3} & (0.01M_{\odot} < m < 0.08M_{\odot}). \end{cases} \tag{3.2}$$

This IMF is 'flat' at low masses but has similar characteristics as the Salpeter IMF for $m > 0.5M_{\odot}$ (Mo et al., 2010). Similarly, Chabrier (2003) also follows the Salpeter IMF at $m > 1.0M_{\odot}$ but for low masses it resembles more the Kroupa IMF, though it adopts a different form. The Chabrier (2003) is of the form:

$$\phi(m) \propto \begin{cases} m^{-1.35} & (m > 1.0M_{\odot}) \\ exp\{-[\log(m/0.2M_{\odot})]^2/0.6\} & (m < 1.0M_{\odot}). \end{cases} \tag{3.3}$$

Salpeter, Kroupa and Chabrier are usually considered as the 'canonical' IMF, even though there are various other ones available. The left panel of Figure 3.2 shows a comparison of the function adopted by those three IMFs at different stellar masses in an 'alpha plot'.

One of the big questions in extragalactic astronomy is the universality of the IMF. Bastian et al. (2010) claim that the variations in IMF are rather small and that observation appearing as non-standard IMF would arise due to other factors, with some speculating that variations in metallicity affects the IMF Peletier (2013). On the other hand, Maraston (2013) claims that some of the latest work on Giant Ellipticals show evidence for non-universal IMF. One step further is the questioning whether the IMF is universal at different radial distances from the nuclear core of galaxies. Here as well the science is still debatable as evidence for both radial non-universality (Martín-Navarro et al., 2015) and radial universality (Alton et al., 2017) have been found in early-type galaxies. In general, we can conclude that when it comes to the IMF, the science is still very unclear and hence it is beyond the current work to investigate the impact of the choice of IMF on star forming galaxies. Instead we adopt a simple approach of choosing one IMF - Chabrier (2003) - for the entire work in this thesis. In appropriate places, we will still convert our results to other IMF to be comparable to literature results.

3.3.2 Single Stellar Population

A Single Stellar Population (SSP) is a population of stars born at the same age, assumed to be made of gas of homogeneous chemical composition. The mass distribution of an SSP is then assumed to follow one specific IMF for simplicity of modelling. Since all the main parameters (such as age or metallicity) are known, one can then build up how the spectrum of such a population would look. Conroy et al. (2009) described that at time t, for a chemical composition of Z, the function is:

$$S(t, Z) = \int_{M_i^l}^{M_i^u} \Phi(M_i)\Lambda[L(M_i, Z, t), T(M_i, Z, t), Z]\mathrm{d}M_i, \tag{3.4}$$

where M_i is the initial mass with M_i^l and M_i^u being the lower and upper mass limits of the

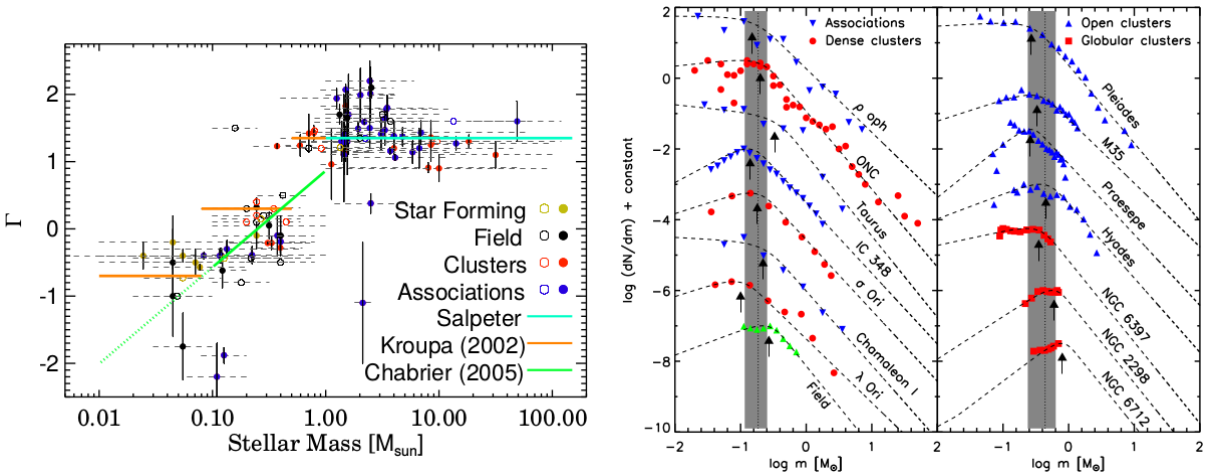

Figure 3.2: *Left panel*: An 'alpha plot' of Scalo (1986) and Kroupa (2002) comparing the 3 main IMFs. The y-axis shows the derivative of the IMF-slope with the x-axis being stellar mass. For low mass regime, Kroupa is segmented into different parts while Chabrier is a continuous function. *Right panel*: The Mass function of a sample of young star forming in open clusters are closer dynamically evolved Kroupa or Chabrier type IMFs. Credit - both figures taken from Bastian et al. (2010)

IMF, Φ. Λ is a spectrum from the stellar library with bolometric luminosity L and an effective temperature T.

3.3.3 Stellar Population Modelling

In recent decades, stellar population modelling has become more feasible with the growing computational power at hand, in the data deluge era, where both ground-based telescopes and space telescopes are used. Astronomers also have a better understanding of the different ingredients such as the IMF, the isochrones and the SSPs involved in the modelling which is crucial. Previously, spectral lines were measured individually to derive properties of astronomical objects. While this approach is still used, the new method is to use the entire spectrum of the objects, rather than specific portion of it to derive properties such as star formation histories, metallicity contents and chemical evolution. For complete reviews on this topic see Walcher et al. (2011); Maraston (2003, 2011).

The light we observe from galaxies is essentially an integration of the diverse population of stars and the gas along our line of sight. The stellar population varies both in age and metal content. To recover all this information from a single observation is unrealistic, but a simple way to achieve this is to assume an IMF (Peletier, 2013). Another important assumption is made when taking the Single Stellar Populations (SSP) as the building blocks of the complex population

residing inside a galaxy. The population of a particular galaxy is then a linear summation of all the different SSPs present. In recent years, various open source tools have become available to perform stellar population modelling, for example, Starlight (Cid Fernandes et al., 2005), pPXF (Cappellari & Emsellem, 2004), STECKMAP (Ocvirk et al., 2006a,b), CIGALE (Burgarella et al., 2005) and ULySS (Koleva et al., 2009). If galaxy evolution consisted of galaxies evolving in a closed box and only had used their initial gas to fuel star formation, then an SSP would probably suffice to appropriately model the population of stars observed. In reality, this is hardly the case since galaxy evolution is a highly violent process where there are collisions between galaxies, feedback processes and chemical enrichment, all together simultaneously. For this reason, a multitude of SSPs are required to properly model galaxies, especially in the currently star forming cases, like LIRGs.

3.3.4 Stellar Evolution and Stellar Libraries

Stellar evolution is the base of population modelling. As a first approximation, stellar evolution is mostly dependent on the initial mass and chemical composition of the star. Massive stars such as O stars, consume their fuel quickly and dies in a supernova explosions, usually within few tens of millions of years. Stars with masses nearer to our Sun, on the other hand spend an extremely long time in the main sequence phase ($\sim$10 Gyr). By the end of its lifetime, a Sun-like star becomes a red giant before transforming into a white dwarf. To properly model a star's evolution, one must accurately track the different phases of its life along the Hertzsprung-Russell (HR) diagram. There are different groups, such as the Geneva (Schaller et al., 1992; Schaerer et al., 1993; Charbonnel et al., 1996) and Padova (Alongi et al., 1993; Bressan et al., 1993; Fagotto et al., 1994a,b,c; Girardi et al., 1996) groups which have extensively modelled the stellar evolution of a large variety of stars with different masses and metallicities. As a result of their work there exists libraries of isochrones for various scenarios.

By using stellar evolution models, one can therefore build up libraries of stellar spectra with a smooth coverage of parameters such as effective temperature, gravity and metallicity. Libraries can be both empirical or theoretical. Empirical libraries consist of observations of sample(s) of local (inside the Milky Way) stars of different parameters required to have good coverage. Gaps in data for some scenarios are either interpolated or extrapolated from the existing data collected. Synthetic libraries on the other hand rely on the different models used. Wavelength range of the spectra produced with this method is wider than with the empirical method. However, theoretical libraries also have issues because our understanding of stellar atmospheres is not complete. Some of the known limitations includes failures to take into account phenomena such as convection, non-local thermodynamic equilibrium and radiatively driven winds (Leitherer, 2012).

3.4 Age Metallicity Degeneracy

The Age-Metallicity degeneracy is a well known effect that makes the accurate determination of parameters during spectral fitting harder. The issue arises because galaxies have redder colours with either increasing age (more stars move to the giant branch), or increasing metallicities (decrease in the effective temperature of stars) (Peletier, 2013). The fact that two different parameters have the same observational consequences on the spectra of galaxies was noted by different authors (O'Connell, 1976, 1980; Worthey et al., 1994). Worthey (1999) later quantified that a doubling of the age is similar to a tripling the metallicities of a galaxy, if relying on optical colour to estimate age. Efforts to mitigate the effect have been explored during the 90's when LICK indices were popular, indices which were sensitive to either age or metallicity, but not both, became crucial. Spectral features such as Fe4668, which is highly sensitive to metallicity, and others, like Hβ, which is insensitive to metallicity, were explored (Cardiel et al., 2003). Another way to minimise the effect of this degeneracy is to use full spectrum fitting (Cardiel et al., 2003), which uses the information of a spectrum across a wide wavelength range instead of using only specific features as was done previously. The condition for the latter to be successful to mitigate age-metallicity degeneracy is that the wavelength range selected needs to be wide enough to contain several independent age and metallicity indices.

3.5 BC03 Model

For this project we make use of the Bruzual & Charlot (2003) (from here-on BC03) synthesis population model, which is probably one of the most popular models used. The GalaxEv model is based on the Bruzual & Charlot (2003) paper, and works with the SteLib Library (Le Borgne et al., 2003), which contains 249 spectra with a wavelength range of $3200 - 9500\mathring{A}$. Out of these, 187 have a recorded metallicity value and can be used in metallicity derivation (Koleva et al., 2008). A Chabrier IMF (Chabrier, 2003) is applied in this case and it follows different laws at 7 different masses. For masses ranging from $0.1\,M_\odot$ to $1\,M_\odot$ the slope is given by $\exp[-(\log m - \log 0.08\ M_\odot)^2/0.9522]$, but for masses from $1\,M_\odot$ to $100\,M_\odot$ it has the usual -1.35 value. The library offers a resolution of $R = 2000$ with a wavelength of $3200\mathring{A} - 9500\mathring{A}$. GalaxEv uses Padova 94 (Bertelli et al., 1994) isochrones and covers a metallicity range from -2.3 dex to 0.4 dex. While the BC03 model has been around for a long time and has some limitations, it still offers good coverage from the very young to the very old stellar populations ($1\,\mathrm{Myr} - 13\,\mathrm{Gyr}$) consistently which libraries such as MILES (Sánchez-Blázquez et al., 2006) lacks. And since for our work the very young population of stars is crucial, BC03 is hence a good choice of template. Figure 3.3 shows the BC03 template used for this thesis with the 45 SSPs grouped by metallicities in three panels and normalised at $\lambda = 5000\mathring{A}$.

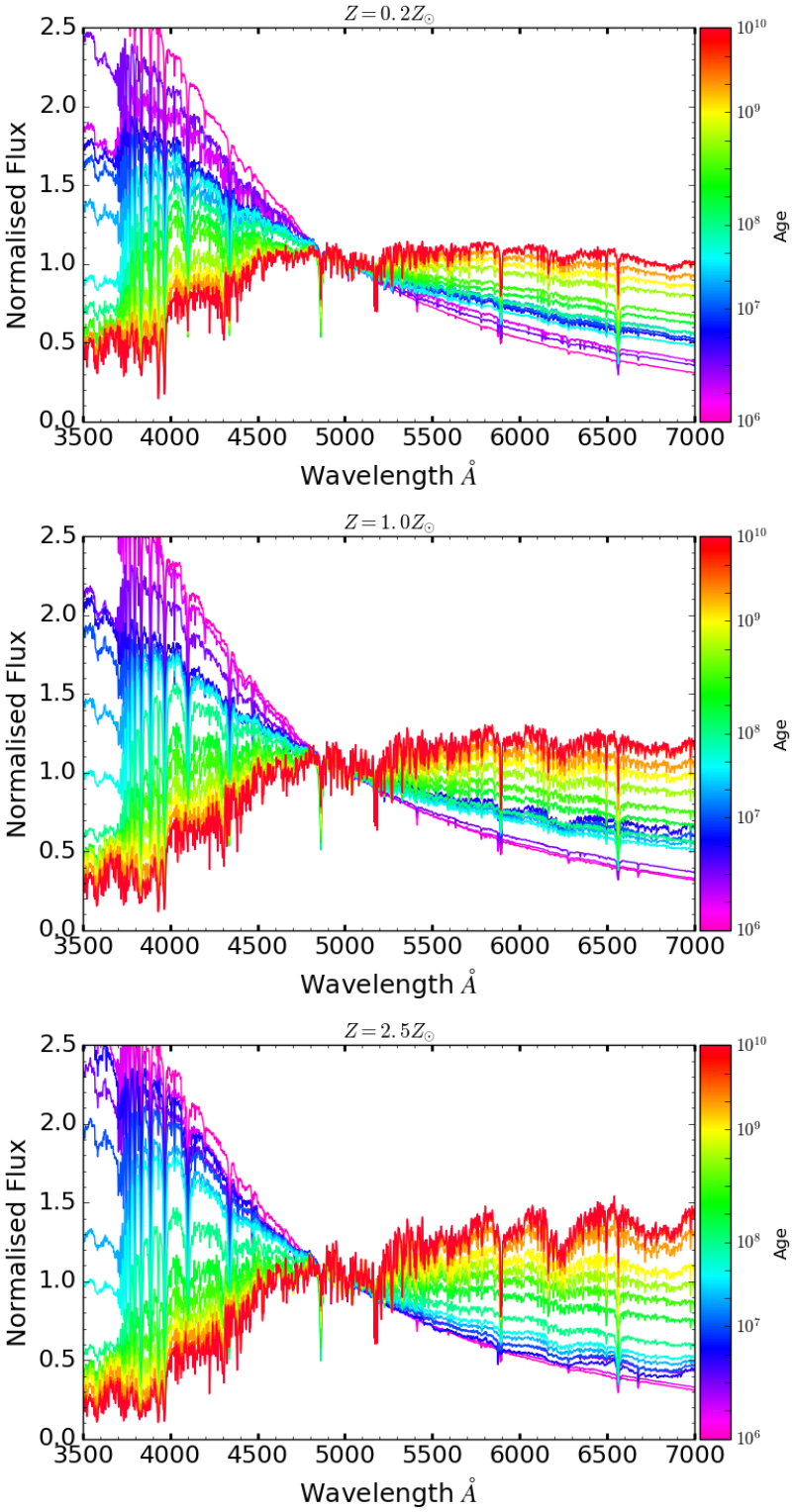

Figure 3.3: The BC03 models used for this project. We plot 3 different metallicities in different panels for clarity, while the line colours indicates the different ages. The flux of the SSPs were normalised at $\lambda = 5000\AA$.

3.6 STARLIGHT

STARLIGHT[1] is an inversion code, written in Fortran, that fits the observed spectrum O_λ of a galaxy to try to derive the linear combination of SSPs present. While STARLIGHT is written in an open source language, the source code has never been made public. The executable available from the website was used to run the software on our computers/servers and no modifications were made to add new features to the code. An in-depth explanation of the underlying mathematical/computational scheme of the code is given in Cid Fernandes et al. (2004, 2005), but we will give a brief description of the relevant parts of the code below.
The SSPs to be fitted to O_λ are input in the form of a library consisting of N_* different SSPs. The software then estimates a model spectrum based the equation:

$$M_\lambda(x, M_{\lambda 0}, A_v, v_*, \sigma_*) = M_{\lambda_0} \left(\sum_{i=1}^{N_*} \boldsymbol{x_i} b_{i,\lambda} r_\lambda \right) \otimes G(v_*, \sigma_*) \tag{3.5}$$

where:
- $M_{\lambda 0}$, is the flux of the model at the normalisation wavelength, λ_0
- $\boldsymbol{x}$ is the fractional contribution of each SSP from the library. It is also commonly referred as the *population vector*.
- $b_{i,\lambda}$ is the normalised spectrum of the ith SSP. $b_{i,\lambda}$ varies when the stellar library is changed.
- $r_\lambda = 10^{(-0.4(A_\lambda - A\lambda_0))}$ describes the extinction of the source.
- $G(v_*, \sigma_*)$ is the line-of-sight velocity centered at v_*, broadened by σ_*, assuming a Gaussian distribution.
- $\otimes$ denotes the convolution as the model spectra are broadened to fit the wings of absorption features in the data.

χ^2 minimisation is then used to get the best fit and is achieved using a simulated annealing method along with a Metropolis scheme:

$$\chi^2 = \sum_\lambda [(O_\lambda - M_\lambda) w_\lambda]^2 \tag{3.6}$$

where w_λ is the weight of each pixel in O_λ, which is the inverse of the error spectrum.

3.6.1 Characteristics of STARLIGHT

STARLIGHT is downloadable as an executable file and therefore should be able to run on most systems. There are different compiled versions which caters to different computer architectures (32-bit and 64-bit) and different operating systems (Linux and Mac). Running STARLIGHT

[1] http://www.starlight.ufsc.br/

is straightforward but requires some preparation of the data. This is detailed in depth in the software's manual[1]. We list the fundamental steps we took to run the code successfully below:

- You are required to provide the code with 5 files - an input spectrum, a mask file, a base master file, a configuration file and a grid file.

- The input spectrum needs to be in ascii format. The two essential columns required are the wavelength and flux at each wavelength interval. The preferred wavelength dispersion is $1\mathring{A}$. If an error spectrum is available it can be added as a 3rd column (the units for the flux and error spectrum needs to be consistent). In this work our data reduction pipeline was designed to output an error spectrum, hence the values from the error spectrum were always used in the 3rd column. Finally, a 4th column can be added to flag bad pixels though this is usually taken care of by the mask file.

- The input spectrum was calibrated using the steps given in data reduction procedures from Chapter 2 section 2.6. Relative flux calibration is adequate for most of the features of the code. Galactic extinction needs to be applied to the flux of the spectrum in the observed frame. The spectrum needs to be shifted to the rest frame (redshift,$z = 0$). Finally, the wavelength sampling needs to be uniform and the dispersion adjusted to the recommended $1\mathring{A}$.

- The mask files provided were tailored for each observation. The spectrum of the nucleus of each galaxy was inspected by eye to select portions which must be masked out of the fitting. CCD gap portions, emission lines, and rare cases of bad pixels were flagged by giving them a weight, $w_\lambda = 0$. In cases where we fit the galaxy spectrum extracted from sections other than the nucleus, the same mask file was used.

- The base master file is the place where the list of N_* SSPs lives. The base master file links STARLIGHT to the stellar library files that will be used for a specific fit. Out of the 7 columns that are required, the code only needs columns 1 and 6 for the fit. Column 1 gives a list of names of the SSP to be used while column 6 is an extinction flag. For simplicity, we set all extinction flags to 0 so that only one extinction value is fitted. Columns 2 to 5 represent the information about age, metallicity, names, initial stellar mass fraction and the α/Fe of each SSP respectively. The information from those columns is an easy way to keep track of which SSP was used when the result files come out.

- The default configuration file that comes in with the software was used except for a few tweaks - a long Monte Carlo chain was selected for all runs where number of chains, N = 12 .

[1] http://www.starlight.ufsc.br/papers/Manual_StCv04.pdf

- The grid file was updated for each fit to direct the code to the relevant directory paths, mask file, base file and configuration file.

- Lastly, STARLIGHT comes built in with a few reddening laws, such as CCM (Cardelli et al., 1989), Calzetti law (Calzetti et al., 2000) and Allen (1976) (known as HYPERZ). Since we work with LIRGs, ULIRGs and Starburst galaxies, we choose to use the Calzetti Law for all the fits for this sample. This is because LIRGs and ULIRGs have strongly starburst regions where the interstellar medium acts as a turbulent screen in front of strong UV emitting OB stars. Fischera et al. (2003) showed that in that in such a scenario, Calzetti law, while being empirically derived, has also a physical basis.

Every time that the code runs, it generates one output file that has three important sections. The first part is values such as extinction, velocity dispersion, scaling factor of the flux, etc... are listed. The second part of the output contains the population vector, $\boldsymbol{x_i}$. The last part of the output consists of four columns, which give the wavelength, input spectrum, fitted spectrum and flagging information. The input and fitted spectrum are both normalised, but the original data can be obtained by using the scaling factor.

3.6.2 Starlight Pipeline and error estimation

One of the main issues with STARLIGHT is that it does not output any uncertainties in the parameters that it estimates. Therefore, some of the strategies described in Cid Fernandes et al. (2014) are adopted to derive uncertainties. A Monte Carlo approach is used for all the fits performed in STARLIGHT, by perturbing the observation with some added noise, and performing the fit several times (typically above 40 times for the work presented in this thesis). Then basic statistics are calculated on all the outcomes to obtain the uncertainties. This method still has the caveat that there is a finite number of SSPs which are being fitted and hence the code will always choose some templates over others for a certain range of uncertainties. But a decent estimation of the variance in the parameters output by the code is obtained through this method. Running many iterations of STARLIGHT requires a lot of computing power and also a good organisation of the input data to avoid confusion. Similarly, analysing the output files of each iteration requires a system to be put into place to efficiently manage the large amount of data generated. A python wrapper around STARLIGHT was therefore written to be able to run the code multiple times, in parallel on a multi-core machine (or computer cluster), and on a number of cores that were deemed optimal beforehand. The newly acquired SAAO computer clusters (Mons and Mensa) were used for the STARLIGHT fittings of this project.

Figure 3.4 shows the flowchart of the different processes that were used to run the STARLIGHT pipeline, which simultaneously can generate results for different SSP bases and also get the

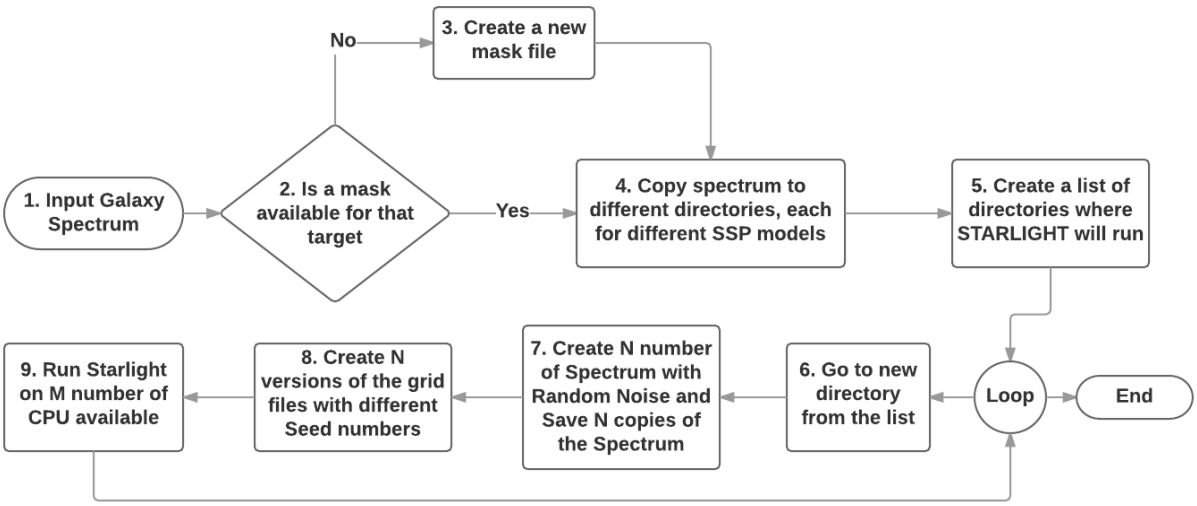

Figure 3.4: A step by step breakdown of the different processes involved in running STARLIGHT in parallel. This is not a fully automated system, but rather the scheme that was followed for consistency. Step 1 to 5 are done either by hand, or by code snippets written in Python while the loop from step 6 to 9 is fully automated in Python and run as a single main program.

uncertainty estimates. Below is a more in-depth description of some of the key steps:

- Step 1 - The input spectrum is extracted from the FITS files of the reduced spectrum and its associated error spectrum.
- Step 4 - The spectrum is then duplicated to different directories which are created through a script. A directory is made for each target and SSP base - e.g. NGC7714 will have one directory for BC03 base and another directory for a MILES base, if two different library were to be used.
- Step 5 - Just before step 5 the data are sent to a computer server which has several CPU nodes. We then create a list of directories in which the STARLIGHT is run.
- The loop - A meta script then takes control of the loop from step 6 to step 9 in each directory.
- Step 7 - A number N of 'observed' spectra are created from the single observed spectrum. Each of these spectra have been randomly perturbed within the noise of each wavelength pixel. The noise follows a Gaussian distribution which has a mean that is equivalent to the flux of the particular pixel, and a standard deviation that is scaled by the corresponding pixel in the error spectrum.

- Step 8 - for each of the N spectra created in step 7, a grid file is created with a different seed number to start the Markov Chain at different places in the parameter space.
- Step 9 - The script uses M number of CPUs to create M processes. Each instance of the STARLIGHT pipeline fits one of the N spectra created using the associated grid file previously saved.

3.7 Pipeline Testing

The previous sections covered the main logical steps in building a pipeline to run STARLIGHT in parallel, to recover parameters of galaxies and the associated uncertainties. We now focus on evaluating how the pipeline performs as well as characterising any peculiar features or systematics associated with our method.

3.7.1 Modelling the noise

The robustness of any results obtained is limited by the performance of the instruments used to acquire the data - in this case the Southern African Large Telescope in Sutherland, South Africa. Having a good model of the signal-to-noise ratio in the different wavelength bins is therefore essential to test the performance of the fitting. Any observed spectrum could in principle vary within the bounds of noise, limiting the amount of information that can be recovered back. A good representation of the noise, can be applied to any simulation set to closely match how real data will be affected. In Chapter 2 it was shown, that for the entire data sample, error frames were derived to model the variance of each pixel bins. The error frames are essentially the base that we use to obtain a global model for the noise in SALT data. By combining the entirety of our dataset for the PG0900 grating (both for nuclear and outer apertures), and using a wavelength resolution of $1\,\mathring{A}$, an average of the signal to noise ratio is derived for each wavelength bin that will be used for spectral fitting.

The noise is binned into three categories: low, medium and high SNR. This is done to create a tunable model of the noise behaviour by fitting the three levels. The three levels are shown in Figure 3.5 along with the derived model of the noise. The model is a crude approximation but is good enough for the pipeline testing purposes. The model is in fact two functions split at $4250\,\mathring{A}$: a straight line for the lower range of the function and a power law for the higher values.

In summary, the purpose of this exercise is to have the ability to add noise typical to our data to known SSP models, and then to feed those noisy models with the STARLIGHT pipeline. At the end an evaluation is done to see how well the fit recovers the underlying SSP.

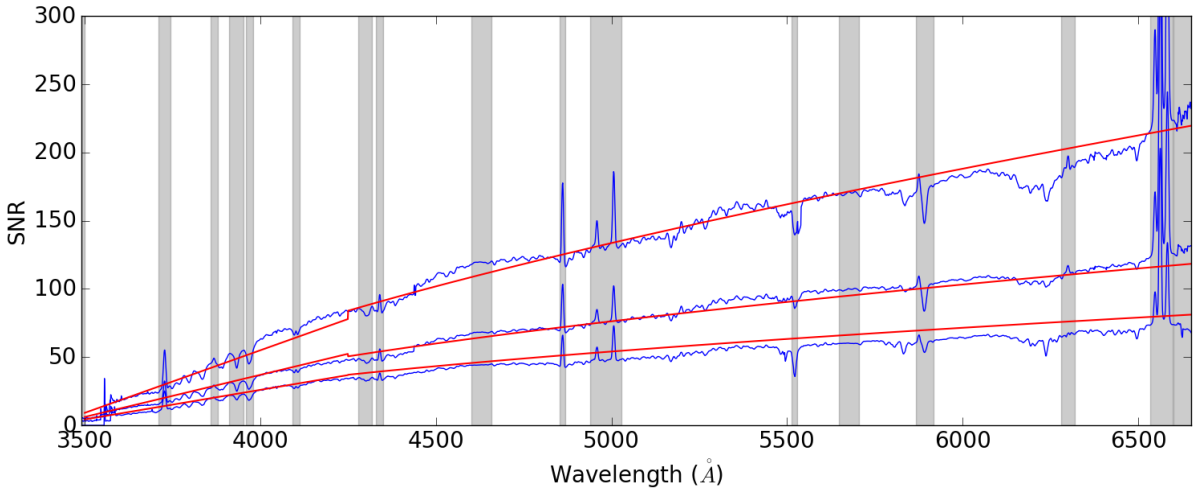

Figure 3.5: The measured SNR of SALT data from our data sample. 3 groups of SNR (low, medium and high) are shown in blue. The grey areas are places with CCD gaps, skylines and emission lines that are masked. The red lines are the derived models from these SNR levels. It can also be seen that even for low SNR values in the blue, the red part of the spectrum reaches quite high SNR.

3.7.2 Testing with SSP

Since SSPs have well defined ages and metallicities, the first testing of the pipeline robustness is done by fitting SSPs with added noise. Two types of noise are tested: Gaussian noise and gradient noise. In the first case, artificial noise following a Gaussian distribution is added on top of SSPs, which are then fed to the pipeline to be fitted through the procedures described in section 3.6.2. Five levels of noise are chosen: 4, 8, 12, 16 and 20. These essentially refers to the SNR level at wavelength 3600 $\AA$, (the SNR varies along the wavelength range for SALT data). For the case of gradient noise, random numbers are used to choose gradients that are then added to the SSPs. Four levels of noise are chosen: 2, 4, 6 and 8 - all referring to percentage increase in the gradient of the SSPs. An SSP that will be used in the fit, is masked for all its absorption features and then a straight line is fit across the remaining parts. In case of level 2, for example, random numbers with a mean of 0 and variance of 2 are generated. Each random number is then used as the percentage increase (or decrease since the random numbers can be negative as well) of the gradient that is applied to the SSP before fitting it through STARLIGHT. The same procedure is done for each of the different levels of the gradient noise.

Each SSPs is fitted 20 times under the different noise levels just discussed, and then the light weighted and mass weighted age and metallicities are calculated for each case. The calculated ages and metallicities are then compared to the original input age and metallicity of the SSPs. A percentage deviation from the original value is calculated for each fit done using the formula:

$$\Delta_i = \frac{A_i - A'_i}{A'_i} \times 100 \tag{3.7}$$

This procedure allows us to compare the quality of the fits. Since the age variation of SSPs has a huge dynamic range (from $10^6 - 10^{10}$ yr), every comparison is done in log space (i.e. $A = \log(Age)$ in Equation 3.7), otherwise the older stellar population fits would bias the variance of the results. The deviation distribution of ages and metallicities weighted by light are shown in Figures 3.6 and 3.7. The Figures for the mass weighted distributions are in the Appendix B (Figure B.1 and Figure B.2). Some of the derived statistics from the distributions are displayed in Table 3.1. Since the distributions are skewed, both mean and median are given, and instead of using a standard deviation, a confidence level to encompass 68% of the distribution is calculated.

Table 3.1: Results from the SSP fitting for both Mass-Weighted and Light-Weighted parameters. For each noise level fitting, the mean, median and 68% confidence interval is listed. Note that for each section the noise level goes down as one goes down the table. In the case of Gaussian noise, level 20 is higher in SNR than level 4, while for gradient noise, 2% noise is less than 8%. All values are calculated as a percentage deviation using equation 3.7.

			Age			***Metallicity***		
	Noise	**Level**	**mean**	**median**	**conf**	**mean**	**median**	**conf**
Light-Weighted	***Gaussian***	20	0.176	-0.001	0.736	10.273	1.617	17.239
		16	0.164	0.009	0.666	9.972	1.192	19.582
		12	0.178	0.008	0.699	11.321	1.402	21.133
		8	0.193	0.010	0.083	12.786	1.033	23.687
		4	0.213	0.015	0.940	14.572	1.471	29.873
	Gradient	2 %	0.379	0.071	0.100	10.600	1.451	19.969
		4 %	0.762	0.124	1.484	14.178	0.499	28.376
		6 %	0.752	0.128	1.580	18.061	0.203	32.415
		8 %	0.902	0.158	1.924	19.743	0.621	37.206
Mass-Weighted	***Gaussian***	20	1.098	0.238	1.917	9.676	0.626	16.219
		16	1.015	0.218	1.726	8.949	0.675	16.520
		12	0.985	0.237	1.787	10.733	0.612	18.500
		8	1.117	0.230	1.952	12.682	0.495	22.554
		4	1.094	0.268	2.098	13.801	0.607	29.193
	Gradient	2 %	1.567	0.294	2.607	11.160	0.357	21.258
		4 %	2.551	0.413	3.249	18.011	0.159	29.153
		6 %	2.498	0.465	3.728	21.749	0.017	30.973
		8 %	2.829	0.526	3.879	26.301	0.535	39.088

The first thing to notice from the fitting results is that the noise introduces a small positive bias and skew to the fitting results. Since the distribution is skewed, median is a more meaningful

indicator than the mean in this case and rightly so, the median in all cases is very close to the true value. Age is a found to be a very stable parameter with the mean having a maximum deviation of 3% in extreme cases, while median only diverges from the expected value by no more that a fraction of a percent even at the very low SNR.

In the case of metallicity, there are systematic divergence from true values from the derived mean, but on the other hand, the median shows that it is very robust. At the most extreme cases the median has a systematic of only 1.6%. It is to be noted that the gradient noise has less effect on metallicities. This is because metallicities are determined by depths of absorption lines across the spectrum, not by it's overall shape. The mass-weighted median metallicities have less systematics than the light-weighted median values. One source for gradient noise in case of SALT spectral data could, for example, be erroneous flux calibration of targets.

Since most of the targets are rigorously flux calibrated, it is not expected that more than 2% flux calibration error will creep into the data. These tests also show the importance of varying the spectra within their uncertainties for each wavelength bin and then fitting with several iterations. Individual fits can often be thrown off by local minima, while averaging over several fits gives more robustness to the derived parameters.

To end, it is found that the best approach to extract accurate SSP fitting results is to perform several iterations of STARLIGHT. From the distribution of results, the median does not suffer much systematic unlike the mean. Based on the tests carried out and the general SNR characteristics of SALT data, using our fitting method, light-weighted ages can be derived to an accuracy of $\Delta \log(\mathrm{Age}_l) < 1\%$ and mass-weighted ages can be obtained at $\Delta \log(\mathrm{Age}_m) < 1\%$. For metallicities the light-weighted values can be achieved to an accuracy of $\Delta \mathrm{Z}_l < 1\%$ and for the mass weighted values it is, $\Delta \mathrm{Z}_m < 1\%$.

3.7.3 Star Formation History Recovery

The SNR testing was essential to understand how fitting would behave with the typical quality of SALT/RSS data. The aim was not primarily to test the stability of STARLIGHT, which has been done over the years in many papers (Cid Fernandes et al., 2005; Asari et al., 2007; Cid Fernandes et al., 2014). Now that we know that SALT spectra are stable enough for spectral fitting and recovery of the associated parameters, another testing is carried out on known standard galaxies from the data from Sloan Digital Sky Survey. This time, it is to get a good grasp of the significance of the results rather than test the viability of the data itself.

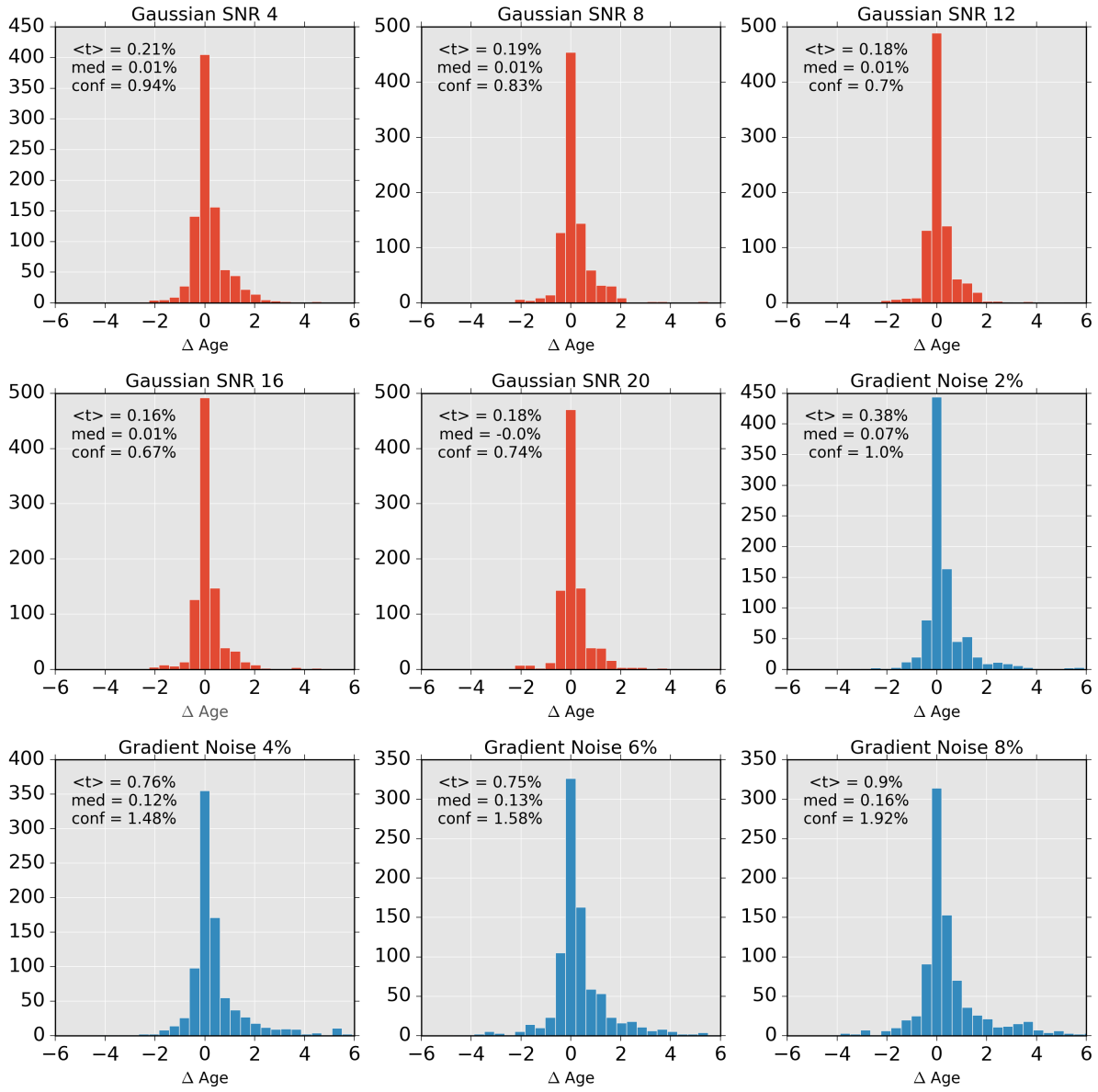

Figure 3.6: Distributions of Light-Weighted Ages (given in percentages deviations) for the different noise level SSP fittings. Red histograms are for Gaussian noise while blue is for gradient noise.

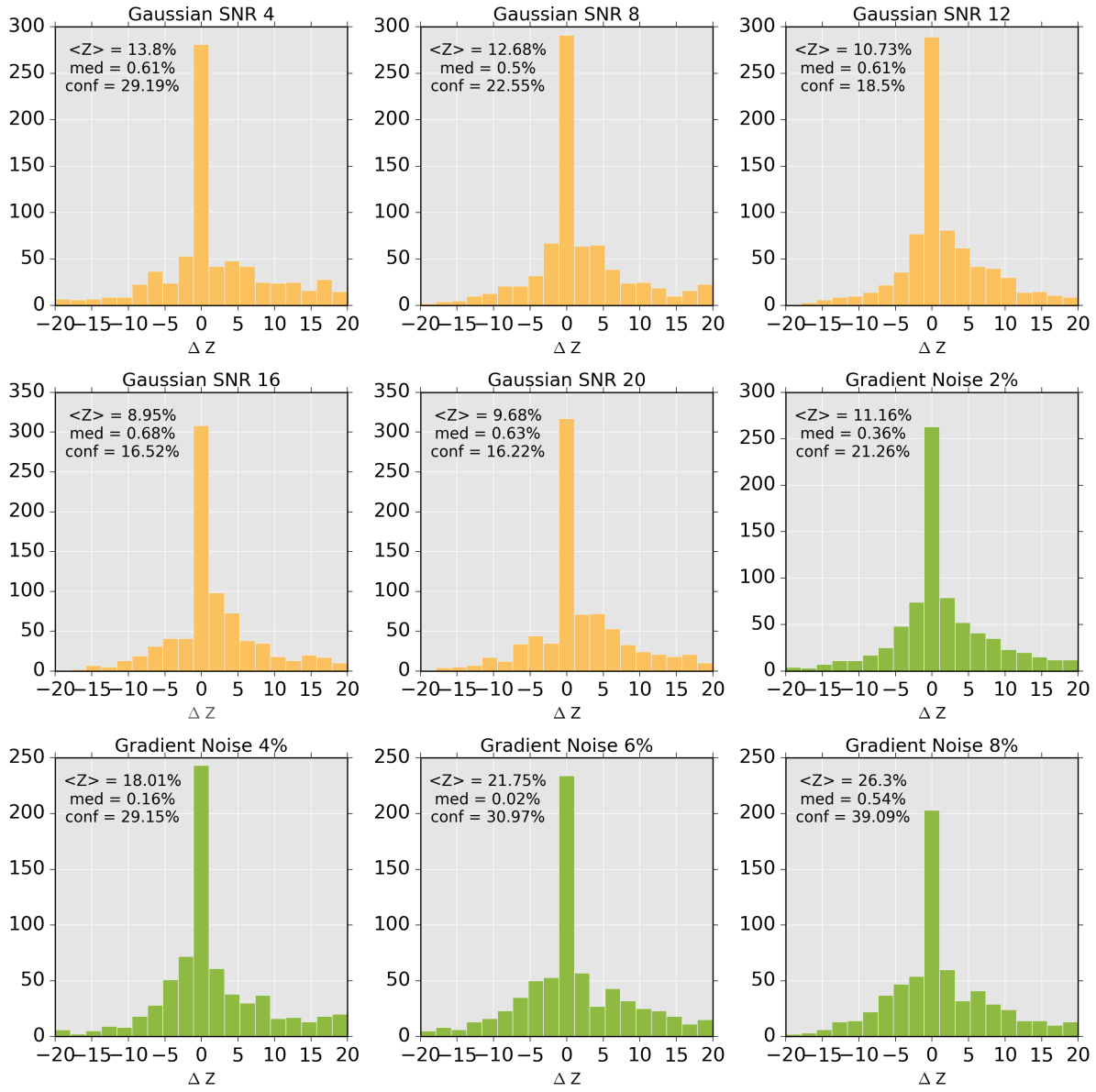

Figure 3.7: Distributions of Mass-Weighted (given in percentages deviations) Metallicities for the different noise level SSP fittings. Yellow is for Gaussian noise while green is for gradient noise.

Since the aim of the thesis is to understand the star formation history (SFH) of very young galaxies which are highly interacting, a good baseline to have, is the SFH of a set of standard galaxies. For this reason, another set of fits were carried out on a few specific cases. One representative of each type of galaxies along the Hubble Sequence was chosen from the SDSS data sample and then fitted with STARLIGHT using the same BC03 base used for this thesis. Some of the recovered parameters from the fits are given in Table 3.2. Light-weighted parameters are weighted by the emitted light from the observation and since the light of galaxies is usually dominated by young stars, this parameter is a reflection on how young a galaxy is. On the other hand, mass weighted parameter is biased towards older stellar populations which contains most of the mass of galaxies. TO recover mass-weighted parameters, one needs to assume an IMF which then allows one to convert the observable light into mass-weighted parameters. In the current case, STARLIGHT is able to output mass-weighted parameters based on the input given to the code. The result of the fits clearly shows a global rejuvenation of the average age of the stellar population (whether weighted by light or mass) as we move from Early to Late-type galaxies along the Hubble Sequence. Similarly, bulge dominated galaxies have higher velocity dispersions than the disc dominated counterparts. Generally the intrinsic extinction increases towards Late-type galaxies. These are expected results which consolidate our trust in the reliability of the fits quality.

Table 3.2: Results from the SDSS sample fits. *Column 1:* Name or Hubble Sequence classification of galaxy; *Column 2:* Velocity Dispersion with uncertainty in km/s; *Column 3:* Intrinsic extinction; *Column 4 & 5:* $\log(Age)$ weighted by light and mass, respectively; *Column 6 & 7:* Metallicity weighted by light and mass, respectively, in Solar Units.

Name	**Vel Disp** (km/s)	**Av**	**log(Age$_l$)** (yr)	**log(Age$_m$)** (yr)	**log(Z$_l$)** ($Z_\odot$)	**log(Z$_m$)** ($Z_\odot$)
(1)	(2)	(3)	(4)	(5)	(6)	(7)
Bulge	450.2 ± 10.8	0.227 ± 0.021	9.93 ± 0.01	10.11 ± 0.01	1.22 ± 0.05	1.41 ± 0.07
Elliptical	358.1 ± 11.8	0.112 ± 0.019	9.82 ± 0.02	10.06 ± 0.01	1.51 ± 0.08	1.68 ± 0.07
S0	381.4 ± 15.6	0.180 ± 0.018	9.84 ± 0.03	10.07 ± 0.02	1.41 ± 0.11	1.36 ± 0.09
Sa	317.2 ± 13.0	0.931 ± 0.034	8.75 ± 0.04	9.82 ± 0.05	1.63 ± 0.14	1.64 ± 0.13
Sb	318.4 ± 15.2	0.573 ± 0.020	9.03 ± 0.04	9.65 ± 0.05	1.47 ± 0.12	1.75 ± 0.14
Sc	207.5 ± 125.1	0.420 ± 0.126	6.73 ± 0.07	9.69 ± 0.14	0.82 ± 0.17	0.58 ± 0.21
Starburst	373.8 ± 71.9	0.556 ± 0.057	7.44 ± 0.05	8.96 ± 0.32	0.54 ± 0.10	0.74 ± 0.21

The SFH of each case is then derived (see Chapter 4 for more details on how SFH is extracted from fits) and plotted in Figure 3.8. The SFH plots shows the evolution of three connected parameters with time: SFR, SSFR and Stellar Mass build up. For the comparison to hold in this case, all galaxies are considered to be of the same mass and redshift, which are set to the median mass and redshift of the SUNBIRD sub-sample respectively. The plots in Figure

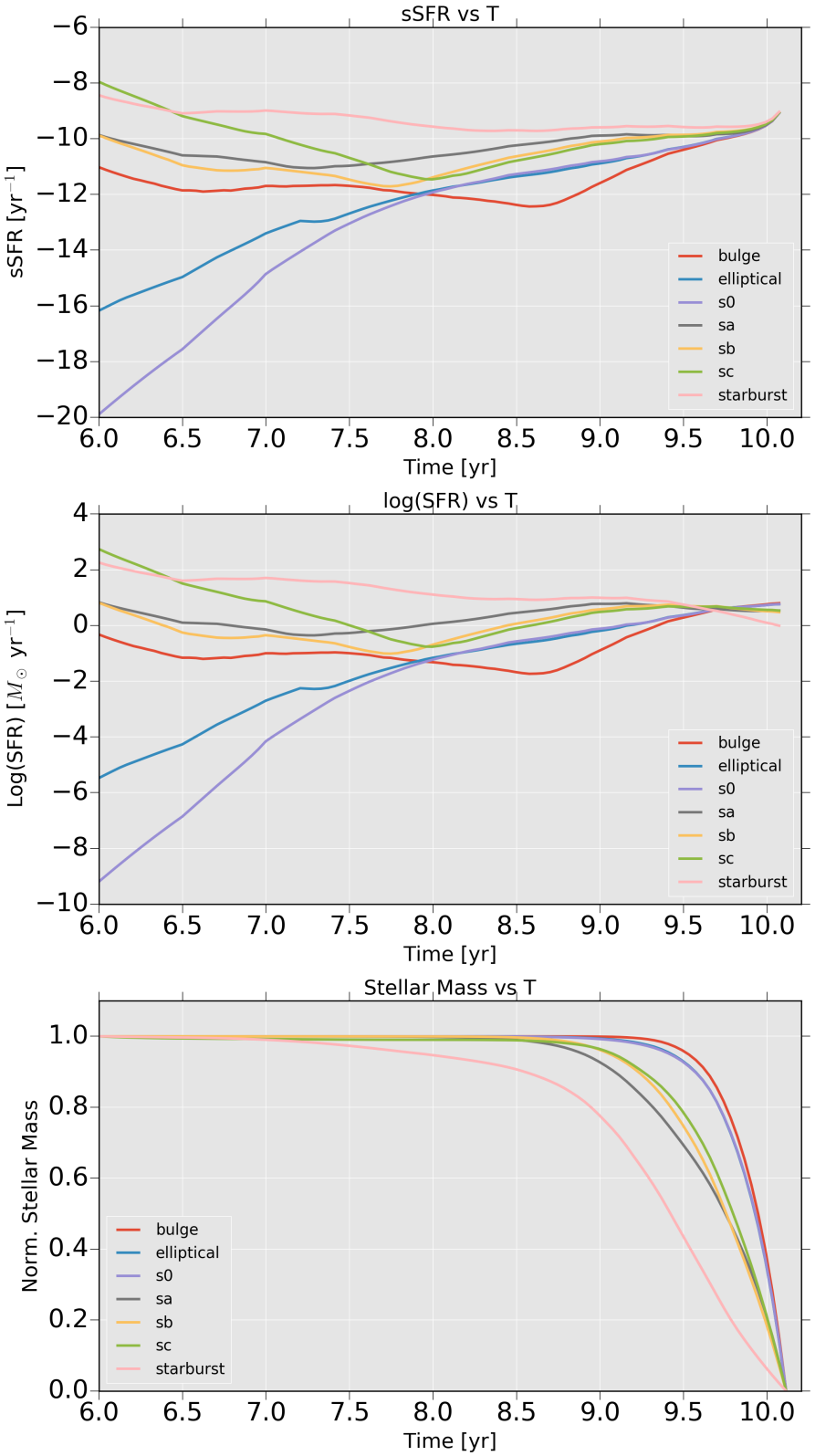

Figure 3.8: The SFH of SDSS representative galaxies. *Top panel* shows the variation of SSFR with time, *Middle panel* shows the how the SFR activity changes as a function of time, and the *Bottom panel* displays the mass build up with time in each case.

3.8 shows that Early-type galaxies have declining SF-activity, while Late-type galaxies seems to have at least one secondary burst of SF in the past few 10^7 years. While Starburst and Sc galaxies, which are expected to be youngest in the sample, displayed stronger SF activities in their recent histories, the Starburst is currently still building up a significant amount of stellar mass, while the Sc galaxy already build up most of its mass at $z > 1$. The results of SSP fitting with STARLIGHT for our sample are discussed in Sections sec:age)-sec:met).

3.8 Emission Line Measurement

Emission lines are expected to originate from the gaseous or AGN components of galaxies. In cases of strongly star-forming galaxies, like the ones in our sample, the gas component plays a crucial role in the evolution of the galaxies. The stellar population modelling, previously described, allows us to model the stellar component that we observe in the continuum of a spectrum. If the modelled stellar population is then subtracted from the observed spectrum ($O_\lambda - M_\lambda$), all that is left is the pure emission line spectrum from the gaseous regions (and any AGN related emission or continuum, though this is not likely in the majority of the cases due to sample selection). The PG0900 grating data that is used to model the Stellar Population, typically covers the rest wavelength range of $\lambda = 3600 - 6600\,\mathring{A}$. The coverage allows us to be able to get continuum subtracted line measurement of [OII] $\lambda\lambda 3726, 3729$ (blended), [NeIII] $\lambda 3868$, Hγ $\lambda 4340$, [OIII] $\lambda 4363$, Hβ $\lambda 4861$, [OIII] $\lambda\lambda 4959, 5007$, [NII] $\lambda 6548$, Hα $\lambda 6563$, [NII] $\lambda 6584$. The wavelength range for the data vary somewhat for different targets depending on the grating angle selected and the redshift of the source.

From the pure emission spectrum, Gaussian profiles are fitted to individual emission lines. Our fitting routine is written in Python, using the MPFIT[1] algorithm in the Kapteyn Package (Terlouw & Vogelaar, 2015). This algorithm has the capability to recover uncertainties on each of the parameters fitted. Each Gaussian profile is described by the 4 parameters; amplitude, mean (wavelength), standard deviation (SD) and noise level to model the residual continuum. From the recovered parameters, the flux of each line is calculated by using the analytical solution to the integration of a Gaussian profile. By doing a Monte Carlo simulation with 2000 iterations, and making use of the uncertainty in each of the 4 parameters of the profile, the uncertainty in the flux is calculated. The algorithm performs profile fits under some basic constraints to get successful line measurements. More advanced constraints, such as flux ratios of different lines or imposing constant width for lines corresponding to the same ions, were not considered since these constraints can potentially prevent the routine from finding the minimum, preventing the latter from running smoothly. Hence a more basic and reliable routine was opted for. In case

[1] http://www.astro.rug.nl/software/kapteyn/kmpfittutorial.html

of the Hα and the two neighbouring [NII] lines, a triple Gaussian fit with amplitude, mean and SD for each line is performed while a singular noise parameter is used for all the lines.

The SSP models can sometimes have more flux than the continuum of the observed spectrum. This results in a wide trough in the residual continuum after subtraction, which is a known systematic effect in the Hβ region while using the BC03 SSP model. Inappropriate flux calibration in the STELIB library for the stated region is the cause of the systematic, for more detailed information see Asari et al. (2007). To circumvent this problem, before any fit is carried out, a nominal flux amount is added across all pixels of the pure emission spectrum. This does not affect the amount of flux measured in the emission line but in fact makes the fit more likely to converge and less likely to crash. Our emission line fluxes are measured from the noise level upwards, and so a higher or lower residual continuum level has no impact on the measurement.

3.9 Extinction

After obtaining the fluxes of the different emission lines observed, the fluxes are then corrected for the intrinsic extinction of the object. The following derivation is the basis of the extinction correction that was applied to all the galaxies in the SUNBIRD sub-sample. The extinction correction was implemented in a code that uses the measured fluxes for each lines derived from the emission line measurement algorithm. The flux observed is related to the intrinsic extinction of the galaxy as follows:

$$I_\lambda = F_\lambda 10^{\ 0.4A_\lambda}, \tag{3.8}$$

where I_λ is the intrinsic flux, F_λ is the observed flux and A_λ is the extinction at λ. At the wavelength of $H\beta$

$$I_{H\beta} = F_{H\beta} 10^{\ 0.4A_{H\beta}}, \tag{3.9}$$

$$\frac{I_\lambda}{I_{H\beta}} = \frac{F_\lambda}{F_{H\beta}} 10^{\ 0.4(A_\lambda - A_{H\beta})}. \tag{3.10}$$

The Calzetti extinction law is a standard one used for star forming galaxies (Calzetti et al., 2000). It takes the form of:

$$k(\lambda) = \frac{A_\lambda}{A_v} k_v. \tag{3.11}$$

Substituting A_λ in Equation 3.10 with A_λ from Calzetti law:

$$\frac{I_\lambda}{I_{H\beta}} = \frac{F_\lambda}{F_{H\beta}} 10^{\ 0.4\ \frac{A_v}{k_v}(k_\lambda - k_{H\beta})}, \tag{3.12}$$

Assuming case B recombination, where electron density is $n_e = 100\ cm^{-3}$, and an electron temperature of $T_e = 10^4$ K, the intrinsic Balmer line ratios for these parameters are given by Osterbrock (1989) as follows:

$$\frac{F_{H\alpha}}{F_{H\beta}} = 2.860, \tag{3.13}$$

$$\frac{F_{H\gamma}}{F_{H\beta}} = 0.469, \tag{3.14}$$

$$\frac{F_{H\delta}}{F_{H\beta}} = 0.260, \tag{3.15}$$

We can find A_v by minimising the difference between the theoretical and the observed values:

$$\Delta H\alpha = \left(1/\Delta \frac{F_{H\alpha}}{F_{H\beta}}\right) \times \left(\frac{F_{H\alpha}}{F_{H\beta}} - 2.860\right)^2, \tag{3.16}$$

$$\Delta H\gamma = \left(1/\Delta \frac{F_{H\gamma}}{F_{H\beta}}\right) \times \left(\frac{F_{H\gamma}}{F_{H\beta}} - 0.469\right)^2, \tag{3.17}$$

$$\Delta H\delta = \left(1/\Delta \frac{F_{H\delta}}{F_{H\beta}}\right) \times \left(\frac{F_{H\delta}}{F_{H\beta}} - 0.260\right)^2, \tag{3.18}$$

$$\Delta = \Delta H\alpha + \Delta H\gamma + \Delta H\delta. \tag{3.19}$$

A_v is determined iteratively, until the sum of the 3 terms in Δ, reaches a minimum. In cases where one or two of the three lines are missing from the observed spectrum, the minimisation is carried over the remaining terms. The absorption coefficient is then calculated as follows:

$$c(H\beta) = 0.4\ k(H\beta)\frac{A_v}{k_v}. \tag{3.20}$$

3.10 Metallicity and Chemical Abundances

It is known from general galaxy evolution that, gas is converted into stars, which over their lifetimes will act as factories to convert Hydrogen and Helium to heavier elements (also known as *metals*). The heavier metals are then expelled to the interstellar medium either through winds during the life of the stars, or through supernova explosions when the stars die. This baryonic cycle enriches the available gas so that the next generation of stars will have heavier elemental abundances. Measuring the metallicity of galaxies is crucial for building a global picture of the star formation histories of galaxies, and also for constraining galaxy evolution models (Kewley & Ellison, 2008, hereafter KE08).

The method defined above in Section 3.3.3, allows one to estimate the stellar metal content of galaxies through the use of stellar population fitting. The next section focuses on the determination of the metallicity of the interstellar ionised gas. This is made possible through the measurement and comparison of strong emission line ratios and the derivation of oxygen abundances, which is a good proxy for overall metallicity (Bianco et al., 2016). Hence, we adopt the popular nomenclature of using oxygen abundance and metallicity interchangeably. While the following will be a brief overview of the different methods of measuring gas-phase oxygen abundances, more comprehensive reviews on the subject such as Stasińska (2002); Moustakas et al. (2010); Blanc et al. (2015); Bianco et al. (2016) can be consulted.

3.10.1 Deriving Metallicity

During the process of star formation and gas collapse, the hot young stars usually emit vast amounts of light in the ultraviolet regime. This UV light heats the nearby nebular gas. Photoionisation is the process by which electrons from hydrogen and the heavier elements constituting the nebular gas absorb the UV photons and escape the potential well of their atoms with some kinetic energy (electron temperature, T_e). An ionised gas is created with free electrons randomly moving around and colliding with each other. During recombination, the ionised electrons are recaptured by the ionised gas into a high-n excited state (Keel, 2007). Following recapture, de-excitation occurs, where the electrons cascade from the high-n state to the ground state of the atom through a series of photon emissions, corresponding to the quantised energy drops. This process allows us to observe the emission lines of the most abundant elements of the nebulae i.e. Hydrogen and any metals. By studying the intensity and ratio of the different emission lines observed, one can then deduce the chemical composition of the gas cloud. Nebular spectrum usually contains permitted Lyman, Balmer and Paschen Hydrogen lines along with lines from other elements such as Helium, Sulphur, Oxygen and Nitrogen. Among these metal lines can be found some forbidden lines which do not occur in the lab due to small sample sizes of elements.

But in cases of gas clouds of astronomical size, those rare transitions can statistically occur and are indeed regularly observed. The heating of the nebula through absorption of photons and cooling via recombination usually achieves a thermal equilibrium at $T_e \sim 10^4$ K (Pagel, 2009). This equilibrium is dependent on the heat input, (stellar temperatures), the chemical ingredients of the nebula and the ionisation parameter, u.

Since the chemical composition of a nebula affects the emitted line spectrum significantly, studying emission lines and their relations to one another leads to an understanding of the metallicity content of the gas in galaxies. KE08 categorised the metallicity estimation system into four different groups: direct, empirical, theoretical and composite (mixture of empirical and theoretical). The *direct* method relies on the weak auroral line [OIII] λ4363. In this method, one usually derives the electron temperature (T_e) from ratios such as [OIII]λ4363/[OIII]λ5007 and the density of the gas, n_e, using the ratio of doublets such as [OIII]$\lambda\lambda 3726, 3729$ or [SII]$\lambda\lambda 6717, 6731$ (Blanc et al., 2015). The next step is then to derive the OII and OIII abundances followed by total oxygen abundances by applying the ionisation correction factor (ICF), which takes into account stages of ionisation that are not observed (Bianco et al., 2016). The auroral line, being quite weak usually, requires large integration time, and hence was not an appropriate tool to derive metallicity in large surveys.

The strong line method, first proposed by Pagel et al. (1979), has since been developed to circumvent the observational difficulty of the weak oxygen auroral line. This method encompasses three different techniques, namely: empirical, theoretical or composite. The empirically derived strong line method was based on large surveys of HII regions and relies on correlations found between optically observed line ratios and metallicities that were calibrated via direct electron temperature method. Some examples of empirically derived calibrators are O_{32} (Pagel et al., 1979), R_{23} (Pilyugin, 2001; Pilyugin & Thuan, 2005, hereafter P01 and PT05), $O3N2$ (Pettini & Pagel, 2004) and the N2 indicators (Denicoló et al., 2002; Pettini & Pagel, 2004, hereafter DO2 and PP04). Theoretical metallicity calibrators rely on photo-ionisation models such as Cloudy (Ferland et al., 1998, 2013) or MAPPINGS (Dopita et al., 1982; Sutherland & Dopita, 1993; Groves et al., 2004), in combination with stellar synthesis models such as Starburst99 (Leitherer et al., 1999), to be able to predict different line ratios for different scenarios of metallicities (Kewley & Ellison, 2008). Theoretical models are limited by the assumptions made, such as the modelling of dust which leads to some systematics between the different methods used. An example of a theoretical model calibrator is the R_{23} (McGaugh, 1991; Zaritsky et al., 1994, hereafter M91, Z94). In the next section, a brief review of the different metallicity indicators that were used for this thesis is presented.

3.10.2 Abundance Diagnostics

Since this thesis is mostly focused on the various observational properties of galaxies, the choice of metallicity calibrators should not favour any particular one. Unfortunately, the presence of large systematics between the different calibrators, means that the most effective way to show abundance results is to choose a at least a few calibrators. A brief review of the different equations and parameters of each calibrators is shown.

3.10.2.1 R_{23} and O_{32} ratios

The R_{23} ratio is used in many strong-line method calibrators. It was introduced by Pagel et al. (1979), but has since been recalibrated, and is given by

$$R_{23} = \frac{[OII]\lambda3727 + [OIII]\lambda4959 + [OIII]\lambda5007}{H\beta}. \tag{3.21}$$

It is unfortunately a degenerate index when plotted against metallicity, where two values of metallicity can correspond to one R_{23} value. Other line ratios can be used as a complement to break down this degeneracy between its "upper branch" and "lower branch" (Kewley & Ellison, 2008). Line ratios such as [NII]/Hα or [NII]/[OII] can properly select on which branch the metallicity of R_{23} actually lies.

Another important ratio is that of O_{32} which is defined by:

$$O_{32} = \frac{[OIII]\lambda4959 + [OIII]\lambda5007}{[OII]\lambda3727}. \tag{3.22}$$

This ratio is primarily sensitive to ionisation due to the presence of the terms [OII] λ3727 and [OIII] λ5007 (Nagao et al., 2006). Since R_{23} is also sensitive to the ionisation parameter due to the same terms, O_{32} can be used to compensate for the ionisation sensitivity of the R_{23} index in abundance calculations. Since both R_{23} and O_{32} are extensively used in the next section for different calibrators, we adopt the convention where $x = \log(R_{23})$ and $y = \log(O_{32})$ from this point onwards, unless otherwise stated. To improve on the degeneracies and limitations of the R_{23} and O_{32} methods, researchers came up with different calibration schemes that are listed in the section that follows.

3.10.3 M91 calibrator

Through the use of HII models derived from the code Cloudy (Ferland et al., 1998, 2013), McGaugh (1991) calibrated the R_{23} ratio. A correction for the ionisation parameter is included in the case of the M91 calibrator. Kobulnicky & Zaritsky (1999) give the equation in a parametric form to discriminate between the two 'branches' while the work in KE08 uses the ratio of

([NII]/[OII]) to update where the break between the lower and upper branch is computed. The equations, which are accurate to ~ 0.15 dex, take the form:

$$12 + \log (O/H)_{lower} = 12 - 4.944 + 0.767x + 0.602x^2 - y(0.29 + 0.322x - 0.331x^2), \tag{3.23}$$

$$\begin{aligned} 12 + \log (O/H)_{upper} = 12 &- 2.939 - 0.2x - 0.237x^2 - 0.305x^3 - 0.0283x^4 \\ &- y(0.0047 - 0.0221x - 0.102x^2 - 0.817x^3 - 0.00717x^4), \end{aligned} \tag{3.24}$$

3.10.4 Z94 calibrator

Using the works of Edmunds & Pagel (1984), Dopita & Evans (1986) and McCall et al. (1985), Zaritsky et al. (1994) [Z94], derived another calibrator that is valid for the upper branch of R_{23}. Z94 is calculated by finding the mean of the three previous calibrations cited above, while the uncertainty (~ 0.1 dex) is derived from the standard deviation from the three calibrators. The equation was derived through polynomial fitting, without correcting for ionisation effects. It takes the form of:

$$12 + \log (O/H)_{upper} = 9.265 - 0.330x - 0.202x^2 - 0.207x^3 - 0.333x^4. \tag{3.25}$$

3.10.5 PT05 calibrator

The PT05 calibration is based on the Pilyugin (2001) calibrator with an updated empirical relationship derived between R_{23} and T_e metallicities, through the use of a larger data sample of 700 HII regions, than included in the original work. The uncertainty of the calibrator is estimated to be of the order of ~ 0.1 dex. An upper branch is defined for metallicities of 12 + log (O/H) > 8.25 while the lower branch is valid for 12 + log (O/H) < 8.0 and the ratio of [NII]/[OII] is the tool to discriminate between the two branches. PT05 is obtained using the following parametric equation:

$$12 + \log (O/H)_{lower} = \frac{R_{23} + 106.4 + 106.8P - 3.40P^2}{17.72 + 6.60P + 6.95P^2 - 0.302R_{23}}, \tag{3.26}$$

$$12 + \log (O/H)_{upper} = \frac{R_{23} + 726.1 + 842.2P - 337.5P^2}{85.96 + 82.76P + 43.98P^2 - 1.793R_{23}}, \tag{3.27}$$

where

$$P = \frac{([OIII]\lambda 4959 + [OIII]\lambda 5007)H\beta}{R_{23}}. \tag{3.28}$$

The parameter P mitigates the effects of ionisation for this calibrator.

3.10.6 PP04; O3N2 and N2 calibrators

3.10.6.1 O3N2

Alloin et al. (1979) first defined the O3N2 indicator from the ratio [OIII]/[NII], which was later updated by Pettini & Pagel (2004) who expressed it in the form:

$$12 + \log(O/H) = 8.73 - 0.32 \times O3N2, \tag{3.29}$$

where,

$$O3N2 = \log\left(\frac{[OIII]\lambda5007/H\beta}{[NII]\lambda6584/H\alpha}\right). \tag{3.30}$$

PP04 used a sample of 137 HII regions calibrated mostly through the direct method to derive this empirical relation. This calibration is expected to be accurate to $\sim$ 0.14 dex and is not influenced by flux calibration or extinction corrections since it uses ratios of lines very close to each other in wavelength, and thus makes it useful for cases when for e.g. extinction corrections are difficult to make This method is valid for values of O3N2 $<$ 2, which corresponds to 8.12 $<$ 12 + log(O/H) $<$ 9.05.

3.10.6.2 N2

The N2 index was first defined by Storchi-Bergmann et al. (1994) before PP04 used the same sample as described for the O3N2 index to derived its relationship with oxygen abundance as,

$$12 + \log(O/H) = 9.37 + 2.03 \times N2 + 1.26 \times N2^2 + 0.32 \times N2^3, \tag{3.31}$$

where,

$$N2 = \log\left(\frac{[NII]\lambda6584}{H\alpha}\right). \tag{3.32}$$

The uncertainty on the N2 index is estimated to be 0.18 dex and is valid for the range 7.17 $<$ 12 + log(O/H) $<$ 8.87. Both O3N2 and the N2 have since been recalibrated by the CALIFA group (Marino et al., 2013) to 12 + log (O/H) = 8.533 $-$ 0.214 $\times$ O3N2 and 12 + log (O/H) = 8.743 + 0.462 $\times$ N2 respectively. In the scope of this project, preference is given the older PP04 definition because it is more widely used, and, due to the conversion done by KE08 that will be elaborated in Section 3.10.8.

3.10.7 D02 calibrators

The DO2 calibrator is derived from a composite modelling. By calculating the metallicities using the direct method for $\sim$100 HII regions and using the theoretical modelling for 55 HII regions, Denicoló et al. (2002) derived the following calibrator through least-squares fitting:

$$12 + \log(O/H) = 9.12 + 0.73 \times N2. \tag{3.33}$$

The theoretical modelling uses a mixture of the M91 method and a recipe provided by Díaz & Pérez-Montero (2000). This method carries an estimated error of ∼0.2 dex.

3.10.8 Comparison of calibrators

There is a large variation between the values given by each of the metallicity calibrators. This discrepancy was noted by Liang et al. (2006) when using strong line calibrators on ∼ 40000 star forming galaxies from the SDSS sample. The source of the systematics between the various calibrators is still not very well understood, although it is expected that temperature gradients and a lack of a proper understanding of the photoionisation models plays a part (Kewley & Ellison, 2008). Figure 3.9 shows the Mass-Metallicity relationship using various calibrators as calculated from KE08. Not only are there offsets in the levels of the different calibrators, but the gradients obtained have a wide variance. By finding the correlation between the different calibrators, KE08 were able to derive the following polynomial conversion equation, that links one diagnostics to another:

$$y = a + bx + cx^2 + dx^3, \tag{3.34}$$

where y is the metallicity of the form 12 + log (O/H) while a-d are the coefficients of the polynomials. The values of the different coefficients are published in KE08 for each possible iteration of conversion.

3.11 BPT Diagram and ionisation

Ionisation of hydrogen gas observed in galaxies is usually caused by three main mechanisms, namely; the O and B stars of a young stellar populations that have a huge output in the UV radiation, the hard radiation field of an AGN (through a power-law continuum) and, finally, the effect of shock heating excitations. Baldwin et al. (1981) were the first to propose a scheme to disentangle the effects of different processes through what is commonly called the *BPT diagram*. The first iteration of the diagram made use of the ratios [NII]λ6583/Hα and [OIII]λ5007/Hβ, before Veilleux & Osterbrock (1987) added two new diagnostics. The latter were based on the relationship of [OIII]λ5007/Hβ with [SII]λ6716/Hα or [OI]λ6300/Hα. Kewley et al. (2001, hereafter Ke01) went further by using stellar population synthesis and photoionisation models to derive an upper limit for starburst galaxies. This implies that any galaxy that lies above the 'maximum starburst line' will inevitably have a different power source to power the observed ionisation. This power source is expected to be AGN activity. The calculated boundaries

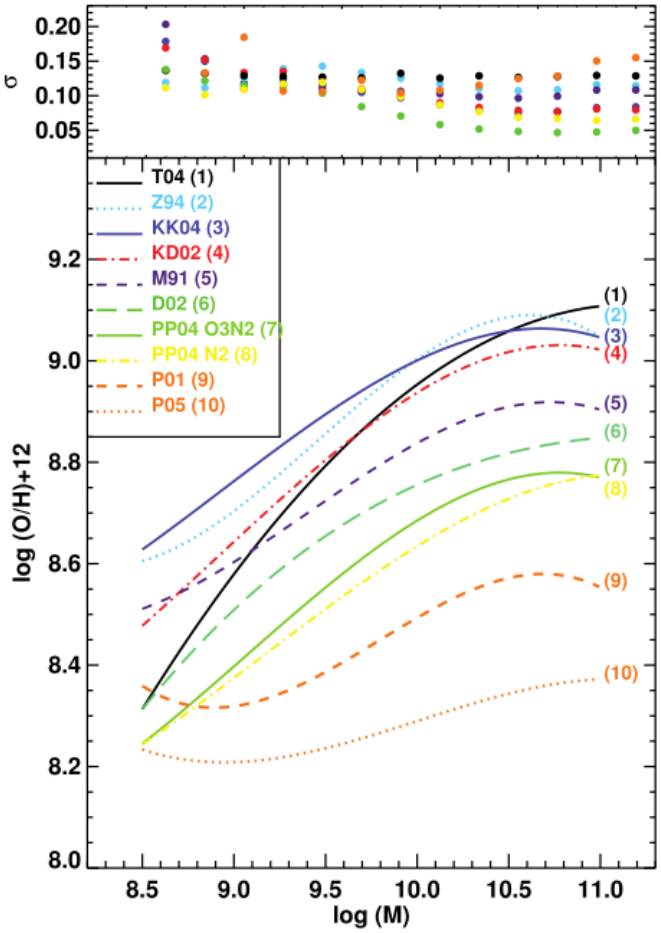

Figure 3.9: The best-fit Mass-Metallicity relation using different calibrators, as shown by KE08. The discrepancies between the results obtained using different calibrators are quite obvious. The top panel shows the RMS scatter in the metallicity about the best-fit position.

between the different regime is given by the following equations:

$$\log\left(\frac{[\mathrm{OIII}]}{\mathrm{H}\beta}\right) = 0.61\left[\log\left(\frac{[\mathrm{NII}]}{\mathrm{H}\alpha}\right) - 0.47\right]^{-1} + 1.19, \tag{3.35}$$

$$\log\left(\frac{[\mathrm{OIII}]}{\mathrm{H}\beta}\right) = 0.72\left[\log\left(\frac{[\mathrm{SII}]}{\mathrm{H}\alpha}\right) - 0.32\right]^{-1} + 1.30, \tag{3.36}$$

$$\log\left(\frac{[\mathrm{OIII}]}{\mathrm{H}\beta}\right) = 0.73\left[\log\left(\frac{[\mathrm{OI}]}{\mathrm{H}\alpha}\right) + 0.59\right]^{-1} + 1.33. \tag{3.37}$$

Figure 3.10 shows an example of the three different types of BPT diagrams that can be plotted. The plot shows the separation between Star formation, Seyfert or LINER dominated objects.

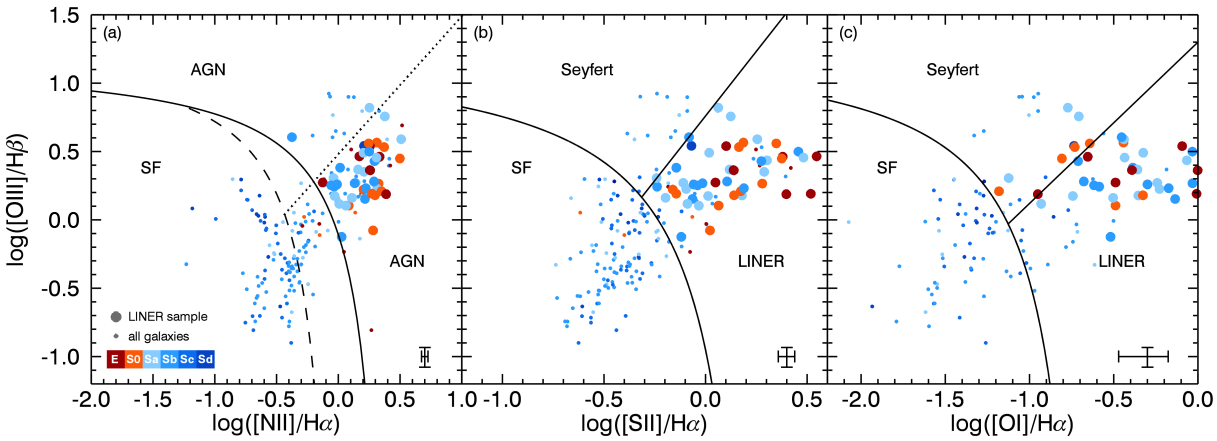

Figure 3.10: Three different types of BPT diagram classifications showing CALIFA galaxies colour coded by Hubble sequence types. The solid curve is from the theoretical model of Ke01 while the dashed curve is from Ka03. The straight dotted line in panel (a) follows the prescription of Cid Fernandes et al. (2010) while the straight lines in panels (b) and (c) are given by the work of Kewley et al. (2006). Image credit Singh et al. (2013).

In the following sections a quantitative description is given as to how to distinguish between the different objects.

3.11.1 Star forming galaxies

While the original equations from Ke01 properly model the diving line between star-forming contributions and other sources, it does not really take into consideration more complex cases where galaxies do not have one dominant power source. Kauffmann et al. (2003b, hereafter Ka03) used the SDSS dataset to derive an empirical line dividing purely star-forming galaxies from composite cases where there are contributions of star formation and AGN activity. The latter usually lie in the area between the Ke01 curve and the Ka03 curve. The Ka03 curve is given by the following inequality:

$$\log\left(\frac{[\mathrm{OIII}]}{\mathrm{H}\beta}\right) < 0.61\left[\log\left(\frac{[\mathrm{NII}]}{\mathrm{H}\alpha}\right) - 0.5\right]^{-1} + 1.3, \tag{3.38}$$

and for the two other BPT diagrams the following applies:

$$\log\left(\frac{[\mathrm{OIII}]}{\mathrm{H}\beta}\right) < 0.72\left[\log\left(\frac{[\mathrm{SII}]}{\mathrm{H}\alpha}\right) - 0.32\right]^{-1} + 1.30, \tag{3.39}$$

$$\log\left(\frac{[\mathrm{OIII}]}{\mathrm{H}\beta}\right) < 0.73\left[\log\left(\frac{[\mathrm{OI}]}{\mathrm{H}\alpha}\right) + 0.59\right]^{-1} + 1.33. \tag{3.40}$$

3.11.2 Composite Galaxies

Composite galaxies show a combination of star formation, shocks and low-luminosity AGN/LINER activity. Their position on the BPT diagram is probably due to the lower resolution of past surveys such as SDSS, in which the combined light of an entire galaxy is averaged onto a fibre spectrum. This average would combine vastly different regions of a galaxy, from the nucleus where there are AGN activities, to the spiral arms which are usually dominated by HII. Composites occupy the narrow area between Ka03 and Ke01 curves on the [OIII]/Hβ vs [NII]/Hα diagram given by the following inequalities:

$$\log\left(\frac{[\mathrm{OIII}]}{\mathrm{H}\beta}\right) < 0.61\left[\log\left(\frac{[\mathrm{NII}]}{\mathrm{H}\alpha}\right) - 0.47\right]^{-1} + 1.19, \tag{3.41}$$

$$\log\left(\frac{[\mathrm{OIII}]}{\mathrm{H}\beta}\right) > 0.61\left[\log\left(\frac{[\mathrm{NII}]}{\mathrm{H}\alpha}\right) - 0.5\right]^{-1} + 1.3. \tag{3.42}$$

3.11.3 AGN

The identification of AGN is of crucial importance especially in large surveys which look to aggregate samples of similar objects together prior to deriving statistical properties. In the nearby universe (z $<$ 0.4), using the line ratios of the BPT diagrams is an effective way to separate HII driven galaxies from the AGN dominated ones. This is because the collisional excitation of the [OIII], [NII] and [OI] is stronger in those cases than the recombination lines of Hα and Hβ that are produced by the young stellar populations (Cid Fernandes et al., 2010). All AGN (Seyferts and LINERS) can be identified on the three diagrams subject to the following conditions:

$$\log\left(\frac{[\mathrm{OIII}]}{\mathrm{H}\beta}\right) > 0.61\left[\log\left(\frac{[\mathrm{NII}]}{\mathrm{H}\alpha}\right) - 0.47\right]^{-1} + 1.19, \tag{3.43}$$

$$\log\left(\frac{[\mathrm{OIII}]}{\mathrm{H}\beta}\right) > 0.72\left[\log\left(\frac{[\mathrm{SII}]}{\mathrm{H}\alpha}\right) - 0.32\right]^{-1} + 1.30, \tag{3.44}$$

$$\log\left(\frac{[\mathrm{OIII}]}{\mathrm{H}\beta}\right) > 0.73\left[\log\left(\frac{[\mathrm{OI}]}{\mathrm{H}\alpha}\right) + 0.59\right]^{-1} + 1.33. \tag{3.45}$$

3.11.3.1 Seyfert Galaxies

Seyfert galaxies are a subset of AGNs and therefore must usually obey the conditions given by the inequalities 3.43, 3.44 and3.45 but Kewley et al. (2006) added two other conditions specific to Seyferts for the ratios [SII]/Hα and the [OI]/Hα:

$$\log\left(\frac{[\mathrm{OIII}]}{\mathrm{H}\beta}\right) > 1.89\,\log\left(\frac{[\mathrm{SII}]}{\mathrm{H}\alpha}\right) + 0.76, \tag{3.46}$$

$$\log\left(\frac{[\mathrm{OIII}]}{\mathrm{H}\beta}\right) > 1.18\,\log\left(\frac{[\mathrm{OI}]}{\mathrm{H}\alpha}\right) + 1.30, \tag{3.47}$$

Cid Fernandes et al. (2010) later added a condition for the [OIII]/Hβ vs [NII]/Hα

$$\log\left(\frac{[\mathrm{OIII}]}{\mathrm{H}\beta}\right) > 1.01\,\log\left(\frac{[\mathrm{NII}]}{\mathrm{H}\alpha}\right) + 0.48. \tag{3.48}$$

3.11.3.2 LINERS

LINERS, Low-Ionization Nuclear Emission-line Region, are low emission AGN which are quite similar to the Seyfert 2. A large portion of LIRGs are either composite objects with contribution from both HII and AGN ionising mechanism or simply LINERs where mostly the AGN dominates the emitted light (Alonso-Herrero et al., 2009). The underlying physics behind the emission is still debatable, whether it is powered by AGN, shocks or star formation. On the BPT diagram, although they fall under the AGN subset. But added to that, and to differentiate them from Seyferts, LINERS follow the inequalities given by:

$$\log\left(\frac{[\mathrm{OIII}]}{\mathrm{H}\beta}\right) < 1.89\,\log\left(\frac{[\mathrm{SII}]}{\mathrm{H}\alpha}\right) + 0.76, \tag{3.49}$$

$$\log\left(\frac{[\mathrm{OIII}]}{\mathrm{H}\beta}\right) < 1.18\,\log\left(\frac{[\mathrm{OI}]}{\mathrm{H}\alpha}\right) + 1.30, \tag{3.50}$$

$$\log\left(\frac{[\mathrm{OIII}]}{\mathrm{H}\beta}\right) < 1.01\,\log\left(\frac{[\mathrm{NII}]}{\mathrm{H}\alpha}\right) + 0.48. \tag{3.51}$$

Chapter 4

Integrated Characteristics

4.1 Introduction

In this chapter, we discuss some of our results from a broad perspective. LIRGs and star forming galaxies are very complex and are home to a wide variety of processes, and thus averaging those complexities into single parameters describing the whole galaxy can be problematic. Yet, studying these objects with an integrated approach can give a good statistical measure on how similar or different these objects are from the main sequence galaxies. It is also important to adopt an approach which links recent results to what is found in the literature from older lower resolution studies. Finally, results of the general properties such as age, metallicity, extinction and ionisation of our sample can also be linked to studies at higher redshift where even the most powerful telescopes are still limited by resolution.

4.2 Integrated Spectrum

For the purpose of the analysis that will follow in this chapter, we will be using what we have defined as the *integrated spectrum*. With the long-slit data that was acquired from RSS/SALT we mostly acquired data along the major axis of our list of galaxies. In some cases, we were able to acquire data with the slit in two different position angles. It is therefore clear that our data are sampled along a limited region of the galaxy. Kennicutt (1992a) invented the *drift scan method* in spectroscopy, in which during the observation of a target, the slit would be moved slowly across the entire galaxy field. While this method allows one to capture the light from the entire observable surface area of a galaxy, the data cannot be used to study radial properties of the object. Nowadays, data from Integral Field Spectroscopy (IFS or IFU in case of Integral Field Unit) such as the CALIFA survey (Sánchez et al., 2012), MaNGA (Bundy et al., 2015) and PINGS (Rosales-Ortega et al., 2010) allows one to acquire data from the entire galaxy field while also keeping radial information. Most of those surveys define an integrated spectrum as a

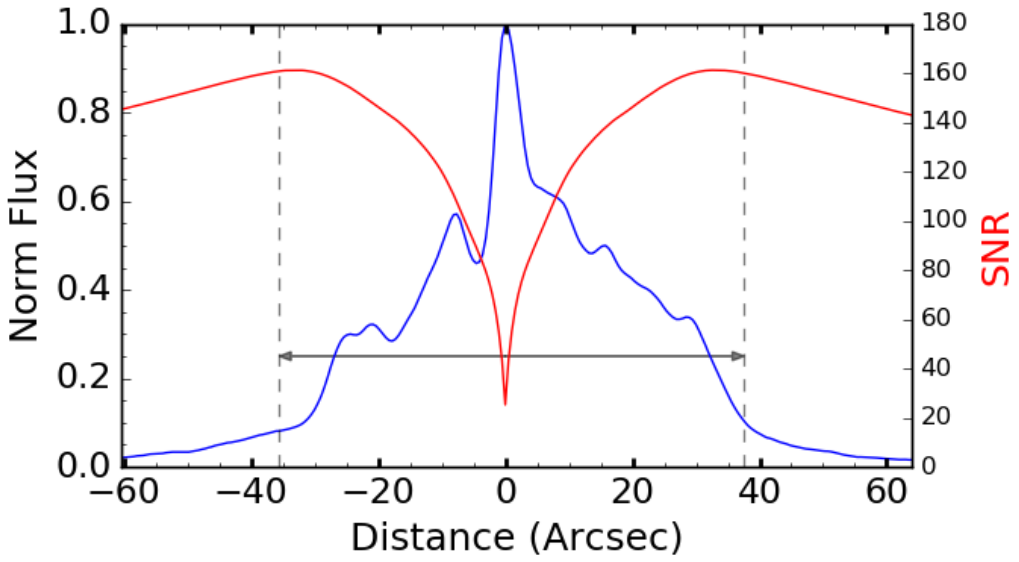

Figure 4.1: The Figure shows a cross section of the 2-dimensional spectrum of NGC4433. The blue line represent the normalised-sum of flux over the wavelength range for each row of data. The red line traces the SNR from the nucleus outwards as more rows are combined in integrated spectrum. The grey-dash lines represent the chosen region to be summed.

summation of the light from all the different fibres of the IFS.

In our work, we define the integrated spectrum as the summation of all the rows (from the CCD) with the galaxy signal. The selection of the apertures to be summed were done by eye. The determining factors were to select as wide an aperture as possible while also preserving the signal-to-noise ratio. Figure 4.1 shows an example of such aperture selection, extracted for NGC 4433, while the plots for the entire list of objects are provided in the appendices. Table C.1 in the Appendix C gives the different distances extracted in effective radius calculated from 2MASS K-band magnitude (see Chapter 5 for more details). The median radius extracted for all the apertures in the integrated section is 2.23 R_{eff}. In cases where foreground stars were present in the data or any object which was not the target of interest, the contaminated region was excluded from the aperture selection. In some cases we had two apertures for one target, at two different position angles. In those situations, we established that the best approach would be to run the entire analyses of the different position angles separately, and, in the end, average the parameters derived (for example age, metallicity, etc.). This will slightly bias the results towards the nuclear region of the galaxy since that section will appear in both slit positions.

4.2.1 Removal of kinematics effects

To be able to do a row by row summation and create a uniform spectrum for a specific target, we need to remove the kinematics effects of the galaxy from the data. Otherwise, emission and absorption lines of the spectrum will be artificially broadened, which will add systematics to the results derived. Here, we will discuss the steps applied to the reduced data from Chapter 2 to correct for the effects of the internal kinematics (both gas and stellar) of galaxies. In most cases, gas kinematics is tied to the stellar motion, but since emission lines offers higher SNR than absorption features, its much easier to use them to model the kinematics of the entire galaxy. The $H\alpha$ line and the two neighbouring NII lines are used to measure the rotation of the target by doing a triple Gaussian fitting of those lines. In cases where those three lines fell outside the wavelength coverage of the data, we use $H\beta$ to model the kinematics. Levenberg-Marquardt least square method, as described in Chapter 3, for emission line fitting was used for the fitting of the three emission lines in Python. In this case though, the amplitude, mean and standard deviation of each Gaussian were allowed to have free parameters, instead of the more rigid simultaneous constraint fitting routine which can, in some cases, run into errors. Essentially the only interest is finding the wavelength of their peaks and therefore by allowing the parameters to be free, there is a higher chance of obtaining convergence.

The position of each line can then be translated to both a velocity and a pixel value. The advantage of using three lines instead of one is that it allows for an average velocity to be calculated, but in some regions, one or even two of the nitrogen lines were not visible. In those cases, only the $H\alpha$ line was used. The fitting is done from the centre/nucleus of the galaxy to the outskirts on both sides on a row by row basis, but in cases of low SNR, the data was binned in the spatial direction. The mapping of the peaks and hence the velocities, for all the rows (with enough SNR), provides a basic rotation curve of the galaxy. A cubic spline function is then used to smooth the rotation curve to get rid of small random jumps in the recovered velocities, which are then translated to pixel coordinates. Taking the central nuclear row as the reference, the amount of pixel shift needed in each row is calculated to a precision of one tenth of a pixel. The next step is to interpolate each row to 10 times its original size, apply the calculated shift, and interpolate back to the original size. This leads to a galaxy spectrum which is free from kinematic features. In cases where there are noticeable divergence between stellar and gas kinematics, the stellar kinematics is found by using the RVSAO (Kurtz & Mink, 1998) in IRAF. By using the nuclear region as a template, the velocity of other regions (or rows) are then measured with respect to the nucleus similar to the schema laid out for the gas kinematics.

The redshift of the nuclear row is then calculated, and redshift correction is applied to the frame via the IRAF task DOPCOR in NOAO.TWODSPEC.LONGSLIT. The steps are applied to the

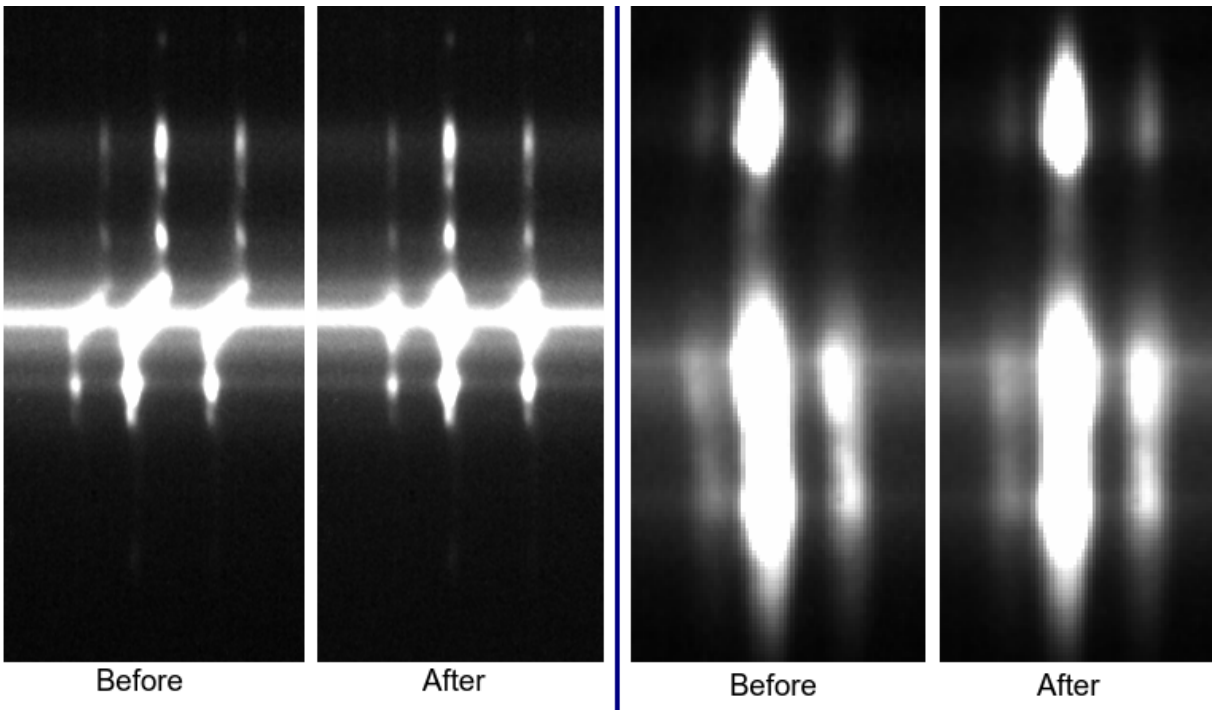

Figure 4.2: The figure shows two examples (NGC 6000 on the left and NGC 1222 on the right)of the difference in the frames after rotation was removed.

error spectrum to keep the one-to-one mapping of each pixel. After all this, the frames are finally ready for further analyses. Figure 4.2 shows two example cases of frames that were corrected for kinematics effect using the procedure described above. In the present case, all the rows were combined into a single aperture while in the next chapter,typically five to six apertures were extracted individually for each galaxy to be able to analyse radial properties.

Table 4.1: The table shows a list of some of the different parameters recovered for the integrated spectra of the SUNBIRD sub-sample. Column (1): Object name; Column (2): The goodness of the STARLIGHT fit given by Formula 4.1; Column (3) & (4): the measured values of Hδ and D_{4000} ; Column (5) & (6); Light weighted and mass weighted age respectively, derived using Formula 4.2; Column (7) & (8): The stellar and nebular extinction; Column (9): The specific star formation rate.

Name	$\overline{\Delta}$ [%]	H_δ	D_{4000}	$\langle \log \mathrm{Age} \rangle_l$ [yr]	$\langle \log \mathrm{Age} \rangle_m$ [yr]	Av_{st} [mag.]	Av_{HII} [mag.]	$\log(sSFR)$ [yr^{-1}]
(1)	(2)	(3)	(4)	(5)	(6)	(7)	(8)	(9)
CGCG049-057	1.43	2.65 ± 0.13	1.42 ± 0.01	9.00 ± 0.01	9.73 ± 0.03	0.79 ± 0.02	3.26 ± 0.20	-9.99 ± 0.03
ESO154-G010	1.59	2.25 ± 0.15	1.48 ± 0.01	8.99 ± 0.02	10.00 ± 0.01	0.89 ± 0.02	2.10 ± 0.10	-10.30 ± 0.01
ESO221-IG008	1.06	4.23 ± 0.32	1.00 ± 0.01	7.48 ± 0.03	9.72 ± 0.09	0.26 ± 0.05	0.88 ± 0.03	-8.85 ± 0.04
ESO221-IG010	0.94	2.60 ± 0.10	1.13 ± 0.01	7.84 ± 0.03	9.99 ± 0.03	0.78 ± 0.04	1.91 ± 0.04	-9.26 ± 0.04
ESO264-G036	0.72	3.49 ± 0.07	1.29 ± 0.01	8.46 ± 0.04	9.81 ± 0.04	0.67 ± 0.02	3.07 ± 0.05	-9.92 ± 0.03
ESO264-G057	1.56	3.04 ± 0.36	1.17 ± 0.01	7.77 ± 0.04	9.97 ± 0.03	1.29 ± 0.03	2.81 ± 0.09	-9.45 ± 0.03
ESO267-G030	1.04	2.82 ± 0.30	1.25 ± 0.01	8.35 ± 0.03	9.94 ± 0.03	1.06 ± 0.02	2.59 ± 0.11	-9.56 ± 0.03
ESO319-G022	1.93	3.00 ± 0.20	1.32 ± 0.01	8.41 ± 0.03	9.82 ± 0.04	0.96 ± 0.03	2.40 ± 0.10	-9.85 ± 0.03
ESO320-G030	1.21	3.00 ± 0.10	1.22 ± 0.01	8.42 ± 0.03	9.90 ± 0.01	0.94 ± 0.03	2.22 ± 0.03	-9.59 ± 0.03
ESO428-G023	1.15	2.84 ± 0.06	1.29 ± 0.01	8.62 ± 0.03	9.88 ± 0.03	0.61 ± 0.03	2.08 ± 0.03	-9.74 ± 0.03
ESO440-IG058-N	1.56	6.14 ± 0.09	1.17 ± 0.01	8.05 ± 0.04	9.71 ± 0.10	0.65 ± 0.05	0.93 ± 0.56	-10.30 ± 0.01
ESO440-IG058-S	2.12	5.09 ± 0.24	1.26 ± 0.01	8.24 ± 0.02	9.91 ± 0.04	1.10 ± 0.01	2.22 ± 1.24	-
ESO491-G020	0.89	2.58 ± 0.10	1.17 ± 0.01	8.40 ± 0.01	9.82 ± 0.07	0.17 ± 0.04	1.29 ± 0.04	-9.46 ± 0.03
ESO550-IG025-N	3.70	4.41 ± 0.22	1.07 ± 0.01	7.34 ± 0.03	9.83 ± 0.06	1.48 ± 0.04	2.19 ± 1.41	-
ESO550-IG025-S	6.62	3.56 ± 0.23	1.06 ± 0.01	7.49 ± 0.04	9.82 ± 0.05	1.42 ± 0.03	2.18 ± 1.47	-
IC2522	1.03	3.82 ± 0.09	1.19 ± 0.01	8.06 ± 0.05	9.94 ± 0.04	0.80 ± 0.03	1.76 ± 0.03	-9.75 ± 0.03
IC2522B	0.87	3.89 ± 0.09	1.20 ± 0.01	8.27 ± 0.05	9.60 ± 0.10	0.34 ± 0.03	0.92 ± 0.04	-9.73 ± 0.03
IRAS06164+0311	6.86	-0.13 ± 0.60	1.36 ± 0.03	8.96 ± 0.07	10.10 ± 0.01	0.74 ± 0.07	1.67 ± 0.87	-10.80 ± 0.01
IRAS12116-5615	5.61	4.88 ± 0.50	1.16 ± 0.02	8.20 ± 0.01	9.86 ± 0.04	1.65 ± 0.04	4.25 ± 2.03	-
IRAS13052-5711	2.25	2.50 ± 0.30	1.28 ± 0.01	8.54 ± 0.04	9.89 ± 0.04	0.77 ± 0.03	1.79 ± 0.05	-9.92 ± 0.03
IRAS17578-0400	4.19	3.48 ± 0.75	1.05 ± 0.02	7.33 ± 0.04	9.77 ± 0.23	0.51 ± 0.06	1.87 ± 0.36	-9.60 ± 0.01
IRAS17578-0400-W	6.26	4.99 ± 1.05	0.95 ± 0.03	6.81 ± 0.10	9.43 ± 0.80	0.74 ± 0.12	0.56 ± 0.06	-9.15 ± 0.04
IRAS17578-0400-E	10.24	3.95 ± 1.79	0.98 ± 0.04	6.93 ± 0.08	9.56 ± 0.70	0.65 ± 0.09	1.13 ± 0.07	-9.20 ± 0.01
IRAS18293-3413	2.59	1.48 ± 0.42	1.44 ± 0.02	9.10 ± 0.01	9.59 ± 0.04	0.49 ± 0.02	1.67 ± 0.95	-11.20 ± 0.01
IRAS18293-3413B	2.89	3.31 ± 0.96	1.19 ± 0.01	7.63 ± 0.05	10.01 ± 0.01	2.08 ± 0.06	3.69 ± 0.42	-9.30 ± 0.01

Table 4.1 – continued from previous page

Name	$\overline{\Delta}$ (%) [%]	H_δ	D_{4000}	$\langle \log \mathrm{Age} \rangle_l$ [yr]	$\langle \log \mathrm{Age} \rangle_m$ [yr]	Av_{st}	Av_{HII}	$\log(sSFR)$ [yr^{-1}]
IRAS19115-2124	1.91	2.98 ± 0.26	1.16 ± 0.01	7.84 ± 0.02	9.94 ± 0.03	1.25 ± 0.03	2.67 ± 0.28	-9.28 ± 0.04
IRAS19254-7245	2.30	2.71 ± 0.23	1.33 ± 0.01	8.92 ± 0.03	9.84 ± 0.03	0.75 ± 0.02	5.28 ± 0.53	-9.58 ± 0.03
IRASF01364-1042	3.62	5.54 ± 0.44	1.21 ± 0.01	8.73 ± 0.04	9.25 ± 0.03	0.51 ± 0.03	0.01 ± 0.01	-
IRASF06076-2139-N	1.85	4.44 ± 0.19	1.30 ± 0.01	8.80 ± 0.01	9.71 ± 0.05	0.82 ± 0.02	3.21 ± 0.09	-9.86 ± 0.03
IRASF06076-2139-S	2.25	1.85 ± 0.27	1.22 ± 0.01	8.65 ± 0.05	9.61 ± 0.07	0.42 ± 0.03	1.44 ± 0.04	-9.60 ± 0.01
IRASF16516-0948	3.18	3.33 ± 0.54	1.10 ± 0.01	7.46 ± 0.05	9.89 ± 0.08	1.01 ± 0.06	2.29 ± 0.06	-9.22 ± 0.04
IRASF17138-1017	30.51	2.42 ± 3.46	1.19 ± 0.11	8.58 ± 0.09	10.00 ± 0.02	2.47 ± 0.05	6.08 ± 0.17	-9.26 ± 0.04
MCG-02-01-051	1.58	4.60 ± 0.20	1.04 ± 0.01	7.64 ± 0.04	9.61 ± 0.11	0.59 ± 0.04	1.23 ± 0.03	-8.97 ± 0.04
MCG-02-01-052	1.30	4.03 ± 0.15	1.07 ± 0.01	7.68 ± 0.02	9.86 ± 0.06	0.45 ± 0.02	0.87 ± 0.02	-9.08 ± 0.04
MCG-02-33-098-E	1.54	4.42 ± 0.14	1.09 ± 0.01	7.54 ± 0.04	9.96 ± 0.05	0.65 ± 0.03	1.82 ± 0.03	-9.24 ± 0.04
MCG-02-33-098-W	1.80	4.23 ± 0.15	1.13 ± 0.01	7.66 ± 0.02	9.97 ± 0.04	0.68 ± 0.03	2.89 ± 0.08	-9.43 ± 0.04
NGC1022	2.09	4.93 ± 0.20	1.11 ± 0.01	8.08 ± 0.04	9.78 ± 0.07	1.14 ± 0.05	2.68 ± 0.05	-9.29 ± 0.04
NGC1068	0.55	3.59 ± 0.19	1.24 ± 0.01	8.74 ± 0.02	9.81 ± 0.04	0.25 ± 0.02	1.22 ± 0.07	-9.78 ± 0.03
NGC1204	1.61	2.77 ± 0.10	1.41 ± 0.01	9.04 ± 0.03	9.82 ± 0.03	0.82 ± 0.02	3.59 ± 0.08	-10.20 ± 0.01
NGC1222	1.40	3.68 ± 0.57	0.98 ± 0.01	7.54 ± 0.03	9.88 ± 0.07	0.75 ± 0.03	1.14 ± 0.04	-8.64 ± 0.05
NGC1819	1.21	3.23 ± 0.07	1.27 ± 0.01	8.52 ± 0.02	9.91 ± 0.02	0.58 ± 0.02	1.77 ± 0.03	-9.79 ± 0.03
NGC253	1.59	2.66 ± 0.20	1.39 ± 0.01	9.05 ± 0.02	9.95 ± 0.01	1.68 ± 0.02	2.68 ± 0.05	-9.73 ± 0.03
NGC3110	1.00	4.13 ± 0.07	1.17 ± 0.01	7.87 ± 0.02	9.89 ± 0.03	1.19 ± 0.02	2.28 ± 0.02	-9.39 ± 0.03
NGC3508	1.01	4.45 ± 0.10	1.15 ± 0.01	7.98 ± 0.03	9.91 ± 0.03	1.12 ± 0.03	1.91 ± 0.02	-9.46 ± 0.03
NGC4433	1.04	4.53 ± 0.09	1.12 ± 0.01	7.75 ± 0.03	9.94 ± 0.05	1.21 ± 0.04	2.59 ± 0.03	-9.33 ± 0.04
NGC4575	1.11	4.60 ± 0.10	1.17 ± 0.01	7.98 ± 0.03	9.95 ± 0.03	1.03 ± 0.03	1.94 ± 0.03	-9.69 ± 0.03
NGC470	1.85	4.11 ± 0.24	1.18 ± 0.01	8.58 ± 0.02	9.79 ± 0.05	0.70 ± 0.02	1.59 ± 0.03	-9.22 ± 0.04
NGC520	2.11	5.16 ± 0.15	1.29 ± 0.01	9.02 ± 0.02	9.27 ± 0.06	0.42 ± 0.02	0.81 ± 0.09	-10.40 ± 0.01
NGC6000	1.33	3.65 ± 0.12	1.16 ± 0.01	8.03 ± 0.02	9.91 ± 0.03	1.20 ± 0.01	2.23 ± 0.03	-9.54 ± 0.03
NGC6835	1.49	6.11 ± 0.12	1.14 ± 0.01	8.25 ± 0.02	9.66 ± 0.09	0.86 ± 0.03	1.64 ± 0.04	-9.82 ± 0.03
NGC7714	2.24	3.39 ± 0.55	1.05 ± 0.01	7.81 ± 0.04	9.89 ± 0.04	0.36 ± 0.03	0.28 ± 0.02	-8.96 ± 0.04
NGC7715	3.04	-	-	8.13 ± 0.05	8.61 ± 0.14	-	-	-
NGC7714C	5.00	4.21 ± 0.55	1.35 ± 0.02	8.57 ± 0.06	9.64 ± 0.06	-	-	-10.10 ± 0.01

4.3 SSP fitting and quality control

Now that integrated spectra are available for the entire sample of galaxies, the STARLIGHT pipeline described in section 3.6 is applied to the data. Figure 4.3 and 4.4 are examples of the fitting done using STARLIGHT for the data sample (Consult the appendices for links to the rest of the plots). Most of the analysis of that follows in this chapter derives from SSP modelling - meaning a that special care has to be given to have the highest possible quality output. Before we can use the results from SSP fitting, the quality of the fitting after it has gone through the pipeline must be assessed. We use the formalism defined in Cid Fernandes et al. (2013) where the fit quality indicator is defined as,

$$\overline{\Delta} = \frac{1}{N_{\lambda}^{eff}} \sum_{\lambda} \frac{|O_{\lambda} - M_{\lambda}|}{M_{\lambda}}, \tag{4.1}$$

where O_{λ} is the observed spectrum and M_{λ} is the SSP fit from starlight. The summation is carried over all wavelength bins except those which were masked, binned and clipped during the fitting. While there are no hard limits on the acceptable range of $\overline{\Delta}$, Cid Fernandes et al. (2013) set their limits to a range of $8 - 10\%$. In Table 4.1 we list the quality of the fits for the entire sample. In the majority of cases, the quality is below the threshold of 10% though in the cases of two galaxies it is above. While in the case of IRAS17578-0400-E the fitting goes very narrowly above the threshold and hence should be good enough for further analysis, the case of IRASF17138-1017 goes well above the accepted limit. The latter is the case of a galaxy with extreme extinction which has almost no emission in the blue end of the spectrum, which made the SSP modelling difficult. For this reason, this target is excluded from any further analysis from the integrated characteristics.

4.4 Age

4.4.1 SSP fitting age

From the previous chapter, we know that STARLIGHT outputs a population vector which is representative of the star formation history, SFH, of the observed galaxy. To recover the age of the galaxy we use the formalism presented in Cid Fernandes et al. (2005):

$$\langle \log \mathrm{Age} \rangle_l = \sum_{j=1}^{N} x_j \log t_j, \tag{4.2}$$

where x_j is the light fraction at the normalisation wavelength ($4020\mathring{A}$), t_j is the age of each SSP and N is the total number of SSP in the base. The age derived from this method, is usually

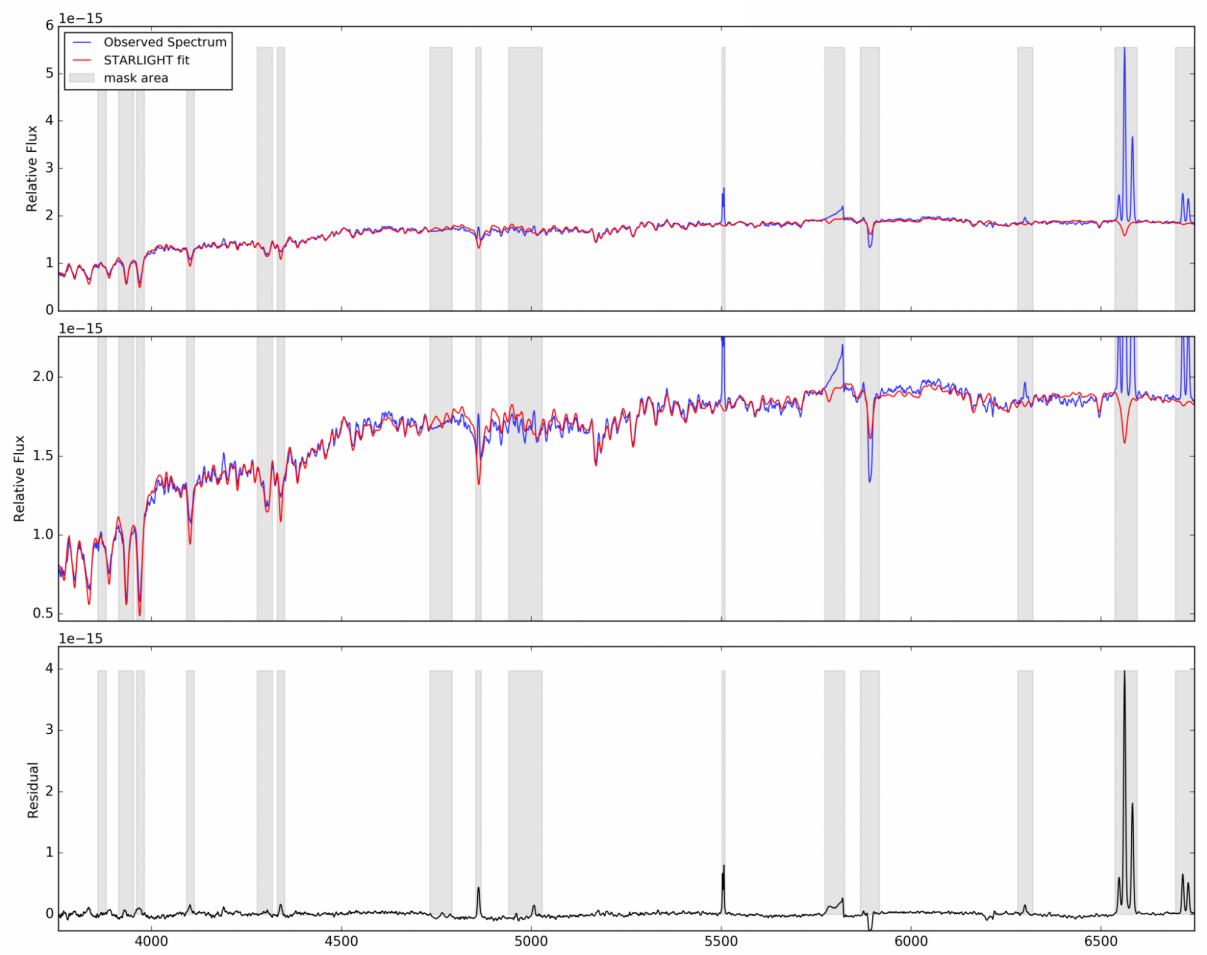

Figure 4.3: The STARLIGHT fit to galaxy CGCG049-057 with the *top panel* showing the observed spectrum in blue and the full stellar population fit in red. The *middle panel* is the same data as the top panel but zoomed on the continuum of the data. The *bottom panel* shows the pure emission spectra in black i.e. the residual spectra after the stellar population fit has been subtracted from the observed spectrum. Grey areas on the plots indicates regions which were masked due to CCD gaps, or contaminating artefacts or emission line features.

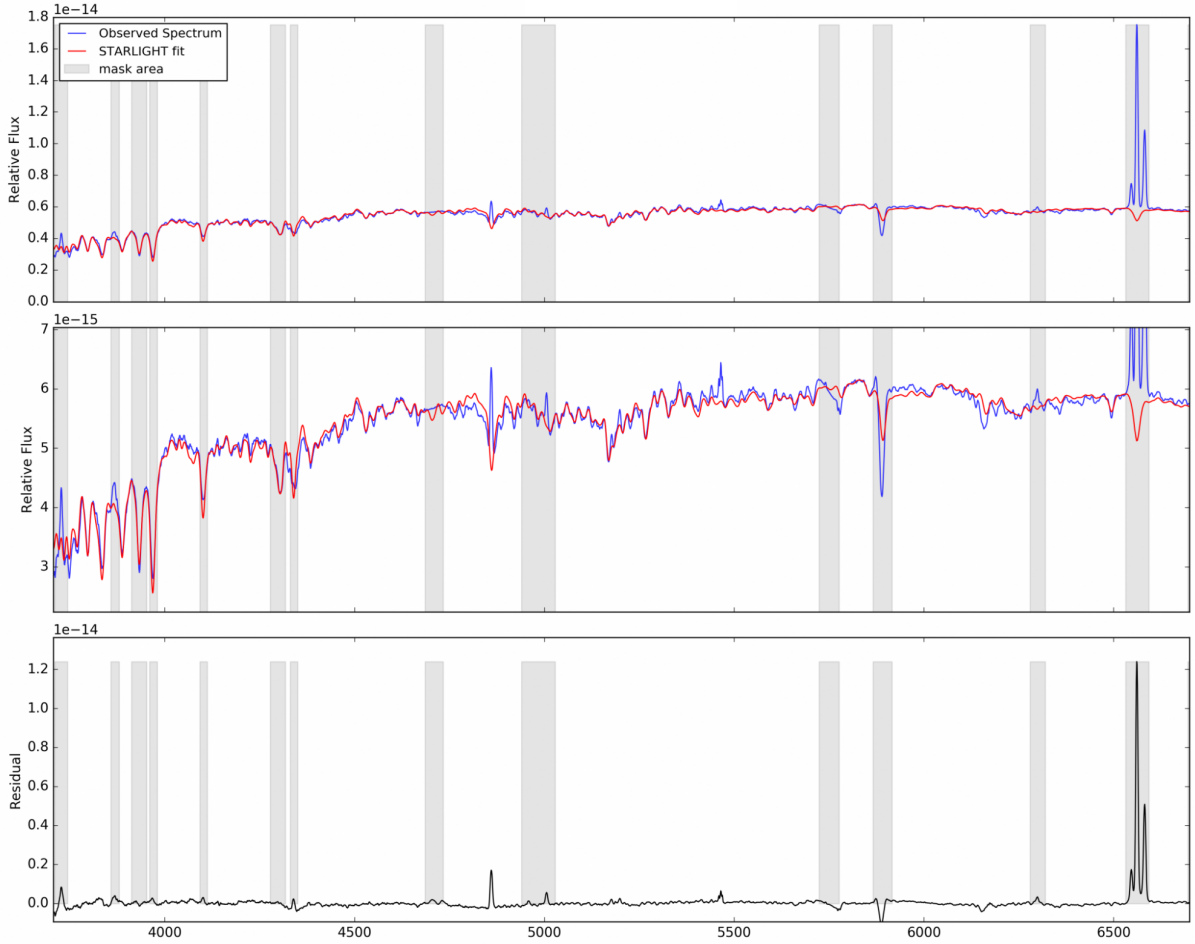

Figure 4.4: Same as Figure 4.3 but for galaxy ESO 264-G036.

that of the object for a single fit. Since many iterations of fitting were performed through our pipeline, an age is derived for each iteration. This leads to a distribution of ages (as well as other properties) from which one can derive a robust mean age as well as an uncertainty estimate. We present the mean ages of our entire list of targets in Table 4.1 while the entire distributions (light- and mass-weighted) for each galaxy is plotted in Figure 4.5. The mean age of a galaxy can be a misleading value as it has little physical meaning on its own in cases where the galaxy does not have a single episode of star formation. Furthermore, for LIRGs and star-forming galaxies, due to the different episodes of star formation present, this value is expected to be very small, indicating that the galaxies are unrealistically young. In fact, younger populations outshine the older ones and since we weigh our age indicator by light contribution, the mean age is therefore biased towards the younger population. But it still offers a good metric for comparing different galaxies or groups of galaxies with each other. To get more physically sensible age values one needs to consider the mass weighted age ($\langle \log \mathrm{Age} \rangle_m$) which uses the assumed IMF to estimate the mass of each SSP contribution.

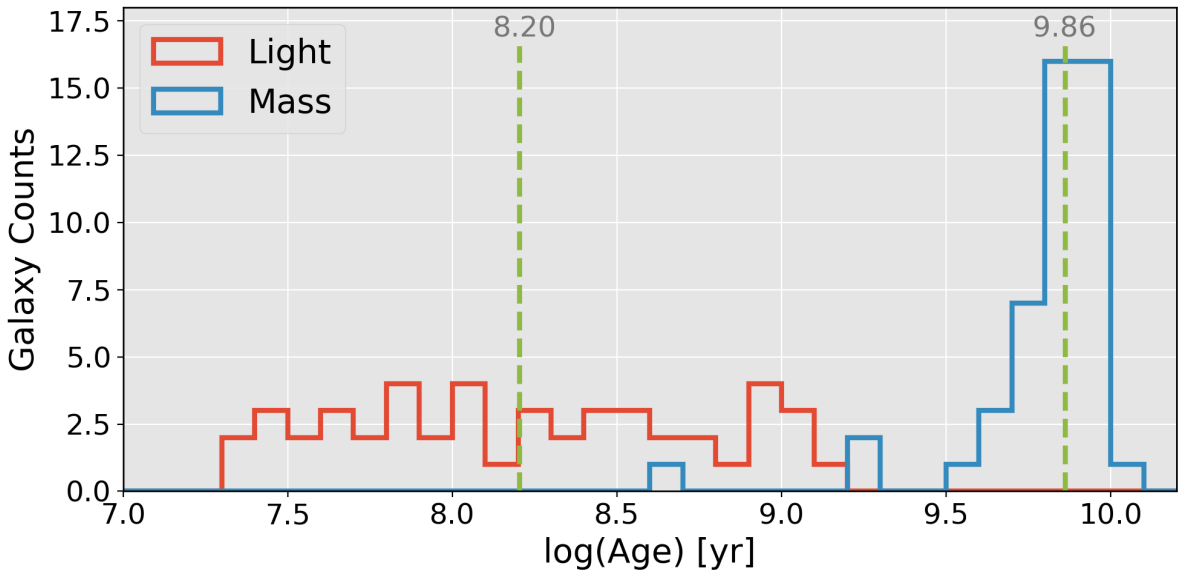

Figure 4.5: Histogram of the mean age of each galaxy with red showing the light-weighted age and the blue showing the mass-weighted age. Green dash line depicts the median ages of each distribution at $10^{8.20} = 158$ Myr and $10^{9.86} = 7.24$ Gyr respectively

To get a better understanding of the different populations in the sample, the stellar population is divided into four bins. This strategy of summarising the results in different age bins has extensively been used previously (Bica et al., 1988; González Delgado et al., 2004; Rodríguez Zaurín et al., 2010). We define a young stellar population (YSP) as a stellar component with

ages $t_{ysp} \leq 15$ Myr, a first intermediate population where $15 < t_{isp1} \leq 150$ Myr, a second intermediate population of $150 < t_{isp2} < 1000$ Myr and an old population of $t_{osp} > 1$ Gyr. In Figure 4.6 the contribution of light (light fraction or light percentage) is shown for each of these four bins from the entire sample. Each panel is a histogram of the light fraction for the specific stellar component age. The histogram is divided into 20 equal bins in the range of 0% to 100%. The y-axis is a number count of targets which fall into the different bins. From the top left panel of Figure 4.6 we can see that the YSP is almost always present in the sample with varying intensity of up to above 90% of the light. There is also an OSP (bottom right panel) in the sample though its light contribution is slightly less than the YSP. This is expected as usually older stellar populations are less luminous. In case of both ISP1 and ISP2, their contributions are less than that of the two other categories. The ISP1 which is still a young bin, has the least influence in the sample. The implication of these results points to the idea that this sample of LIRGs contains an older population of stars presumably when the progenitor galaxies were formed. In the last 15 Myr, presumably due to a triggering event, the SF activity has started again. In between these two distinct star forming episodes (current and old one), the sample of galaxies goes through some SF-activity, the details of which can vary from case to case.

4.4.2 $D_n(4000)$ and $H\delta_A$ age

$D_n(4000)$ is an index that uses the gradient of a galaxy spectrum at 4000 $\mathring{A}$-break to quantify how old its stellar population is. Similarly the $H\delta_A$ is an age sensitive Lick index, but it has a more complex variation with age than the quasi-monotonic function of $D_n(4000)$. Somewhat depending on the exact model used, $H\delta_A$ increases to a maximum at around 350 Myr before decreasing slowly back to below zero as the age continue to increase. Kauffmann et al. (2003a) used a method based on these two indices to measure the SFH in the SDSS sample. A simple Python routine based on the definition from Balogh et al. (1999) of the $D_n(4000)$ index, was devised for the measurement of the ratio of flux from a red-continuum ($4000 - 4100$ $\mathring{A}$) to that of a blue continuum ($3850 - 3950$ $\mathring{A}$). In the case of $H\delta_A$, the narrow definition from Worthey & Ottaviani (1997) was used to quantify it by applying the software LECTOR (Vazdekis, 2011) to the data. Section 3.8 gives an explanation on how pure emission line spectrum is achieved. This pure emission spectrum consisting of only emission lines and no residual continuum is subtracted from the overall galaxy spectrum prior to the measurement of $H\delta_A$ to get rid of any contamination.

Figure 4.7 depicts the measurement of the D_{4000} and $H\delta_A$ for the SUNBIRD sub-sample. The green and red lines are time evolution of the two indices for a BC03 model using two different metallicities, 2.5 and 1.0 times Solar, respectively. The assumption is that star formation

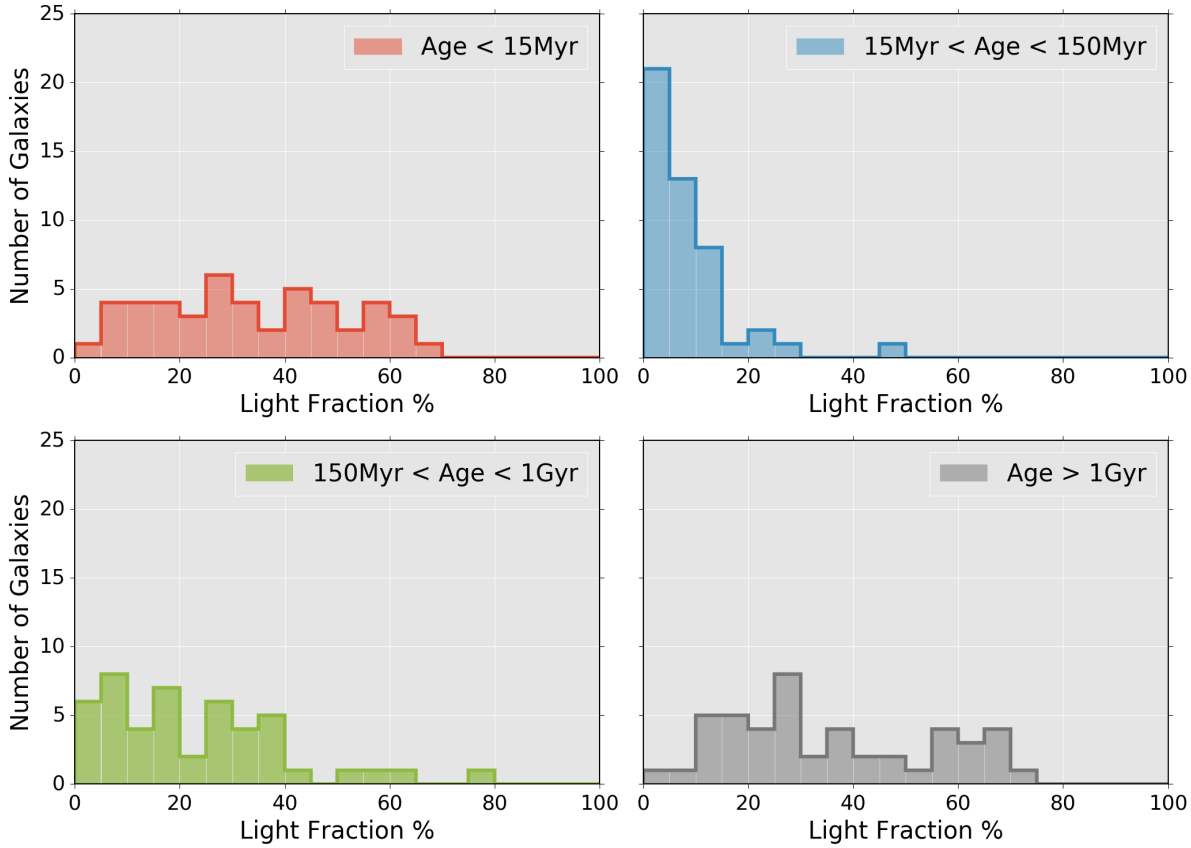

Figure 4.6: The light fraction of the different stellar population components of the SUNBIRD sub-sample. Top left panel shows the YSP, top right panel the ISP1, bottom left panel shows ISP2 and bottom right panel displays the OSP.

happens in bursts rather than continuously, and the age of each burst is plotted for a solar metallicity model. Grey squares are points taken from Kauffmann et al. (2003a) for the SDSS main sample. The lower tail ($D_{4000} > 1.5$) of the SDSS sample falls exactly on the BC03 tracks which points to old stellar populations without any recent episode of SF-activity. The higher end of the SDSS data ($D_{4000} < 1.5$) is outside the track of the BC03 model. To achieve such indices, the galaxies must have an older population (> 2.5 Gyr) and a younger intermediate population ($55 - 200$ Myr). The SUNBIRD sub-sample is represented by the coloured circles in the plot. The colouring scheme is used to represent the age derived by STARLIGHT fitting. Most of our galaxies lie in the same region of the D_{4000} vs H_δ plot as the sample of LIRGs analysed by Alonso-Herrero et al. (2009, 2010). In most cases it requires a combination of (at least) a very young population (~ 10 Myr) with that of an older population (> 2.5 Gyr) to be able to achieve the observed indices. Some galaxies with higher values of $H\delta_A$ seem to point to the necessity of adding an Intermediate Stellar component. The median value of D_{4000} was

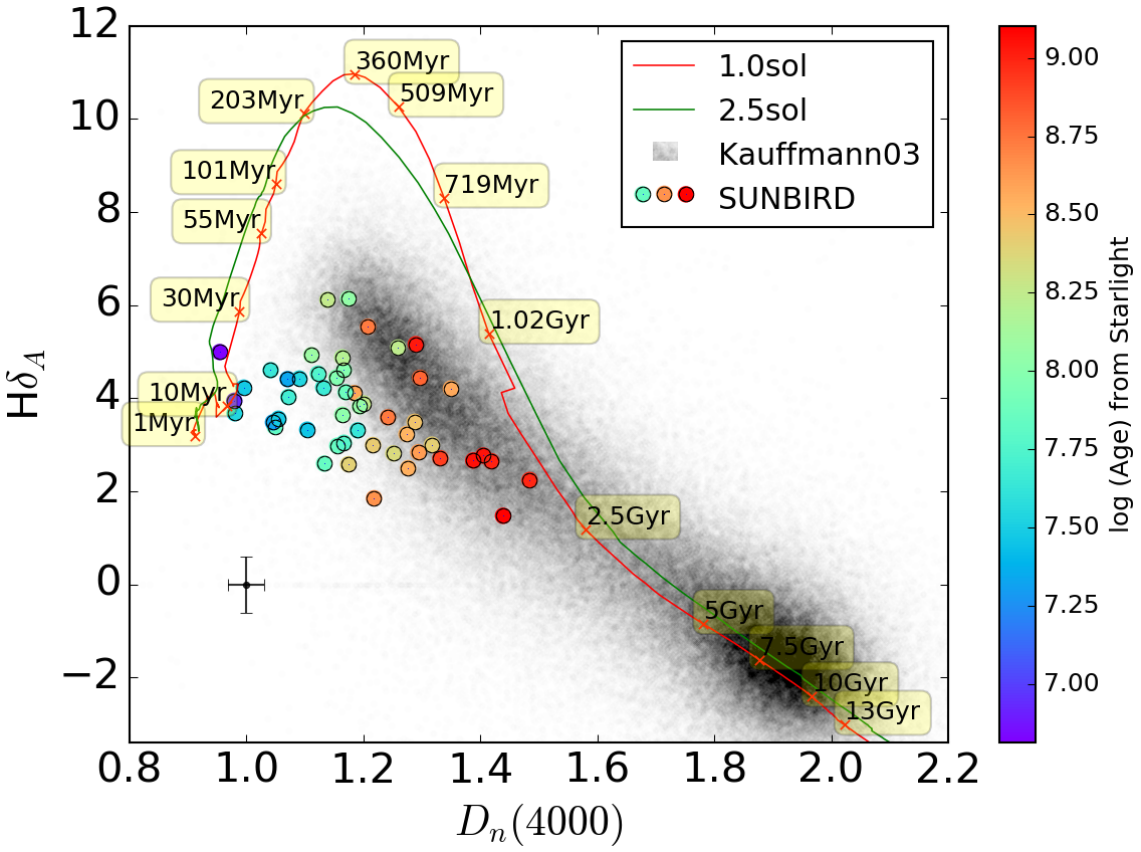

Figure 4.7: D_{4000} vs $H\delta_A$ plot of our sample. The lines (red and green) indicate the locus of the two indices for single burst events at different ages and two metallicities following BC03 models. Yellow boxes indicate the location of the different ages along the locus for solar metallicity bursts. The grey areas show where a general population of galaxies should lie. The data were taken from the SDSS survey (Kauffmann et al., 2003a). Data points from our survey are marked by circular markers which are colour coded by the age derived from Starlight fitting. The point at (1,0) depicts the upper limits of the error-bars of the circular markers.

found to be 1.17±0.12 and the median value of $H\delta_A$ was 3.65±1.14. This D_{4000} value is strongly indicative of a young mean age for the galaxy. For comparison, values of 1.25 and 1.30 were obtained by Marcillac et al. (2006) and Alonso-Herrero et al. (2010) respectively for local LIRGs.

Given that the colour of the circular markers in the D_{4000} vs $H\delta_A$ plot in Figure 4.7 is an indicator of age, we can visually evaluate the consistency of the age determination from the two methods. From the plot, we see a gradual change from blue (very young) to red (old) as D_{4000} increases, which is expected. While the D_{4000} vs $H\delta_A$ plot cannot offer precise measurements on the contribution of the different stellar components, it offers an excellent independent sanity check of the SSP method. The mixture of stellar populations observed in this sample is consistent

with the study made by Alonso-Herrero et al. (2009, 2010) which had a very evolved population along with a very young population. For a nearby sample ($0.018 < z < 0.149$) of ULIRGs, Rodríguez Zaurín et al. (2009) also get best fits with two component stellar population models. But in their case, the age of the older population was less evolved, being in the range of only $0.1 - 2$ Gyr.

4.4.3 $D_n(4000)$ vs Mean Age

We investigate how well the mean age indicator the $D_n(4000)$ index correlate. The relationship between the two variables are plotted in Figure 4.8. A linear relationship between the two variables is clear at $D_n(4000) < 1.35$. Similar results were observed by Hou et al. (2011) for a sample of 398 ULIRGs from the SDSS main sample. At higher values of $D_n(4000)$ the relationship changes and flattens. This flattening is observed also in the CALIFA sample where there is a bigger diversity of galaxies, and therefore a larger fraction of early-type galaxies, than in SUNBIRD sub-sample (López Fernández et al., 2016). There is a relatively large scatter of the points around the best-fit line, as expected when using any singular index to measure a parameter such as mean age. Overall, this confirms the that $D_n(4000)$ is a good index to measure the luminosity weighted mean age of LIRGs, since they are young and will mostly occupy the linear regime. But the caveat is that even in the linear regime, $D_n(4000)$ is not as precise an age indicator as other methods which relies on several indices or full spectrum fitting.

4.4.4 $D_n(4000)$ vs Mass

Older galaxies are generally more massive than their younger counterparts - this follows from the hierarchical formation scenario where bigger galaxies attract satellites to merge on to them, making their potential wells even larger. Figure 4.9 shows a plot of mass vs $D_n(4000)$ for the SDSS sample (plotted in grey). As stellar mass increases, the value of $D_n(4000)$ also increases, though the evolution is far from a linear correlation. The SUNBIRD sub-sample (coloured circles) is over-plotted on top and displays mostly higher mass but extremely low values of $D_n(4000)$. A similar observation was done by Marcillac et al. (2006). The interpretation is that our population of SF galaxies and LIRGs consist of massive galaxies which through the process of a trigger mechanism had a burst of star formation. This burst, then has the effect of lowering the overall $D_n(4000)$ index of the galaxy. This is also another way of seeing how LIRGs are away from the "main-sequence" of galaxies.

4.5 Star Formation History

The SFH of galaxies has been a very loosely defined term in the study of galaxy evolution. Different sub-fields define the term according to the parameters that can be derived from the

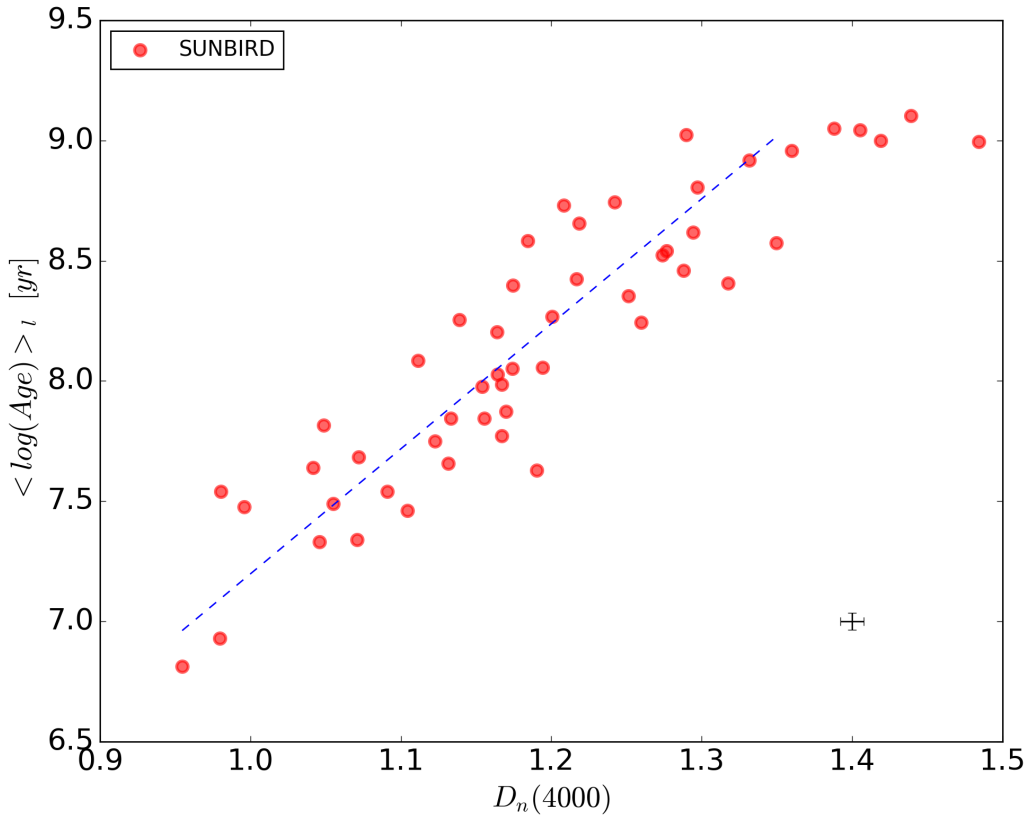

Figure 4.8: Plot of$\langle \log(Age) \rangle_l$ vs $D_n(4000)$. The dashed line indicates a least squares fit for $D_n(4000) < 1.35$. The equation of the dashed line is $D_n(4000) = -0.384 + 0.192\langle \log(\mathrm{Age}) \rangle$ for a distribution of points which shows a relatively large scatter. The point at (1.4,7.0) shows the typical size of error bars for the plot.

available data. In the last section, we touched on the subject of the SFH by looking at the mass of galaxies compared to their mean age. We now move on to look at the time evolution of different parameters during the lifetime of galaxies. Asari et al. (2007) introduced a simple way of calculating the time variation of the SFR of galaxies by using

$$SFR(t_\star) = \frac{\mathrm{d}M^c_\star(t_\star)}{\mathrm{d}t_\star} \approx \frac{M^c_\star \log e}{t_\star} \frac{\mu^c_s(t_\star)}{\Delta \log t_\star}, \tag{4.3}$$

where $M^c_\star$ is the gas to stellar mass conversion rate and μ^c_s is a smoothed mass fraction vector over a grid of $t_\star = 6$ to 10.2. A Gaussian kernel is applied to the population vector in steps of $\Delta \log\ t_\star = 0.7$ dex. This smoothing allows us to obtain a continuous population vector instead of the discrete values from STARLIGHT output. We can also obtain the time variation of the sSFR for each galaxy following the same steps by removing the mass:

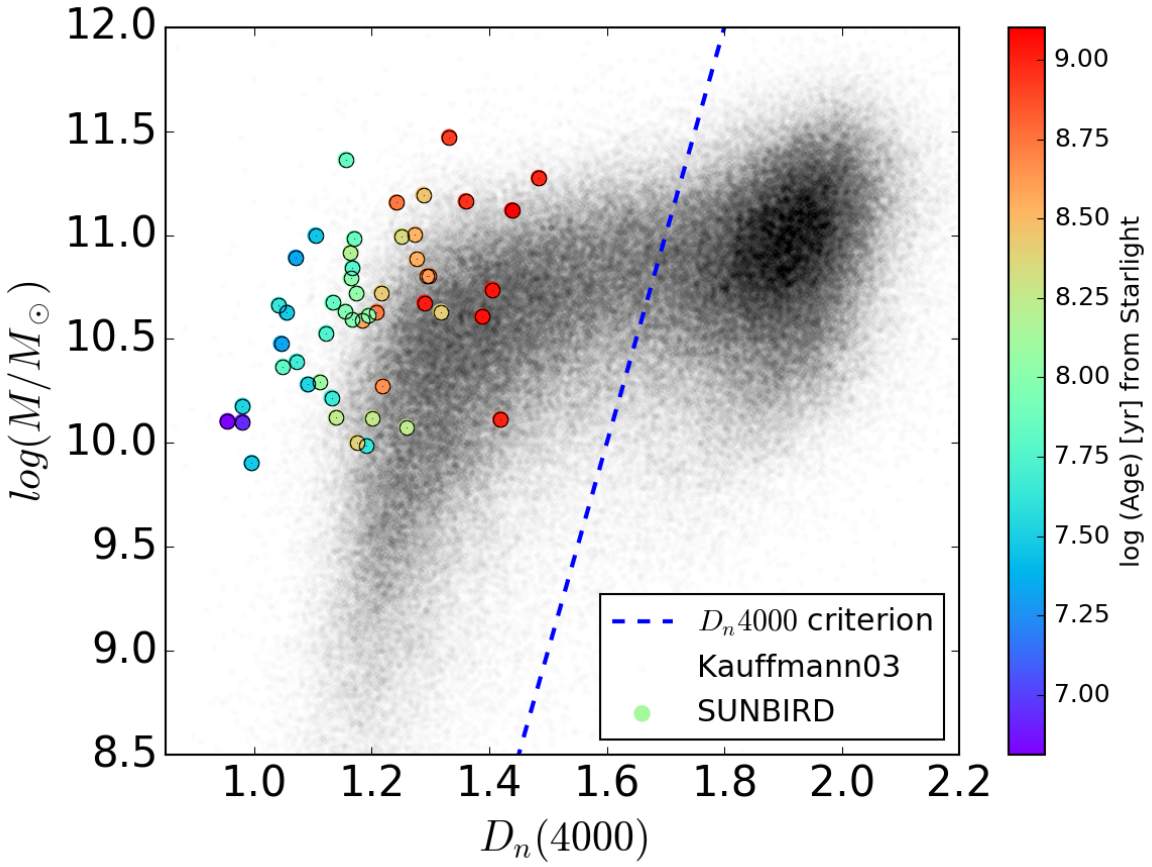

Figure 4.9: Plot of stellar Mass vs $D_n(4000)$ with SDSS galaxies in black and the SUNBIRD sub-sample shown as coloured circles. The blue dashed line is the quench criterion derived by Geha et al. (2012), so that any dwarf galaxies lying on the right of the line are not forming stars. All SDSS masses were converted from a Kroupa to a Chabrier IMF masses.

$$sSFR(t_\star) = \frac{1}{M^c_\star}\frac{\mathrm{d}M^c_\star(t_\star)}{\mathrm{d}t_\star} \approx \frac{\log e}{t_\star}\frac{\mu^c_s(t_\star)}{\Delta \log t_\star}, \tag{4.4}$$

Since absolute flux calibration is difficult to perform on our SALT data (due to the slits covering only a small fraction of the galaxies), the $M^c_\star$ term derived from STARLIGHT is usually wrongly scaled for an individual target. One way to work around this issue is to first to derive the time dependent sSFR, and then use the stellar masses that were derived from K-band magnitudes to then rescale the $M^c_\star$ term at $t_\star = 0$. The value can then be applied back to equation 4.4 to derive properly calibrated SFR evolution. By making use of equation 4.3 and 4.4, the star formation history for the entire sample of galaxies is calculated and plotted in Figure 4.10. The left panel shows the time evolution of the sSFR and the right panel is the SFR evolution. Each

of the grey lines represent a target galaxy, while the red and green lines represent the mean and median of the sample, respectively.

Similarly in Figure 4.11, the cumulative mass fraction conversion rate into stars is plotted. The evolution of SFR and sSFR are almost the same with the exception of the early stages of the galaxies. In the early stages of the galaxies' lifetime, the stellar mass conversion rate calculated has a steep rise which gives the observed sharp decline in sSFR for the same period. For that era, SFR gives a more accurate representation of the SFH of the galaxies, while beyond that sSFR is a better indicator since it is mass independent. Overall the SFH of LIRGs shows that after their early stages, their SFR has a slow decline until 100 Myr ago. The SFR then slowly picks up until 3 Myr ago where there is an increase of SF-activity by an order of magnitude. The evolution at < 100 Myr and very recently, is presumably due to triggered recent SF events, the very reason these galaxies were picked up to be part of our sample. When we compare the results obtained for our galaxy sample to those obtained previously in section 3.7.3, Figure 3.8 with the SDSS sample, the SFH shows similarities with the typical Sc and Starburst galaxies, showing a huge increase in activity in the last 100 Myr. But a noticeable difference is how SUNBIRD galaxies shows two distinct episodes of increase SF-activity around 100 Myr and around 3 Myr while SDSS typical galaxies shows more gradual increase in SF-activity over the last 100 Myr period.

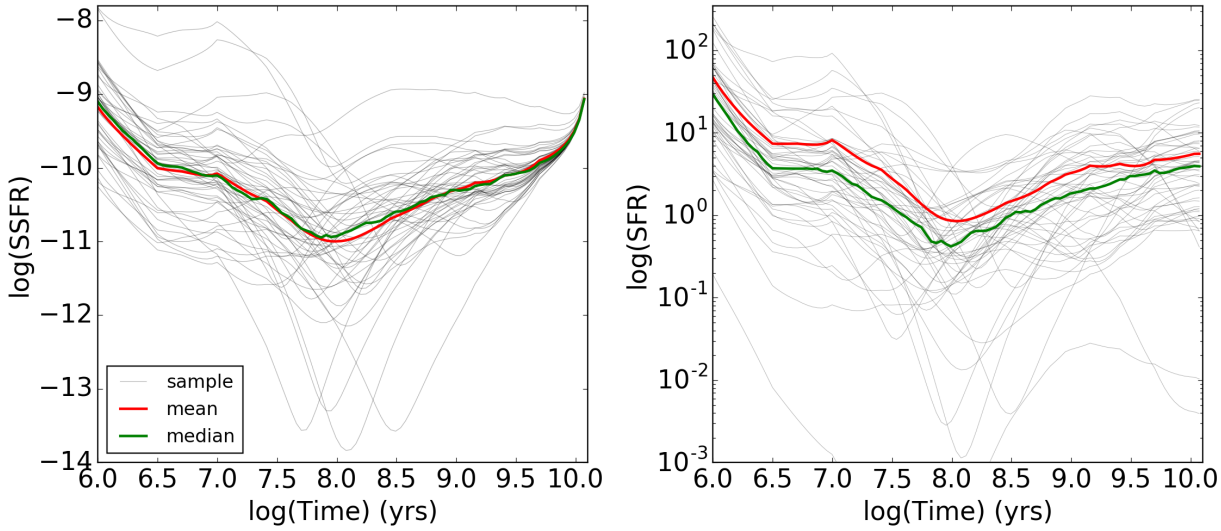

Figure 4.10: *Left panel*: Time evolution of sSFR for each galaxy. *Right panel*: The change of SFR with time. Each grey line represent one target with the green and the red lines representing of the median and mean values of the sample.

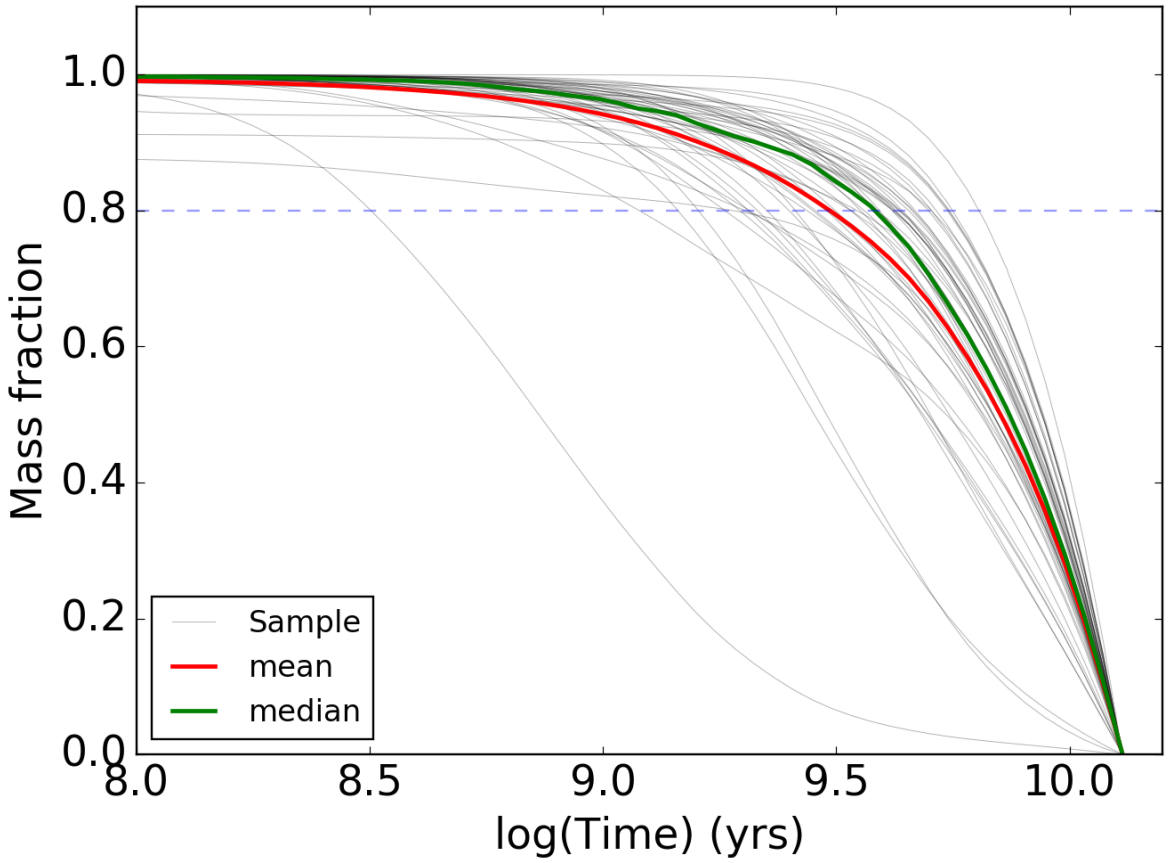

Figure 4.11: The mass conversion rate of LIRGs.

Table 4.2: The table shows a second set of parameters recovered for the integrated spectra of the SUNBIRD sub-sample. Column (1): The name; Column (2) & (3): The mean metallicities weighted by light and mass respectively using the formula 4.5; Column (4) & (5): The line ratios derived for the BPT diagnostics; Column (6): The BPT classification of the galaxy; Column (7): The log of u, the ionisation parameter; Column (8): The metallicity weighted by mass given by Formula 4.6 - given separately to avoid confusion. '-' denotes places where the parameter could not be measured.

Name	$\langle \mathbf{Z} \rangle_l$	$\langle \mathbf{Z} \rangle_m$	$\log \frac{[\mathbf{NII}]}{\mathbf{H}\alpha}$	$\log \frac{[\mathbf{OIII}]}{\mathbf{H}\beta}$	**Classification**	**log u**	$\langle \mathbf{log\ Z} \rangle_m$
(1)	(2)	(3)	(4)	(5)	(6)	(7)	(8)
CGCG049-057	1.31 ± 0.08	1.08 ± 0.11	-0.34 ± 0.04	-0.44 ± 0.06	HII	-	-0.24 ± -0.03
ESO154-G010	1.25 ± 0.07	1.30 ± 0.08	-0.17 ± 0.01	-0.18 ± 0.02	Comp	-	-0.05 ± -0.01
ESO221-IG008	0.95 ± 0.05	0.34 ± 0.09	-0.82 ± 0.01	0.33 ± 0.01	HII	-3.09 ± 0.01	-0.63 ± -0.07
ESO221-IG010	1.20 ± 0.07	1.44 ± 0.16	-0.32 ± 0.01	-0.60 ± 0.01	HII	-3.57 ± 0.07	-0.11 ± -0.01
ESO264-G036	0.72 ± 0.05	1.32 ± 0.12	-0.38 ± 0.01	-0.52 ± 0.02	HII	-3.60 ± 0.05	-0.09 ± -0.01
ESO264-G057	0.75 ± 0.06	1.72 ± 0.11	-0.35 ± 0.02	-0.60 ± 0.04	HII	-3.58 ± 0.26	0.09 ± 0.01
ESO267-G030	0.81 ± 0.06	1.78 ± 0.09	-0.34 ± 0.02	-0.05 ± 0.02	Comp	-3.11 ± 0.48	0.07 ± 0.01
ESO319-G022	0.98 ± 0.07	1.44 ± 0.12	-0.12 ± 0.01	-0.51 ± 0.02	Comp	-3.59 ± 0.05	-0.07 ± -0.01
ESO320-G030	0.71 ± 0.06	1.76 ± 0.16	-0.34 ± 0.01	-0.64 ± 0.01	HII	-3.60 ± 0.06	0.06 ± 0.01
ESO428-G023	0.64 ± 0.06	1.60 ± 0.13	-0.21 ± 0.01	-0.42 ± 0.01	Comp	-3.35 ± 0.45	-0.03 ± -0.00
ESO440-IG058-N	0.28 ± 0.04	0.77 ± 0.36	-	-0.10 ± 0.01	-	-3.30 ± 0.05	-0.41 ± -0.06
ESO440-IG058-S	0.66 ± 0.06	1.17 ± 0.21	-	-0.32 ± 0.02	-	-3.56 ± 0.12	-0.23 ± -0.03
ESO491-G020	0.40 ± 0.08	0.27 ± 0.09	-0.50 ± 0.01	-0.11 ± 0.01	HII	-3.36 ± 0.04	-0.67 ± -0.07
ESO550-IG025-N	1.06 ± 0.08	0.94 ± 0.07	-	-0.45 ± 0.03	-	-3.71 ± 0.23	-0.12 ± -0.01
ESO550-IG025-S	1.06 ± 0.06	0.82 ± 0.07	-	-0.12 ± 0.04	-	-3.71 ± 0.15	-0.19 ± -0.02
IC2522	0.59 ± 0.07	1.65 ± 0.18	-0.41 ± 0.01	-0.47 ± 0.01	HII	-3.57 ± 0.01	-0.00 ± 0.00
IC2522B	0.32 ± 0.07	0.32 ± 0.08	-0.56 ± 0.01	-0.28 ± 0.01	HII	-3.48 ± 0.04	-0.64 ± -0.07
IRAS06164+0311	0.99 ± 0.13	1.56 ± 0.10	-0.37 ± 0.18	0.04 ± 0.17	Comp	-	0.08 ± 0.01
IRAS12116-5615	0.52 ± 0.06	1.58 ± 0.12	-	-0.28 ± 0.03	-	-3.53 ± 0.23	-0.01 ± -0.00
IRAS13052-5711	0.97 ± 0.09	0.99 ± 0.15	-0.26 ± 0.01	-0.28 ± 0.01	Comp	-3.50 ± 0.04	-0.19 ± -0.02
IRAS17578-0400	0.37 ± 0.04	1.34 ± 0.59	-0.41 ± 0.07	-0.38 ± 0.11	HII	-	-0.06 ± -0.01
IRAS17578-0400-W	1.97 ± 0.13	1.48 ± 0.89	-0.69 ± 0.01	0.17 ± 0.01	HII	-3.25 ± 0.16	-0.09 ± -0.02
IRAS17578-0400-E	1.20 ± 0.18	0.56 ± 0.59	-0.54 ± 0.01	-0.10 ± 0.01	HII	-3.26 ± 0.46	-0.50 ± -0.10
IRAS18293-3413A	0.92 ± 0.10	1.23 ± 0.07	-0.16 ± 0.59	0.97 ± 0.62	AGN	-3.35 ± 0.69	-0.14 ± -0.01
IRAS18293-3413B	0.99 ± 0.07	1.68 ± 0.08	-0.37 ± 0.07	-0.48 ± 0.10	HII	-3.50 ± 0.19	0.09 ± 0.01

Table 4.2 – continued from previous page

Name	$\langle \mathbf{Z} \rangle_l$	$\langle \mathbf{Z} \rangle_m$	$\log \frac{[\mathbf{NII}]}{\mathbf{H}\alpha}$	$\log \frac{[\mathbf{OIII}]}{\mathbf{H}\beta}$	**Classification**	**log u**	$\langle \mathbf{log\ Z} \rangle_m$
(1)	(2)	(3)	(4)	(5)	(6)	(7)	(8)
IRAS19115-2124	0.71 ± 0.05	1.31 ± 0.14	-0.37 ± 0.05	-0.20 ± 0.06	HII	-3.52 ± 0.26	-0.05 ± -0.01
IRAS19254-7245	1.03 ± 0.08	1.95 ± 0.06	-	0.41 ± 0.09	-	-3.41 ± 0.10	0.17 ± 0.02
IRASF01364-1042	0.46 ± 0.07	0.59 ± 0.12	-	0.17 ± 0.03	-	-3.44 ± 0.05	-0.45 ± -0.05
IRASF06076-2139-N	0.43 ± 0.04	1.29 ± 0.09	-0.08 ± 0.02	-0.29 ± 0.03	Comp	-3.62 ± 0.05	-0.15 ± -0.02
IRASF06076-2139-S	0.81 ± 0.10	0.93 ± 0.15	-0.29 ± 0.01	-0.11 ± 0.01	Comp	-3.32 ± 0.03	-0.33 ± -0.04
IRASF16516-0948	0.50 ± 0.06	0.87 ± 0.13	-0.47 ± 0.01	-0.13 ± 0.01	HII	-3.44 ± 0.17	-0.15 ± -0.02
IRASF17138-1017	0.00 ± 0.00	0.00 ± 0.00	-0.34 ± 0.03	-0.28 ± 0.04	Comp	-	-
MCG-02-01-051	1.40 ± 0.10	0.51 ± 0.18	-0.58 ± 0.01	0.09 ± 0.01	HII	-3.25 ± 0.04	-0.51 ± -0.06
MCG-02-01-052	0.88 ± 0.07	0.75 ± 0.20	-0.53 ± 0.00	-0.04 ± 0.00	HII	-3.23 ± 0.02	-0.38 ± -0.05
MCG-02-33-098-E	0.61 ± 0.05	1.25 ± 0.28	-0.48 ± 0.01	-0.07 ± 0.01	HII	-3.45 ± 0.03	-0.19 ± -0.03
MCG-02-33-098-W	0.74 ± 0.06	1.18 ± 0.30	-0.28 ± 0.01	-0.31 ± 0.02	Comp	-3.73 ± 0.03	-0.22 ± -0.03
NGC1022	0.33 ± 0.03	1.30 ± 0.18	-0.29 ± 0.01	-0.66 ± 0.02	HII	-3.60 ± 0.04	-0.07 ± -0.01
NGC1068	0.96 ± 0.09	1.10 ± 0.14	-0.13 ± 0.01	0.32 ± 0.01	AGN	-2.78 ± 0.02	-0.24 ± -0.03
NGC1204	0.62 ± 0.05	1.54 ± 0.08	-0.15 ± 0.01	-0.27 ± 0.02	Comp	-3.81 ± 0.02	-0.05 ± -0.01
NGC1222	1.25 ± 0.08	0.24 ± 0.06	-0.80 ± 0.01	0.40 ± 0.01	HII	-2.93 ± 0.01	-0.68 ± -0.07
NGC1819	0.81 ± 0.05	1.77 ± 0.08	-0.29 ± 0.01	-0.60 ± 0.01	HII	-3.47 ± 0.03	0.06 ± 0.01
NGC253	0.70 ± 0.04	1.28 ± 0.05	-0.21 ± 0.01	-0.41 ± 0.01	Comp	-3.35 ± 0.03	-0.11 ± -0.01
NGC3110	0.58 ± 0.04	1.52 ± 0.13	-0.40 ± 0.00	-0.52 ± 0.01	HII	-3.60 ± 0.03	-0.03 ± -0.00
NGC3508	0.68 ± 0.05	1.59 ± 0.13	-0.47 ± 0.01	-0.29 ± 0.01	HII	-3.49 ± 0.02	-0.03 ± -0.00
NGC4433	1.14 ± 0.07	2.04 ± 0.16	-0.45 ± 0.01	-0.30 ± 0.01	HII	-3.58 ± 0.02	0.18 ± 0.02
NGC4575	0.57 ± 0.04	1.79 ± 0.13	-0.45 ± 0.01	-0.56 ± 0.01	HII	-3.58 ± 0.02	0.07 ± 0.01
NGC470	0.39 ± 0.04	0.84 ± 0.17	-0.39 ± 0.01	-0.84 ± 0.02	HII	-3.51 ± 0.08	-0.38 ± -0.04
NGC520	0.27 ± 0.03	0.26 ± 0.04	-0.28 ± 0.02	-0.24 ± 0.02	Comp	-3.54 ± 0.02	-0.65 ± -0.07
NGC6000	0.62 ± 0.04	1.67 ± 0.11	-0.24 ± 0.01	-0.78 ± 0.01	HII	-3.53 ± 0.04	0.01 ± 0.00
NGC6835	0.57 ± 0.06	1.31 ± 0.21	-0.42 ± 0.01	-0.49 ± 0.01	HII	-3.47 ± 0.03	-0.07 ± -0.01
NGC7714	0.76 ± 0.07	0.66 ± 0.13	-0.60 ± 0.01	0.29 ± 0.00	HII	-3.03 ± 0.30	-0.44 ± -0.05
NGC7715	0.38 ± 0.06	0.73 ± 0.14	-	-		-	-0.39 ± -0.04
NGC7714C	1.40 ± 0.13	1.07 ± 0.13	-0.40 ± 0.01	0.02 ± 0.01	Comp	0.00 ± 0.00	-0.17 ± -0.02

4.6 Metallicity

sec:met)

Since the STARLIGHT fitting was performed on a base which has multiple metallicities, it means that the stellar metallicity of a galaxy can be calculated a posteriori from the output stellar population vector, similarly to age. The only difference in this case is that metallicity does not have a high dynamic range of values, and therefore does not necessarily require the use of logarithm to get a mean value. Following Asari et al. (2007), the calculated average is given by,

$$\langle \mathrm{Z} \rangle_m = \sum_{j=1}^{N} \mu_j Z_j, \tag{4.5}$$

where the subscript m is for the mass weighted value that is calculated. μ is the mass fraction vector recovered and Z_j is the metallicity of each of the SSP in the base. Calculation of metallicities in literature can also differ and since some authors (González Delgado et al., 2014; López Fernández et al., 2016) use the log of metallicities. This is also calculated in our case, using the following equation,

$$\langle \log \mathrm{Z} \rangle_m = \sum_{j=1}^{N} \mu_j \log Z_j. \tag{4.6}$$

For obvious arithmetic reasons $\log(\langle \mathrm{Z} \rangle_m) \neq \langle \log Z \rangle_m$. Using the two definitions just laid out, the metallicities are derived for the integrated spectra of the SUNBIRD sub-sample. The distributions of mean metallicity is shown in Figure 4.12.

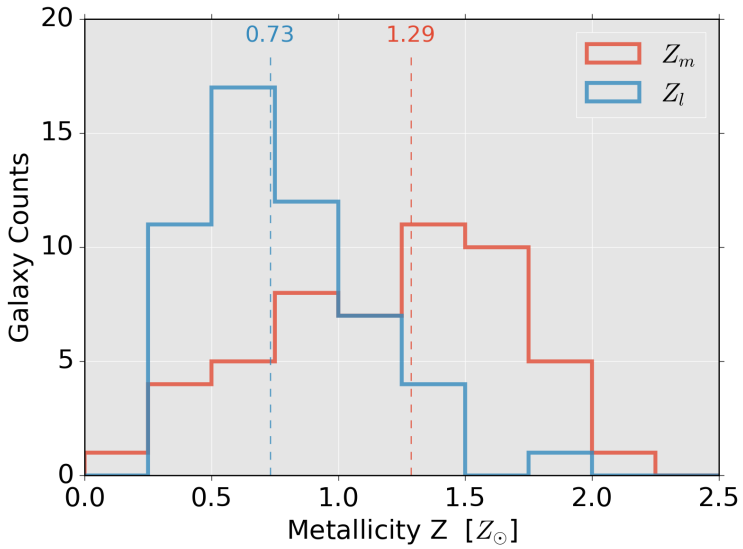

Figure 4.12: Distribution of the different metallicity means: Blue represents light weighted while Red denotes the mass weighted mean metallicities. Vertical dashed lines shows the median value of each distribution.

Both the light weighted (Blue) and mass weighted (Red) metallicities are given for comparison.

Most studies report only light weighted metallicities, but stellar population fitting allows to also derive the mass weighted metallicity by assuming an IMF. An expected discrepancy is hence expected to arise between the two quoted values. But in the case of the current sample this also allows some physical interpretation as to the overall history of the LIRGs. The higher than solar median value (1.29 $Z_{\odot}$) of the mass weighted metallicity once again points to an old evolved underlying stellar population which is expected to have a slightly enriched gas. On the other hand, the light weighted value (0.73 $Z_{\odot}$) being biased towards younger stellar populations, is sub solar. This indicates that the younger stars being born are in general from a pristine hydrogen gas which has not yet been enriched by previous episodes of star formation. If the current star formation made use of the same recycled gas as that of the evolved population, the light weighted metallicity content would have, at the minimum been the same or higher than the mass weighted value. One logical explanation hence, is the presence of gas inflows which would reduce the overall metallicity content of the galaxy as well as trigger the birth of a new generation of low metallicity stars.

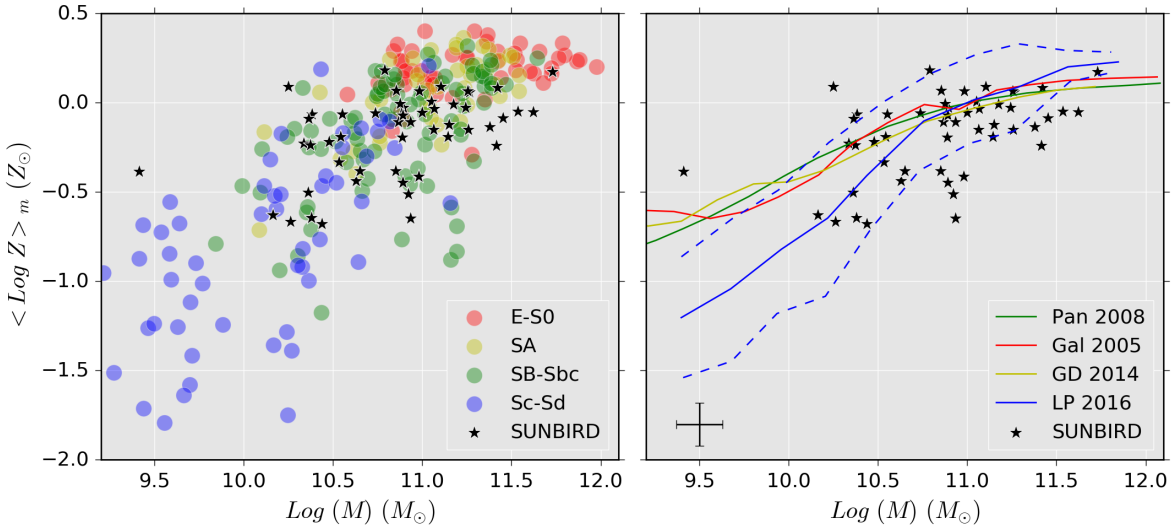

Figure 4.13: *Left Panel*: The Stellar Mass-Metallicity relation of the SUNBIRD sub-sample as compared to the CALIFA galaxies (López Fernández et al., 2016). Coloured round symbols are for the different Hubble type galaxies in the CALIFA sample while the black diamonds represent the SUNBIRD galaxies. *Right Panel*: The same Stellar MZ relation in relation to other previous work done on SDSS galaxies; in red the line from Gallazzi et al. (2005) and in green the line of Panter et al. (2008); and on the CALIFA galaxies in yellow the line derived by González Delgado et al. (2014) and in blue the trend from López Fernández et al. (2016) using simultaneous spectroscopic and photometric fitting. The error-bar at coordinate [9.5, −1.8] is representative of the size of the uncertainty on the different data points of our galaxies for both panels.

The mass-stellar metallicity relation of the sample is analysed by comparing the obtained values of $\langle \log Z \rangle_m$ to values obtained by previous studies. To be consistent we make use of the work of López Fernández et al. (2016) and González Delgado et al. (2014) which uses the same metallicity definition after applying stellar population fitting to the CALIFA sample. The results are plotted in Figure 4.13 where the left panel shows the latest work by López Fernández et al. (2016), who uses a combination of spectroscopic data and UV photometric values for the fit. This allowed them to recalibrate the relation that was derived by González Delgado et al. (2014). SUNBIRD galaxies in general correspond to the regions occupied by SA-SBc galaxies. This picture is totally consistent when the mass of galaxies is considered - SUNBIRD galaxies being a relatively massive group were unlikely to be the extreme Late-type galaxies which are known to be smaller and less massive; at the same time, since they are still actively forming stars, it is improbable that they would fall with the Ellipticals or even Lenticulars. The right panel of Figure 4.13 shows SUNBIRD as compared to the mass-metallicity trend from the CALIFA sample and the SDSS sample. Metallicities derived using spectroscopic data only (Gallazzi et al., 2005; Panter et al., 2008; González Delgado et al., 2014), usually have flatter gradients than the newer work of López Fernández et al. (2016), which shows that the lower mass tail has lower metallicities than previously estimated. We note, however, that the region where the bulk of our sample is found on the diagram, has very little difference between the purely spectroscopic studies and the updated work of López Fernández et al. (2016) which uses UV photometry, hence, our results should be robust.

4.7 Fitting Emission Lines

From this section onwards, we analyse the emission line properties of the galaxies in the sample. To be able to study emission lines free from contamination, we subtract from the observed spectrum with the derived stellar continuum result of STARLIGHT. In principle this step should yield a pure emission line spectrum, but in practice, there are regions where SSP modelling does not match the observed data due to flux calibration issues or problems in the templates used. Hence we mask the emission lines, and then perform a fifth-order polynomial fitting in different windows across the spectra. The polynomial result is then subtracted from the residual continuum to produce a spectrum with an almost zero-level continuum.

The resulting pure emission spectrum can then be fitted with Gaussian profiles at locations where emission lines are expected. A multi-component Gaussian fitting is performed simultaneously on all lines, allowing the mean wavelength and amplitude of each line to be free parameters. All the lines were constrained to have the same standard deviation i.e. width of the line, which meant that lines with higher signal-to-noise like $H\alpha, H\beta$ usually dominated the determination

of the line width. Some constraints were added during the fitting with respect to the allowed positions of the different lines and the maximum width allowed. The Python routine used for the minimisation, used Levenberg-Marquardt least squares fitting to reduce the χ^2. The program then outputs the different derived parameters along with their estimated uncertainties.

Using the methodology described above, we measured the following lines: [OII] $\lambda\lambda 3726, 3729$ (blended), [NeIII] $\lambda 3868$, Hγ $\lambda 4340$, [OIII] $\lambda 4363$, Hβ $\lambda 4861$, [OIII] $\lambda\lambda 4959, 5007$, [OI][NII] $\lambda 6300$, $\lambda 6548$, Hα $\lambda 6563$, [NII] $\lambda 6584$. The fluxes of the Balmer lines are then used to calculate the extinction, after which all the emission line fluxes are then corrected for the derived extinction (see section 3.9). This entire procedure was carried out on our data sample and the measured fluxes are given in Tables C.2 and C.3 in the appendices. All the emission lines (except [OIII] (4363 $\AA$) which was present in only four cases) were present in 36 targets while the rest of the targets either did not present all those lines or the lines could not be measured due to limited wavelength range of the data in some cases. Simultaneous fitting was able to take care of cases of line blending between Hα $\lambda 6563$ and the two [NII] $\lambda 6548, 6584$ lines. In the current case, our main focus is measuring line fluxes, hence measuring line intensities to an accuracy of 5-10% is still reasonable. On the other hand, in future works concerning kinematics of our sample, implementing more sophisticated line de-blending methods will be a requirement. The only target where lines were heavily blended was IRAS19254-7245 which will be excluded from the integrated analysis from here on.

4.8 Specific Star Formation Rate (sSFR)

The equivalent width of the Hα (EW(Hα))line is directly related to the specific star formation rate of a galaxy. The code using the same principle as described above is used for measuring the equivalent width of the Hα line. In this case the code fits a triple Gaussian profile to the two [NII] lines and the Hα line. The local continuum is also fitted during the process. A standard procedure for the measurement of equivalent width was applied - the flux of Hα was measured for the line, then two separate windows with a width of 30 $\AA$ each, are chosen on both sides of the line to sample the continuum. The two windows were at 100 $\AA$ from the central position of the Hα line. Since our data often ends soon after the [NII] (6583 $\AA$) line, sometimes the red side of the continuum was not available for measurement. Since during the fitting we also fit for the continuum, in cases where the red continuum window was not available, an average between the blue and the fitted continuum is calculated. This average is then used to calculate the equivalent width.

Sánchez et al. (2013) derived an empirical relation between EW(Hα) and sSFR from the CALIFA DRI sample containing 150 local galaxies making use of data from 3000 individual HII regions. The redshift range covered by the CALIFA survey is similar to the SUNBIRD survey and it is therefore acceptable to apply this model to our data. The linear function used to convert values of EW(Hα) to the values of sSFR for the entire sample is shown below. The sSFR values for each target were given in Table 4.1 and is plotted in Figure 4.14.

$$\log\left(\mathrm{sSFR}/yr\right) = -11.38_{\pm 0.01} + (1.23_{\pm 0.02} \times \log\left[EW(H\alpha)/\mathring{A}\right]). \tag{4.7}$$

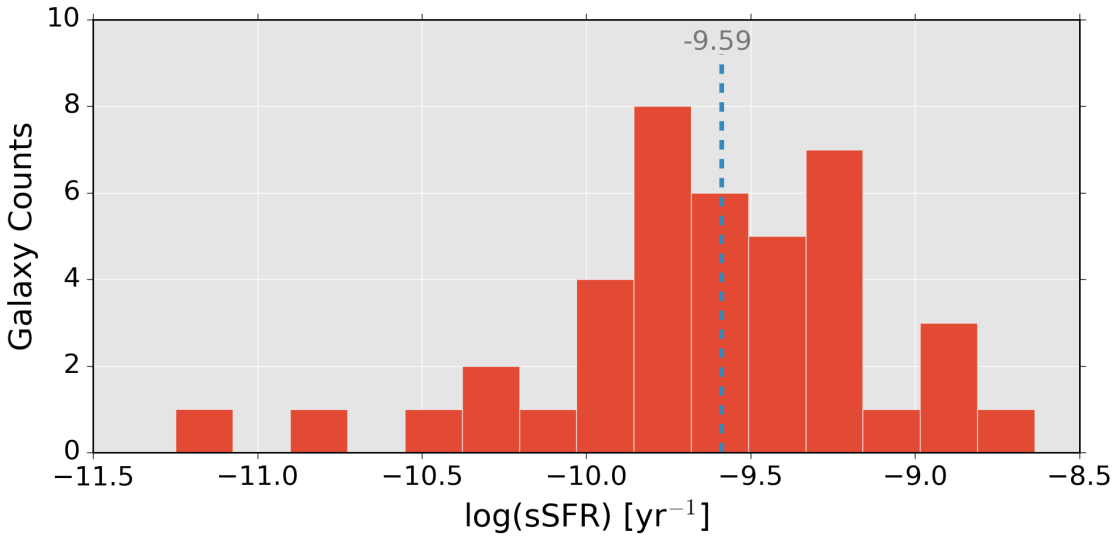

Figure 4.14: The distribution of log(sSFR) for the SUNBIRD sub-sample with the dashed line representing the median value of log(sSFR) = -9.59 corresponding to sSFR = 2.60×10^{-10} yr^{-1} for the sSFR of the sample.

The derived median of sSFR for the sample was 2.60×10^{-10} yr^{-1} corresponding to a mass-doubling time-scale of 3.9 Gyr, showing high star formation activity. In comparison, Barrera-Ballesteros et al. (2015) found a central sSFR of 2.30×10^{-10} yr^{-1} for a SF sub sample from the CALIFA survey. They also quote a value of 9.30×10^{-11} yr^{-1} for a control sample in their study. In their study both the SF sample and the control sample consisted of > 30 galaxies. The aperture where Barrera-Ballesteros et al. (2015) measured the EW values was defined $0.3R_{eff}$, the effective radius, which translated to $0.6-3$ kpc in real scale i.e. the aperture gives a central value for EW. Barrera-Ballesteros et al. (2015) also measured sSFR for extended apertures (2.5 R_{eff}) and found median values of 1.07 and 1.18 for the EW(Hα) which translate to $\sim 8.7 \times 10^{-11}$ yr^{-1} and $\sim 1.2 \times 10^{-10}$ yr^{-1} for SF and the control sample respectively.

What is evident is that the sSFR of LIRGs in the local universe is at least higher by a factor of $\sim 2 - 2.5$ than it is for the normal main sequence galaxies in the extended apertures. Since the apertures used in this case are integrated, our sSFR are being observed and averaged on an extended scale. The main caveat is that our observations are for the limited size of aperture that long-slit spectroscopy offers. Only the nucleus of centrally active SF galaxies have comparable sSFR as the LIRGs in the SUNBIRD sub-sample. We also note a similar large scatter in the EW(Hα) and hence sSFR, as Barrera-Ballesteros et al. (2015), with a standard deviation of 0.40 log($\AA$) for a median EW(Hα) of 1.46 log($\AA$).

Comparing this result to the Great Observatories All-sky LIRG Survey (GOALS) sample (Armus et al., 2009), the calculated median sSFR was found to be 3.90×10^{-10} yr^{-1} (Howell et al., 2010). In the case of the latter's work, which also samples the local universe, their sample contains more ULIRGs and extreme LIRGs than in our case. Other work from the literature, from the AKARI Deep Field South (ADF-S) where the measured sSFR for a ULIRGs and LIRGs sample was found to be 1.05×10^{-9} yr^{-1} and 3.31×10^{-10} yr^{-1} respectively (Małek et al., 2017). Part of the reason why SUNBIRD will be lower than the latter's work is the fact that $\sim 40\%$ of our sample is just below the LIRG lower IR limit. Also methodology of how the sSFR value is calculated will also account for some discrepancy. Another sample that is very similar to the SUNBIRD sub-sample is that from Pereira-Santaella et al. (2015) which studied local starburst and LIRGs in similar luminosity range as our sample and in similar distance range. Their measured median sSFR was found to be 2.51×10^{-10} yr^{-1} which is very similar to that of our sample within uncertainty limits.

To ensure the robustness of the result, further comparison with literature is done with our derived sSFR. In Figure 4.15, in the left panel, the sSFR is plotted against the masses of the galaxies given in Table 2.1 in Chapter 2. We overplot the results of Fumagalli et al. (2012), who studied the evolution of sSFR in the redshift range of $0 - 2.2$, for three different mass bins for SF galaxies with the 3D-HST data. The sSFR of the SUNBIRD sub-sample is observed to be an order of magnitude higher than that of other local SF galaxies. The plotted dashed line is is indicative of how in every mass bins across the diagram the SUNBIRD sub-sample is $\sim$ a magnitude higher in terms of sSFR as compared to more standard galaxies.

4.9 Extinction

The extinction for each galaxy was determined using the method described in Chapter 3 - in brief, a Calzetti law was applied and the prescription of Osterbrock (1989) for Balmer line ratios, in Case B recombination was followed. A Monte Carlo method was implemented to propagate

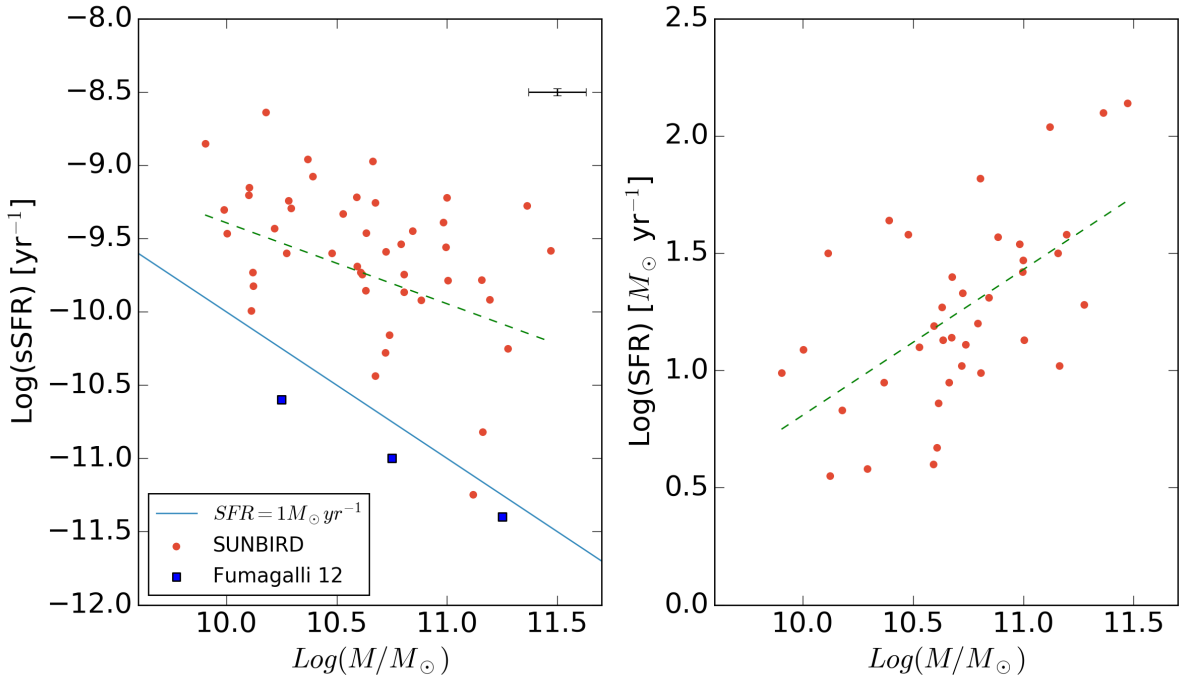

Figure 4.15: *Left Panel*: Log(sSFR) as a function of Log(Mass) with the red circles representing the SUNBIRD sub-sample. The blue squares are data points of other local SF galaxies (Fumagalli et al., 2012). The green dashed line is the weighted best-fit line of our sample indicating the decreasing sSFR with increasing mass of galaxies. The black error-bar is an indication of the uncertainty of each data point. The blue line is the locus of galaxies with SFR of $1 M_\odot yr^{-1}$. *Right Panel*: The evolution of SFR with stellar mass. The dashed green line is the best-fit of the points. The SFR is derived from IR luminosity taken from Table 2.1

uncertainties of the extinction and any relevant parameters. The reddening-correction was then applied to the line fluxes of each of the measured lines from the integrated spectrum. Table 4.1 shows the value of both the stellar extinction, $A_{\rm v,star}$, determined by STARLIGHT during SSP-fitting, and the extinction of the star forming regions, $A_{\rm v,HII}$. In Figure 4.16 the $A_{\rm v,HII}$ is plotted against $A_{\rm v,star}$ and by performing a least-squares fit to the data the following relation was derived:

$$A_{\rm v,HII} = 2.37\ ^{\pm 0.11} \times A_{\rm v,star}. \tag{4.8}$$

The observed ratio of attenuation is slightly higher than the $2.27\ ^{\pm 0.16}$ measured by Calzetti et al. (2000) for low redshift SF galaxies. The two values are consistent within their uncertainty limits, while the minor offset might be due to the aperture effect in our sample - our long-slit data covering mostly the major axes of galaxies. We also note the small sample size of eight

local galaxies used by Calzetti et al. (2000) calculating of this ratio. SFR being a good tracer for dusty environment, hence high extinction, it is relevant to mention the significant difference between the Calzetti et al. (2000) sample (mean $\sim$ 10.3 $M_{\odot}$ yr^{-1}, median $\sim$ 4.0 $M_{\odot}$ yr^{-1}) and the SUNBIRD sub-sample (mean $\sim$ 22.2 $M_{\odot}$ yr^{-1}, median $\sim$ 14.3 $M_{\odot}$ yr^{-1}) in that respect. This shows that similar trends exists in even more extreme SF environment.

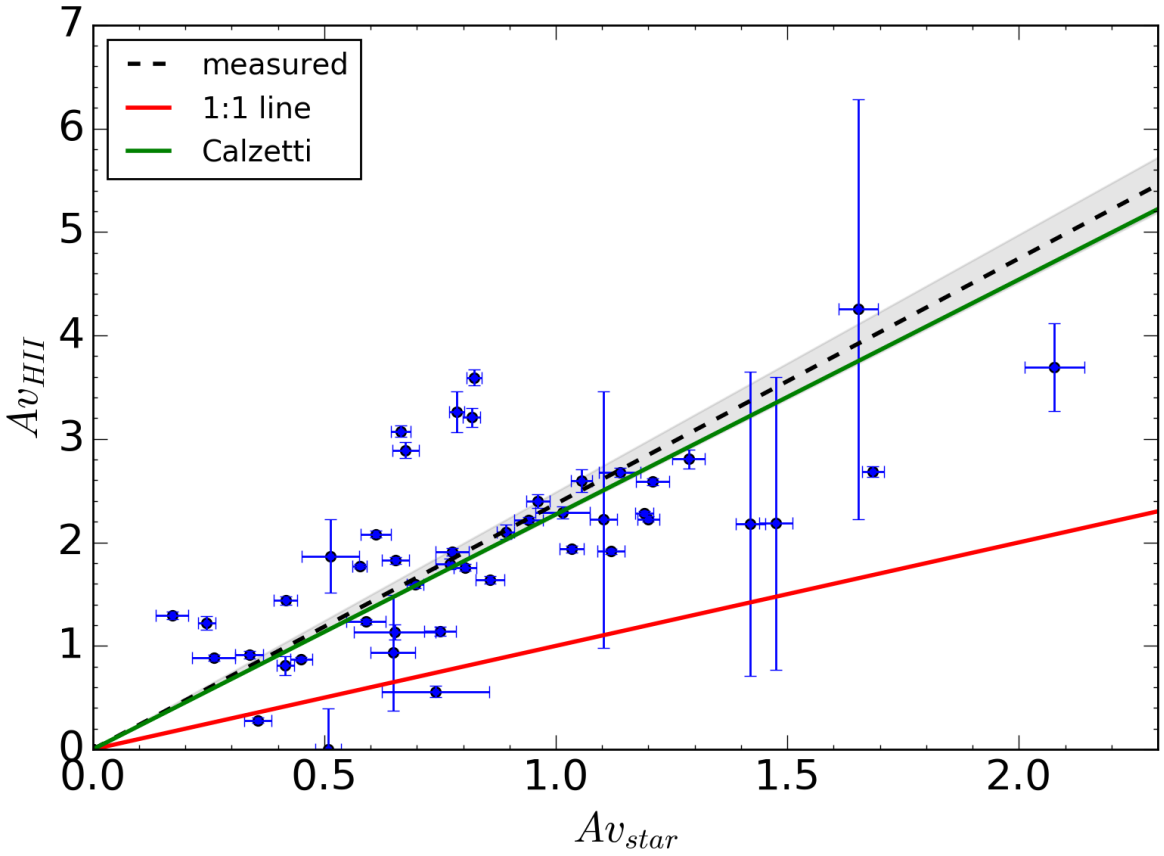

Figure 4.16: $A_{\mathrm{v,HII}}$ plotted as a function of $A_{\mathrm{v,star}}$ for all targets with good quality data. The dashed Dark line is the weighted fit of the data with the Grey region the uncertainty from the derived parameters. The Green line is the line derived by Calzetti et al. (2000) while the Red line represents the line of no extra attenuation that is 1:1 ratio.

The next step was to analyse how the excess attenuation varies with the sSFR similar to the work of Price et al. (2014). Figure 4.17 shows excess attenuation ($A_{\mathrm{v,HII}} - A_{\mathrm{v,star}}$) and the ratio of attenuation as a function of log(sSFR). The left panel shows the trend of the excess attenuation with sSFR following a derived relation of:

$$A_{\rm v,excess} \equiv A_{\rm v,HII} - A_{\rm v,star} = -9.608\ ^{\pm 2.190} - 1.121\ ^{\pm 0.230}\ \log\left({\rm sSFR/yr}\right). \tag{4.9}$$

This is similar and within the uncertainty limits of the derived equation of $A_{\rm v,excess} = -10.93^{+8.72}_{-8.26} - 1.25^{+0.87}_{-0.91}$ Log(SSFR) in Price et al. (2014) for a sample of star forming galaxies in a redshift range of $1.36 < z < 1.5$. The right panel of Figure 4.17 shows the relation of the ratio of extinction to the specific SFR. The derived equation in this case also uses weighted least square fit and is:

$$\frac{A_{\rm v,HII}}{A_{\rm v,star}} = -12.092\ ^{\pm 3.359} - 1.493\ ^{\pm 0.353}\ \log\left({\rm sSFR/yr}\right). \tag{4.10}$$

In both cases, the general trend is a decreasing excess or ratio of extinction as the sSFR goes up. The large scatter in the data is expected since we are plotting different galaxies which has big differences in the extinctions of their HII regions. In the cases of unresolved large sample of data, stacking spectra in bins of sSFR or SFR is usually done to mitigate the scatter in the data. In our case, there is no need to resort to such scheme since best-fit lines should be sufficient to provide general trends in the data. It has been suggested in numerous papers that this trend fits a two component dust model (Calzetti et al., 1994; Wild et al., 2011; Price et al., 2014). In this model, there is a diffuse (but possibly clumpy) ISM dust which affects the entire galaxy, but in regions of SF activity another short lived component exist as well. This would explain why $A_{\rm v,star}$ is constant across all values of sSFR while there is a clear negative gradient in the values of $A_{\rm v,HII}$) as the sSFR increases. This trend is then translated to both the $A_{\rm v,excess}$ and the ratio of extinction to negative trends as a function of log(sSFR).

4.10 Ionisation

In Chapter 3 section 3.11, the main idea behind the BPT diagram was introduced and explained. After the different line fluxes were measured and corrected for the intrinsic extinction of the galaxies, line ratios were then calculated where available. In the case here, since our wavelength coverage stops around 6600 $\mathring{A}$ in rest wavelength, the Sulphur lines were outside of reach with the PG0900 grating observations. The only two line ratios that are hence relevant are: [NII]/Hα and [OIII]/Hβ. In Figure 4.18, the line ratios are plotted in a BPT diagram to be able to know the different mechanism at play for the integrated flux of the SUNBIRD sub-sample. The data are given in Table 4.2 along with the classification derived from the BPT diagram. As expected, the bulk of the sample lies in the HII dominated region, while quite a few targets are found in the

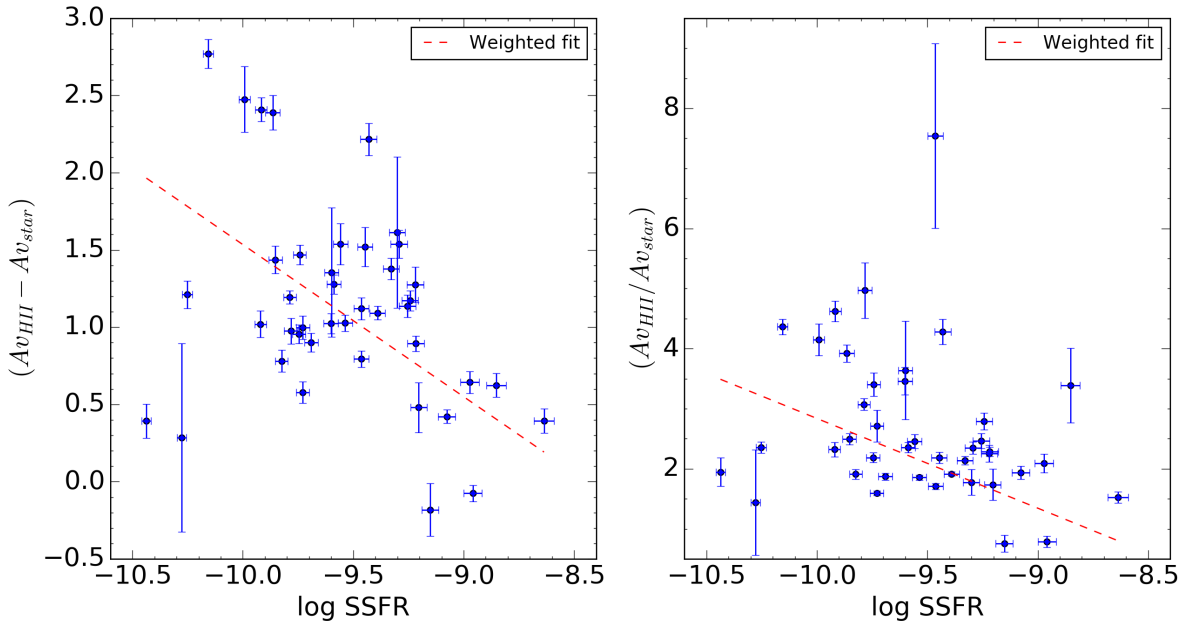

Figure 4.17: *Left Panel*: Extra attenuation as a function of sSFR. *Right Panel* : Extinction Ratio plotted against sSFR. In both cases the red dashed line represents the weighted best-fit line.

composite region which is the area enclosed by the lines of Kewley et al. (2001) and Kauffmann et al. (2003b). Composite galaxies in this case could be either those which have AGN activities or shock regions where gas is colliding. Lastly, two galaxies, namely NGC1068 and IRAS18293-3413, are shown to display AGN activities. Of these, the former is a well known AGN. The latter characterisation is unexpected, and in the spatially resolved study of the targets later on, we will investigate where the apparent AGN signal comes from. The work from Cid Fernandes et al. (2010) allows to further classify the type of AGN of the two objects to LINER and Seyfert activity respectively.

4.11 Oxygen Abundances

Oxygen abundance is known to be a good proxy for the overall metallicity content of HII regions of galaxies as oxygen constitute around 50% of the mass of heavier elements than helium. Studies of abundances for galaxies are crucial as they allow for good constraints on their chemical evolution. This in turn allows astrophysicists to create a more accurate picture of galaxy evolution from the Big Bang to the present day. Studies of integrated oxygen abundances are numerous (Kobulnicky & Zaritsky, 1999; Moustakas et al., 2006) and are usually comparable to measurements done at higher redshifts where spatially resolved HII areas are inaccessible.

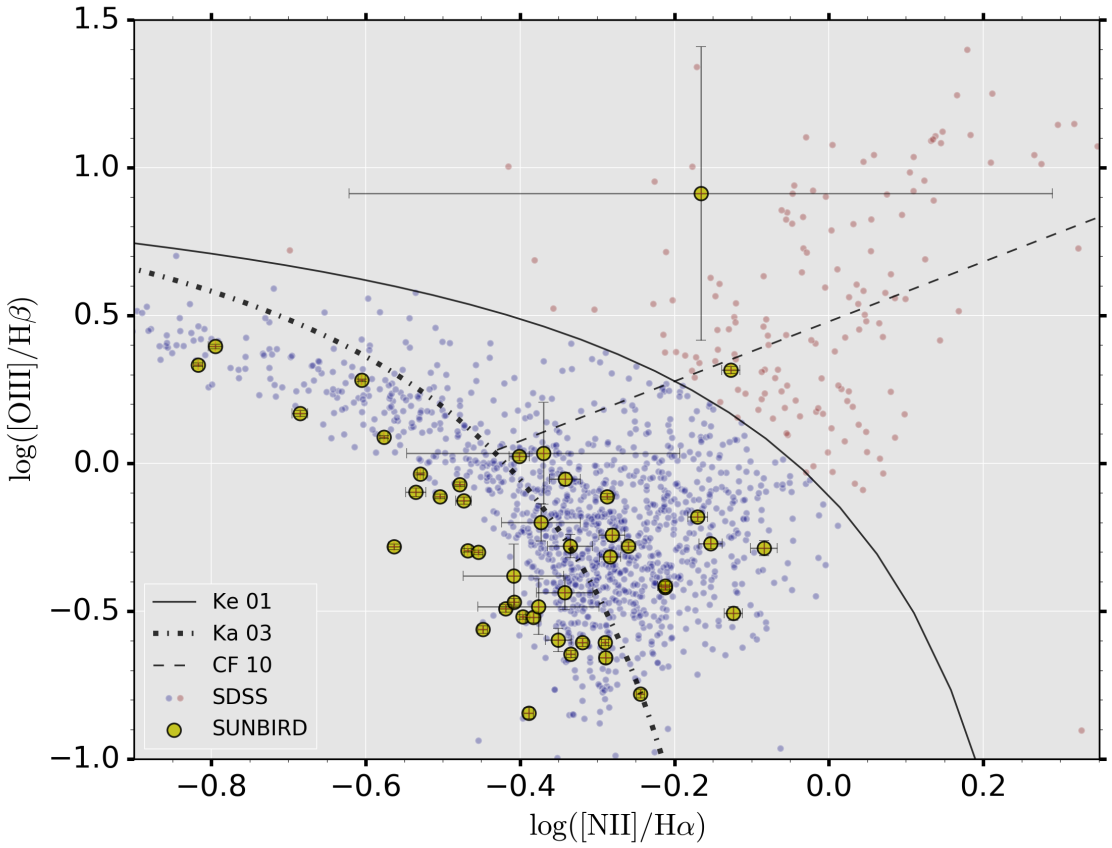

Figure 4.18: BPT diagram of 44 galaxies from the SUNBIRD sub-sample. Yellow points are the SUNBIRD data while red and blue coloured points are the SDSS sample. Demarcation lines for the different regimes calculated by Kewley et al. (2001); Kauffmann et al. (2003b); Cid Fernandes et al. (2010) are shown in the different labelled line-styles.

As presented in section 3.10, there are several abundance diagnostics with each having different systematics. To circumvent this issue, our approach is to use the work and calibration of Kewley & Ellison (2008, Ke08) to derive abundances using different diagnostics. Ke08 derived a polynomial of the form of Equation 3.34 to relate each calibration to one another. Our choice is to use the O3N2 as the base calibrator, meaning that all measured abundances will be converted to the base value through the use of polynomial equation of Ke08. The list of coefficients used for the conversion is shown in Table 4.3.

Table 4.3: Polynomial coefficients to convert different calibrators to O3N2 calibrator.

Calibrator	**Coefficients**				**Range**
	a	**b**	**c**	**d**	
Z94	52.2389	-18.67559	2.447698	-0.1011578	8.40 – 9.30
M91	-65.0991	15.74995	-0.837514	0	8.50 – 9.10
N2 (PP04)	-8.0069	2.74353	-0.093680	0	8.05 – 8.80
D02	664.8453	-225.75330	25.768880	-0.9761368	8.05 – 8.90

While converting to the new O3N2 base, limits of the range of validity of the polynomials as per Ke08 are applied - values outside the different ranges are void. Once all calibrators are converted to the O3N2 base, then a mean metallicity is derived by using four of the converted calibrators along with the measured O3N2 abundance. The standard deviation of the different values is then used as the uncertainty of the mean. One of the caveats of this method is that not all galaxies have all of the five O3N2 values (four converted and one measured), therefore the standard deviation can be based on too small a sample size. In cases where only one calibrator was available, the mean is the converted value while the uncertainty is propagated from the measurement. The different oxygen abundances measurement (measured and converted) are shown in Table 4.4. The table also list values for R_{23} and O_{32} indices.

Table 4.4: Table showing values related to the oxygen abundances measured. Columns 2 & 3 are the R_{23} and O_{32} ratios. Columns 4: PT05 calibrator, which does not have direct conversion to other bases. Column 5-9: the measured values of the Z94, M91, D02, N2 and O3N2 calibrators respectively. Columns 10-13: The conversion values of columns 5 - 8 to O3N2 base respectively. Column 14 is the average oxygen abundance values of columns 9-13. The different uncertainties of columns that are not displayed explicitly are generally $0.1-0.2$ dex (see Chapter 3 to get the exact uncertainty of each calibrator)

Name	**Original Measurement**								**PP04 O3N2 Base**				⟨**O3N2**⟩
	R_{23}	**O_{32}**	**PT05**	**Z94**	**M91**	**D02**	**N2**	**O3N2**	**Z94**	**M91**	**D02**	**N2**	
(1)	(2)	(3)	(4)	(5)	(6)	(7)	(8)	(9)	(10)	(11)	(12)	(13)	(14)
CGCG049-057	-	-	-	-	-	8.87	8.81	8.76	-	-	8.62	8.76	8.689 ± 0.071
ESO154-G010	-	-	-	-	-	9.00	9.06	8.73	-	-	8.74	-	8.735 ± 0.002
ESO221-IG008	6.35 ± 0.13	0.82 ± 0.03	8.22 ± 0.11	8.62	8.57	8.52	8.38	8.36	8.34	8.36	8.29	8.40	8.352 ± 0.036
ESO221-IG010	1.85 ± 0.32	0.21 ± 0.04	8.42 ± 0.36	9.16	8.98	8.89	8.84	8.82	8.80	8.80	8.64	-	8.762 ± 0.074
ESO264-G036	2.50 ± 0.30	0.19 ± 0.03	8.32 ± 0.25	9.08	8.90	8.84	8.76	8.77	8.74	8.74	8.59	8.84	8.736 ± 0.082
ESO264-G057	1.98 ± 1.21	0.20 ± 0.15	8.40 ± 1.25	9.14	8.96	8.86	8.80	8.81	8.79	8.79	8.61	8.88	8.775 ± 0.089
ESO267-G030	2.70 ± 2.11	0.77 ± 1.05	8.58 ± 3.87	9.06	8.90	8.87	8.81	8.64	8.72	8.74	8.62	-	8.679 ± 0.051
ESO319-G022	2.27 ± 0.26	0.20 ± 0.03	8.36 ± 0.26	9.11	8.93	9.03	9.14	8.85	8.76	8.76	8.77	-	8.785 ± 0.039
ESO320-G030	1.94 ± 0.26	0.19 ± 0.03	8.39 ± 0.26	9.15	8.97	8.88	8.82	8.83	8.79	8.79	8.62	-	8.758 ± 0.079
ESO428-G023	1.93 ± 1.80	0.38 ± 0.49	8.53 ± 3.08	9.15	8.97	8.97	8.99	8.80	8.79	8.79	8.71	-	8.772 ± 0.036
ESO440-IG058-N	3.39 ± 0.31	0.44 ± 0.06	8.39 ± 0.33	8.98	8.82	-	-	-	8.66	8.67	-	-	8.663 ± 0.004
ESO440-IG058-S	-	-	-	-	-	-	-	-	-	-	-	-	-
ESO491-G020	3.65 ± 0.28	0.37 ± 0.04	8.32 ± 0.25	8.95	8.79	8.75	8.63	8.60	8.63	8.64	8.50	8.69	8.613 ± 0.062
ESO550-IG025-N	3.75 ± 0.91	0.15 ± 0.04	8.11 ± 0.39	8.93	8.76	-	-	-	8.62	8.60	-	-	8.612 ± 0.011
ESO550-IG025-S	8.03 ± 2.08	0.16 ± 0.05	7.61 ± 0.46	8.42	8.31	-	-	-	8.14	-	-	-	8.142 ± 0.261
IC2522	2.75 ± 0.07	0.21 ± 0.01	8.30 ± 0.08	9.05	8.88	8.82	8.73	8.75	8.72	8.72	8.57	8.81	8.712 ± 0.077
IC2522B	3.12 ± 0.30	0.27 ± 0.03	8.31 ± 0.25	9.01	8.84	8.71	8.57	8.64	8.68	8.68	8.46	8.62	8.618 ± 0.083
IRAS06164+0311	-	-	-	-	-	8.85	8.78	8.60	-	-	8.60	8.85	8.684 ± 0.120
IRAS12116-5615	-	-	-	-	-	-	-	-	-	-	-	-	-
IRAS13052-5711	3.27 ± 0.27	0.25 ± 0.03	8.28 ± 0.21	8.99	8.82	8.93	8.92	8.74	8.67	8.67	8.68	-	8.688 ± 0.028
IRAS17578-0400	-	-	-	-	-	8.82	8.73	8.72	-	-	8.57	8.80	8.698 ± 0.097
IRAS17578-0400-W	5.68 ± 1.75	0.52 ± 0.24	8.17 ± 1.17	8.70	8.61	8.62	8.47	8.46	8.42	8.42	8.37	8.51	8.434 ± 0.045
IRAS17578-0400-E	3.33 ± 2.93	0.49 ± 0.65	8.42 ± 3.36	8.98	8.83	8.73	8.60	8.59	8.67	8.68	8.48	8.65	8.612 ± 0.073
IRAS18293-3413	-	0.40 ± 0.76	-	3.16	5.42	9.00	9.07	8.38	-	-	8.74	-	8.562 ± 0.178
IRAS18293-3413B	2.50 ± 0.86	0.32 ± 0.26	8.38 ± 1.60	9.08	8.90	8.85	8.77	8.76	8.74	8.74	8.59	8.85	8.738 ± 0.082

Table 4.4 – continued from previous page

Name	Original Measurement								PP04 O3N2 Base				⟨O3N2⟩
	R_{23}	O_{32}	PT05	Z94	M91	D02	N2	O3N2	Z94	M91	D02	N2	
(1)	(2)	(3)	(4)	(5)	(6)	(7)	(8)	(9)	(10)	(11)	(12)	(13)	(14)
IRAS19115-2124	-	-	-	-	-	8.85	8.77	8.67	-	-	8.60	8.85	8.707 ± 0.106
IRAS19254-7245	-	-	-	-	-	-	-	-	-	-	-	-	-
IRASF01364-1042	7.90 ± 0.82	0.30 ± 0.04	7.79 ± 0.31	8.44	8.37	-	-	-	8.16	-	-	-	8.158 ± 0.135
IRASF06076-2139-N	4.82 ± 0.59	0.18 ± 0.03	8.01 ± 0.24	8.81	8.65	9.06	9.21	8.79	8.51	8.47	8.79	-	8.642 ± 0.152
IRASF06076-2139-S	3.46 ± 0.22	0.42 ± 0.04	8.37 ± 0.23	8.97	8.82	8.91	8.88	8.67	8.65	8.66	8.66	-	8.660 ± 0.008
IRASF16516-0948	4.28 ± 1.59	0.30 ± 0.15	8.19 ± 1.00	8.87	8.72	8.77	8.66	8.62	8.57	8.56	8.52	8.72	8.599 ± 0.069
MCG-02-01-051	4.83 ± 0.35	0.51 ± 0.06	8.26 ± 0.28	8.81	8.68	8.70	8.56	8.52	8.51	8.52	8.45	8.61	8.521 ± 0.052
MCG-02-01-052	3.47 ± 0.12	0.55 ± 0.03	8.43 ± 0.14	8.97	8.82	8.73	8.60	8.57	8.65	8.66	8.48	8.66	8.606 ± 0.070
MCG-02-33-098-E	4.92 ± 0.37	0.29 ± 0.03	8.11 ± 0.20	8.80	8.65	8.77	8.65	8.60	8.50	8.48	8.52	8.72	8.564 ± 0.087
MCG-02-33-098-W	5.29 ± 0.30	0.13 ± 0.01	7.89 ± 0.10	8.75	8.58	8.91	8.89	8.74	8.46	8.39	8.66	-	8.562 ± 0.144
NGC1022	1.82 ± 0.14	0.19 ± 0.02	8.41 ± 0.18	9.16	8.98	8.91	8.88	8.85	8.80	8.80	8.66	-	8.775 ± 0.072
NGC1068	4.20 ± 0.12	1.99 ± 0.11	8.57 ± 0.27	8.88	8.79	9.03	9.13	8.59	8.58	8.63	8.77	-	8.641 ± 0.074
NGC1204	6.99 ± 0.38	0.10 ± 0.01	7.64 ± 0.09	8.55	8.39	9.01	9.09	8.77	8.27	-	8.75	-	8.594 ± 0.231
NGC1222	-	-	-	-	-	8.54	8.39	8.35	-	-	8.30	8.42	8.357 ± 0.047
NGC1819	1.58 ± 0.15	0.27 ± 0.03	8.51 ± 0.26	9.19	9.01	8.91	8.88	8.83	8.82	8.82	8.66	-	8.781 ± 0.072
NGC253	1.91 ± 0.11	0.39 ± 0.03	8.54 ± 0.22	9.15	8.97	8.96	8.99	8.79	8.79	8.79	8.71	-	8.772 ± 0.036
NGC3110	2.50 ± 0.16	0.19 ± 0.01	8.32 ± 0.13	9.08	8.90	8.83	8.74	8.77	8.74	8.74	8.58	8.82	8.729 ± 0.081
NGC3508	3.35 ± 0.13	0.26 ± 0.01	8.27 ± 0.10	8.98	8.82	8.78	8.66	8.67	8.66	8.66	8.53	8.73	8.650 ± 0.067
NGC4433	4.02 ± 0.22	0.20 ± 0.01	8.13 ± 0.11	8.90	8.74	8.79	8.68	8.68	8.60	8.58	8.54	8.75	8.628 ± 0.076
NGC4575	2.20 ± 0.10	0.20 ± 0.01	8.37 ± 0.11	9.12	8.94	8.79	8.68	8.77	8.77	8.77	8.54	8.75	8.719 ± 0.089
NGC470	0.98 ± 0.17	0.24 ± 0.05	8.57 ± 0.43	9.27	9.07	8.84	8.75	8.88	8.87	8.85	8.58	8.83	8.802 ± 0.110
NGC520	3.77 ± 0.19	0.22 ± 0.02	8.19 ± 0.16	8.93	8.77	8.91	8.89	8.72	8.62	8.61	8.66	-	8.652 ± 0.042
NGC6000	1.25 ± 0.12	0.23 ± 0.03	8.52 ± 0.23	9.23	9.04	8.94	8.94	8.90	8.85	8.84	8.69	-	8.791 ± 0.073
NGC6835	-	-	-	-	-	8.81	8.72	8.75	-	-	8.56	8.79	8.702 ± 0.099
NGC7714	5.89 ± 4.60	1.23 ± 2.13	8.35 ± 4.55	8.68	8.63	8.68	8.54	8.45	8.40	8.44	8.43	8.59	8.460 ± 0.066
NGC7715	-	-	-	-	-	-	-	-	-	-	-	-	-
NGC7714C	-	-	-	-	-	8.83	8.74	8.59	-	-	8.58	8.81	8.661 ± 0.108

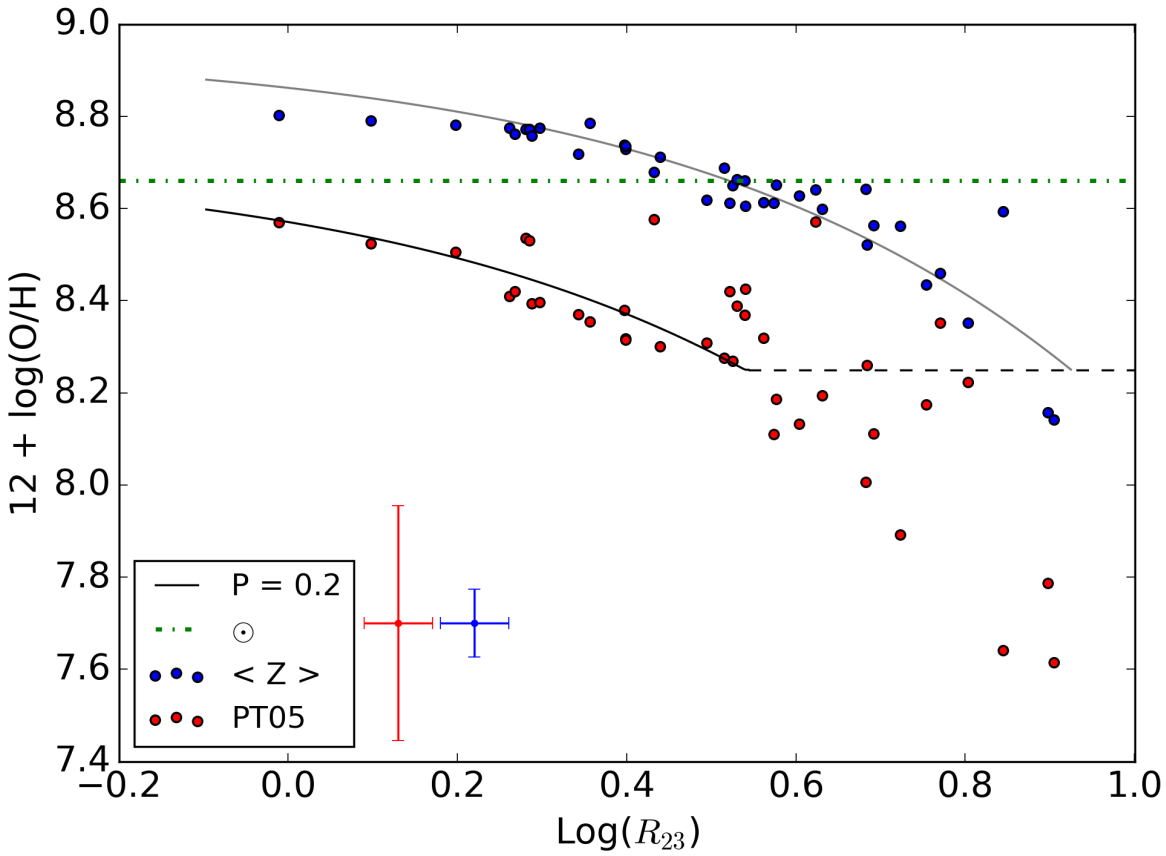

Figure 4.19: Plot of $12+\log(O/H)$ vs $\log(R_{23})$ for the SUNBIRD sub-sample. Two calibrators are shown: PT05 (blue) and mean of O3N2 base (red). The green dotted dashed line depicts solar abundance for O3N2 calibrator. Black dashed curve depicts the locus of value for P, the excitation parameter, when equals to 0.2. The grey curve is for P = 0.7 while the dashed black horizontal line shows the lower limit of the PT05 calibrator. Points at coordinates $[0.13, 7.7]$ and $[0.22, 7.7]$ show the median size of the error-bars of PT05 and O3N2 respectively.

Figure 4.19 shows the relation between $\log(R_{23})$ and $12 + \log(O/H)$ oxygen abundances for galaxies where data were available. Two different calibrators are shown, PT05 (red) and the mean of the O3N2 base (blue). From the typical error-bar sizes of each calibrators, the mean O3N2 shows already a significant improvement as compared to PT05. The plot also shows the loci of excitation parameter P (equation 3.28) at two different values. The parameter is mainly valid for PT05 points but does give a guide for the O3N2 points in terms of scatter. In the case of PT05 there is a greater scatter around a single P value while the distribution of O3N2 points are tighter to a unique value of P. The plot also contains PT05 points in the R_{23} transition region even though this is discarded usually. The aim is just to show a comparison with the values derived for the mean O3N2 value - for which the transition region does not apply, since

some of the calibrator used are not dependent on R_{23}.

4.11.1 Mass Metallicity Relation

The main aim of this section is to explore the Mass-Metallicity (hereafter M-Z) relation in the context of strongly star forming galaxies. Stellar mass is the amount of Hydrogen gas that is locked up in stars, while metallicity is a measure of how much gas has been converted to heavier elements through the stars in a galaxy. Both parameters are therefore expected to be inextricably linked. Therefore an understanding of the M-Z relation and the position of different types of galaxies in such a parameter space is crucial to properly understand chemical evolution. It has been known for the past decade that LIRGs and ULIRGs generally display an under-abundance of metals (Rupke et al., 2008, Hereafter Ru08). Since then, no concentrated effort has been done to cross validate those results. The SUNBIRD sub-sample, consisting of SF galaxies in the nearby universe, offers a good opportunity to investigate the M-Z relation in LIRGs.

Figure 4.20 explores the relationship of gas-phase abundance with the stellar mass of galaxies based on K-band luminosities. The left panel shows the results of converting our R_{23} values to oxygen abundances via the equation (1) in Tremonti et al. (2004, Hereafter T04). Median values of 3 bins containing equal number of points are also shown in yellow. The under abundance of metals is apparent with each of the bins having a $0.15-0.2$ dex difference with the trend of T04. The issue with T04 results is the limits of the aperture of the SDSS fibre which in principal will have different coverage for different galaxy angular sizes. Another problem is that the Bayesian approach of T04 tend to yield results that would overestimate the metallicity by $0.2-0.4$ dex (Sánchez et al., 2012). Ru08 in their analysis, pushed the trend-line of T04 a further 0.1 dex upwards because they focused on nuclear abundances which are expected to be higher than for the entire galaxy. In our case, since the flux was integrated for the entire width of the galaxy, our abundance values are expected to be slightly diluted. Even taking into consideration all these elements along with how much scatter the measured R_{23} index has, it is difficult to properly quantify all the effects stated above. Since Ru08 used T04 as the reference at the time, the plot is given as a guide to give context to both works (Ru08 and this work). In both panels, our masses were converted to the IMFs that were used in literature so as to make a fair comparison.

This is where the right panel of Figure 4.20 provides some more insight. In that case, our comparison is with the M-Z relation derived by Sánchez et al. (2013) using a sample of 150 CALIFA galaxies. This newer and more up-to-date result is based on a general population of local galaxies ($z \sim 0.01-0.03$) for which the O3N2 calibrator was measured in a similar way as ours (emission line flux measurement after stellar population absorption is removed). The main difference is that their measurement is done at the effective radius of the galaxy, which

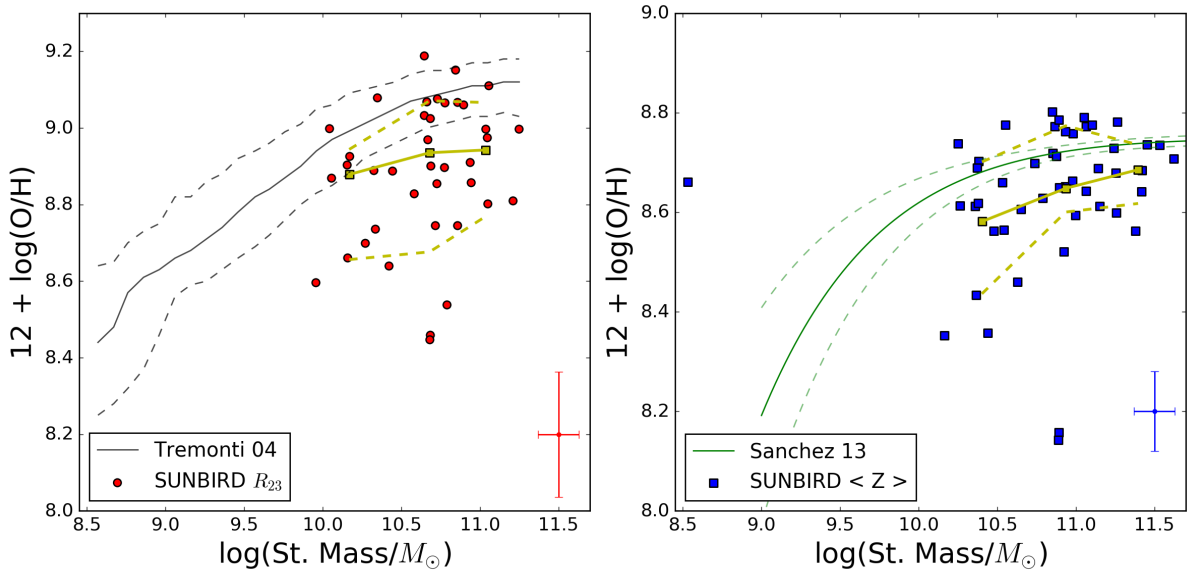

Figure 4.20: *Left Panel*: Mass-Metallicity plot comparing the SUNBIRD sub-sample to the results of Tremonti et al. (2004). The R_{23} index is used to convert our data to the corresponding oxygen abundance calibrator. *Right Panel*: Mass-Metallicity plot comparing the SUNBIRD sub-sample to the results of Sánchez et al. (2013). Here the mean O3N2 calibrator is used. In both plots the dashed lines represents the confidence interval of the relations derived by the two authors and the error-bars in the lower right side of the plots gives an indication of the typical size of the uncertainties. The yellow lines and symbols indicates median mass and metallicity values of SUNBIRD sub-sample for 3 bins with equal number of points with the yellow dashed line showing a 68% confidence interval. Kroupa IMF is used for the left panel to align our data with that of T04 and a Salpeter IMF is assumed in the right panel. The different IMFs is purely to allow for direct comparison with the literature values.

is expected to lower the metallicity. Using the work done on metallicity gradients in Sánchez et al. (2014), it can be estimated that at effective radius, metallicities in the CALIFA sample are 0.10 dex lower than at the very centre. Hence, an average metallicity within the central 1.0× effective radius is only biased by ~ 0.05 dex which is minimal. Similarly as will be shown in the next chapter, our sample has very shallow metallicity gradients. Therefore we do not expect a big changes between the integrated metallicities and the nuclear metallicities overall. Therefore, the comparison between our data and the relation derived by Sánchez et al. (2013) is robust and valid. The results points to the fact that SF and LIRG galaxies are under abundant by ~ 0.1 dex over a mass range of 1 order of magnitude. This is in contradiction to the result of Ru08, for which the deviation of LIRGs and ULIRGS, from the M-Z relation of T04, was found to be much larger $0.3 - 0.4$ dex, respectively.

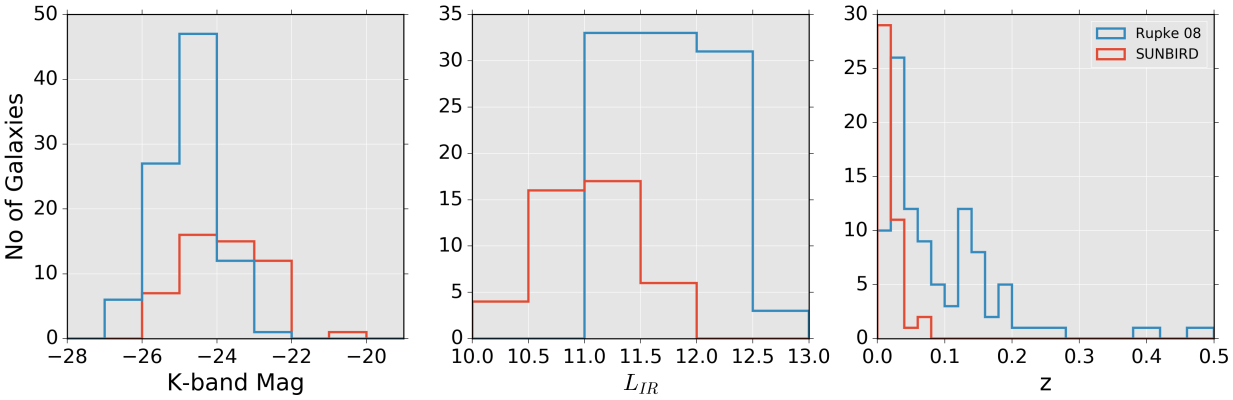

Figure 4.21: A comparison between the sample of Rupke et al. (2008) (blue) and the SUNBIRD sub-sample (red). The 3 panels shows distributions of K-band Magnitude (left panel) which is linked to mass, Infrared Luminosity (middle panel) which is directly linked to SFR and the redshift range (right panel) of the two samples.

We now look at some possible reason why there might be differences between our results and that of Ru08. First consideration is given to the samples themselves. In Figure 4.21, a statistical comparison is made between the two samples. The figure shows distributions of absolute K-band luminosity, which is a proxy for mass, infrared luminosity, which is a proxy for SFR, and finally the redshift range of the two datasets. The main differences lies in the IR luminosity, where Ru08 samples more extreme IR galaxies - mainly LIRGs and ULIRGs. In the case of SUNBIRD half of the galaxies are extremely IR luminous but just fall short of the LIRG definition and the other half are galaxies that are LIRGs. The second difference is the depth of the Ru08 dataset which reaches a redshift of 0.3 and have a couple of targets just below $z = 0.5$. Our galaxies are in the very nearby local universe and for the most part includes with galaxies up to $z = 0.05$. This difference in sampling means that the Ru08 galaxies are less evolved and potentially contains purer hydrogen gas as compared the SUNBIRD sub-sample, since between the typical redshift of the two samples ($z \sim 0.13$ for Ru08 and $z \sim 0.02$ for SUNBIRD) there is around 1.3 Gyr that. For galaxies of the same mass Pilyugin et al. (2013) has shown that at around $z \sim 0.3$, oxygen abundances would decrease on an average by ~ 0.1 dex as compared to targets at $z \sim 0$. Secondly, Pilyugin et al. (2013) shows that oxygen abundances also negatively correlates with sSFR (observed in our sample as well). Since the mass range of Ku08 highly overlaps our sample, while their SFR is higher due to the high IR luminosity, this will automatically point to their sample having an overall higher sSFR than ours. This would in turn probably be a factor that could contribute to a lower the observed abundance. These two main factors in principal should be the main reason of the discrepancy observed in the M-Z relation. In turn, some of the biases in the calibration of T04 would have exacerbated the overall under abundance of LIRGs and ULIRGs in Ru08.

4.12 Summary

The work presented in this chapter aims to characterise the integrated properties of a sample of local star forming and infrared galaxies using SALT/RSS long-slit spectroscopic data. The basis of our work is the stellar population modelling of a sample of highly star forming and luminous infrared galaxies. From the product and by-product of this SSP modelling, we then performed a multi-faceted analysis on the different line intensities observed. Below is a list of the main findings of this section of our work.

- It was found that the vast majority of the observed data are of good quality. Out of 50+ individual datasets for different galaxy nuclei, only one target was deemed unusable.

- Stellar population modelling using a BC03 template with Chabrier IMF, allowed to disentangle the different ages contributing to the light emitted by our sample. The median ages are 160 Myr and 7.2 Gyr for the light-weighted and mass-weighted values, respectively. Both are indicative of a very young stellar population that biases integrated results towards the younger end. By binning the ages in four groups at the ages of < 15 Myr, $15 - 150$ Myr, $150 - 1000$ Myr and > 1000 Myr, it was shown that the two groups; corresponding to the oldest and the youngest bins are always present, with less involvement of the two intermediate ages. This points to a typical case where rather relaxed galaxy is being triggered in the past 15 Myr by an event (interaction or gas inflow), which then results in a burst of SF, rather than continuous SF, all along the galaxy's lifetime.

- The D_{4000} and H_δ indices are also used to validate the scenario given above and independently check the validity of SSP fitting results. In the case of young galaxies, we show that D_{4000} is a very reliable indicator of mean age of galaxies. Using the mass of galaxies, it is shown that similarly to the results of Marcillac et al. (2006), the SUNBIRD sub-sample are massive galaxies that are going through a phase of starburst, which lowers their observed mean age.

- SFH of the entire sample of galaxies is recovered from the SSP fitting results. By calculating the mean and median SFH of the entire sample, it is shown that the current phase of SF that LIRGs are going through is extremely young (< 40 Myr). The SFH also shows that the overall active phase of SF has spiked by an order of magnitude over the last 3 Myr.

- The median metallicity of the sample is derived to be 0.73 $Z_\odot$ for the light-weighted, and 1.29 $Z_\odot$ for the mass weighted values. This indicates that the latest episode of star formation is being fuelled by pristine gas - hinting at the influence of gas inflows. By

studying the Mass-Stellar Metallicity relationship in the context of previous studies, we infer that the majority of the galaxies present in our sample are Sa-Sbc galaxies.

- By measuring the equivalent width of Hα line, sSFR is derived. It is found that the median sSFR of SUNBIRD is $2.60 \times 10^{-10}\ yr^{-1}$ corresponding to a mass doubling rate of 3.9 Gyr. While these values are at least $2 - 2.5$ times higher than main sequence galaxies, they are lower than the GOALS sample which contains more extreme LIRGs and ULIRGs cases.

- A direct correlation between stellar extinction, $A_{\rm v,star}$ and nebular extinction $A_{\rm v,HII}$ is derived. The results are consistent with Calzetti et al. (2000) while the SUNBIRD subsample has a more extreme environment. By studying the excess nebular attenuation, it is shown that SUNBIRD follows a two component dust model proposed by Calzetti et al. (1994), where one component is active over all areas of a galaxy, and a secondary component adds extra extinction in regions of star formation.

- Through the study of the BPT diagram and by applying general classification schemes, it is shown that the majority (29) of galaxies are HII driven with two targets being dominated by AGN activity, and the rest (14) being composites.

- By using a myriad of oxygen abundance indicators and the work of Kewley & Ellison (2008), a mean O3N2 base abundance is derived. The mean O3N2 indicator is shown to be more stable and have less scatter than singular abundance indicators. Deriving the mean abundance for each galaxy and their corresponding K-band mass from 2MASS, the M-Z relation of the sample is analysed. It is found that the under-abundance of the SUNBIRD galaxies is only ~ 0.1 dex over the mass range from $10^{10} - 10^{11.5}\ M_{\odot}$. This is partly in conflict with the results of Rupke et al. (2008) where the under-abundance was quantified to be in the range of $0.3 - 0.4$ dex. Some contributing factors, such as sample differences and the issue with calibration of the SDSS M-Z relation could partially account for such a discrepancy.

Chapter 5

Spatially Resolved Characteristics

5.1 Introduction

This chapter focuses on the radial properties of the SUNBIRD sub-sample. After having studied the galaxies on a broad perspective in Chapter 4, the interest from here on lies in having an in-depth understanding of the LIRGs and star forming galaxies. The long-slit data sample provides a two-dimensional dataset mostly along major axes of objects. It provides an opportunity to understand star formation, stellar populations, ionisation and oxygen abundances radially. Another aspect that is explored is how much influence does interaction stage have on LIRGs properties.

5.2 Radial Apertures

The first task prior to any analysis was to select apertures to extract from the observed data. The process of selecting the number of apertures as well as their locations was done by eye while trying to maximise the SNR of each aperture. As much as possible, we kept different visibly-distinct regions separate during the selection of the extracted windows. Table 5.1 shows the list of galaxies, the SNR achieved in each window, and also the fit qualities that were achieved for each window as per equation 4.1 from Chapter 4. For each window, or spectrum, the quoted SNR is calculated by taking the median value of signal-to-noise ratio per pixel (effectively per wavelength bin). The variation of fit quality as a function of SNR is shown in Figure 5.1. In total, 353 apertures were extracted for the SUNBIRD sub-sample and fitted with STARLIGHT, with the BC03 base of 45 SSP templates, through the SAAO computer clusters. Out of the fitted ones, we apply a cut at 11% on the fit quality for each aperture instead of the nominal value of 10% to be included in the analysis. In the current case, a threshold of 11% only allows for 6 more apertures to be included in the analysis as compared to the 10% threshold value. In total, out of the 353 apertures, 326 are deemed good enough to be included for the analysis that

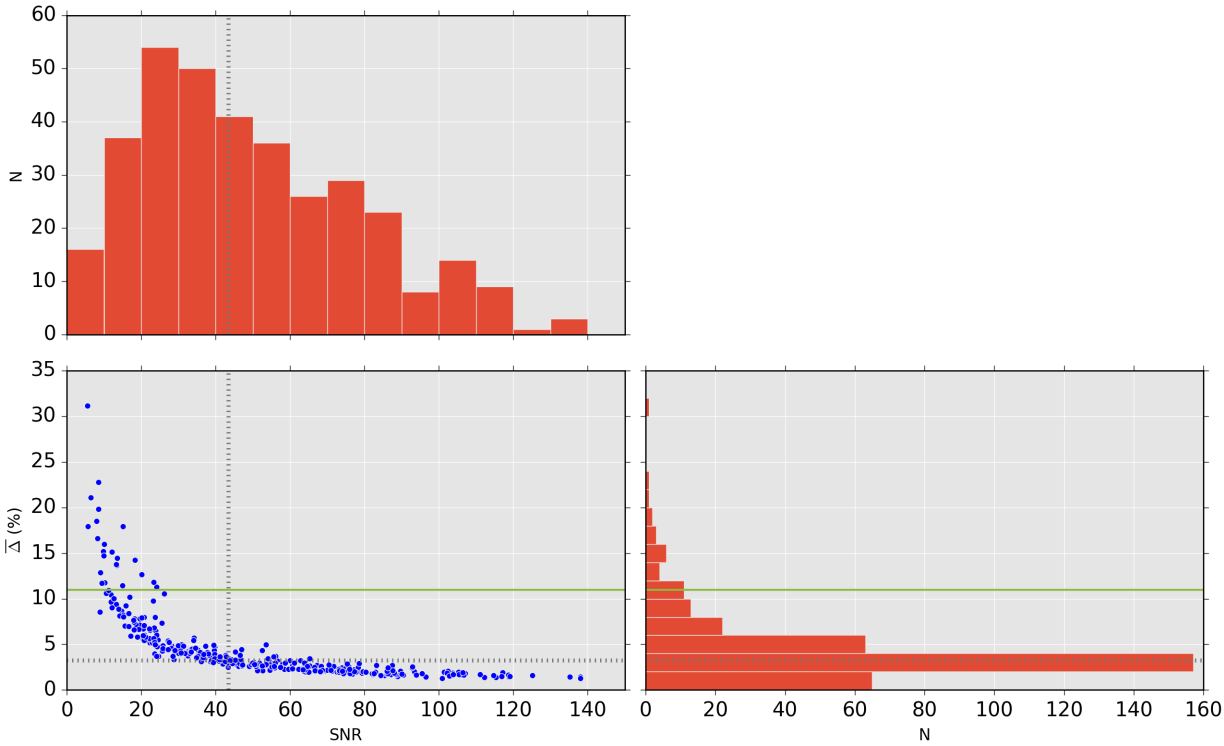

Figure 5.1: *Bottom Left Panel*: Variation of fit quality as a function of SNR. *Bottom Right Panel*: Histogram of for the fit quality ($\overline{\Delta}$ (%)) values obtained for all the apertures. *Top Left Panel*: The histogram for the SNR of all the radial apertures. Black dotted lines indicates median values which are 43.5 for the SNR and 3.2 % for the fit quality while the green lines indicates the fit quality cut applied at 11%. Any aperture above the green line was rejected from the analysis.

follows in this Chapter. All analysis that follows from here on will only include the apertures which satisfy the fit quality criteria. Apertures that were excluded from the fits in general had low SNR as seen in Figure 5.1 leading to fitting of low quality.

Table 5.1: Table listing the number of apertures per target at different position angle. The signal-to-noise ratio at each aperture and the corresponding fit quality are also listed in the respective orders. Column 1: Target name; Column 2: Position Angle; Column 3: Number of apertures; Column 4: Radial distance of apertures in kpc; Column 5: Fit quality; Column 6: Signal-to-noise ratio.

Name	**PA**	**Aps**	**Radial distance (kpc)**	$\overline{\Delta}$ **(%)**	**SNR**
(1)	(2)	(3)	(4)	(5)	(6)
CGCG049-057	199	7	-3.0, -1.2, -0.4, 0.2, 0.9, 1.7, 3.4	3.2, 3.0, 2.9, 2.5, 2.8, 2.6, 4.0	36.3, 42.9, 42.6, 52.4, 45.6, 46.1, 30.4
ESO154-G010	24	7	-8.3, -3.8, -1.2, 0.4, 1.9, 4.1, 8.9	5.2, 2.7, 2.6, 2.3, 3.3, 2.9, 4.9	22.3, 47.1, 49.0, 59.6, 40.2, 42.6, 25.8
ESO221-IG008	315	7	-3.6, -1.2, -0.4, 0.1, 0.7, 1.6, 4.1	2.8, 2.2, 2.4, 1.6, 2.1, 3.0, 3.4	46.9, 62.2, 73.9, 85.4, 69.5, 44.0, 40.8
ESO221-IG008	283	7	-3.3, -1.1, -0.3, 0.2, 0.7, 1.4, 3.2	4.7, 2.3, 1.7, 1.8, 1.8, 3.7, 4.4	39.7, 59.5, 82.2, 76.7, 82.1, 38.6, 39.6
ESO221-IG010	150	9	-4.2, -1.9, -0.8, -0.2, 0.2, 0.5, 1.4, 3.0, 4.9	3.8, 2.2, 2.6, 1.6, 1.5, 1.9, 1.9, 1.9, 4.2	38.4, 76.0, 65.2, 106.2, 118.8, 85.9, 103.7, 101.4, 32.7
ESO264-G036	294	8	-5.0, -3.1, -1.7, -0.7, 0.2, 1.3, 2.7, 5.2	2.0, 1.5, 1.6, 1.5, 1.4, 1.6, 1.8, 2.3	64.0, 88.8, 84.4, 96.5, 112.2, 106.1, 87.6, 66.9
ESO264-G057	276	7	-6.3, -2.7, -0.6, 0.4, 1.2, 3.1, 6.3	3.5, 4.2, 3.0, 2.7, 3.3, 3.8, 3.1	35.3, 30.9, 54.8, 67.2, 39.7, 32.6, 38.5
ESO267-G030	135	6	-1.7, -0.6, 0.1, 0.8, 2.1, 5.3	2.0, 1.9, 2.0, 2.1, 2.6, 3.2	72.7, 82.5, 82.9, 71.2, 55.7, 43.5
ESO319-G022	295	7	-3.9, -1.7, -0.4, 0.3, 1.0, 2.2, 4.3	5.2, 3.8, 3.9, 3.7, 4.3, 4.4, 4.8	22.9, 35.2, 32.9, 35.9, 31.1, 29.0, 24.2
ESO320-G030	315	8	-6.0, -3.0, -1.2, -0.4, 0.1, 0.6, 1.4, 4.2	3.9, 3.3, 2.0, 1.7, 1.9, 2.0, 2.1, 3.2	39.9, 54.2, 93.4, 118.6, 117.2, 105.2, 102.4, 59.9
ESO428-G023	261	7	-3.4, -1.3, -0.3, 0.2, 0.7, 1.9, 4.0	2.6, 3.2, 1.8, 1.7, 2.1, 1.7, 2.8	71.7, 62.8, 107.0, 111.1, 89.6, 105.4, 57.9
ESO440-IG058-N	65	5	-3.5, -0.9, 0.3, 1.4, 4.0	5.5, 2.8, 2.1, 2.8, 4.4	20.5, 43.5, 63.7, 41.9, 26.0
ESO440-IG058-S	237	5	-6.9, -1.8, 0.4, 2.5, 7.7	6.7, 4.1, 3.8, 4.4, 5.3	20.5, 37.8, 42.7, 35.3, 27.7
ESO491-G020	18	5	-4.3, -1.3, 0.2, 1.4, 3.3	2.0, 1.8, 1.4, 2.2, 2.2	74.5, 86.0, 115.3, 70.1, 70.9
ESO550-IG025-N	175	5	-10.5, -2.5, 0.5, 2.5, 5.4	10.4, 3.9, 4.8, 5.0, 7.8	11.8, 39.7, 37.3, 30.9, 18.2
ESO550-IG025-S	175	3	-1.9, 0.4, 4.2	8.8, 7.3, 15.2	14.3, 25.5, 9.8
IC2522	7	9	-8.9, -3.8, -1.3, -0.3, 0.2, 0.6, 1.5, 3.0, 6.5	5.5, 2.8, 2.5, 1.7, 1.7, 2.0, 2.6, 2.4, 4.9	24.5, 54.7, 66.5, 90.4, 87.1, 79.0, 60.6, 63.3, 29.9
IC2522B	31	7	-4.8, -1.9, -0.5, 0.1, 0.5, 1.7, 4.2	2.3, 2.0, 1.7, 1.7, 2.3, 2.1, 2.4	58.4, 65.1, 88.6, 106.6, 74.9, 66.7, 60.5
IRAS06164+0311	87	5	-2.6, -0.4, 0.0, 0.5, 3.0	17.9, 11.3, 11.8, 10.6, 12.7	15.0, 24.1, 23.4, 26.2, 20.2
IRAS12116-5615	231	3	-1.8, 0.1, 2.2	14.4, 9.8, 13.7	13.5, 23.2, 13.4
IRAS13052-5711	270	3	-1.6, 0.5, 3.8	3.5, 3.4, 4.2	43.5, 40.9, 35.8
IRAS17578-0400-W	106	3	-2.9, -0.1, 2.3	22.8, 8.0, 19.8	8.5, 23.7, 8.5
IRAS17578-0400-E	106	3	-1.3, 0.2, 1.7	31.1, 13.8, 43.2	5.6, 13.3, 3.8
IRAS17578-0400	110	6	-3.6, -1.4, -0.2, 1.0, 2.3, 3.7	16.0, 10.2, 18.5, 11.4, 21.1, 7.8	10.0, 16.9, 8.0, 15.0, 6.4, 19.5
IRAS18293-3413	127	3	-2.4, 0.2, 3.4	17.9, 5.5, 8.7	5.6, 23.4, 14.7

Table 5.1 – continued from previous page

Name	PA	Aps	Radial distance (kpc)	$\overline{\Delta}$ (%)	SNR
(1)	(2)	(3)	(4)	(5)	(6)
IRAS18293-3413B	127	2	0.3, 2.3	7.1, 10.6	19.5, 10.5
IRAS19115-2124	190	5	-12.9, -3.8, -1.1, 1.6, 8.9	8.5, 3.3, 3.7, 4.0, 3.7	8.8, 28.7, 24.6, 23.5, 24.1
IRAS19254-7245	347	5	-10.0, 0.3, 5.5, 11.0, 20.3	5.5, 4.0, 4.9, 3.8, 5.8	21.2, 38.0, 24.1, 32.4, 18.9
IRASF01364-1042	222	2	-3.2, 7.2	8.2, 10.9	15.1, 11.2
IRASF06076-2139-N	158	6	-8.8, -5.5, -2.9, -1.2, 0.4, 1.8	12.9, 5.1, 3.4, 2.7, 3.0, 4.5	9.0, 23.7, 37.0, 53.5, 63.9, 33.4
IRASF06076-2139-S	158	4	-1.6, 0.4, 2.5, 5.3	3.7, 3.3, 5.7, 8.2	35.2, 44.2, 22.2, 14.1
IRASF16516-0948	86	5	-4.6, -1.4, -0.1, 1.2, 4.7	8.4, 8.0, 4.9, 6.0, 11.8	16.6, 20.8, 28.1, 20.9, 10.1
IRASF17138-1017	-170	2	-0.6, 1.5	162.3, 58.9	3.7, 4.4
MCG-02-01-051	170	4	-7.1, -1.9, 1.5, 7.1	7.0, 2.3, 2.2, 4.5	15.6, 59.6, 54.6, 25.8
MCG-02-01-052	170	6	-9.1, -5.1, -2.1, 0.6, 4.3, 10.6	5.9, 2.1, 2.5, 2.1, 3.7, 4.3	17.1, 52.6, 43.3, 51.2, 28.4, 25.7
MCG-02-33-098-E	245	6	-7.7, -4.1, -2.4, -1.1, 0.2, 1.5	4.6, 3.1, 3.2, 3.0, 2.0, 2.7	28.0, 39.4, 38.8, 43.2, 75.4, 50.5
MCG-02-33-098-W	245	5	-0.9, 0.3, 1.7, 3.5, 7.7	3.2, 3.0, 3.0, 2.9, 3.3	40.9, 50.3, 45.2, 47.1, 43.2
NGC1022	-38	5	-0.6, -0.2, 0.0, 0.2, 0.6	4.8, 3.1, 2.6, 3.5, 8.0	24.2, 42.5, 50.9, 34.9, 15.1
NGC1068	-148	16	-4.0, -2.5, -1.7, -1.1, -0.7, -0.3, -0.0, 0.2, 0.6, 1.1, 1.5, 2.0, 2.5, 3.2, 3.9, 5.6	2.6, 3.0, 2.2, 1.5, 1.4, 1.2, 1.4, 1.3, 1.2, 1.3, 1.7, 3.0, 3.7, 1.8, 3.5, 6.5	68.4, 61.2, 77.2, 116.9, 138.0, 177.3, 150.7, 153.7, 160.6, 138.1, 88.2, 51.7, 41.0, 86.3, 39.7, 23.8
NGC1204	73	7	-6.5, -2.7, -1.0, 0.2, 1.4, 3.1, 6.9	4.4, 3.2, 2.6, 2.7, 2.9, 2.7, 3.5	46.9, 56.5, 75.8, 87.5, 75.4, 70.5, 54.1
NGC1222	-132	6	-2.5, -0.7, -0.1, 0.4, 1.2, 2.9	2.9, 2.8, 2.3, 2.9, 4.1, 4.1	46.4, 50.9, 60.6, 44.5, 32.6, 31.4
NGC1819	135	7	-7.9, -2.5, -1.0, -0.2, 0.6, 2.4, 7.6	5.7, 3.4, 1.8, 2.3, 2.1, 3.8, 5.4	34.1, 65.2, 102.2, 73.1, 86.1, 46.5, 34.1
NGC253	-39	12	-1.5, -1.1, -0.8, -0.5, -0.3, -0.1, -0.0, 0.2, 0.4, 0.6, 0.9, 1.3	14.2, 4.9, 3.7, 3.7, 2.7, 2.9, 2.6, 4.9, 4.4, 4.2, 3.0, 15.1	18.3, 39.4, 56.1, 55.5, 83.1, 78.6, 92.8, 53.5, 52.5, 45.3, 56.0, 12.2
NGC3110	185	7	-9.6, -3.3, -1.1, 0.3, 1.8, 5.0, 12.3	4.0, 1.9, 1.9, 1.5, 1.8, 2.3, 3.4	33.0, 79.3, 88.0, 119.0, 90.0, 63.1, 41.1
NGC3110	111	7	-7.5, -3.4, -1.1, 0.3, 1.5, 3.4, 7.3	3.1, 1.3, 1.8, 1.6, 2.4, 1.8, 5.5	36.1, 100.9, 74.3, 102.8, 55.8, 76.1, 20.7
NGC3508	194	7	-6.4, -2.9, -1.2, 0.1, 1.1, 2.9, 6.1	2.7, 2.3, 2.0, 2.0, 2.2, 2.0, 4.0	47.2, 62.3, 77.6, 79.5, 68.6, 73.2, 30.1
NGC4433	187	7	-5.5, -2.6, -1.1, 0.1, 1.7, 3.8, 6.9	2.8, 2.5, 2.6, 2.1, 2.0, 2.2, 2.7	49.5, 55.0, 55.7, 73.2, 80.4, 63.9, 53.5
NGC4575	280	7	-7.3, -3.7, -1.4, 0.0, 1.3, 3.2, 6.6	3.5, 2.1, 2.0, 2.1, 2.3, 1.8, 2.9	36.7, 74.0, 77.2, 87.6, 76.0, 82.5, 49.9
NGC470	-160	7	-3.5, -1.3, -0.4, 0.0, 0.4, 1.5, 3.6	6.0, 6.8, 3.7, 2.5, 3.3, 7.9, 7.1	24.0, 23.4, 42.9, 57.5, 45.2, 20.0, 20.8
NGC520	132	7	-2.0, -0.3, 2.1, 4.6, 7.2, 11.0, 13.7	9.7, 2.8, 3.9, 5.4, 4.5, 9.2, 41.0	11.9, 50.4, 36.7, 27.1, 33.7, 15.8, 1.8
NGC6000	170	7	-2.0, -0.9, -0.4, -0.0, 0.3, 1.0, 2.2	5.6, 7.2, 4.2, 3.3, 4.3, 7.4, 7.6	23.3, 18.6, 33.4, 41.0, 30.6, 18.0, 18.0
NGC6000	174	11	-6.7, -3.6, -1.7, -0.7, -0.3, 0.1, 0.5, 1.1, 2.2, 4.6, 7.0	5.2, 2.6, 1.4, 1.9, 1.3, 0.9, 2.4, 1.7, 1.6, 2.8, 9.4	27.6, 64.6, 135.1, 106.5, 183.2, 192.9, 86.3, 103.9, 114.7, 53.5, 13.3
NGC6835	-109	7	-1.7, -0.7, -0.2, 0.1, 0.4, 1.0, 2.2	5.2, 3.2, 2.3, 2.0, 2.7, 3.6, 4.6	27.5, 43.8, 63.5, 68.0, 52.5, 41.2, 34.5

Table 5.1 – continued from previous page

Name	**PA**	**Aps**	**Radial distance (kpc)**	$\overline{\Delta}$ **(%)**	**SNR**
(1)	(2)	(3)	(4)	(5)	(6)
NGC7714	-90	5	-4.8, -3.0, -1.6, -0.4, 1.6	10.0, 8.9, 5.3, 4.3, 5.8	12.6, 13.9, 23.6, 29.0, 21.2
NGC7714	180	6	-3.2, -1.2, 0.0, 1.1, 2.4, 4.8	6.6, 4.0, 3.0, 4.1, 6.0, 6.6	19.4, 31.7, 39.3, 30.7, 20.6, 18.1
NGC7715	-105	5	-3.7, -1.5, -0.1, 1.0, 2.6	9.0, 5.0, 4.4, 7.0, 11.7	12.1, 23.8, 27.2, 16.7, 9.4
NGC7714C	-105	3	-2.4, 0.0, 3.6	14.7, 6.7, 16.6	9.9, 22.1, 8.2

As another sanity check of the robustness of the results of the radial aperture SSP fitting, the weighted mean of the different interesting parameters are computed for all the values of one specific target. The mean is calculated by weighing each aperture by the total amount of flux it contains. The result is then compared to the integrated value that was computed for the same parameter (from Chapter 4). In theory, both values should be the same, since the radial apertures are just a decomposition of the integrated aperture into smaller quantised parts. In practice, due to varying noise levels and SNR values, radial apertures carry a higher risk of unstable results with higher variance. Also, in case of nebular emission dependent parameters, the integrated value may be dominated by a single spatial location, whereas the mean of the apertures would be weighed differently. Hence, some differences are to be expected. To quantify the difference between the each pair of parameters (integrated vs weighted mean), a δ parameter is calculated for each target using the following equation:

$$\delta_i = \frac{\alpha[int.]_i - \alpha[mean]_i}{\alpha[int.]_i} \times 100 \tag{5.1}$$

where alpha is any parameter such age, calculated for any galaxy, i, $[int.]$ and $[mean]$ represent the integrated and weighted mean. By calculating δ for each galaxy, a distribution of δ_i is obtained and their median Δ represents the percentage deviation of the parameter from the expected 1:1 correlation.

Figure 5.2 shows the comparison between the mean of radial apertures with the integrated values. The plot displays nine different parameters namely: light-weighted (LW) age, mass-weighted (MW) age, log(sSFR), LW metallicity, MW metallicity, PP04 base mean oxygen abundance, nebular extinction, stellar extinction and $D_n(4000)$. In most cases there is little bias, as the distribution of points vary uniformly around the 1:1 correlation line (shown in red). Stellar extinction is an exception. For the majority of instances the deviation from the 1:1 correlation line is below 5% but in the case of stellar extinction it is around 10%. This could be explained by the fact that the integrated spectrum combines a vast number of regions into one and the spectral fit cannot properly disentangled all the different radial components during the fit hence the systematic arises. Some of the outliers on the plots are due to lack of SNR in radial apertures which compromises to some extent the quality of the fits hence creating a systematic in the mean value calculated. But from a global perspective the numbers demonstrate the stability of our radial aperture fits. Since the validity of our integrated aperture results was extensively discussed in Chapter 4, and that in the current case, very little deviation is found between the integrated parameters and the mean of radial parameters, it is safe to assume that the results can be trusted.

Figure 5.3 shows an example of the different radial parameters that can be recovered from each

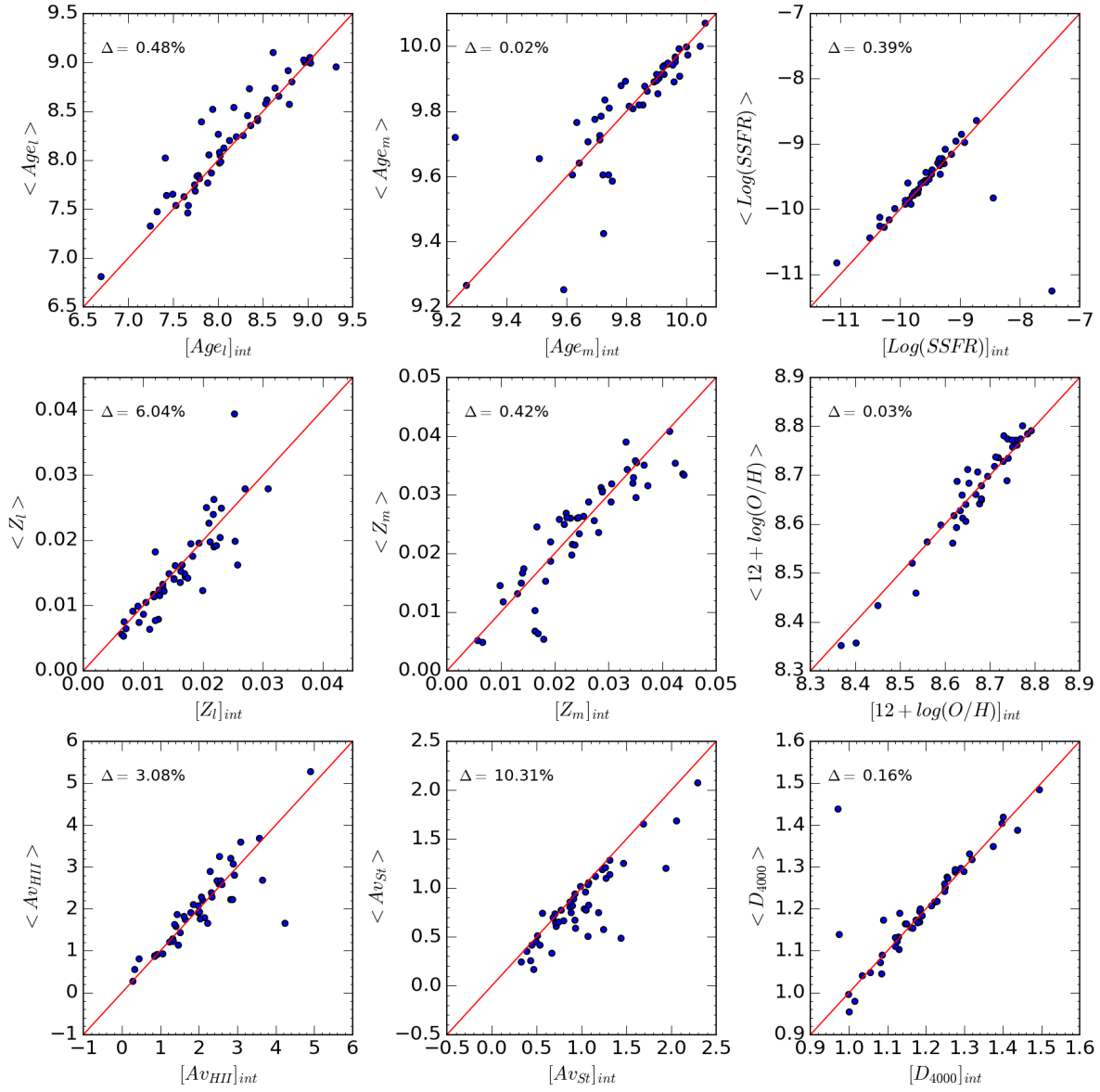

Figure 5.2: Spatially resolved mean values of different parameters as a function of their derived integrated counterparts. The plot shows the variations (from left to right and top to bottom) of LW age, MW age, sSFR, LW stellar metallicity, MW stellar metallicity, Gas phase oxygen abundances (PP04 base), Nebular extinction, Stellar Extinction and $D_n(4000)$ respectively. The red line indicates the 1:1 correlation line. Δ values indicate the percentage difference between the median value of a specific distribution with respect to the corresponding 1:1 correlation line.

target. The figure contains six panels. The top left panel shows the flux distribution (blue) as well as the fit quality index (red) of each aperture (demarcated by black dashed lines). Top right panel shows the BPT diagram of each aperture with the circular symbols colour coded by their distance from the central nucleus of the galaxy. The middle left panel shows the radial distribution of stellar metallicity (red) and the gas phase abundances (blue). In most cases those two parameters are highly correlated. The radial distribution of mean age (red) and sSFR (blue) is displayed in the middle right panel. The left hand lower panel compares the radial variation of stellar extinction (red) to the reddening in SF-regions (blue). As was shown in Chapter 4 section 4.9 these parameters are linked by a linear relationship. Therefore, it is expected that in most cases the two types of extinctions will be highly correlated. The lower right panel shows the derived velocity dispersion (blue) at each radial point, as well as the relative normalised mass (red) in each aperture. Both parameters are recovered from STARLIGHT fitting. As for derived mass, since we cannot derived absolute calibrated SALT spectra, for integrated apertures this parameter is not defined. But for radial analysis, the STARLIGHT results do not suffer from the same limitations as we are comparing apertures from within the same spectra, and we derive and plot the relative masses in the apertures. Figure 5.3 shows an example of the radial distribution of different parameters for galaxy CGCG049-057. The same type of a plot for each galaxy in the SUNBIRD sub-sample is provided in the Appendices of this thesis.

5.2.1 Multiple PA observations

Most of the galaxies in our sample were observed once in one position angle along the major axis, but a few cases were observed at two different position angle. These cases needed to be combined separately first, then they can be compared to other galaxies on an equal footing to create a global picture of radial distribution of parameters for our sample. The galaxies for which two observations were available are: ESO221-IG008, IRAS18293-3413B, NGC1819, NGC3110, NGC6000 and NGC7714A. Projection effects were taken into account to align radial distances with that of the major axes.

5.2.2 Radial Distributions

To obtain the radial distribution of a specific parameter, one needs to plot it as a function of radius. The problem is that absolute values of a specific parameter have a large variances from galaxy to galaxy. Radial distributions are interesting mostly for the gradients they show rather than for the absolute values of specific parameters, which are better probed by looking at the statistical distributions. To analyse purely the overall gradients, we adopt a strategy which consists of subtracting the integrated value of a specific parameter of a target from the derived values of each radial apertures for the same target. We showed in above, that the integrated

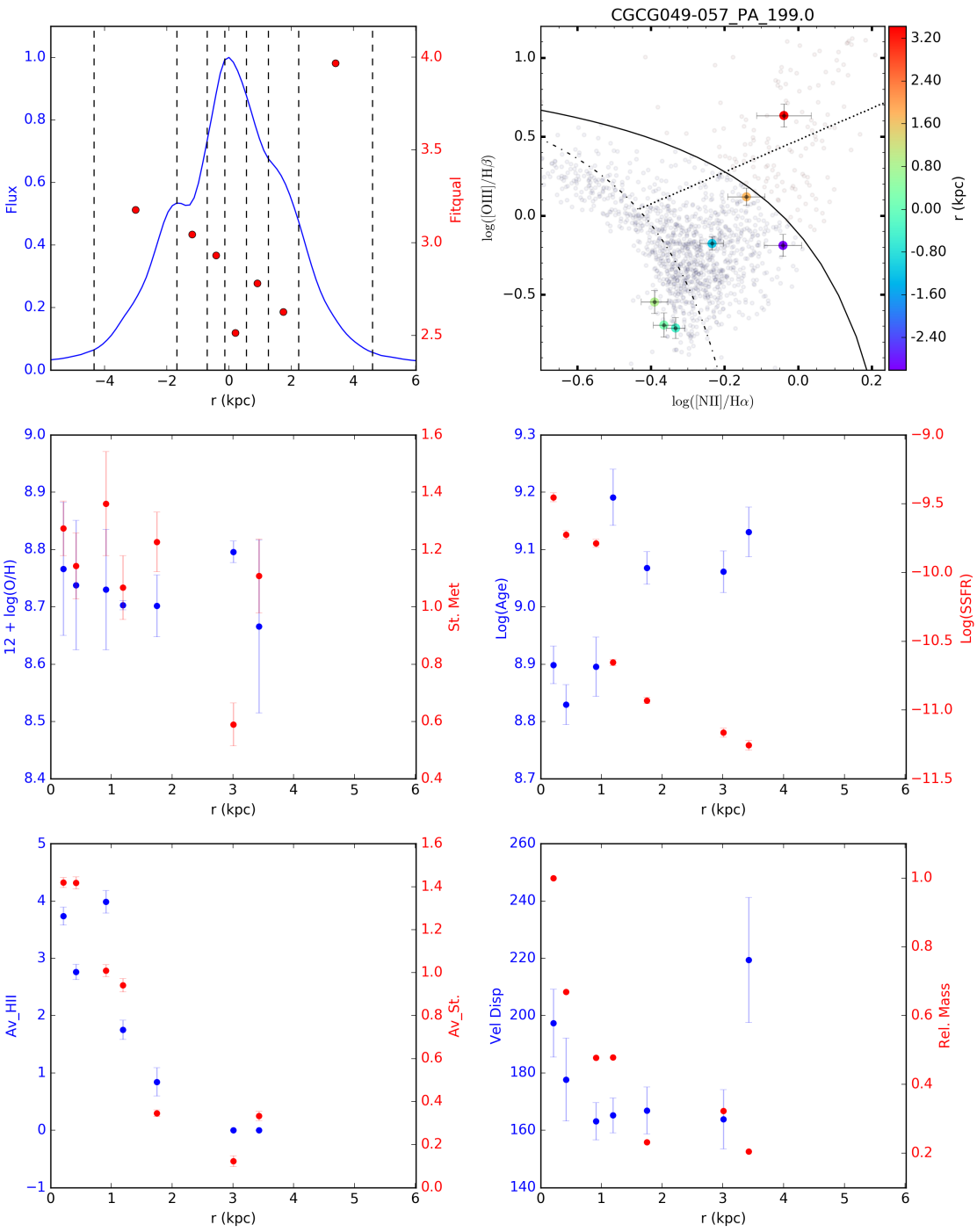

Figure 5.3: Radial distribution of parameters for galaxy CGCG049-057. The *top left* panel shows the Flux distribution (blue) and Fit quality (red) and the BPT location for each aperture (*top right*). *Middle left* panel gives the distribution for gas phase oxygen abundances (blue) and stellar metallicity (red) while the *middle right* panel shows the distribution for STARLIGHT derived mean age (blue) and equivalent width measurement of the sSFR (red). The *bottom left* panel gives the distribution of both extinctions (Red - stellar; Blue - nebular) and *bottom right* panel gives velocity dispersion (blue) and relative mass distribution for each aperture (red).

values are a very accurate representation of the mean of radial aperture values. Essentially, we want to over-plot the residual radial distribution of a specific parameter for all the targets and then analyse if there are structures that are hidden in the data.

The second important part is the idea of what constitutes a good measure of sizes for different galaxies. Essentially, the standard is to use the effective radius, or half light radius, to convert all galaxies on a unity scale. One of the challenges of our data is the lack of photometric measurements which would have provided us with the sizes of the galaxies, and hence an estimate for the effective radius. Fortunately, the 2MASS catalogue offers some size measurement for Infrared galaxies listed in Table 5.2. While effective radius is available in all of the three infrared bands, namely J, H and K, we select to use the K-band effective radius as K-band is related to mass.

The adopted methodology to give a sense of the data 'trends' is to use median boxes. The original dataset, comprising of all the apertures at their different locations relative to the centres of their hosts, is first divided in n equal bins from the centre (at radius zero) towards the outside. Each bin contains an equal number of data points and a median for the distance and a median for the desired parameter (age, metallicity, extinction, etc) is calculated for the bin. This n number of median points is then over-plotted on top of the scattered data to show the tendency of data. Obviously, since there is better coverage near the centre of the galaxies, the number of bins is higher at smaller radii, and smaller at higher radii. In some other cases where the data is good enough, equidistant median boxes are used to show the radial profile of the data.

5.3 Age

5.3.1 Radial profile

In stellar population modelling, age is a complex indicator as it summarises many things into a single number. For instance, as was explained in Chapter 4, the light-weighted age averages all stellar populations in a location and weighs them by their light intensity. Mass-weighted age assumes an IMF and then calculates the mass of each individual stellar population present before averaging them. In the case of integrated apertures, the ages were averaged over an entire galaxy while for spatially resolved apertures, the two types of age are just averaged over a smaller portion of the galaxy. Potentially this could lead us to identify regions of higher SF-activity as compared to its surrounding neighbourhood on a case by case basis, but this is beyond the scope of the current work. Here the focus is mainly to generalise over the sample of galaxies, how age varies radially, if any at all.

Table 5.2: Table showing the 2MASS K-band effective radius in arcseconds and in kpc for (52 targets) SUNBIRD galaxies.

Target	R_{eff}		**Target**	R_{eff}	
	’	kpc		’	kpc
CGCG049-057	5.05	1.390	IRAS19254-7245	4.50	6.098
ESO154-G010	13.66	5.414	IRASF01364-1042	2.90	3.043
ESO221-IG008	6.10	1.356	IRASF06076-2139-N	4.04	3.264
ESO221-IG010	14.18	3.098	IRASF06076-2139-S	2.70	2.181
ESO264-G036	8.23	3.695	IRASF16516-0948	10.29	4.986
ESO264-G057	13.47	4.923	IRASF17138-1017	12.70	4.679
ESO267-G030	8.22	3.233	MCG-02-01-051	3.35	1.960
ESO319-G022	12.17	4.226	MCG-02-01-052	9.52	5.571
ESO320-G030	8.03	1.830	MCG-02-33-098-E	7.40	2.501
ESO428-G023	22.61	4.823	MCG-02-33-098-W	7.40	2.501
ESO440-IG058-N	4.00	1.981	NGC1022	21.99	2.244
ESO440-IG058-S	5.29	2.620	NGC1068	15.16	1.209
ESO491-G020	24.14	5.045	NGC1204	10.74	3.504
ESO550-IG025-N	6.52	4.511	NGC1222	6.81	1.173
ESO550-IG025-S	3.20	2.214	NGC1819	12.41	3.924
IC2522	21.07	4.483	NGC253	213.47	3.631
IC2522B	10.50	2.234	NGC3110	11.86	4.247
IRAS06164+0311	23.64	4.834	NGC3508	11.48	3.162
IRAS12116-5615	3.02	1.752	NGC4433	15.77	3.335
IRAS13052-5711	8.54	3.864	NGC4575	19.27	4.030
IRAS17578-0400-E	5.51	1.640	NGC470	24.06	4.020
IRAS17578-0400-W	5.33	1.587	NGC520	16.88	2.709
IRAS17578-0400	7.33	2.182	NGC6000	14.40	2.221
IRAS18293-3413	3.20	1.237	NGC6835	14.80	1.675
IRAS18293-3413B	2.20	0.850	NGC7714	12.30	2.425
IRAS19115-2124	4.97	5.269	NGC7715	8.15	1.607

As explained in the previous section (5.2.2), for radial profiles, the residual values (after subtraction with the integrated mean age) are plotted as a function of radius to identify potential gradients. This is illustrated in Figure 5.4, where the top panel shows the light-weighted age distribution as a function of absolute radial distances, while the bottom panel shows the same distribution as a function of the 2MASS effective radius. Absolute age distributions (or for any other parameters) shows higher scatter of points, and are provided in the Appendices.

The first observation that can be made is that the log(Age) is relatively flat as a function of distance. This is similar to what Cortijo-Ferrero et al. (2017) observed using IFU data for two of LIRGs undergoing major mergers. The highest point density being in the inner 4 kpc of galaxies

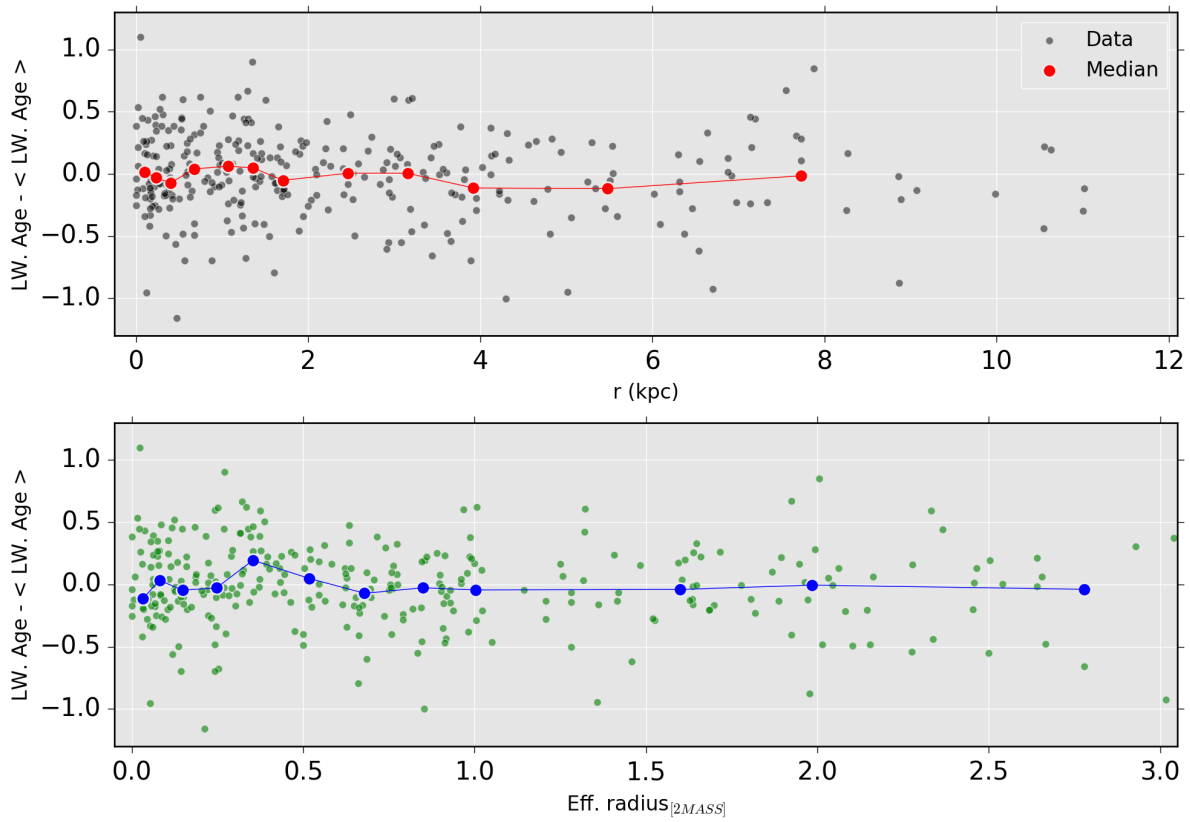

Figure 5.4: The light-weighted age profile as a function of radius. *Top panel* shows the distribution of age (black) against absolute distances for the full sample with median of bins (red) showing the trends. The *Bottom Panel* shows the same profile (green) vs 2MASS effective radius.

leads to more accurate median values inside that distance range. However, the fact that the median boxes used have equal numbers of points (rather than being at regular distance intervals), tend to mitigate the lack of sampling in the outskirts of galaxies. The same observation is made when looking at the Mass-Weighted Age (plot provided in Appendices: Figure D.5) which is even flatter than the LW age. To compare our results, we take a look at the results from González Delgado et al. (2015) on a sample of 300 galaxies from CALIFA. The radial distribution that they published for different Hubble type galaxies was in absolute values. To work around that, the central LW age for each Hubble type is subtracted from their corresponding profiles. The results are plotted in Figure 5.5 along with the median for SUNBIRD galaxies. Prior to any meaningful conclusions, it should be noted that the effective radius of CALIFA is calculated from optical photometry, while we use 2MASS K-band values. This will potentially result in scaling issues, but our interest lies mostly in a qualitative understanding rather than a quantitative one.

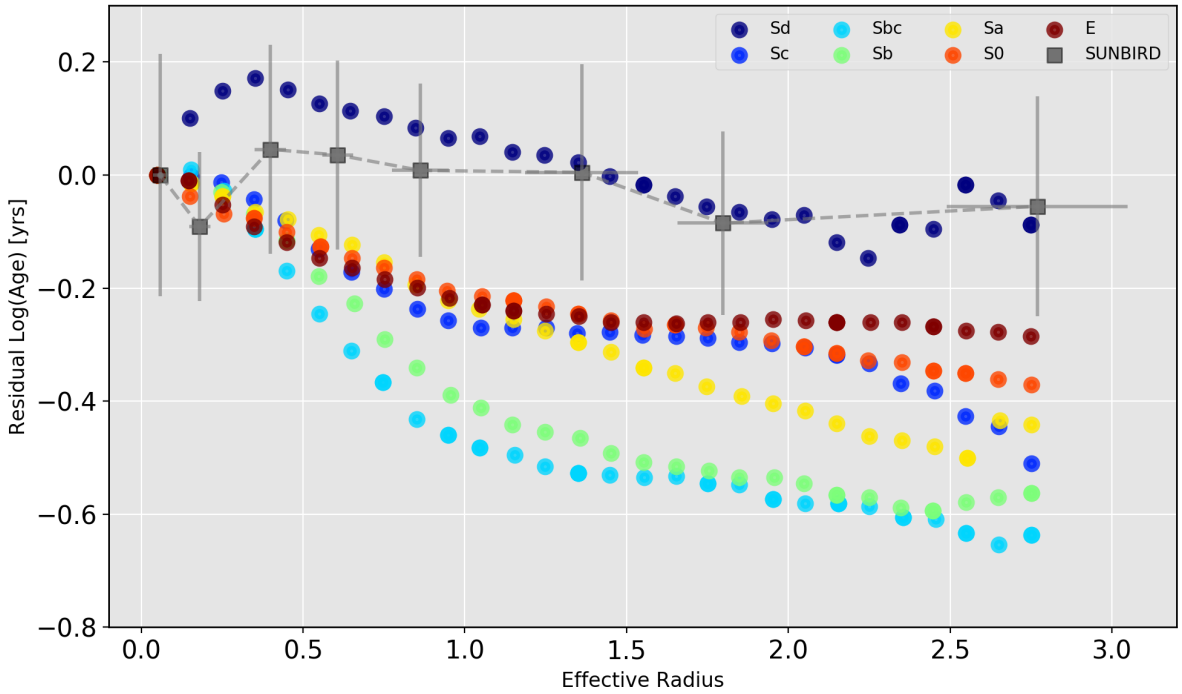

Figure 5.5: The radial profiles residuals for different galaxy morphologies as compared to that of SUNBIRD. The different morphologies, shown in coloured circles are taken from González Delgado et al. (2015), while SUNBIRD median is represented in grey squares with dashed lines

The only type of galaxies that LIRGs have some resemblance with, from the perspective of their radial profiles, are the extreme Late-types (Sd) galaxies. While, LIRGs display very young stellar populations that are similar to the characteristics of the late-type galaxies, we showed in Chapter 4 that from the perspective of mass and stellar metallicities, they are closer to the morphologies of Sa-Sc galaxies. But even purely in terms of stellar population, the age of an Sd galaxy ($\log(\text{Age})_l = 8.55$ (González Delgado et al., 2015)) is older than that of LIRGs ($\log(\text{Age})_l = 8.2$). While the use of different types of stellar population bases could lead to some age discrepancies, Cortijo-Ferrero et al. (2017), found similar ages to our results, for two LIRGS using the same base as González Delgado et al. (2015). The lack of smooth structure and gradient in the age profile of LIRGs could be explained by their highly interacting nature. Interactions will lead to mixing of different components of the galaxies, and gas migration.

5.3.2 Impact of Interaction on Age

It is a known fact that galaxy interaction shapes the formation and evolution of galaxies in the universe. How do such interactions affect observable parameters of galaxies? Figure 5.6 shows the age distribution of the the five identified interaction stages (See Chapter 2 section 2.3). The

two last stages, Class III and IV are combined into a singular class because of the low number of galaxies in each of them separately. Median values for each of the plotted distribution are shown at the top of the histograms. The age value is seen to be highest at the start (Class 0) and at the end of merging (Class III & IV) with $\log(\text{Age})_l = 8.52$ and 8.32 respectively. The two stages where galaxies are interacting, the age drops ($\log(\text{Age})_l = 8.24$ for Class I and 7.88 for Class II). This suggests how merging triggers episodes of star formation that lead to a drop in the measured mean age. Another feature that can be observed in Figure 5.6 is that most age distributions appears bimodal. One possible explanation is that there are subclasses to the interaction scheme that was used. Also, since galaxies are complex objects with different components and radial apertures from different region/component being independent will exhibit different distribution in any parameter - here age.

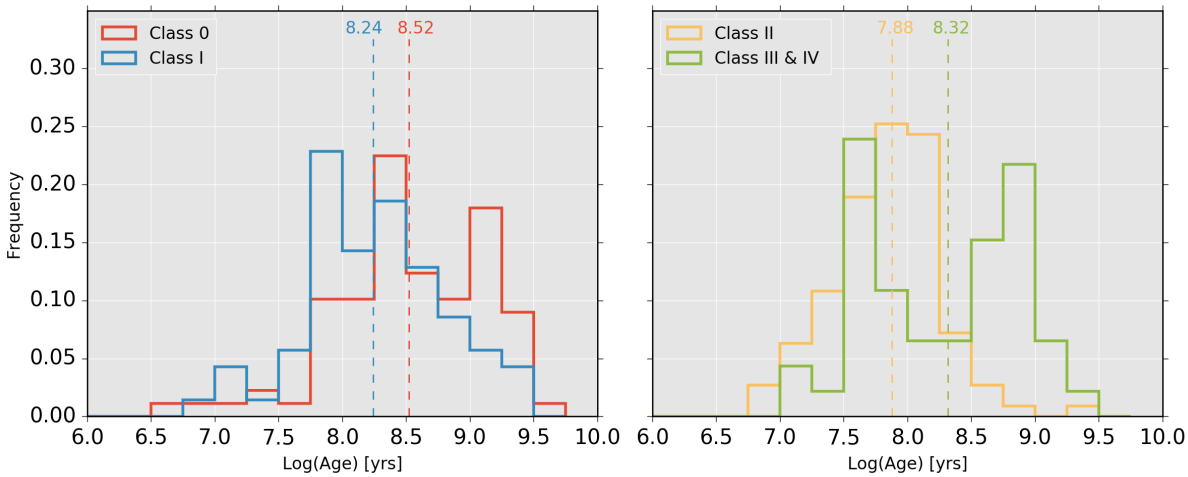

Figure 5.6: Distribution of the age of radial apertures as a function of interaction Class.

5.4 Stellar Metallicity

Stellar Metallicity is a parameter that has for a long time been under-studied because it requires first to recover stellar population information. But stellar metallicity holds some valuable information that helps to recover the SFH of galaxies. Because stars formation is a continuous process in galaxies, and because the stellar environment that new stars are being born in continuously changes due to different feedback processes, studying stellar metallicities can in principle help to unpack the complex history of galaxies. But from a practical perspective, stellar metallicity (especially mass-weighted) is mostly a snapshot of how evolved the gas reservoir of galaxies is at the moment of their births.

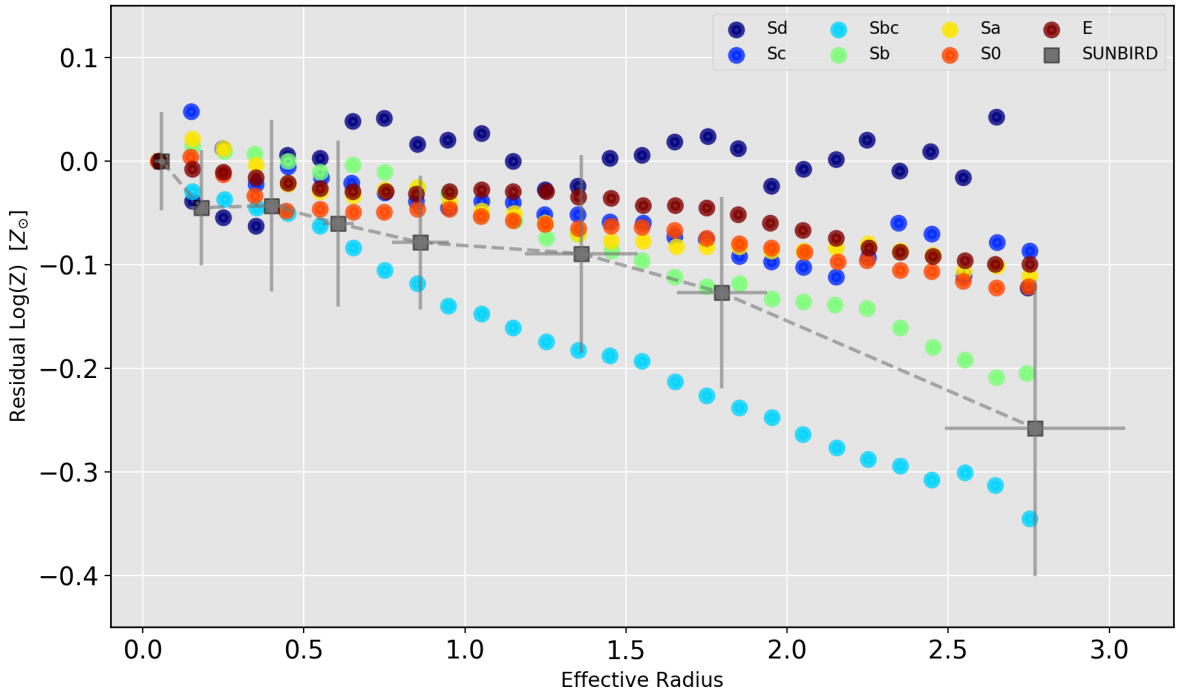

Figure 5.7: The stellar metallicity profile of LIRGs as compared to the different types of galaxies in the Hubble Sequence (taken from González Delgado et al. (2015)).

The radial metallicity profile (here metallicity is $\langle \log Z \rangle$ from equation 4.6 in Chapter 4)for SUNBIRD is recovered following similar methodology as in 5.3.1. The stellar metallicity profile is plotted in Figure 5.7 along with profiles of different morphological types of galaxies, that were published in González Delgado et al. (2015). The trend of LIRGs shows a negative stellar metallicity gradient, which is halfway between Sb and Sbc galaxies.

In terms of absolute distance scale, the gradient of the combined LIRGs population is measured to be -0.029 ± 0.018 dex/kpc by doing a simple least square fitting to the median data point of equidistant bins. The use of such bins is to prevent any bias to the gradient calculation towards the first few kpc of data. The result shows a shallower gradient than that of some local spirals which are known to be of the order of -0.05 dex/kpc (Pilkington et al., 2012). The negative metallicity trend points towards an inside-out galaxy formation process (Pérez et al., 2013) where galaxy cores form earlier, become more evolved while the SF process of outer regions starts with a delay and occurs at a much gentler rate than interior. The latter will also benefit from gas inflows due to disk instability which will trigger SF. Because of the delay the interior of galaxies gets enriched quicker than the outer regions creating the observed gradient. This usually predicts gradient both in age and metallicity although interaction are known to

Table 5.3: The progression of Radial profile gradient as a function of Interaction Stage.

Class	Number of Apertures	Age Gradient (dex/kpc)	Met. Gradient (dex/kpc)
0	96	-0.062 ± 0.029	-0.103 ± 0.018
I	70	-0.047 ± 0.038	-0.015 ± 0.021
II	114	-0.009 ± 0.046	-0.002 ± 0.020
III & IV	46	$+0.052 \pm 0.024$	$+0.001 \pm 0.020$
All	326	-0.021 ± 0.014	-0.029 ± 0.017

flatten this effect (Kewley et al., 2010). Outside-in galaxy formation (Gallart et al., 2008), which affects mostly low mass galaxies with shallow potential well, will on the other hand be more active in the outer regions of a galaxy creating positive gradients of age or metallicity. While the SUNBIRD sub-sample does not have the extremely massive galaxies, it is still expected from the median mass that inside-out will be the favoured formation scenario and the negative metallicity gradient is a confirmation of such scenario.

5.4.1 Impact of Interaction on Metallicity

To investigate the impact of interaction, the radial profiles for each interaction class are analysed and a least square method is used to fit a straight line to the median bins of age and metallicity. The results are shown in Table 5.3 where gradients for each Class and its corresponding uncertainty are listed and the values are plotted in Figure 5.8 . The isolated cases show the less shallow gradient for both age and metallicity and as the interaction stage goes up, the gradient gets shallower until at the merger remnant stage slightly positive gradients are observed. There is a quite definitive trend for both age and metallicity showing the effect that interaction has on such type of galaxies even though our sample is small in terms of apertures available to us. In comparison, had a similar number of galaxies been observed with IFU data, the number of apertures/fibres would have been around two orders of magnitude higher offering better ability to constrain the trends that are being derived. In chapter 4, it was discussed that discrepancies in mass and light weighted metallicities could be due to interactions or gas inflows. Now, it is clear that galaxy interaction is influencing the metallicity of gas in the outer regions. In fact following the logic of Barnes & Hernquist (1996) and Kewley et al. (2010), from both simulations and observations, it is expected that merger induced gas inflows are responsible for the flattening of the metallicity and age gradients. Obviously, this in no way excludes independent gas inflows from the ISM, are also playing a significant role to lowering the stellar metallicities as well.

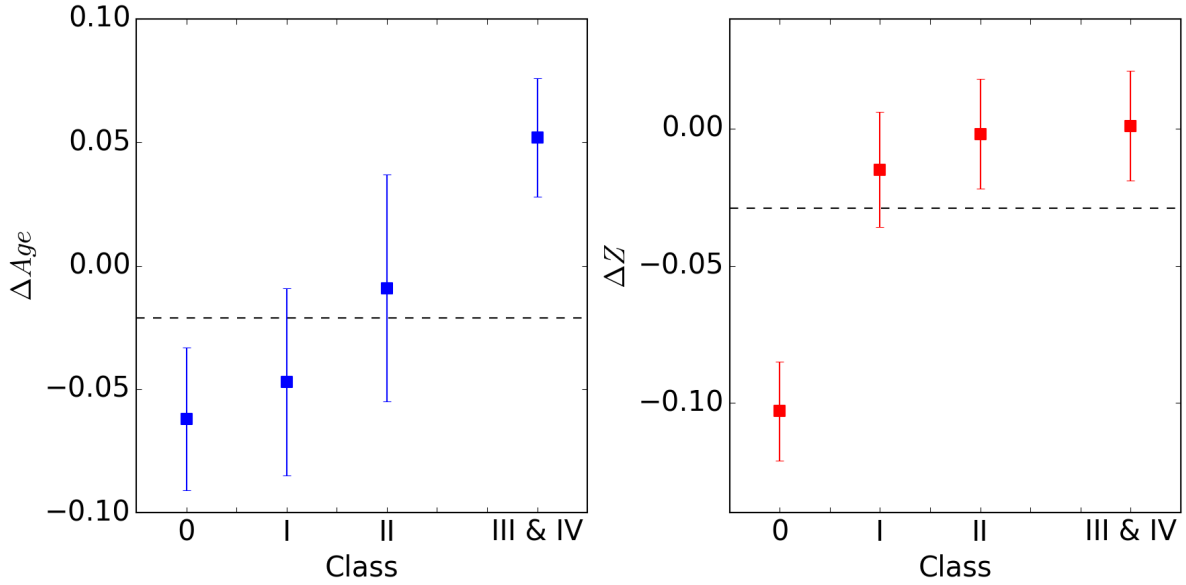

Figure 5.8: The evolution of age and metallicity gradients with interaction stage. The dashed black lines indicate the 'All' values - the gradients when all apertures are considered.

5.5 Extinction

The extinction profile of the different galaxies offer possibilities to understand where star formation is happening the most in LIRGs. Since the sample of galaxies that we observed has a range in redshift, the resolution at which each galaxy is observed in varies. This has the effect that apertures in different galaxies have a range of sizes. This in itself is not an issue, but when dealing with the central areas of the galaxies, the nuclear region, having a large variance in the aperture sizes could in principle create problems. For the nuclear regions, one would prefer to have a consistent physical size which can be compared across the board. For the purpose of this project, we select the nuclear regions to not exceed a size of 1 kpc in size. By using the same method explained in Chapter 3 and 4, the nebular and stellar extinction of all the apertures is calculated and is shown in Figure 5.9. The main panel of Figure 5.9 shows the ratio of the two types of extinction for all the apertures with the best fit line (dashed blue) having a gradient of 2.19. This is consistent both with our result for the integrated apertures as well as the results of Calzetti et al. (2000). The smaller panels on the right hand side of Figure 5.9 shows the extinction ratios for the nuclear regions (top) and the outer regions (bottom). In both cases the results are similar and consistent with the results of all apertures, as well as the results presented in Chapter 4 for the integrated apertures. Variations that are observed in the gradient of the best-fit line are within uncertainty limits.

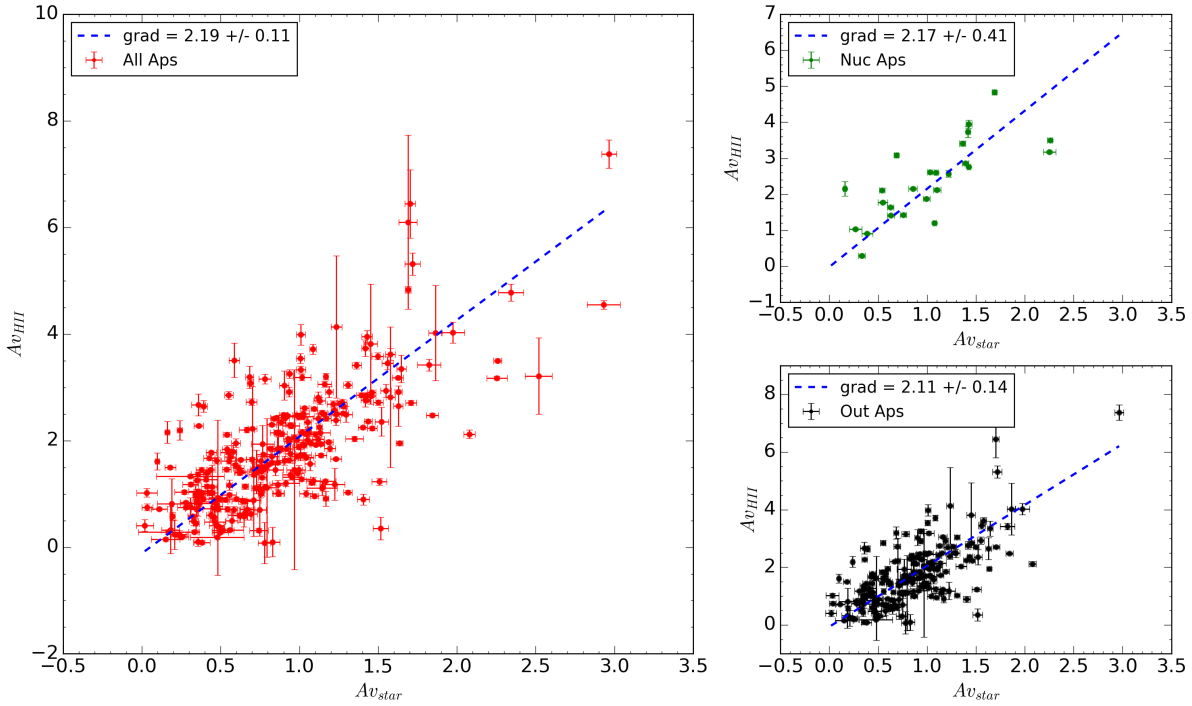

Figure 5.9: The ratio of extinctions. The *Left Panel* shows the ratio of extinction for all apertures with the blue line indicating the best fit line for all the point after minimising for uncertainties in both dimensions. The *Right Panels* show the same ratio when plotted for only nuclear apertures (*Top*) and outer region apertures (*Bottom*). In both cases the dashed line indicates the best fit line. All three panels are consistent with one another within the limits of uncertainties.

We analyse the excess extinction ($A_{\rm v,HII}$ - $A_{\rm v,star}$) and ratio of extinction ($A_{\rm v,HII} \div A_{\rm v,star}$). In the case of integrated apertures, studying these two parameters as a function of sSFR lead to the conclusion of a two component dust model (Calzetti et al., 1994; Charlot & Fall, 2000). The excess and ratio of extinction is calculated for three distinct regions to see whether nuclear and other regions behave differently: for nuclear regions at a radii below 1 kpc from the centre of the systems, for outer regions not further than 4 kpc from the centre, and lastly for outer regions above the 4 kpc threshold region. The results are plotted in the Figure 5.10, and show in the case of nuclear apertures (top panels) that excess extinction is observed similar to what was observed in integrated apertures, pointing to the two-component dust model Wild et al. (2011) and Price et al. (2014).

However, for non-nuclear apertures the trend is not evident. For apertures below the 4 kpc range, the gradient of excess attenuation is ~ 0, while for cases beyond 4 kpc, almost the reverse effect is observed, namely a positive gradient. We note that the lower end of sSFR of both of

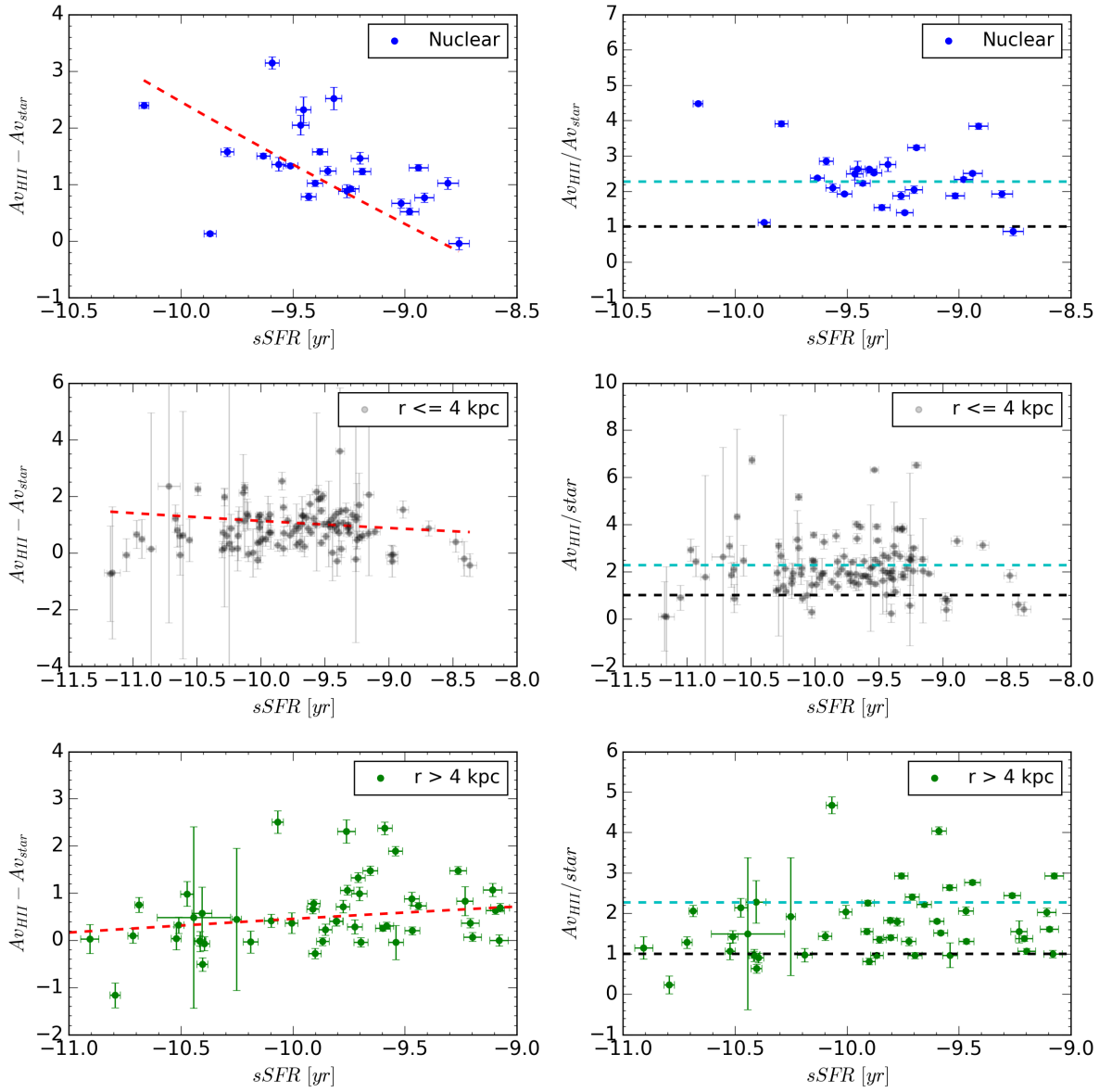

Figure 5.10: A comparison of excess extinction and ratio of extinction at different radii. The *Left panels* shows the extinction excess with the best-fit line shown in dashed red line while the *Right Panels* plot the ratio of extinction with the black dashed line indicating a 1:1 correlation and the cyan dashed line showing the Calzetti ratio of 2.27. The *Top Panels* describe the nuclear regions below 1 kpc from centre, the *Middle Panels* shows the outer regions not exceeding a radius of 4 kpc and the *Bottom Panels* display regions that are further than 4 kpc away from nucleus of galaxies.

those two cases seem to 'pull' the trend downwards. This effect at the lower end of the sSFR was also observed in the data of Price et al. (2014) - in their case they stacked all their galaxies into

three distinct bins where two of the bins lied in the regime of $\log(\text{sSFR}) > -9.5$. This leads to the higher sSFR region having a higher weight in the determination of their best-fit line giving the same overall result and trend as Wild et al. (2011). But the data point with the lowest sSFR had less attenuation than the two-component dust model would predict. The results brought forward by Wild et al. (2011) mainly focused on the range of $\log(\text{sSFR}) > -10.1$ which is a relatively high threshold value - hence potentially missing any decrease in excess attenuation at the lower end of sSFR. In the current case, since we plot individual data points (and not stacked values), there are large variations from one aperture to the next.

What is obvious though, is that nuclear apertures have highest sSFR values (median: $\log(\text{sSFR}) = -9.36$), followed by apertures < 4 kpc (median: $\log(\text{sSFR}) = -9.68$), and then lastly the apertures at higher radii (median: $\log(\text{sSFR}) = -9.78$). As one moves beyond a certain threshold value towards the lower end of sSFR intensities, the excess extinction decreases again. In the case of apertures beyond the 4 kpc range, the lower extinction excess region dominates giving rise to the observed positive gradient. Integrated apertures, which is what the majority of studies have observed either in long-slit mode or single fibre studies of galaxies, are dominated by the light of the nuclear region and will hence be biased by that region.. Since Wild et al. (2011) showed variations in extinction law depending on intensity of sSFR, while we have used a single extinction law, for all apertures, independent of sSFR, this could in principle affect our results.

5.6 Ionisation

The BPT diagram helps to understand different ionising mechanisms in place in galaxies. In chapter 4 it was shown that most of our galaxies are SF dominated, with a few showing shock signatures, and a couple of candidates being in the AGN dominated regime. The ability to have spatially resolved data means that one can separate different regions showing different mechanisms. Four different BPT plots are shown in Figure 5.11 where the top left panel is for nuclear regions (defined as regions $< 0.3\,r_{eff.}$), the top right panel is for outer regions in the distance range $1\,r_{eff.} < r < 2\,r_{eff.}$, the bottom left panel is for outer regions beyond the $2\,r_{eff.}$ range, and finally the bottom right panel shows all the apertures in the radial analysis, which serves as a baseline for comparison. Statistics of the percentage of apertures found in a specific region of the BPT is also displayed on the plot. Being able to measure nuclear regions separately means that any AGN signatures should easily be classified properly and not be mixed with shocked regions, which are usually found in spiral arms of galaxies.

From Figure 5.11, it is found that the distribution of points in all areas of the BPT plot is very

similar for all cases and at all radii. The percentages for the four different areas (HII-dominated, Composite, Liner, Seyfert) are very similar for nuclear regions, radial regions below $2\,r_{eff.}$ and beyond as well. We note also that the distribution of the combined radial apertures (bottom right panel) is also very similar to the integrated apertures which had a distribution of 65.9%, 29.5%, 2.3% and 2.3% for HII-dominated, Composite, Liner and Seyfert respectively (The same distribution is found when dealing with absolute distance - consult the Figure D.11 from Appendices).

These results paint a picture whereby Infrared dominated galaxies have a homogeneous amount of HII dominated regions in all areas of the galaxies. While for the contribution in composite and AGN demarcated regions also stays the same, the dominant mode of ionisation is not the same. Obviously on a case by case basis, large variations will be observed in different regions of a specific galaxy. This result implies that a lot of mixing could be happening inside LIRGs due to their high likelihood of interaction, making all areas look very alike in terms of diagnostic line ratios.

One thing that should also be noted is the low percentage of AGN contribution in our sample. This happens for a couple of reasons that we now discuss. Firstly, the the SUNBIRD sub-sample was selected to be cool IRAS IR-colours avoiding most AGN dominated ones from the outset, even the obscured cases. Secondly, from the work of Veilleux et al. (1999) and Yuan et al. (2010) (shown in Figure 1.12 in Chapter 1), we know that the fraction of AGN-dominant galaxies increases with IR luminosity, while the SUNBIRD sub-sample is on the lower side of the LIRGs categorisation with no ULIRGs in the sample. It is also known from Petric et al. (2011) that only 18% of LIRGs contains AGN, while Alonso-Herrero et al. (2012) showed that only $\sim 8\%$ of local LIRGs have significant AGN contributions, which makes the our sample highly unlikely to be affected by AGN statistically (which is of course seen in from our observed BPT diagram). Lastly, while at the nuclei of the galaxies at $< 0.3\,r_{eff.}$, some AGN contribution should still be present (as seen in Figure 5.11), in the outer apertures (for e.g. at $r > 2\,r_{eff.}$) any apparent AGN signature in the BPT would more likely originate from the presence of shocks and outflows (see e.g. Rich et al. (2014)). These interesting cases will be investigated in more detail in future works using the higher resolution data of PG1800.

While the different regions of LIRGs look very similar in the BPT diagram, does the interaction stage have an effect on the ionisation mechanism in LIRGs? Figure 5.12 illustrates the BPT diagram of the SUNBIRD sub-sample at four different stages (Class III and IV is regrouped into one single stage because of the low number of galaxies in each category and since they are adjacent in chronological order) with the symbols colour-coded by their light-weighted age. Isolated galaxies, i.e Class 0 (top left panel), show diverse ionisation mechanisms with a distribution of

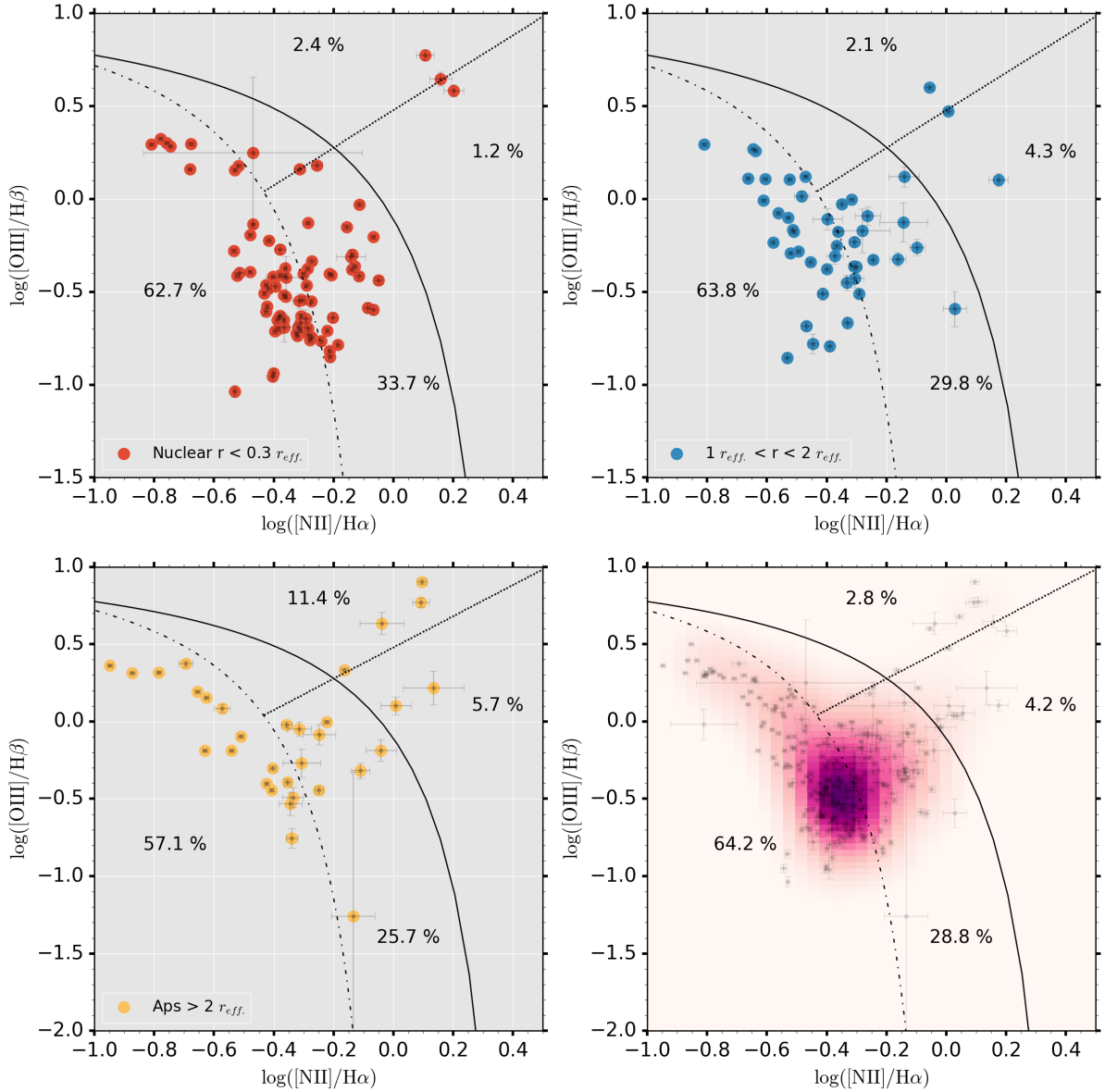

Figure 5.11: The BPT diagrams for different radii of SUNBIRD galaxies. The *Top left* panel is for nuclear apertures ($< 0.3\,r_{eff.}$), the *Top right* panel shows outer apertures in a distance range of $1\,r_{eff.} < r < 2\,r_{eff.}$, the *Bottom left* panel is for outer apertures beyond $2\,r_{eff.}$ radial distance and *Bottom right* panel shows the BPT plot for all radial apertures with the background colour intensity scaled by point density. For all the four plots the solid black curve is the Kewley et al. (2001) line, the dashed black curve is the line of Kauffmann et al. (2003b) and lastly the black dashed straight line is that of Cid Fernandes et al. (2010). The percentages displayed gives the fraction of points lying in a specific area of the BPT diagram.

points all around the BPT diagram over both the 'left branch' and 'right branch'. At Class I (top right panel), where mild interaction is happening, we find that there is a shift towards the bottom left side of the BPT diagram, where HII dominated activity and shock regions lie. It is the intersection point of the two branches. This is expected, since interaction will start having tidal effect on the galaxies and will start triggering SF in the galaxy. As the galaxy moves to Class II (bottom left panel), where tidal tails are observed, the gas gets highly triggered and fuels more extreme SF-activity, and the BPT rightly displays a significant shift towards higher up areas of the 'left branch', where HII is dominant. The mean age displayed by the aperture drops due to the newer SF-activity giving extreme blue colours to observations. The point density also shows that more than 85% of apertures are in the SF phase.

Class III is where the merging of galaxies occurs, and therefore in principle, there should be a dominance of SF-activity, although a significant portion of the gas was already triggered in Class I or II. Class IV is the post merging phase, where the newly formed galaxy relaxes hence, SF is expected to drop at this stage - the younger populations of Class I and II have grown older as well. Since the last two stages are combined, a compound effect of both is observed with apertures dominated by both SF-activity and some composite activity. This could indicate the start of AGN activity following a gas-rich major merger according to the Hopkins et al. (2008) scenario. Based on the work of Veilleux et al. (2002) and Miralles-Caballero et al. (2011), Class I is expected to precede Class II by 200-400 Myr, while the combination of Classes III and IV should happen after 700 Myr.

Yuan et al. (2010) did important work on the impact of interaction stage on the the spectral classification of ULIRGs, but also on LIRGs. They found that interaction stage has an impact mostly on ULIRGs, while their lower luminosity counterparts, the LIRGs, had relatively uniform percentages of HII, LINERs, Seyferts and composites at all stages of merging. This would seem to be at odd with the our results but there are a couple of caveats to such conclusions. First, our sample, while diverse in interaction stage, does not contain many AGN driven galaxies (only 2 from Chapter 4 classification), which introduce some bias in the results. Secondly, there are obvious differences in the interpretation of a spatially geared analysis as compared to that of studying integrated properties. A single galaxy can present itself with very different processes at different areas - something that would translate to the spatial apertures, while integrated spectrum of the same galaxy would be highly biased towards the most luminous regions of the galaxy - usually the nuclear regions, but in cases of Starburst galaxies it could also be highly SF-regions in outer regions.

Figure 5.13 shows a similar BPT as in Figure 5.12 but with log([OI]/Hα) line ratio . OI λ6300

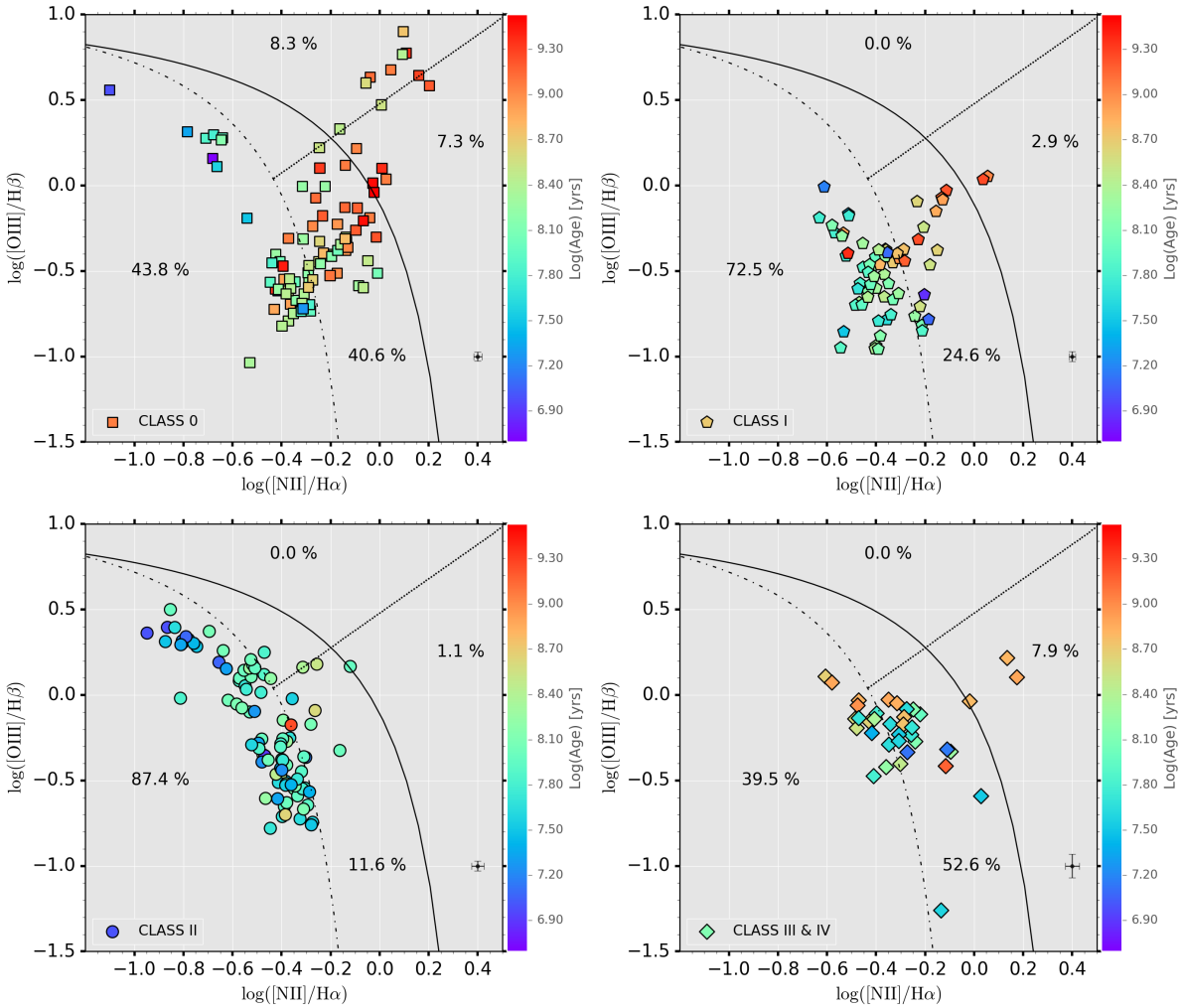

Figure 5.12: BPT diagram of radial apertures grouped by Interaction Stage and colour-coded by Light Weighted age from STARLIGHT. Four panels showing the BPT plots of the 5 different interaction classes with Class III and IV grouped into last panel. Sizes of error-bars are similar to that of previous BPT diagram and a typical error-bar is provided at (0.4, −1).

being a line which is much more sensitive to shocks (Dopita & Sutherland, 1995) and radiation hardness, is potentially a better tracer of such activity than [NII] although it is less easy to measure. By studying this new set of diagnostics, it is found that more apertures fall into the categories of AGN driven mechanism. These ambiguous cases are hard to disentangle unless a thorough case by case analysis is performed on each one of them - which is beyond the scope of this work. However, the main pattern of having higher proportion of SF-driven apertures for interacting stages I and II, as compared to isolated cases and post merger phase, is observed to be similar to the analysis of the log([NII]/Hα) line ratio BPT. We note that the proportion of

SF-driven cases in Class I here is higher than Class II - which is slightly different to the results of from the log([NII]/Hα). But in the case of the previous BPT diagrams, a considerable amount of apertures fall into the composite area both in Class I and II.

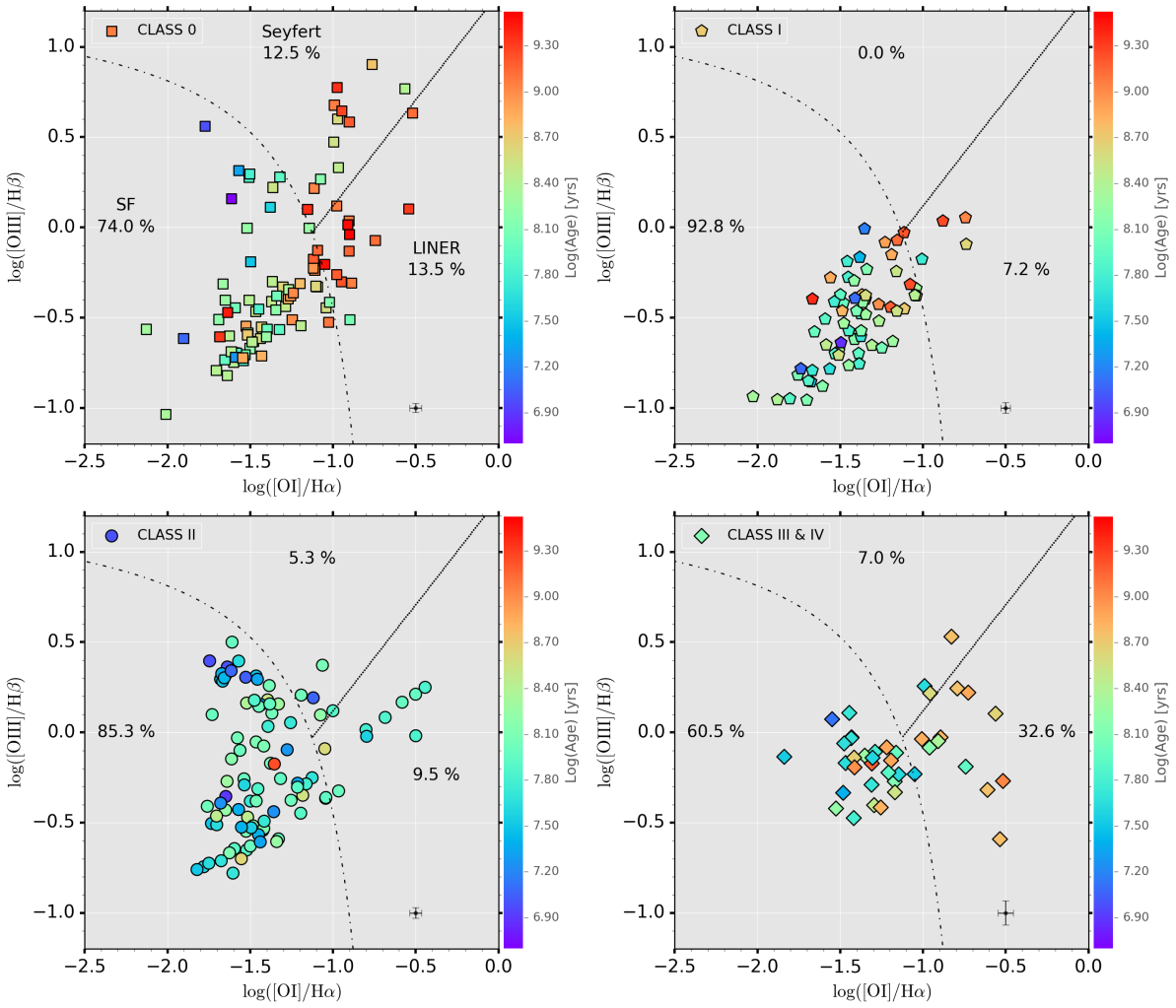

Figure 5.13: Similar BPT diagram of radial apertures grouped by Interaction Stage and colour-coded by Light Weighted age from STARLIGHT using the log($[OI\lambda6300]/H\alpha$) vs log($[OIII]/H\beta$). Typical error-bar size shown at (−0.5, −1).

Table 5.4 shows some derived line ratios for different interaction stages for the sample of radial apertures. We can compare our results with that of Monreal-Ibero et al. (2010) who used IFU data from 32 local LIRGs to study shock ionisation at different stages of interaction. In their work, they derived three line ratios namely: log([NII]/Hα), log([SII]/Hα) and log([OI]/Hα). One of their main findings is that log([NII]/Hα) has very little variation with interaction stages

Table 5.4: Line ratios derived for different interaction Stages for all the radial apertures. For each line ratio median, standard deviation and number of aperture used to derive those statistics are listed.

Class	$\log([NII]/H\alpha)$			$\log([OIII]/H\beta)$			$\log([OI]/H\alpha)$		
	Median	Std. Dev.	N	Median	Std. Dev.	N	Median	Std. Dev.	N
0	-0.255	0.215	96	-0.370	0.433	96	-1.355	0.317	96
I	-0.382	0.143	70	-0.464	0.263	70	-1.389	0.256	69
II	-0.444	0.202	114	-0.256	0.352	114	-1.457	0.296	95
III & IV	-0.304	0.175	46	-0.171	0.162	46	-1.193	0.320	38
All	-0.362	0.214	326	-0.333	0.371	326	-1.385	0.310	298

while the other two ratios showed some variations. In our case, with the SUNBIRD sub-sample, a relatively big variation of the log([NII]/$H\alpha$) is seen at our four different interaction stages. But overall their median of log([NII]/Hα) of all their spaxels was -0.37 which is very similar to our result of -0.36 for all apertures, and that of -0.35 for the LIRGs in Alonso-Herrero et al. (2010). In the case of Monreal-Ibero et al. (2010), they defined three classes namely: Isolated cases, Interacting cases and post merger galaxies. Translating their classification scheme to ours, their Isolated cases is basically our Class 0, Interacting cases is a mixture of Class I and II while post merger remnants are the combined class of III and IV in our case. Hence, in principle the comparison between the two systems should be possible and valid. They also derived log([OI]/Hα) ratios in their work and getting different results to what we observe with SUNBIRD there as well. Their isolated galaxies have a median value of -1.57 for the ratio log([OI]/Hα) slowly increasing to -1.43 and then -1.35 for interacting and post merger phase respectively. In the SUNBIRD sub-sample on the other hand, the log([OI]/Hα) decreases slowly as interaction stages increase. Potentially, the difference in our work as compared to that of Monreal-Ibero et al. (2010) is that we fit stellar population models first and correct line ratios for absorption features underneath emission lines potentially giving more accurate line fluxes and ratios.

5.7 Specific Star Formation Rate (sSFR)

Specific star formation rate, the mass-normalised SFR, probes the active SF regions of galaxies, and studying its radial profile gives perspective to how LIRGs operate. There is a definite negative gradient of sSFR (see radial plots in appendices). To provide insight to the work done in Chapter 4, the sSFR is grouped into 3 bins at different distance ranges and compared. The frequency distribution for each bin is displayed in Figure 5.14 along with the median values of each bin. The nuclear regions display high SF activity with a median sSFR of 3.333×10^{-10} yr^{-1}. This is around 1.28 times higher than the median integrated values of sSFR values derived in

Chapter 4. Comparing this to the values derived by Barrera-Ballesteros et al. (2015) for central regions ($< 0.3\, r_{eff.}$) of 'normal' SF galaxies in the CALIFA sample, our nuclear values are around 1.45 times higher. For the outer regions, the derived values of sSFR are 1.88×10^{-10} yr^{-1} and 8.66×10^{-11} yr^{-1} for the areas in a distance range of $1\, r_{eff.} < r < 2\ r_{eff.}$ and beyond 2 $r_{eff.}$ respectively. The first outer region is in a higher mode of SF than the nuclear regions of the control sample of Barrera-Ballesteros et al. (2015), which consisted of 80 non-interacting galaxies. The second outer region is in a comparable mode of SF as the quoted control sample. While SUNBIRD is on the lower end of sSFR because of the inclusion of $\sim 40\%$ targets that are below the IR luminosity threshold for LIRGs, the sample is still a highly active group of galaxies. We also note that the spread of the distributions increases as we move to the outer regions. The standard deviation of the three distributions are 0.467, 0.572 and 0.730 respectively, with the nuclear regions the narrowest and the outermost region the widest.

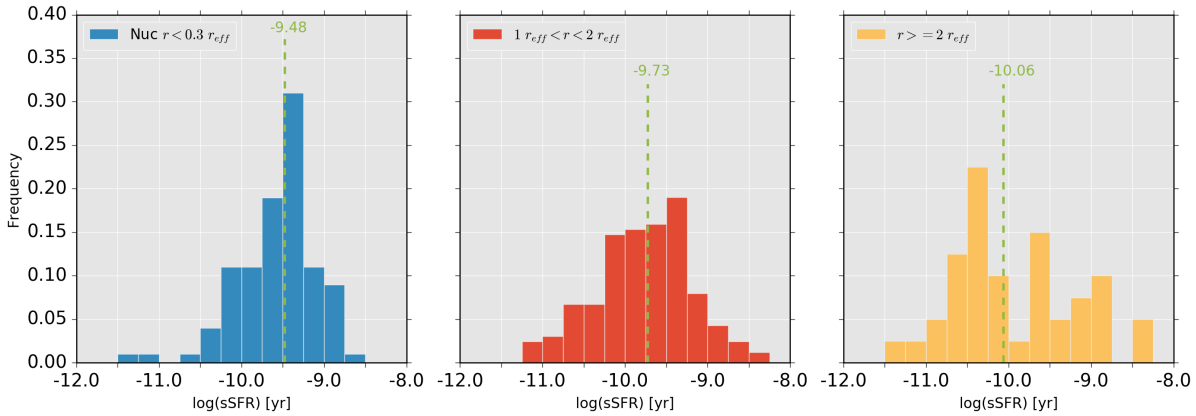

Figure 5.14: The frequency distribution of sSFR at different radius of SUNBIRD. The *left panel* shows distribution for nuclear apertures ($< 0.3\, r_{eff.}$), the *middle panel* correspond to aperture in the distance range of, $1\, r_{eff.} < r < 2\ r_{eff.}$ and the *right panel* shows the outer region beyond 2 $r_{eff.}$. Median values for each distribution are shown with the green dashed line.

5.7.1 Impact of interaction stage on sSFR

We investigate the impact that interaction plays on sSFR in the SUNBIRD sub-sample. The median sSFR is taken along with the median absolute deviation to represent the uncertainties at the following radii: $r < 0.3\ r_{eff}$ for the nuclear region, $0.3\ r_{eff} < r < 1.0\ r_{eff}$ for the radial bin just beyond the nuclear region, and $r > 1.0\ r_{eff}$ for the outskirts of galaxies. The measured values are shown in Table 5.5 and are plotted in Figure 5.15. Such measurements will always suffer from large scatter due to the different galaxies included in the samples, but as we have seen previously, median values give a good estimate of the expected value. The most interesting observation is the different behaviour of the nuclear apertures as compared to the outer regions

of the galaxies. At Stage I, the enhancement in sSFR is mostly seen in the outer regions of the galaxies. At Stage II, extended enhancement of sSFR is observed, with both the nuclear and the first radial bin just after the nucleus, showing the major increase in SF activity. The outermost region is also experiencing a starburst, since it reaches a sSFR is comparable to that of the nuclear region for isolated case (Class 0). If we use the mean age of apertures at different stages of interaction (from section 5.3.2), it can clearly be seen that the overall mean LW age for Stage II is extremely young as well. At the last stage of interaction, namely III and IV, the nuclear region keeps the same level of sSFR, while the two outer region show a noticeable decrease in sSFR. This evolutionary scenario is consistent to the different stages of merging from Hopkins et al. (2008) similar to what is observed from the study of the line ratio.

Table 5.5: The measured specific star formation at different radius for each interaction stage. For each distance from the centre, an sSFR value is given along with the associated uncertainty and the number of apertures, n, used for each calculations.

Class	**Nucleus**		**Outer1**		**Outer2**	
	$r < 0.3\ R_{eff}$		$0.3\ R_{eff} < r < 1.0\ R_{eff}$		$r > 1.0\ R_{eff}$	
	$\log(sSFR)$	n	$\log(sSFR)$	n	$\log(sSFR)$	n
0	-9.66 ± 0.28	37	-9.88 ± 0.36	27	-9.87 ± 0.62	25
I	-9.65 ± 0.26	24	-9.87 ± 0.23	30	-9.81 ± 0.22	16
II	-9.36 ± 0.20	31	-9.30 ± 0.31	43	-9.68 ± 0.42	37
III & IV	-9.38 ± 0.09	12	-9.78 ± 0.33	17	-10.31 ± 0.39	17

5.8 Oxygen Abundances

Oxygen abundances is often considered to be the main indicator of metallicity of a specific object. As was laid out earlier in this chapter, deriving stellar metallicities is a more complex task, therefore in many of studies, oxygen abundances is used as the proxy. The same methodology as laid out in Chapter 4 to obtain oxygen abundances is also used here, namely: a set of different calibrators of abundances is first calculated and then converted to the PP04 O3N2 base before an average is calculated. The results of the radial profile that was derived is shown in Figure 5.16. A negative (which is expected from the stellar metallicity gradient) but quite shallow gradient is observed for the radial profile. The difference between the oxygen abundances in the nuclear region and the outer regions ($\sim$ 6 kpc) is around -0.05 dex at most.

Rich et al. (2012) derived metallicity gradients as a function of merger stage for different abundance calibrators. In the case of PP04 calibrators, the gradient variations are between ~ -0.045 dex/kpc and $\sim +0.015$ dex/kpc for their Stage 0 and Stage 3. Since the merger stages of their work does more or less corresponds to our work, comparisons are valid. The amount of data

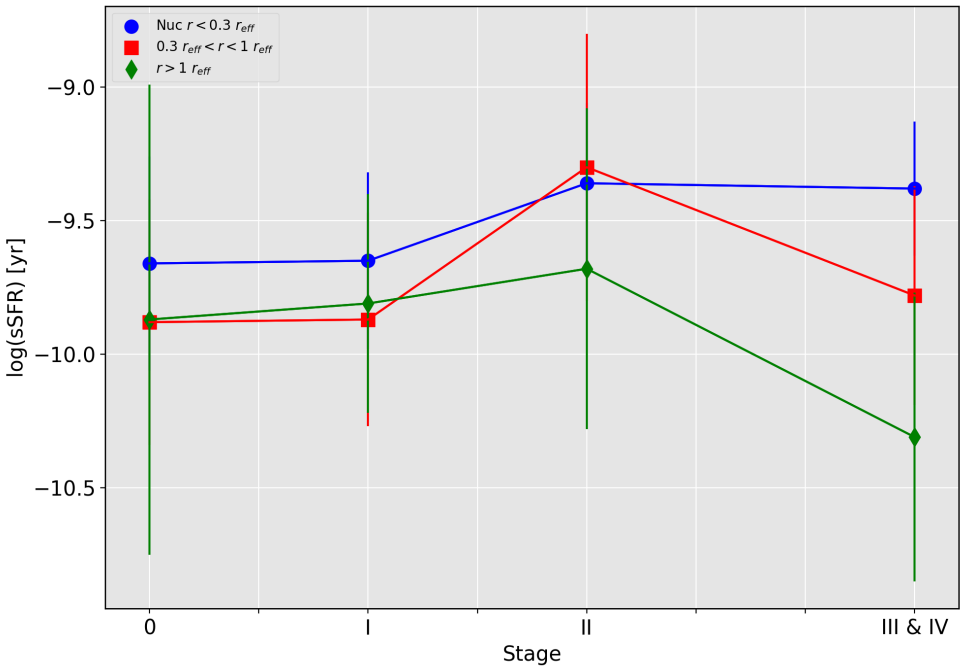

Figure 5.15: The variation of sSFR with interaction stages at different 3 distance bins.

points for each merger stages is not high enough to properly calculate the gradients at each stages for us in this section, we are therefore limited to using only the overall sample gradient. The measured gradient from a simple least square fitting to the median bins data points is -0.0087 ± 0.0019 dex/kpc. Our results are within the expected range of Rich et al. (2012) work, although the the derived gradient is on the lower end of what is expected for a sample containing all merging stages.

Linking the current result to the stellar metallicity gradients, we find that the change in gradients for stellar metallicities (Table 5.3 and Figure 5.8) at later stages of merging, is less that one would expect (considering the change in age gradient is smoother). Since gas phase abundance and stellar metallicity are linked to one another, it can be expected that the radial gradients of metal abundance will be shallow.

Finally we investigate if interaction stage has an impact on the oxygen abundances. The results are plotted in Figure 5.17. A slight decrease in the median oxygen abundances is noted from as the stage of interaction moves from Class 0 to Class III & IV. This is in line with the picture of mergers causing tidal gas inflows, which then decreases the overall metallicity of galaxies. Since overall gas-phase metallicity takes more time to get enriched, metallicity does not increase instantly in the post merger stage (Class III & IV), unlike age which reaches a minimum at

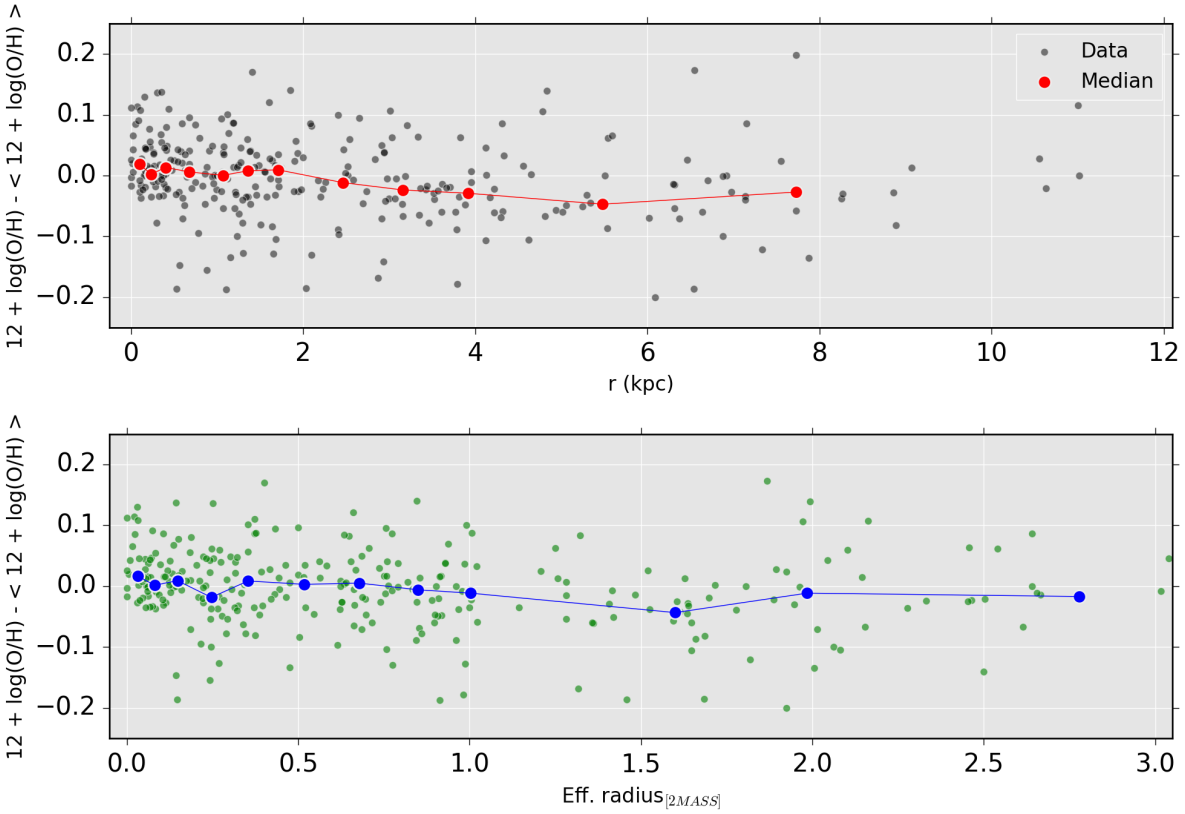

Figure 5.16: The radial profile of oxygen abundance residual.

Class II and then starts to go back up in the last interaction stages.

When deriving the Mass-Metallicity relation in for LIRGs Chapter 4 section 4.11.1, one assumption that was made was the fact that the oxygen abundance gradient would be shallow. This enabled us to compare our work, which used integrated spectra from an entire galaxy, with that derived by Rupke et al. (2008) using nuclear apertures. From the work done above, it can be stated that while nuclear metallicities would differ from that of integrated values, the difference would be minimal. In fact, other factors mentioned, such as the difference in redshift range or higher sSFR than our sample due to the higher IR luminosities, could have a higher impact on the abundances derived than the size of the apertures used, hence making the comparison with Rupke et al. (2008) a fair one. But even taking all these contributing factors into consideration, we believe that the under-abundance of LIRGs and by extension ULIRGs has been previously over estimated.

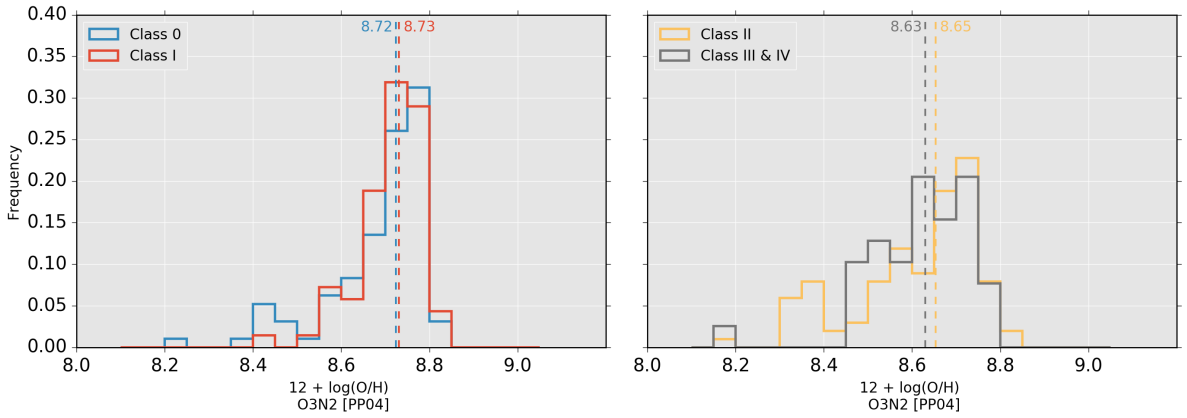

Figure 5.17: The evolution of the oxygen abundance distribution with interaction stages. The median of each distribution are shown with dashed line of the same colour.

5.9 Summary

Throughout this chapter, the long-slit spectroscopy of a sample of 52 different Starbursts or LIRGs were analysed radially. First, 353 apertures were identified by eye in the available spectra before being extracted. After that, the stellar populations of each aperture were derived before being subtracted from each aperture to allow for line intensity measurements. A quality control of the SSP fitting was applied to the dataset to weed out the apertures with too small SNR, or where it was too difficult to model the stellar population. The second quality control, was to check that mean derived parameters for each target corresponded to the integrated parameters for the same target that was derived in Chapter 4. Finally, in cases of galaxies been observed at two position angles on sky, the data were combined to form a singular radial profile for the specific galaxy. The main results are as follows:

- The radial profile of age for the SUNBIRD sub-sample is relatively flat with a gradient very similar to the extreme Late-type galaxies from the work of González Delgado et al. (2015). The flat age profile is similar to the results of Cortijo-Ferrero et al. (2017) on a few merging LIRGs.

- The stellar population age of galaxies shows a noticeable drop during merging stages for isolated galaxies and post merging stages, the age is higher. Tidally induced star formation during Class I and Class II interaction stages decreases the overall mean age of the different areas in a galaxy.

- Stellar metallicity describes a negative gradient of -0.029 ± 0.018 dex/kpc that is consistent with inside-out galaxy formation scenario, which is an expected scenario due to the mass range of the sample of galaxies that we have.

- By investigating the impact that interaction has on metallicities and age of galaxies, we found that there is an evolution of both age and metallicity gradients at the different interaction stages. Isolated cases have steeper negative gradients. As interaction stage increases, the gradients gets shallower until they even gets slightly positive for merger remnant stage. This is in agreement with the simulations of Barnes & Hernquist (1996) and observations and of Kewley et al. (2010).

- The ratio of extinction for all apertures is found to be consistent with results of Chapter 4 as well as the expected ratio of extinction for star forming galaxies published by Calzetti et al. (2000). By studying the attenuation excess, the nuclear apertures in a 1 kpc range are shown to be consistent with a two-component dust models. However the same trend is not found at other distances. Apertures at the low end of sSFR have a much lower than expected excess extinction that predicted by the two-component dust model. We note that a single attenuation curve was used across the board for all sSFR values, which could have influenced the result, since Wild et al. (2011) showed a dependence of extinction on sSFR values. We conclude that since galaxy light is dominated by nuclear regions, the expected trend of the two component dust model is observed when analysing integrated spectra.

- The BPT diagram shows similar distributions at different radial distance ranges where the percentage of apertures classified in a given mode of ionisation is more or less constant at all distances. HII dominated regions are constant across the entire distance range, which is also consistent with results from integrated apertures. The proportion of AGN dominated regions also stays constant across different distance bins. The mode of ionisation is expected to be different for nuclear apertures where AGN is a high possibility while for outer regions the mode of ionisation that should be prevalent is through shock.

- Excitation is shown to have some dependency on interaction stage, while as the merging process reaches Class II, the age of stellar population drops, and diagnostic in both log([NII]/Hα) and log([OI]/Hα) is shown to be HII dominated. Monreal-Ibero et al. (2010) does not observe same changes in log([NII]/Hα) with interaction in a LIRG sample similar to that of our SUNBIRD sub-sample. A difference in methodology of measuring line ratios, where they do not correct for underlying absorption lines could be a reason of such discrepancy. The post merging phase class, shows a tendency to have lines in composite or AGN areas of diagnostics. The entire evolution of the line ratios across different interaction stages is in line with the merging scenario put forward by Hopkins et al. (2008).

- The sSFR intensity in LIRGs is high with nuclear values being 1.45 times higher than values obtained for normal SF galaxies in the CALIFA sample. The outer regions of our galaxies are also highly active in SF being either higher or on par with the intensity of the

nuclear regions of a control sample from Barrera-Ballesteros et al. (2015). By studying the impact that interaction has on sSFR, it is found that nuclear region experiences a continued Starburst period even in the post-merger phase while, for outer regions of the galaxies see an increase in SF-activity only at the stages prior to coalescence and sSFR drops back in the post merging phase.

- The oxygen abundance gradient is derived and shown to be consistent though slightly lower than in Rich et al. (2012). Interaction stages seems to lower gas-phase abundances, and a likely reason put forward for that is tidally induced low metallicity gas inflows.

- The relatively flat gas-phase metallicity gradient indicates that metallicity values derived for integrated apertures are reasonably accurate. This validates the accuracy of our data for the updated version of Mass-Metallicity relation that we derived in Chapter 4. The implication of this newer relation is that the under-abundance of LIRGs and possibly ULIRGs has been overestimated previously.

Chapter 6

Conclusions and perspectives

6.1 Introduction

This chapter is the final part of this thesis. It highlights the most important results from this work as well as gives some perspective on the future possibilities that will be possible with current and future generation instruments.

6.2 Thesis Summary

In the past 40 years, infrared astronomy has developed significantly after the Infrared Astronomical Satellite (IRAS) surveyed the sky, and formalised the impact of IR dominated galaxies in the universe. Based on these early works (Sanders & Mirabel, 1996) came the identification of Luminous Infrared Galaxies (LIRGS), $L_{IR} > 10^{11} L_{\odot}$, and their higher energy counterparts, the Ultra-LIRGs (ULIRGs), $L_{IR} > 10^{12} L_{\odot}$, which were shown to play a fundamental role in the mass assembly of the universe, in the earlier days of the universe. Studying galaxies at high redshift is both limited in terms of resolution, and the signal-to-noise ratio. This makes it essential to study local galaxies for physical intricacies, before then using that knowledge to understand their high redshift counterparts. LIRGs have been shown to play a crucial role in the cosmic star formation history of the universe mainly due to their highly interacting nature, often placing them in mergers. This highly active nature makes them the perfect candidates to study star formation at different scales; from the disk instabilities that leads to the formation of Giant Molecular Clouds and Super Star Clusters, to the larger scale impact of feedback processes such as Active Galactic Nuclei or tidally induced gas inflows or gas outflows.

The work done in this thesis has focused on characterising the behaviour of LIRGs in multi-faceted approach using spectroscopic data. With the advent of computational power over the last two decades, several techniques were developed to study the stellar population of clusters

and galaxies. While much research has been carried out on ellipticals and spirals, studies on the stellar populations of LIRGs have been very few, mostly exploratory. The main aim of this work was to bridge that gap and base our understanding of LIRGs, by first modelling their stellar populations, and then studying any other aspects that ensues. To this end, data were collected for the ongoing SUperNovae and starBursts in the InfraReD (SUNBIRD) survey, from SALT using the Robert Stobie Spectrograph. A representative sample of 52 galaxies was identified, in a luminosity distance range of 3.5 Mpc up to 280 Mpc and infrared luminosity in the range $10.30\ L_{\odot} < L_{IR} < 11.91\ L_{\odot}$. The galaxies are therefore just short of the ULIRG threshold but samples the starburst dominated regime nicely. The galaxies were selected to cover a wide and diverse range of interaction stages and morphologies.

Spectroscopic data reduction techniques applied to SALT/RSS data were discussed in detail in Chapter 2. First, the stratagem used for optimal data acquisition on SALT was shown, then, since it became clear that the amount of data was too large to handle on a case by case basis, a data reduction pipeline was written. The pipeline allowed for consistent data quality throughout the different steps of data reduction while also providing estimates for uncertainty on the output science frames. In short, the data acquired at the telescope were flat-fielded, cleaned from cosmic-rays, wavelength calibrated, sky-background subtracted, corrected for any tilt in the spectrograph using the pipeline. The data were also aligned and combined in cases where several frames were observed to increase the signal-to-noise ratio. Beyond that, relative flux calibration and correction for the extinction of the Milky Way were applied. To end, we were able to produce science quality spectroscopic data, acquired using the grating PG0900 at a resolution of $0.91\,\mathring{A}$ covering a wavelength range of $3640 - 6740\,\mathring{A}$ in the galaxies rest-frame. This wavelength range is wide enough to observe lines from [OII] $\lambda\,3727$ up until just after [NII] $\lambda\,6584$.

In Chapter 3, the methodologies upon which the entire work of this thesis is built are explored. First, the workhorse of this thesis, stellar population synthesis, is discussed in depth by reviewing key ingredients such as Stellar tracks and libraries and the IMF. A BC03 base which covers the entire wavelength range of our data is chosen as the stellar population template of this thesis. The base covers stellar ages from 1 Myr to 13 Gyr and beyond, making use of a Chabrier IMF and Padova 94 stellar tracks. To perform the stellar population fitting, STARLIGHT is chosen because of its ease of use and extensive use in literature. One of the drawbacks is the lack of uncertainty provided by the software, but a Monte Carlo method is implemented to run the software several times on the same data with added noise on top. The cumulative effect of both the amount of apertures to fit with STARLIGHT as well as the Monte Carlo method for uncertainty determination, meant that a pipeline for the software had to be written so that it could run in parallel on computer clusters. To test the pipeline, a mock dataset is created by

adding different levels of noise that mimics SALT data quality, on to SSPs, before feeding the dataset to STARLIGHT. The testing results show that median values of both Age and Metallicities are recovered at an accuracy of $< 1\%$ and $< 3\%$ respectively. SFH of typical galaxies along the Hubble sequence taken from the SDSS are analysed to create a baseline for comparison. After the stellar population is derived, it is subtracted from the original galaxy spectrum to create a pure emission line spectrum. By using self-implemented Gaussian fitting routines, the emission lines are automatically measured. From the line intensities of hydrogen lines, the Balmer decrement is calculated through an iterative process. A review of the different oxygen abundance calibrators is given as well as how different ionising mechanisms are distinguished from one another through the use of the BPT diagrams.

6.2.1 Integrated characteristics of IR-dominated galaxies

Integrated characteristics are important and interesting as they reflect the state of a galaxy as a whole, which then allows for comparisons with surveys at higher redshifts where only broad properties can be measured, or with older surveys when telescopes were less powerful. After fitting for the stellar population of the entire sample, the data of only one target was deemed unusable out of 53 different objects. The findings of the integrated properties analysis are listed below:

- The median light-weighted and mass-weighted ages were found to be 160 Myr and 7.2 Gyr respectively, which are extremely young values in both cases hinting at the intense SF-activity. By grouping the stellar populations into four bins, at ages of < 15 Myr, $15 - 150$ Myr, $150 - 1000$ Myr and > 1000 Myr, and then comparing their light fractions, we find that in most cases the very young and very old populations are always present, while intermediate ages have moderate influence on the life of local SF galaxies. The same picture is also painted by analysing the SFH of the SUNBIRD sub-sample where, the SFR of LIRGs and SF-dominated galaxies across time, slowly decays from the peak at the start of their lifetimes in very similar way to ellipticals. Then, in general, in the past ~ 50 Myr the SF-activity rises slowly, but gets even more active in the past 3 Myr when there is an order of magnitude rise in the intensity of Star forming activity.

- The stellar metallicity of the sample is shown to be sub-solar at 0.73 $Z_{\odot}$ when weighted by light, while the mass weighted metallicity is found to be super-solar at 1.29 $Z_{\odot}$. Since in the first case, younger stellar populations are weighted higher, while in the latter one, the weighting is more biased towards older stellar populations, the 'discrepancy' indicates that the younger stellar populations are made up from purer gas than the older generation of stars. We infer that one possibility for this to happen involves metal poor gas inflows

which then triggers the newer SF episodes in our sample of galaxies. By comparing the Mass-Stellar Metallicity relation of our sample with work done by López Fernández et al. (2016) it is inferred that the majority of the galaxies in our sample are Sa-Sbc on the Hubble sequence.

- The sSFR of SUNBIRD is measured to be 2.60×10^{-10} yr^{-1} which is equivalent to a mass doubling rate of 3.9 Gyr. In comparison, this amounts to $2 - 2.5$ times more than what is measured in main sequence galaxies using the same method while still lower than the intensity of GOALS sample which contains more intensely SF galaxies. By using the BPT diagram for objects where line ratio measurements are possible, it is found that $\sim 64\%$ of galaxies of our sample are dominated by SF, while $\sim 31\%$ are composite galaxies, and only $\sim 4\%$ are AGN driven objects.

- By measuring the oxygen abundances through a number of calibrators and then converting them to the same base, using the work of Kewley & Ellison (2008), a more stable mean O3N2 indicator is derived. Using the K-band derived mass, the M-Z relation of SUNBIRD is compared with the latest M-Z relation from the CALIFA sample. It is shown that our sample of galaxies are under-abundant by ~ 0.1 dex, which is in conflict with the works from Rupke et al. (2008). While there are differences in the sample selection of galaxies, we estimate they should not amount to that size of a discrepancy. This points to the fact that Rupke et al. (2008) have overestimated the difference between the expected M-Z relation and the abundance of LIRGs and ULIRGs, especially since they used the work of Tremonti et al. (2004), who used a Bayesian approach to derived their oxygen abundances, which is known to overestimate metallicity as compared to direct methods.

6.2.2 Spatially resolved characteristics of IR-dominated galaxies

Spatially resolved analysis offers a different perspective to that of integrated ones as it allows for us to find global structures in different interesting parameters. Out of the 52 targets, 353 spatially distinct apertures were extracted and fed to the STARLIGHT pipeline. An 11 % goodness of fit cut was applied as a quality control measure, which brought down the number of apertures to 326. After obtaining the effective radius from 2MASS K-band catalogue, the data were analysed to find radial gradients, but also to find if interaction classes differ from one another in their behaviours. The main results are:

- The combined age profile of all galaxies in the SUNBIRD sub-sample is relatively flat and very similar to the type of gradients observed in two LIRGs in the work of Cortijo-Ferrero et al. (2017). When compared with the work of González Delgado et al. (2015) who classified the age gradients for the Hubble sequence, our galaxies are closer to the

Late-Type, Sd galaxies. This result can be explained by the highly interacting nature of SF galaxies and LIRGs as interaction changes a lot to the more 'standard' relaxed type galaxies where gradients are usually observed. Apart from the gradient a noticeable drop in age is seen when the different apertures are classified by the different interaction classes. At both ends of the interaction stages, where galaxies are more relaxed, the mean ages are higher, while the stages where interaction is playing an active role galaxies' dynamics, the ages observed are lower. We infer that tidally induced star formation plays a crucial role in lowering the ages when interaction is at play.

- The overall stellar metallicity ($\nabla\langle Z_m\rangle$) is found to be -0.029 ± 0.018 dex/kpc. Also, when comparing the metallicity gradient (in this case $\nabla\langle\log(Z_m)\rangle$ with CALIFA data, the gradient of our sample is found to be very similar to Sb or Sbc galaxies. The negative metallicity gradient is an indicator of inside-out galaxy formation scenario, where the galaxies cores form earlier and get more evolved than the outer regions of the galaxies. By analysing the impact that interaction stage has on both age and metallicity, it is found that isolated cases have deeper and more pronounced gradients in both parameters. As the interaction stage increases and gets more active, the gradients for both parameters becomes flatter, until in the last stage of interaction, they become slightly positive. These findings are in agreement with other observations and simulations.

- In terms of ionisation, no radial dependence is found. At different distance bins the distribution of points on the BPT diagram is more or less similar to one another. On the other hand, interaction stage has an influence on the ionising mechanism present in galaxies, with the two stages where interaction force is stronger, HII is the dominant mechanism present. Meanwhile the stages prior to interaction and post merging, more areas are either AGN driven or a mixture of HII and either shock or some AGN activity being involved.

- The SUNBIRD sub-sample is shown to have high intensity sSFR in the nuclear regions. Interestingly, evidence is found that sSFR is extended during in the Class II of interaction, while in the post merger phase, the sSFR remains at a high level in the nuclear region but drops considerably in the outer regions.

- Oxygen abundance is also shown to have a small negative radial gradient, which is consistent with literature. The more advanced the interaction stage of our sample, the lower the gas phase abundance which also points to tidally induced star formation just like the analysis of integrated stellar metallicities. The very mild negative gradient of abundance, suggest that our derived integrated gradients are very representative of nuclear metallicities as well, which would validates our M-Z relation.

6.3 Future prospects

After having worked on the understanding of the physics behind the galaxies involved in the SUNBIRD sub-sample for the past few years, there are still much more that could be done. For starters, during the course of this thesis, we collected photometric data in all the optical bands (UBVRI) as well as in the infrared (JHK) for the same sample of galaxies. With the photometric bands, by applying SED fitting with a software like Magphys (da Cunha et al., 2008), one could recover the stellar mass of the sample giving better constraints to the M-Z relation that we derived for example. SED modelling also allows the dust modelling and determining dust contents of galaxies. As we saw from this thesis, at the low end of sSFR, it was not entirely clear if the two-component dust model was still applicable, which is why studying the dust is essential. Work from Pereira-Santaella et al. (2015) showed that the SFH of LIRGs can be recovered from SED fitting as well, which could be used to validate the current results, obtained through spectral synthesis modelling.

Medium resolution spectroscopic data using PG1800 were also collected from SALT, during the course of this thesis, at similar settings to that of PG0900 involved in the current work. With the PG1800 data, we are currently deriving the stellar kinematics and velocity dispersion of our sample (Sisay et al. in prep.) through the study of rotation curves. By analysing the stellar kinematics the detection of gas inflows/outflows would become more evident, which then could be in principle linked to the interaction stages of our sample. PG1800 has also access to [SII] lines that could be added as the third BPT diagnostic to resolve some of the ambiguous cases, where we are not sure which ionising mechanisms are dominant. By deriving the dynamical masses of SUNBIRD galaxies, from the PG1800, we could address a mass-controversy evident in the literature (Rothberg & Joseph, 2006), where one method derives much higher masses for gas-rich spiral galaxy mergers than the other method, which impacts the models of early-type galaxy formation.

In the broader perspective, with the extension of current surveys or with upcoming projects such as as SAMI (Croom et al., 2012), CALIFA (Sánchez et al., 2012), and MANGA (Bundy et al., 2015) optical datasets involving highly SF-galaxies or (U)LIRGs will be available at different redshifts in IFU datasets which offers better ability to separate independent HII regions from one another (as opposed to long-slit spectroscopy). A study on the stellar population of these types of galaxies at different epochs of the universe would be interesting given the context of how the peak of star formation happened at $z \sim 2$. This could help the understanding of how the chemical enrichment of galaxies affect the efficiency of star formation as well. In radio for example, we have seen that with KAT-7 that it was possible to identify starburst outflows (Lucero et al., 2015). With the upcoming MeerKAT which is expected to start observing later

this year and which will be much more sensitive that KAT-7, better quality data is expected and should allow us to study SF-galaxies in greater details. Surveys like MHONGOOSE will help our understanding of how molecular gas is linked to neutral hydrogen and how the latter is transformed into stars.

To end, humanity's journey to understand the universe has been a long and tedious one for the most part. But over the past few centuries, collectively because of the scientific enlightenment, we have been blessed to be able to stand over the shoulders of giants, which allowed us a more formal understanding of our surroundings through reasoning, mathematics, science, physics and statistics. This is the legacy that was handed to us, and it is a privilege time to be alive and to try to answer questions about the nature of the universe. As Carl Sagan said: " Somewhere, something incredible is waiting to be known."

Appendices

NOTE

While some extra plots are provided in the following pages, all the relevant plots and data for this thesis are found at the following repository:

https://cloudcape.saao.ac.za/index.php/s/0Y5u5JbL2r5qLHh

This is done, to keep the size of this thesis to a standard amount. If for any reasons, you have trouble accessing the folder, please feel free to contact me at: rajin250@yahoo.com

Appendix A

Finding Charts (From Chapter 2)

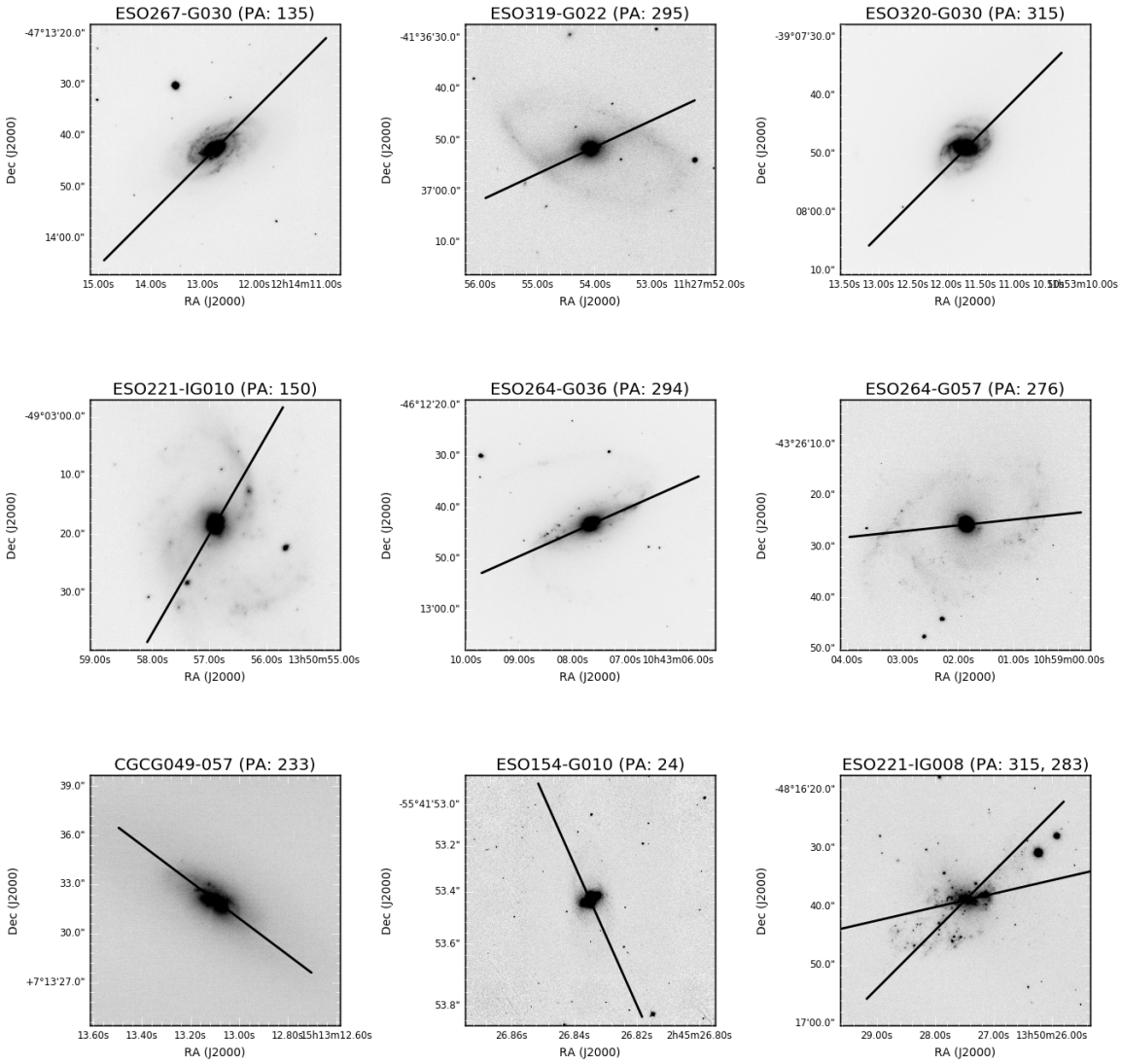

Figure A.1: Finding charts showing slit positions when observing the targets. Name of targets and position angle given above each plot - part1

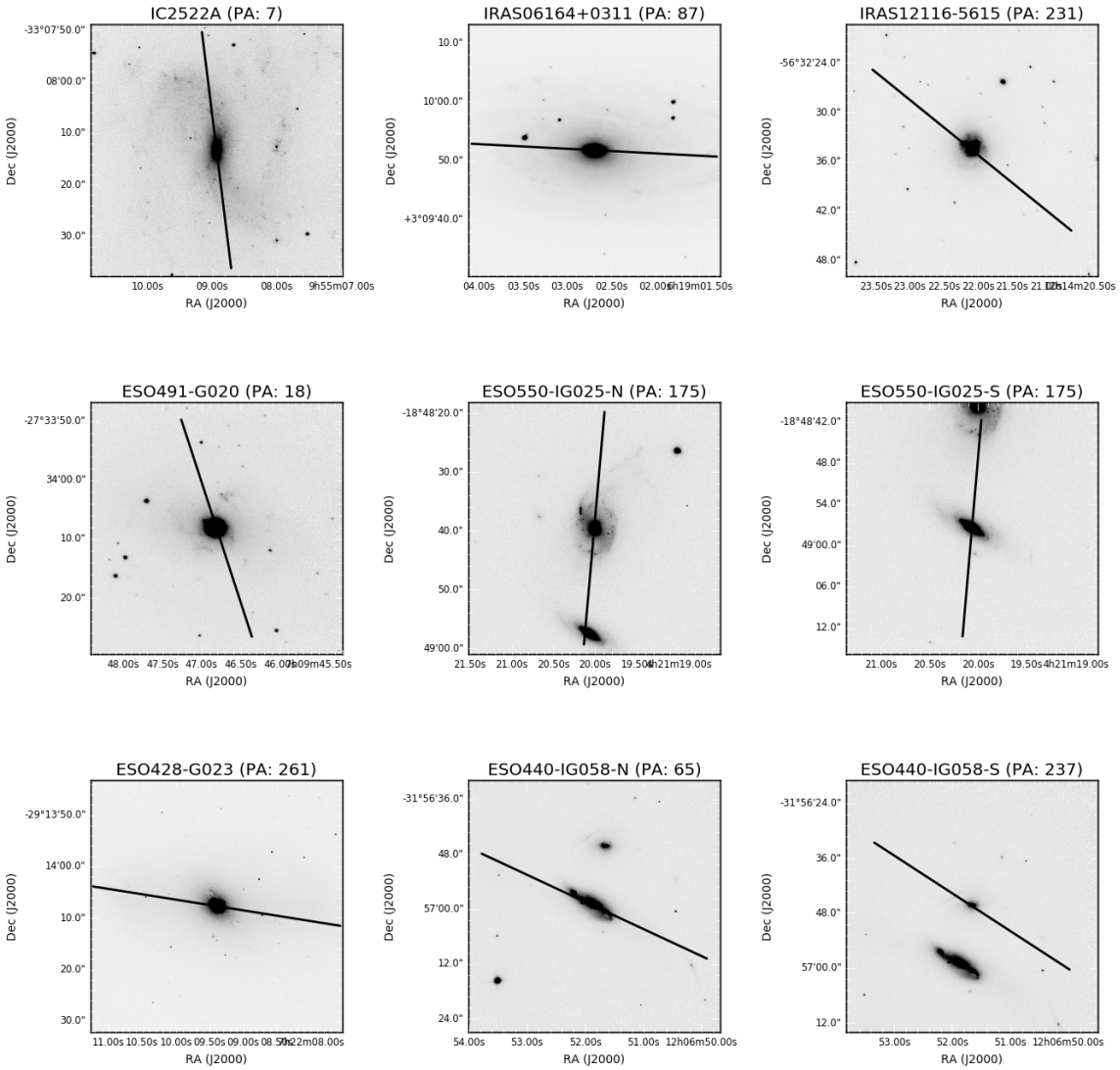

Figure A.2: Finding charts showing slit positions when observing the targets. Name of targets and position angle given above each plot - part2

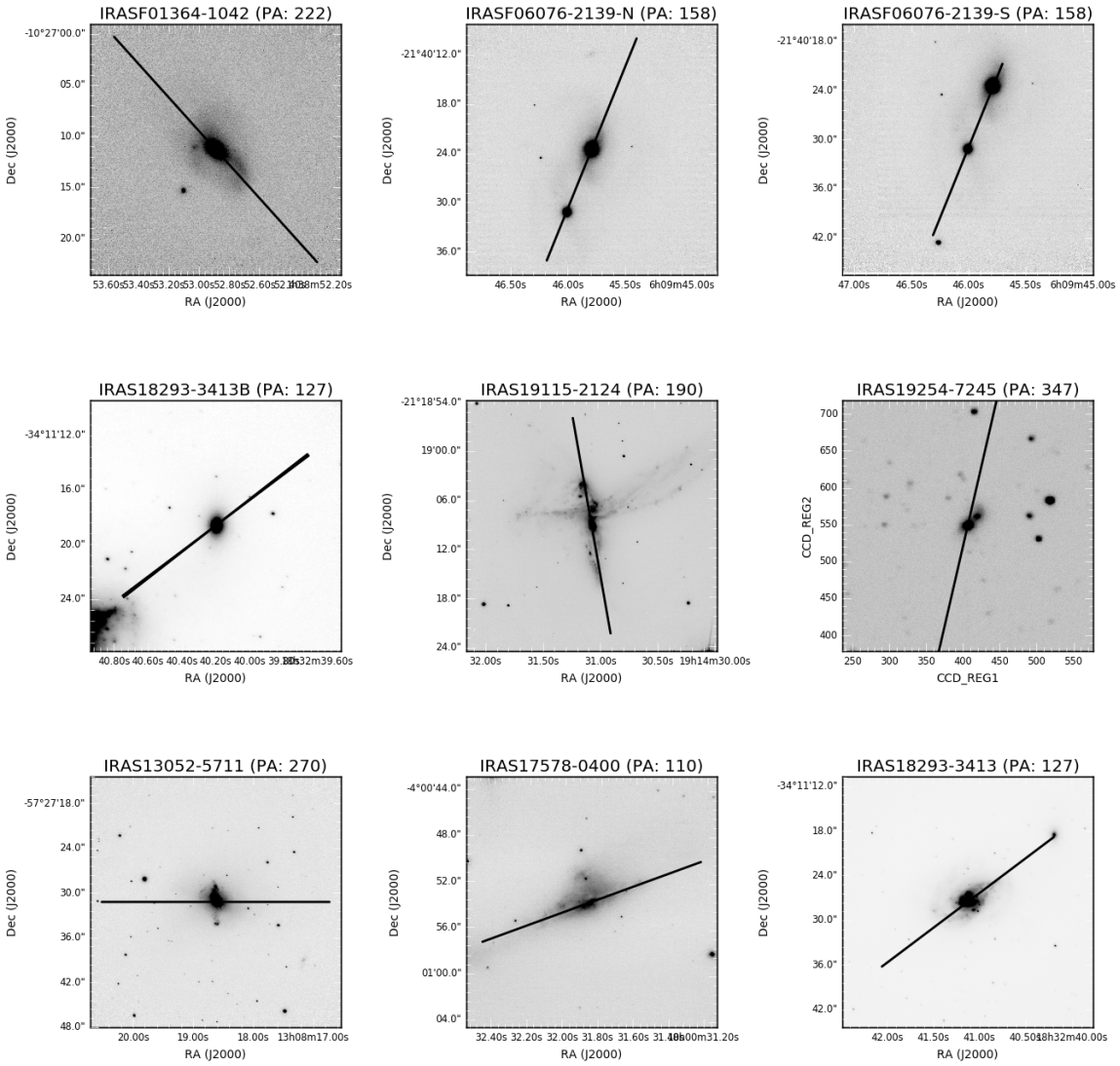

Figure A.3: Finding charts showing slit positions when observing the targets. Name of targets and position angle given above each plot - part3

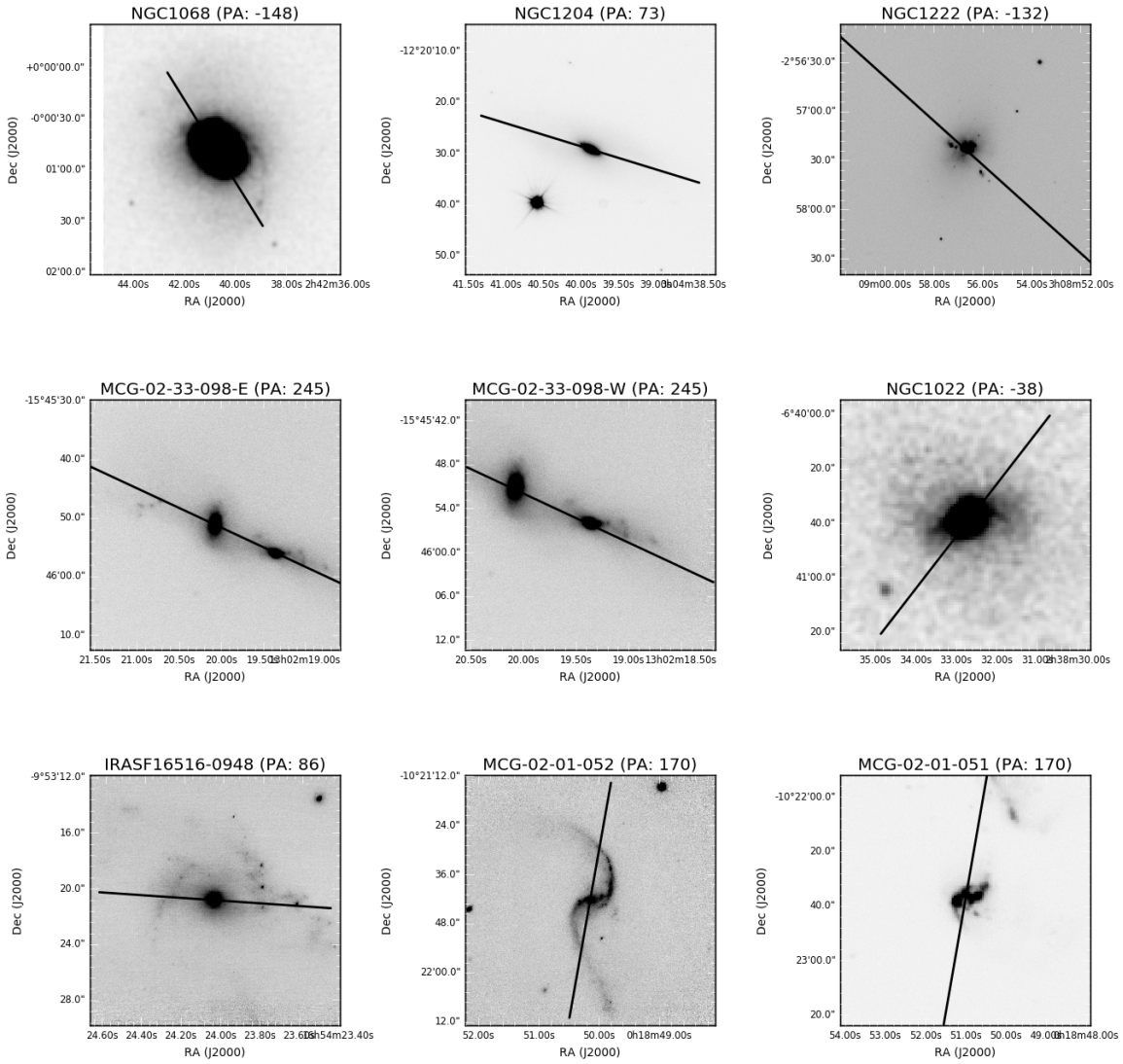

Figure A.4: Finding charts showing slit positions when observing the targets. Name of targets and position angle given above each plot - part4

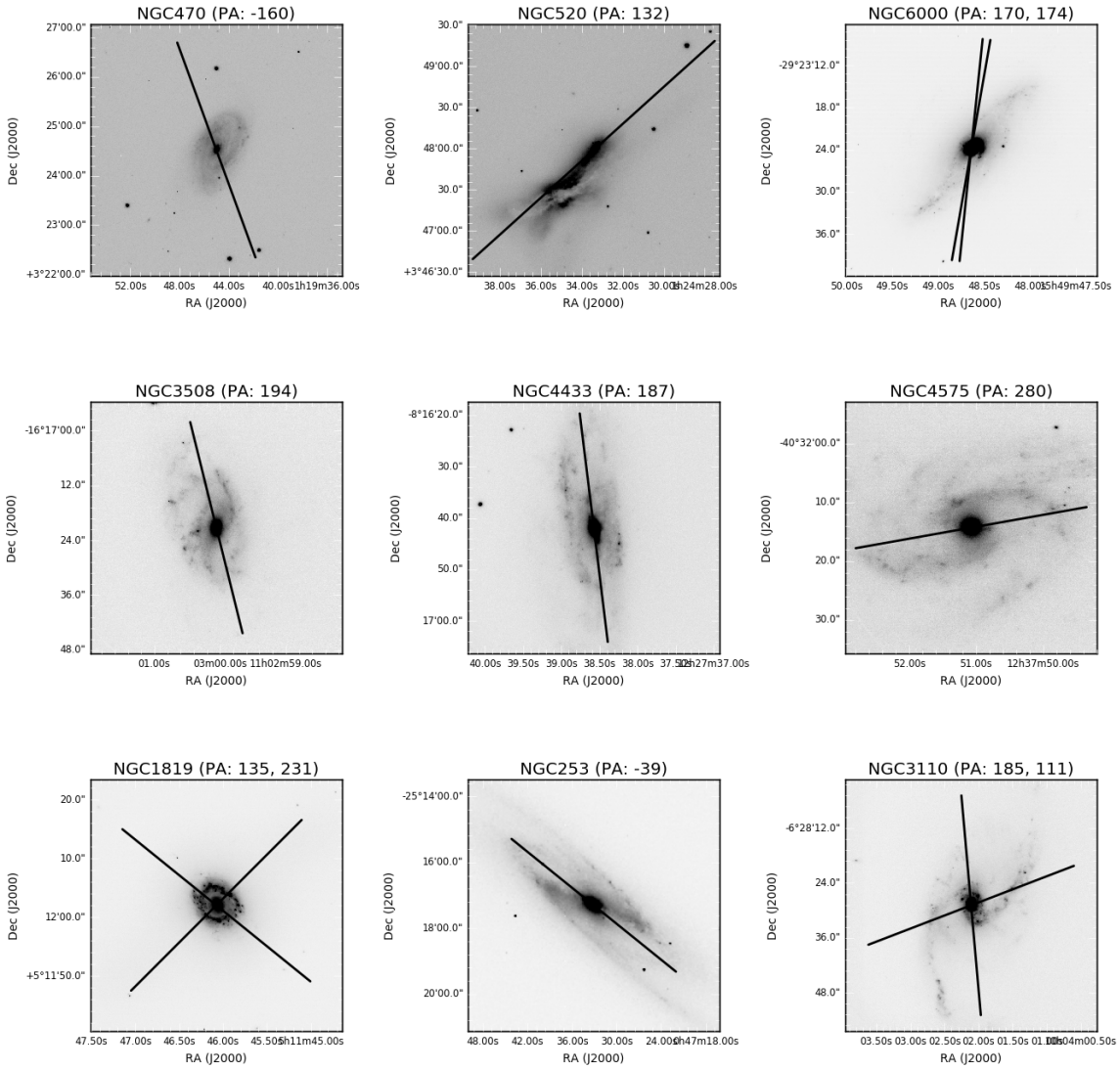

Figure A.5: Finding charts showing slit positions when observing the targets. Name of targets and position angle given above each plot - part5

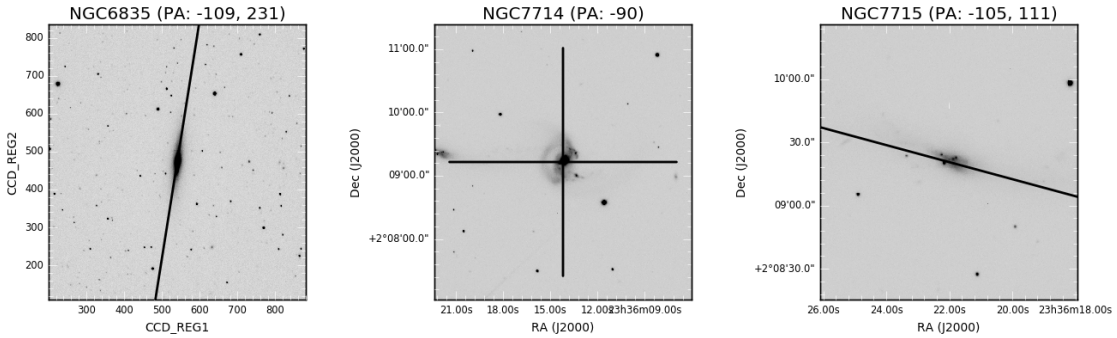

Figure A.6: Finding charts showing slit positions when observing the targets. Name of targets and position angle given above each plot - part6

Appendix B

STARLIGHT pipeline testing results (From Chapter 3)

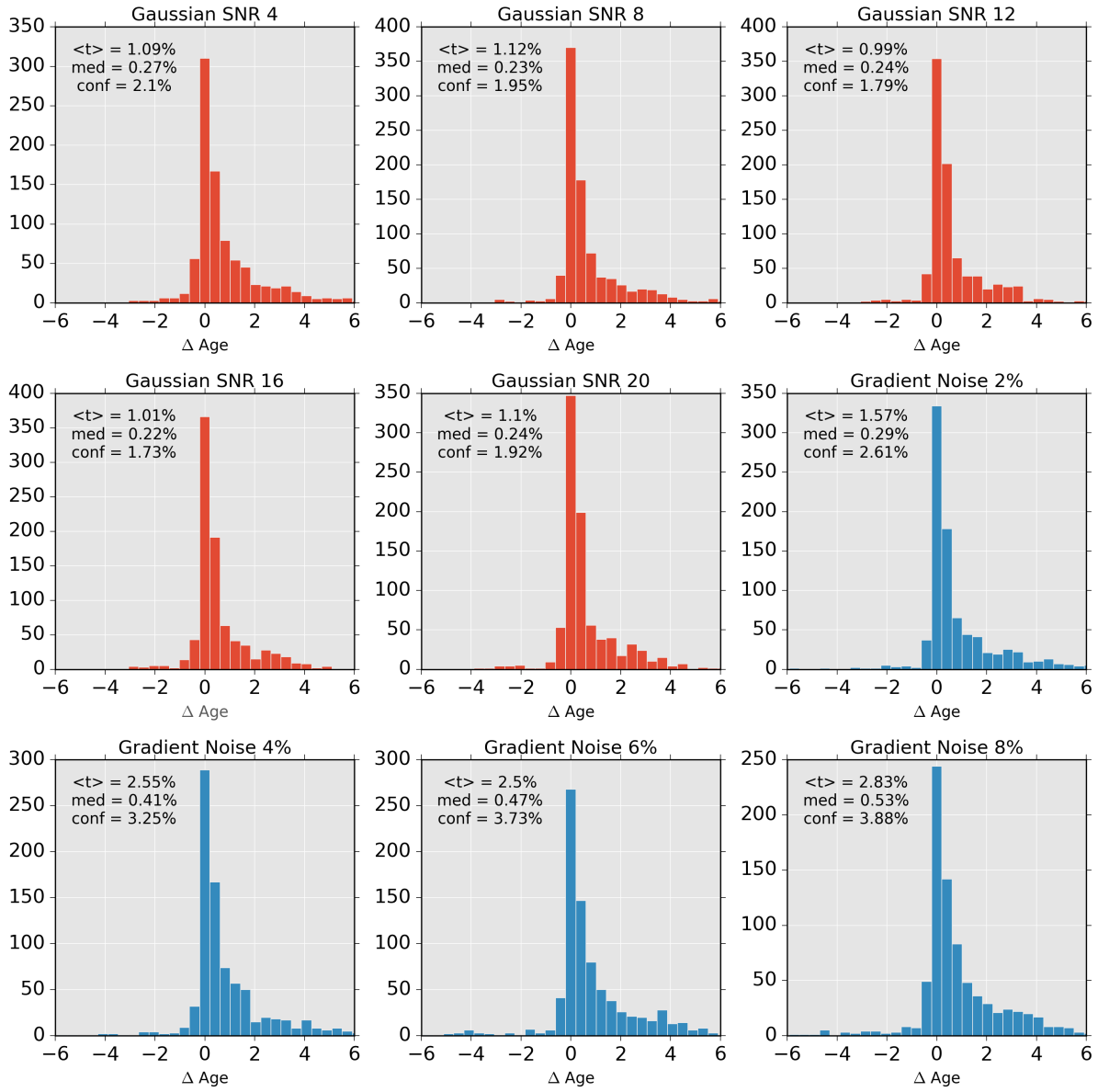

Figure B.1: Distributions of Mass-Weighted Ages (given in percentages deviations) for the different noise level SSP fittings. Red histograms are for Gaussian noise while blue is for gradient noise.

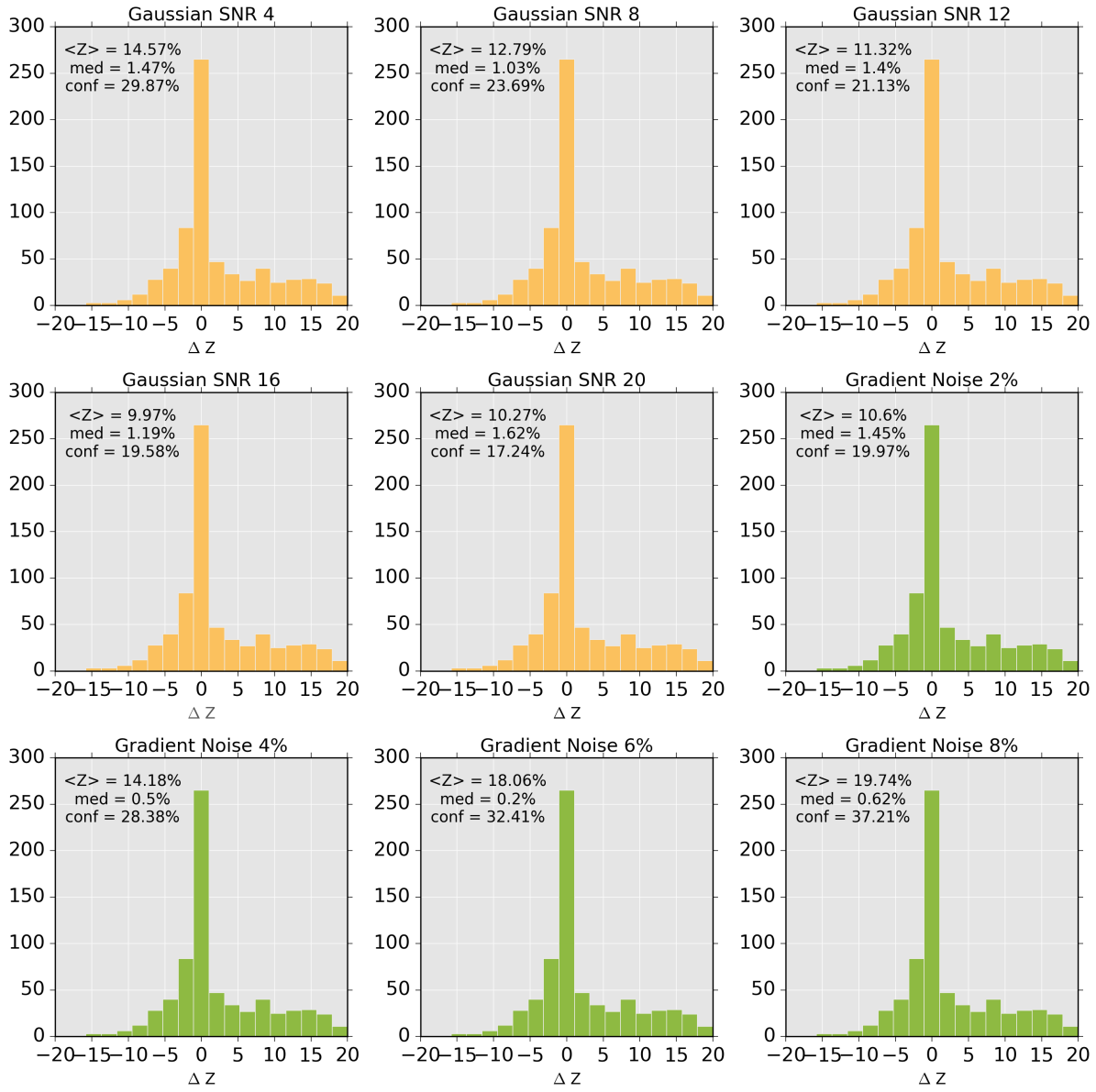

Figure B.2: Distributions of Light-Weighted Metallicities (given in percentages deviations) for the different noise level SSP fittings. Yellow is for Gaussian noise while green is for gradient noise.

Appendix C

Emission line Measurements (From Chapter 4) and other integrated related data

Table C.1: Radius of the extracted integrated apertures given in Effective radius. The median extracted radii is 2.23 R_{eff} for the entire sample

Name	**Extr. Rad. (R_eff)**	**Name**	**Extr. Rad. (R_eff)**
CGCG049-057	3.370	IRAS19115-2124	3.066
ESO154-G010	2.343	IRAS19254-7245	3.556
ESO221-IG008	4.330	IRASF01364-1042	3.679
ESO221-IG008	3.706	IRASF06076-2139-S	3.951
ESO221-IG010	1.970	IRASF06076-2139-N	1.949
ESO264-G036	1.759	IRASF16516-0948	1.481
ESO264-G057	1.735	IRASF17138-1017	0.700
ESO267-G030	2.225	MCG-02-01-052	2.161
ESO319-G022	1.336	MCG-02-01-051	1.660
ESO320-G030	3.859	MCG-02-33-098-E	2.574
ESO428-G023	0.977	MCG-02-33-098-W	3.329
ESO440-IG058-N	3.112	NGC1022	0.312
ESO440-IG058-S	4.321	NGC1068	3.418
ESO491-G020	1.473	NGC1204	2.436
ESO550-IG025-N	2.552	NGC1222	2.835
ESO550-IG025-S	6.509	NGC1819	2.159
IC2522	1.001	NGC253	0.378
IC2522B	2.637	NGC3110	1.927
IRAS06164+0311	0.564	NGC3508	2.522
IRAS12116-5615	1.934	NGC4433	2.319
IRAS13052-5711	1.755	NGC4575	1.964
IRAS17578-0400	2.391	NGC470	0.528
IRAS17578-0400-W	2.335	NGC520	2.001
IRAS17578-0400-E	2.688	NGC6000	1.279
IRAS18293-3413	5.040	NGC6835	1.485
IRAS18293-3413B	7.100	NGC7714	1.771
		NGC7715	1.699

Table C.2: SUNBIRD emission line flux measurements part 1.

Name	**[OII]λ3727**	$H\delta$ **λ4101**	$H\gamma$ **λ4340**	$H\beta$ **λ4861**	**[OIII]λ4959**	**[OIII]λ5007**
NGC7714C	-	0.192 ± 0.031	0.439 ± 0.025	1.0 ± 0.019	0.230 ± 0.018	1.056 ± 0.028
NGC7714B	-	-	-	0.0 ± 0.000	-	-
NGC7714A	0.936 ± 1.627	0.273 ± 0.010	0.474 ± 0.008	1.0 ± 0.006	0.678 ± 0.007	1.967 ± 0.015
NGC6835	-	0.307 ± 0.023	0.588 ± 0.019	1.0 ± 0.011	0.164 ± 0.009	0.324 ± 0.009
NGC6000	0.659 ± 0.080	0.347 ± 0.016	0.515 ± 0.012	1.0 ± 0.008	0.069 ± 0.006	0.167 ± 0.005
NGC520	0.607 ± 0.095	0.363 ± 0.042	0.421 ± 0.035	1.0 ± 0.026	0.112 ± 0.021	0.574 ± 0.025
NGC470	0.706 ± 0.117	0.323 ± 0.015	0.497 ± 0.011	1.0 ± 0.009	0.048 ± 0.006	0.143 ± 0.006
NGC4575	0.757 ± 0.067	0.307 ± 0.018	0.526 ± 0.015	1.0 ± 0.010	0.096 ± 0.007	0.275 ± 0.007
NGC4433	1.768 ± 0.156	0.284 ± 0.015	0.496 ± 0.013	1.0 ± 0.009	0.166 ± 0.007	0.502 ± 0.008
NGC3508	1.474 ± 0.096	0.300 ± 0.012	0.494 ± 0.009	1.0 ± 0.007	0.173 ± 0.006	0.508 ± 0.006
NGC3110	1.299 ± 0.111	0.295 ± 0.011	0.511 ± 0.009	1.0 ± 0.006	0.094 ± 0.005	0.303 ± 0.005
NGC253	1.376 ± 0.102	0.329 ± 0.028	0.529 ± 0.023	1.0 ± 0.015	0.147 ± 0.010	0.386 ± 0.012
NGC1819	0.517 ± 0.045	0.382 ± 0.015	0.541 ± 0.011	1.0 ± 0.007	0.085 ± 0.006	0.248 ± 0.006
NGC1222	-	0.262 ± 0.018	0.461 ± 0.016	1.0 ± 0.012	0.850 ± 0.015	2.487 ± 0.035
NGC1204	4.301 ± 0.240	0.496 ± 0.058	0.861 ± 0.039	1.0 ± 0.020	0.115 ± 0.019	0.537 ± 0.019
NGC1068	1.403 ± 0.077	0.393 ± 0.027	0.572 ± 0.025	1.0 ± 0.019	0.725 ± 0.019	2.070 ± 0.042
NGC1022	0.299 ± 0.104	0.259 ± 0.029	0.487 ± 0.021	1.0 ± 0.013	0.070 ± 0.010	0.221 ± 0.011
MCG-02-33-098B	4.267 ± 0.205	0.493 ± 0.047	0.607 ± 0.035	1.0 ± 0.020	0.127 ± 0.017	0.485 ± 0.018
MCG-02-33-098A	2.495 ± 0.259	0.282 ± 0.019	0.543 ± 0.014	1.0 ± 0.010	0.264 ± 0.008	0.850 ± 0.011
MCG-02-01-052B	1.892 ± 0.249	0.259 ± 0.011	0.455 ± 0.009	1.0 ± 0.008	0.401 ± 0.007	1.229 ± 0.012
MCG-02-01-052A	1.128 ± 0.083	0.265 ± 0.008	0.447 ± 0.007	1.0 ± 0.005	0.308 ± 0.004	0.922 ± 0.007
IRASF17138-1017	-	-	-	1.0 ± 0.047	0.129 ± 0.034	0.526 ± 0.040
IRASF16516-0948	1.721 ± 1.117	0.117 ± 0.046	0.466 ± 0.030	1.0 ± 0.016	0.242 ± 0.010	0.749 ± 0.016
IRASF06076-2139B	2.645 ± 0.444	0.319 ± 0.070	0.525 ± 0.051	1.0 ± 0.026	0.201 ± 0.024	0.518 ± 0.027
IRASF06076-2139A	1.722 ± 0.156	0.236 ± 0.020	0.486 ± 0.015	1.0 ± 0.011	0.255 ± 0.009	0.774 ± 0.013
IRASF01364-1042	6.067 ± 0.748	0.350 ± 0.066	0.754 ± 0.061	1.0 ± 0.041	0.345 ± 0.041	1.490 ± 0.075
IRAS19254-7245	-	-	0.328 ± 0.278	1.0 ± 0.143	0.723 ± 0.152	2.595 ± 0.392
IRAS19115-2124	-	0.201 ± 0.285	0.400 ± 0.125	1.0 ± 0.078	0.195 ± 0.064	0.632 ± 0.076
IRAS18293-3413B	1.194 ± 0.565	0.229 ± 0.192	0.495 ± 0.180	1.0 ± 0.120	0.157 ± 0.078	0.330 ± 0.063
IRAS18293-3413A	9.183 ± 20.430	3.070 ± 3.626	11.217 ± 14.234	1.0 ± 0.807	2.896 ± 3.807	9.342 ± 10.985
IRAS17578-0400B	1.475 ± 2.053	0.097 ± 0.094	0.338 ± 0.051	1.0 ± 0.021	0.302 ± 0.018	0.799 ± 0.022
IRAS17578-0400A	2.179 ± 1.244	0.225 ± 0.054	0.465 ± 0.038	1.0 ± 0.016	0.467 ± 0.013	1.476 ± 0.026
IRAS17578-0400	-	-	0.692 ± 0.270	1.0 ± 0.102	0.096 ± 0.089	0.417 ± 0.094
IRAS13052-5711	2.164 ± 0.173	0.191 ± 0.032	0.458 ± 0.026	1.0 ± 0.015	0.132 ± 0.011	0.525 ± 0.014
IRAS12116-5615	-	-	0.467 ± 0.092	1.0 ± 0.015	0.172 ± 0.011	0.527 ± 0.035
IRAS06164+0311	-	1.679 ± 0.613	-	1.0 ± 0.261	0.980 ± 0.316	1.084 ± 0.326
IC2522B	1.299 ± 0.210	0.329 ± 0.016	0.488 ± 0.014	1.0 ± 0.011	0.141 ± 0.008	0.523 ± 0.009
IC2522A	1.240 ± 0.045	0.336 ± 0.017	0.519 ± 0.015	1.0 ± 0.010	0.128 ± 0.008	0.341 ± 0.008
ESO550-IG025B	3.447 ± 1.037	0.116 ± 0.126	0.501 ± 0.104	1.0 ± 0.052	0.294 ± 0.046	0.749 ± 0.064
ESO550-IG025A	1.173 ± 0.399	0.210 ± 0.055	0.257 ± 0.032	1.0 ± 0.023	0.160 ± 0.014	0.354 ± 0.022
ESO491-G020	1.589 ± 0.197	0.238 ± 0.016	0.382 ± 0.014	1.0 ± 0.010	0.218 ± 0.007	0.774 ± 0.010
ESO440-IG058B	-	0.268 ± 0.056	0.461 ± 0.063	1.0 ± 0.011	0.138 ± 0.008	0.478 ± 0.020
ESO440-IG058A	1.551 ± 0.266	0.265 ± 0.027	0.462 ± 0.031	1.0 ± 0.006	0.248 ± 0.005	0.794 ± 0.015
ESO428-G023	0.251 ± 1.271	0.306 ± 0.017	0.539 ± 0.013	1.0 ± 0.009	0.152 ± 0.007	0.381 ± 0.007
ESO320-G030	0.718 ± 0.176	0.298 ± 0.014	0.477 ± 0.012	1.0 ± 0.009	0.083 ± 0.006	0.227 ± 0.006
ESO319-G022	1.343 ± 0.163	0.384 ± 0.036	0.514 ± 0.029	1.0 ± 0.018	0.061 ± 0.016	0.311 ± 0.015
ESO267-G030	0.772 ± 1.783	0.274 ± 0.063	0.453 ± 0.047	1.0 ± 0.031	0.285 ± 0.027	0.887 ± 0.037
ESO264-G057	0.943 ± 0.776	0.215 ± 0.079	0.456 ± 0.055	1.0 ± 0.026	0.074 ± 0.024	0.253 ± 0.022
ESO264-G036	0.926 ± 0.222	0.255 ± 0.032	0.441 ± 0.026	1.0 ± 0.015	0.092 ± 0.013	0.302 ± 0.011
ESO221-IG010	0.974 ± 0.225	0.289 ± 0.019	0.463 ± 0.014	1.0 ± 0.010	0.068 ± 0.006	0.248 ± 0.007
ESO221-IG008	1.935 ± 0.082	0.268 ± 0.014	0.468 ± 0.013	1.0 ± 0.009	0.709 ± 0.007	2.159 ± 0.020
ESO154-G010	-	0.624 ± 0.033	0.679 ± 0.029	1.0 ± 0.019	0.137 ± 0.017	0.661 ± 0.020
CGCG049-057	-	0.524 ± 0.111	0.550 ± 0.093	1.0 ± 0.051	0.060 ± 0.045	0.366 ± 0.045

Table C.3: SUNBIRD emission line flux measurements part 2.

Name	**[OI] λ6300**	**[NII] λ6548**	**$H\alpha$ λ6563**	**[NII] λ6583**	**C($H\beta$)**
NGC7714C	0.329 ± 0.015	0.302 ± 0.012	2.508 ± 0.051	0.996 ± 0.022	-
NGC7714B	-	-	-	-	-
NGC7714A	0.113 ± 0.003	0.269 ± 0.004	2.882 ± 0.003	0.726 ± 0.008	0.128 ± 0.011
NGC6835	0.106 ± 0.004	0.415 ± 0.007	2.926 ± 0.009	1.115 ± 0.018	0.745 ± 0.018
NGC6000	0.076 ± 0.003	0.607 ± 0.007	2.923 ± 0.008	1.665 ± 0.020	1.012 ± 0.013
NGC520	0.378 ± 0.018	0.693 ± 0.028	2.892 ± 0.013	1.514 ± 0.058	0.368 ± 0.041
NGC470	0.047 ± 0.003	0.423 ± 0.006	2.907 ± 0.007	1.187 ± 0.016	0.723 ± 0.015
NGC4575	0.141 ± 0.005	0.369 ± 0.006	2.910 ± 0.008	1.036 ± 0.015	0.879 ± 0.015
NGC4433	0.102 ± 0.003	0.362 ± 0.005	2.900 ± 0.008	1.020 ± 0.014	1.175 ± 0.015
NGC3508	0.108 ± 0.003	0.346 ± 0.004	2.899 ± 0.005	0.987 ± 0.010	0.869 ± 0.011
NGC3110	0.090 ± 0.002	0.422 ± 0.004	2.906 ± 0.006	1.166 ± 0.011	1.037 ± 0.011
NGC253	0.146 ± 0.006	0.637 ± 0.014	2.932 ± 0.017	1.798 ± 0.039	1.219 ± 0.024
NGC1819	0.093 ± 0.003	0.559 ± 0.006	2.933 ± 0.006	1.505 ± 0.016	0.804 ± 0.012
NGC1222	0.079 ± 0.004	0.182 ± 0.005	2.877 ± 0.006	0.461 ± 0.009	0.520 ± 0.020
NGC1204	0.240 ± 0.009	0.850 ± 0.026	3.303 ± 0.052	2.321 ± 0.070	1.633 ± 0.035
NGC1068	0.176 ± 0.008	0.812 ± 0.023	2.949 ± 0.014	2.200 ± 0.060	0.555 ± 0.030
NGC1022	0.086 ± 0.004	0.534 ± 0.010	2.886 ± 0.011	1.481 ± 0.028	1.216 ± 0.021
MCG-02-33-098B	0.132 ± 0.007	0.623 ± 0.019	3.054 ± 0.035	1.590 ± 0.048	1.314 ± 0.034
MCG-02-33-098A	0.072 ± 0.003	0.375 ± 0.006	2.909 ± 0.007	0.967 ± 0.014	0.829 ± 0.015
MCG-02-01-052B	0.127 ± 0.003	0.271 ± 0.004	2.875 ± 0.004	0.762 ± 0.009	0.560 ± 0.013
MCG-02-01-052A	0.070 ± 0.002	0.299 ± 0.003	2.876 ± 0.003	0.850 ± 0.007	0.396 ± 0.009
IRASF17138-1017	0.084 ± 0.006	0.445 ± 0.030	2.878 ± 0.002	1.330 ± 0.090	2.761 ± 0.075
IRASF16516-0948	0.124 ± 0.004	0.357 ± 0.009	2.867 ± 0.009	0.964 ± 0.023	1.040 ± 0.026
IRASF06076-2139B	0.202 ± 0.011	0.836 ± 0.032	2.922 ± 0.034	2.407 ± 0.092	1.458 ± 0.043
IRASF06076-2139A	0.134 ± 0.005	0.588 ± 0.011	2.880 ± 0.006	1.485 ± 0.025	0.654 ± 0.018
IRASF01364-1042	-	-	-	-	0.000 ± 0.181
IRAS19254-7245	0.400 ± 0.082	1.444 ± 0.303	2.798 ± 0.170	-	2.400 ± 0.240
IRAS19115-2124	0.128 ± 0.026	0.431 ± 0.051	2.851 ± 0.070	1.207 ± 0.138	1.214 ± 0.127
IRAS18293-3413B	0.156 ± 0.040	0.255 ± 0.022	2.934 ± 0.163	1.244 ± 0.193	1.677 ± 0.193
IRAS18293-3413A	3.726 ± 4.064	2.044 ± 1.692	12.650 ± 9.900	8.795 ± 9.692	0.757 ± 0.432
IRAS17578-0400B	0.063 ± 0.004	0.304 ± 0.010	2.863 ± 0.005	0.835 ± 0.025	0.514 ± 0.034
IRAS17578-0400A	0.069 ± 0.003	0.234 ± 0.006	2.877 ± 0.005	0.594 ± 0.014	0.254 ± 0.025
IRAS17578-0400	0.080 ± 0.019	0.379 ± 0.057	2.928 ± 0.079	1.143 ± 0.168	0.848 ± 0.162
IRAS13052-5711	0.162 ± 0.005	0.601 ± 0.014	2.867 ± 0.007	1.577 ± 0.035	0.814 ± 0.025
IRAS12116-5615	-	-	-	-	1.933 ± 0.922
IRAS06164+0311	0.509 ± 0.188	-	4.068 ± 0.723	1.735 ± 0.638	0.757 ± 0.396
IC2522B	0.096 ± 0.005	0.307 ± 0.007	2.899 ± 0.006	0.793 ± 0.013	0.416 ± 0.018
IC2522A	0.105 ± 0.004	0.409 ± 0.007	2.915 ± 0.008	1.140 ± 0.017	0.799 ± 0.016
ESO550-IG025B	-	-	-	-	0.909 ± 0.664
ESO550-IG025A	-	-	-	-	1.073 ± 0.647
ESO491-G020	0.076 ± 0.003	0.353 ± 0.006	2.857 ± 0.004	0.895 ± 0.014	0.587 ± 0.016
ESO440-IG058B	-	0.714 ± 0.255	-	-	1.010 ± 0.563
ESO440-IG058A	-	-	-	-	0.424 ± 0.256
ESO428-G023	0.112 ± 0.003	0.631 ± 0.008	2.916 ± 0.007	1.790 ± 0.022	0.945 ± 0.014
ESO320-G030	0.087 ± 0.004	0.473 ± 0.006	2.895 ± 0.007	1.340 ± 0.017	1.008 ± 0.014
ESO319-G022	0.103 ± 0.007	0.869 ± 0.023	2.941 ± 0.020	2.211 ± 0.058	1.090 ± 0.029
ESO267-G030	0.090 ± 0.009	0.455 ± 0.022	2.878 ± 0.025	1.309 ± 0.060	1.179 ± 0.050
ESO264-G057	0.079 ± 0.008	0.443 ± 0.018	2.867 ± 0.020	1.279 ± 0.049	1.275 ± 0.042
ESO264-G036	0.096 ± 0.004	0.419 ± 0.010	2.868 ± 0.014	1.187 ± 0.027	1.397 ± 0.025
ESO221-IG010	0.064 ± 0.003	0.488 ± 0.008	2.884 ± 0.007	1.383 ± 0.021	0.869 ± 0.016
ESO221-IG008	0.071 ± 0.002	0.168 ± 0.002	2.880 ± 0.004	0.439 ± 0.006	0.402 ± 0.014
ESO154-G010	0.222 ± 0.010	0.782 ± 0.023	3.182 ± 0.031	2.150 ± 0.061	0.955 ± 0.032
CGCG049-057	0.098 ± 0.017	0.487 ± 0.039	3.085 ± 0.103	1.403 ± 0.108	1.482 ± 0.089

Table C.4: SUNBIRD Hα equivalent width measurements

Name	**EW(Hα)**	**Name**	**EW(Hα)**
CGCG049-057	13.45 ± 0.17	IRAS19254-7245	28.96 ± 0.86
ESO154-G010	8.26 ± 0.15	IRASF01364-1042	-
ESO221-IG008	113.69 ± 1.87	IRASF06076-2139-S	27.96 ± 0.56
ESO221-IG010	53.36 ± 1.15	IRASF06076-2139-N	17.07 ± 0.64
ESO264-G036	15.46 ± 0.20	IRASF16516-0948	57.11 ± 0.79
ESO264-G057	37.32 ± 0.60	MCG-02-01-052	74.56 ± 1.23
ESO267-G030	30.32 ± 0.56	MCG-02-01-051	90.77 ± 1.87
ESO319-G022	17.43 ± 0.52	MCG-02-33-098-E	54.63 ± 0.85
ESO320-G030	28.67 ± 0.42	MCG-02-33-098-W	38.44 ± 1.13
ESO428-G023	21.45 ± 0.25	NGC1022	49.79 ± 1.09
ESO440-IG058-N	7.88 ± 0.04	NGC1068	19.89 ± 0.49
ESO440-IG058-S	-	NGC1204	9.88 ± 0.13
ESO491-G020	36.11 ± 0.55	NGC1222	169.98 ± 2.57
ESO550-IG025-N	-	NGC1819	19.71 ± 0.16
ESO550-IG025-S	-	NGC253	21.96 ± 0.44
IC2522	21.33 ± 0.36	NGC3110	41.47 ± 0.53
IC2522B	21.99 ± 0.34	NGC3508	36.20 ± 0.57
IRAS06164+0311	2.86 ± 0.14	NGC4433	46.49 ± 0.75
IRAS12116-5615	±	NGC4575	23.66 ± 0.42
IRAS13052-5711	15.39 ± 0.15	NGC470	57.30 ± 1.07
IRAS17578-0400	28.05 ± 0.38	NGC520	5.85 ± 0.10
IRAS17578-0400-W	64.80 ± 0.96	NGC6000	31.54 ± 0.40
IRAS17578-0400-E	58.78 ± 0.49	NGC6835	18.38 ± 0.22
IRAS18293-3413	1.28 ± 0.06	NGC7714	93.07 ± 1.10
IRAS18293-3413B	48.94 ± 0.88	NGC7715	-
IRAS19115-2124	51.27 ± 1.00	NGC7714C (Tidal Tail)	10.59 ± 0.19

Appendix D

Radial Profiles of all derived parameters (From Chapter 5)

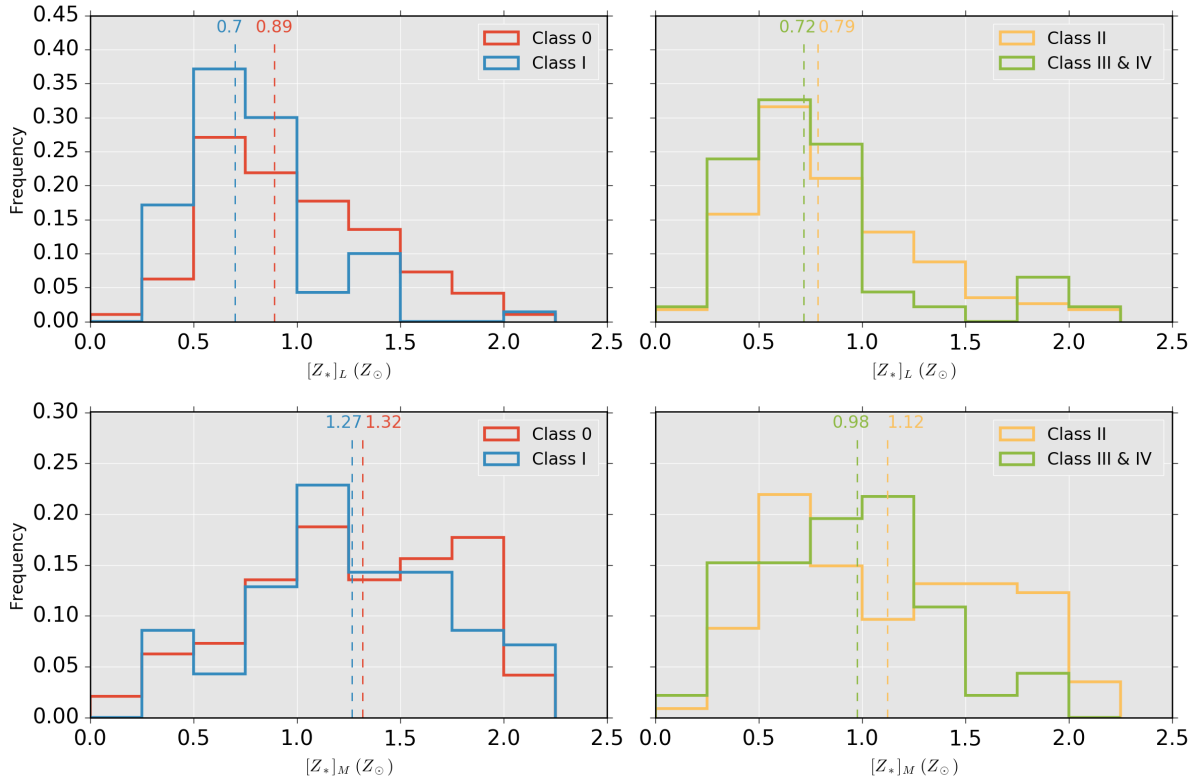

Figure D.1: Light Weighted (Top Panel) and Mass Weighted (Bottom Panel) Metallicity distribution

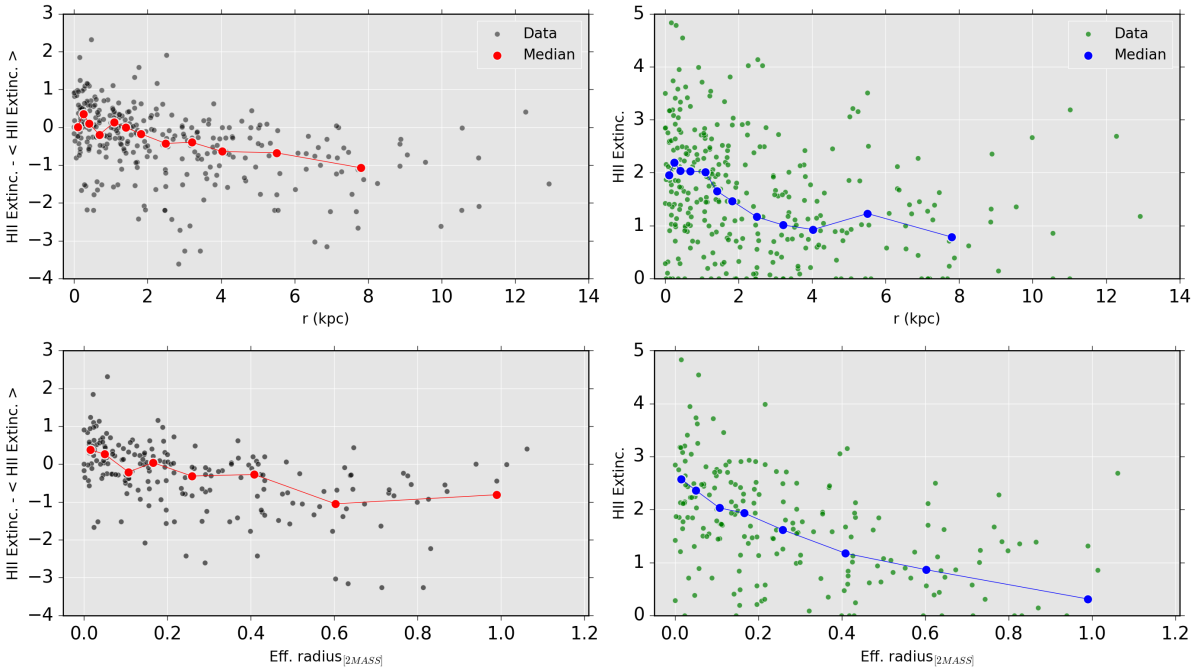

Figure D.2: Radial profile for nebular extinction

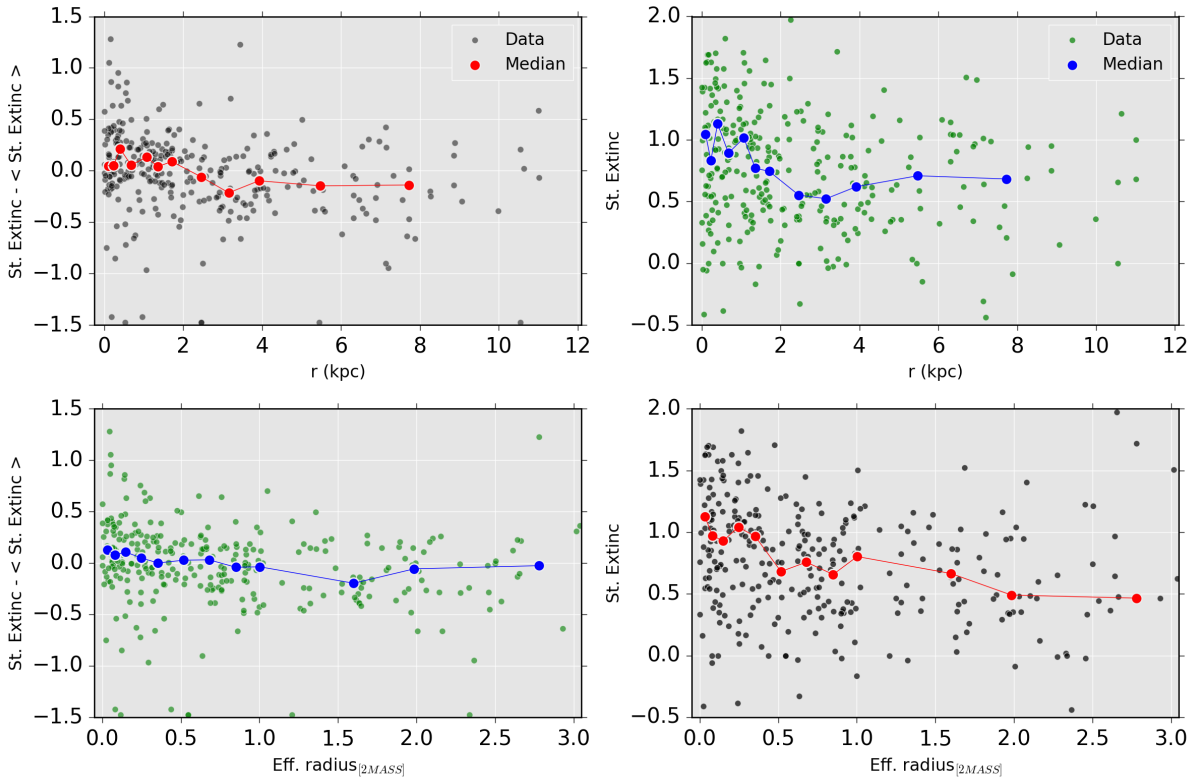

Figure D.3: Radial profile for stellar extinction

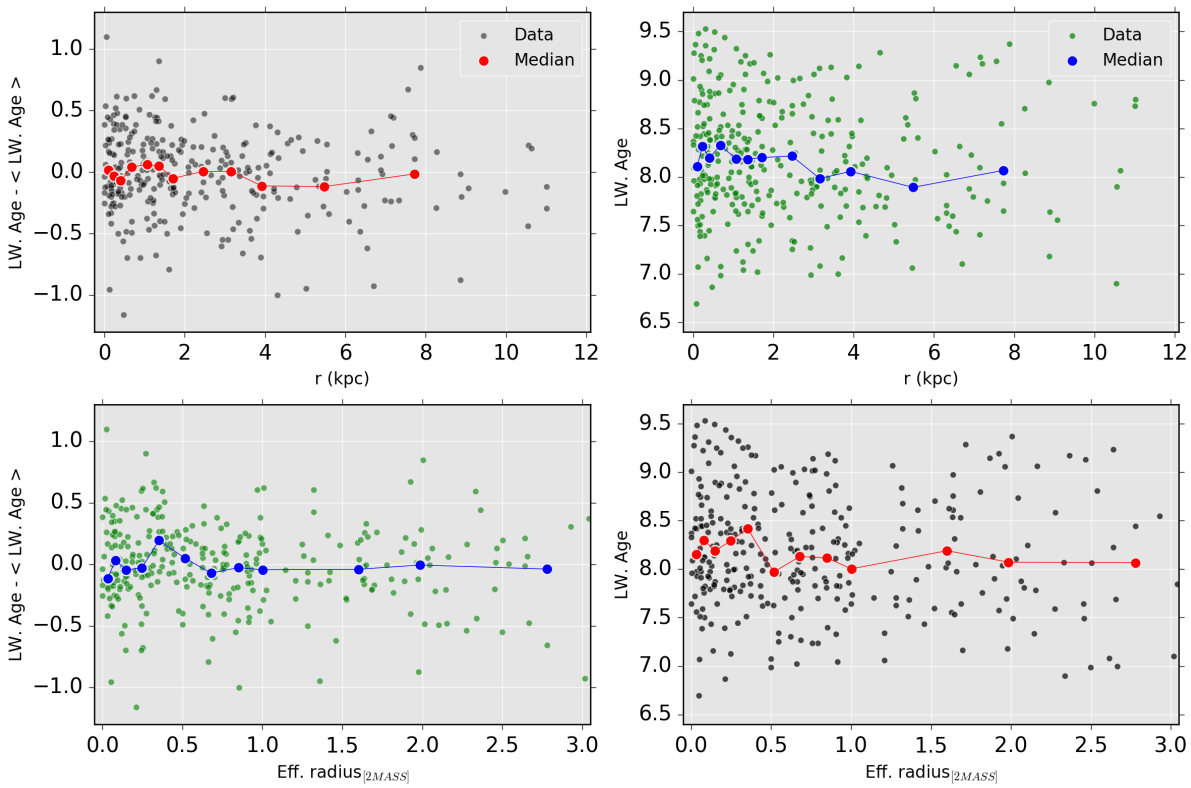

Figure D.4: Radial profile for Light-Weighted Age

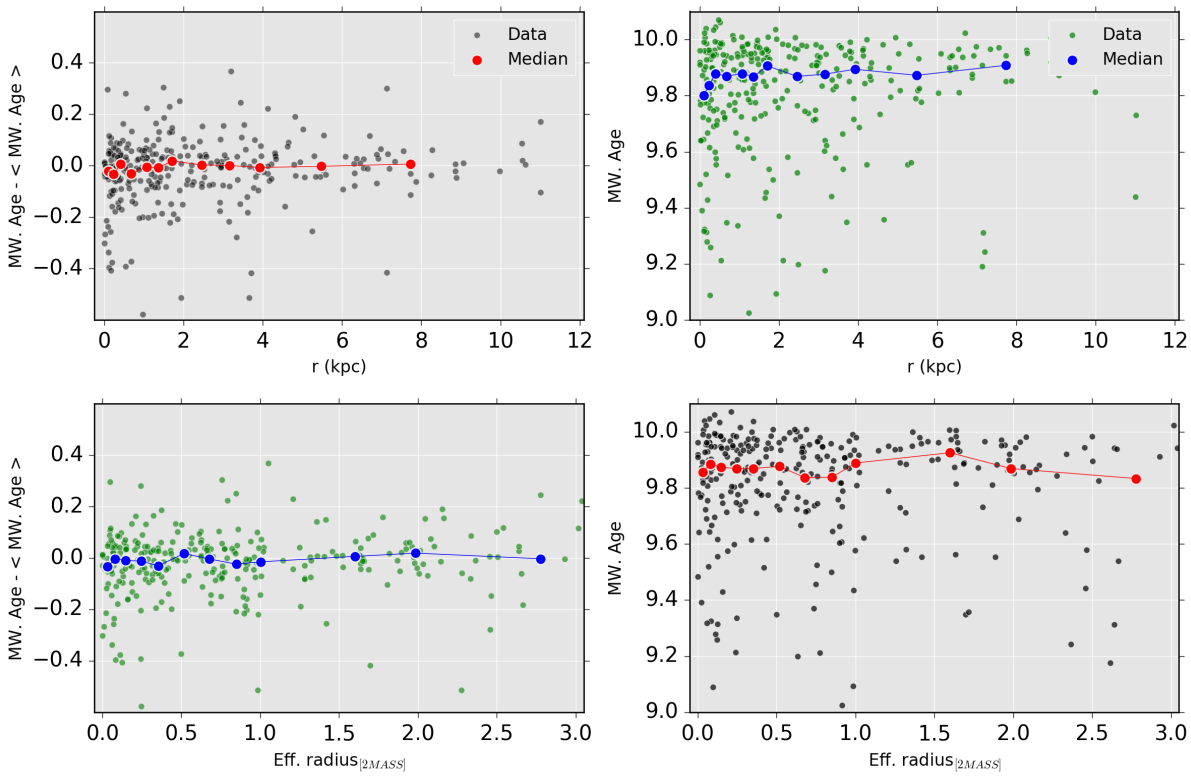

Figure D.5: Radial profile for Mass-Weighted Age

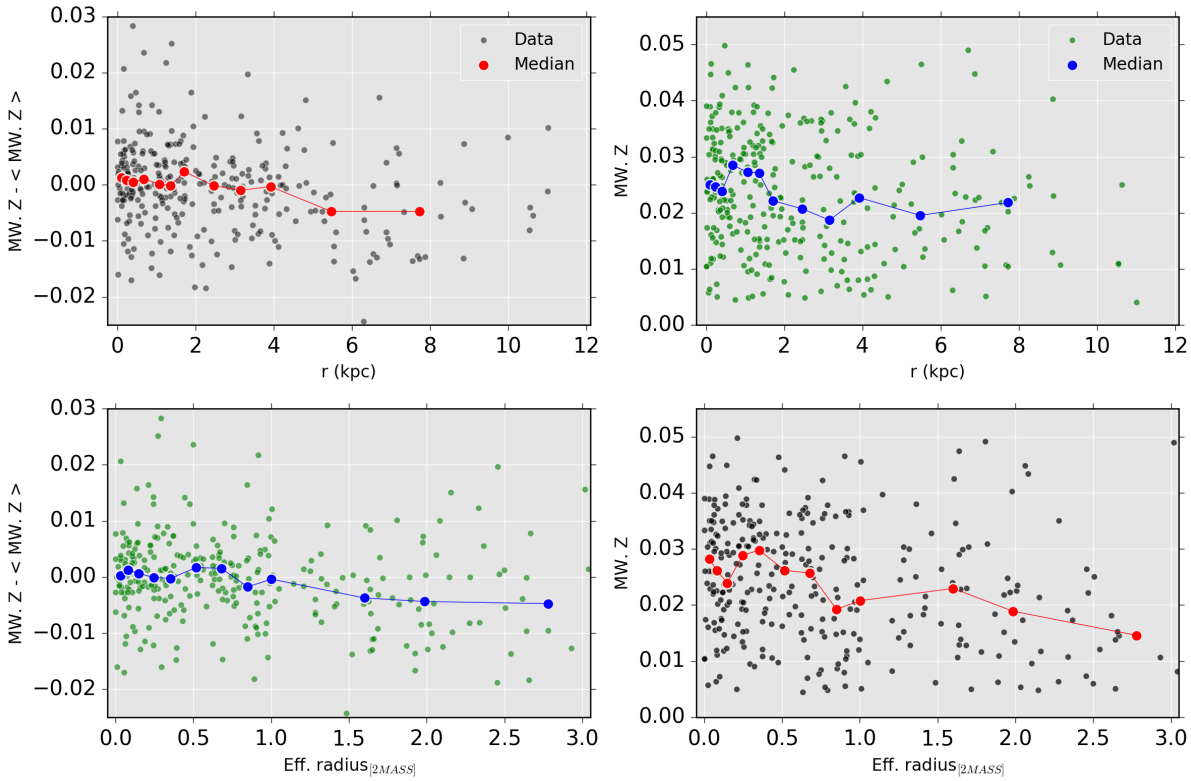

Figure D.6: Radial profile for Mass-Weighted Metallicity

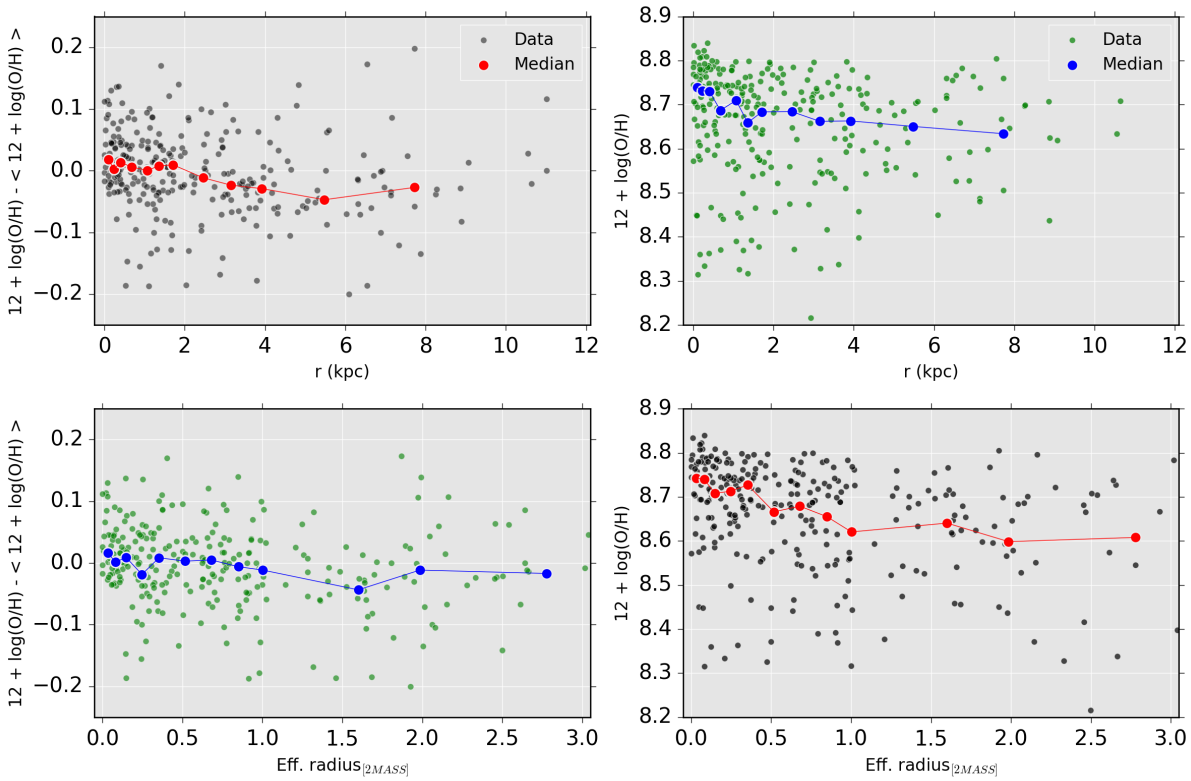

Figure D.7: Radial profile for oxygen abundances

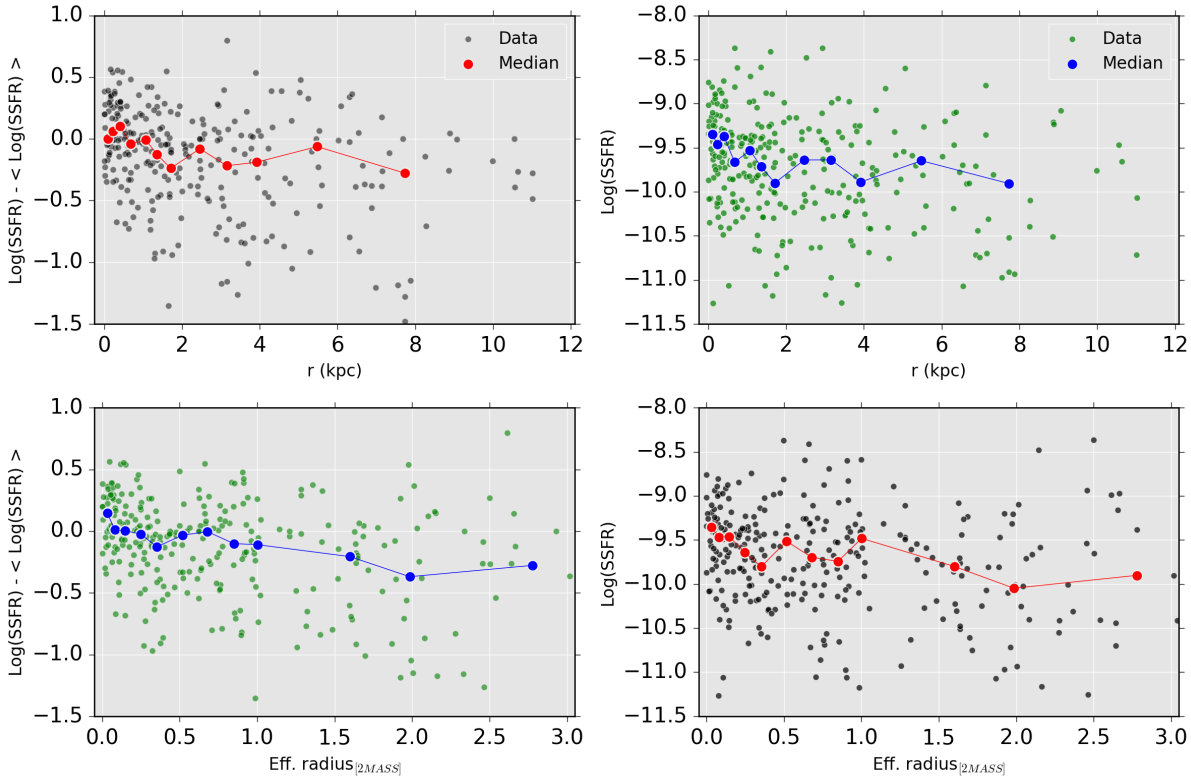

Figure D.8: Radial profile of sSFR

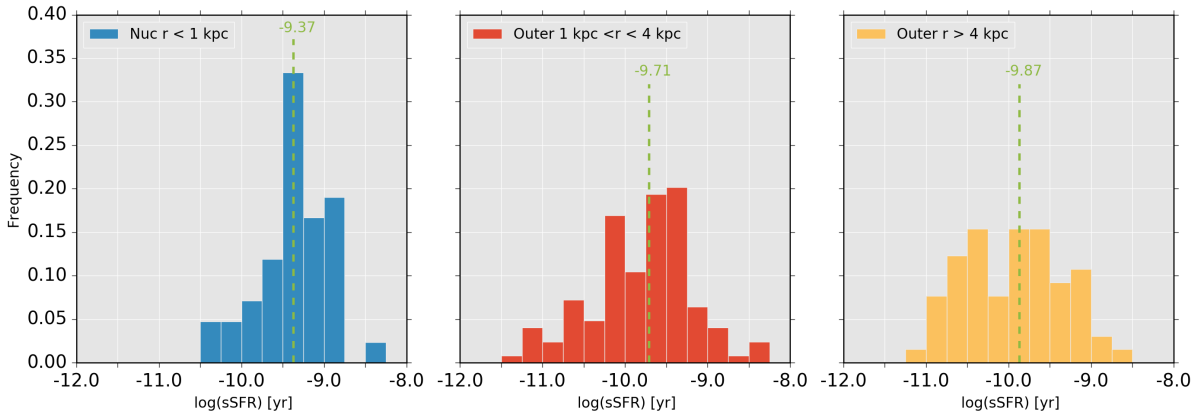

Figure D.9: The frequency distribution of sSFR at different radius of SUNBIRD. The *left panel* shows distribution for nuclear apertures, the *middle panel* correspond to aperture in the distance range between 1 kpc and 4 kpc and the *right panel* shows the outer region beyond 4 kpc. Median values for each distribution are shown with the green dashed line.

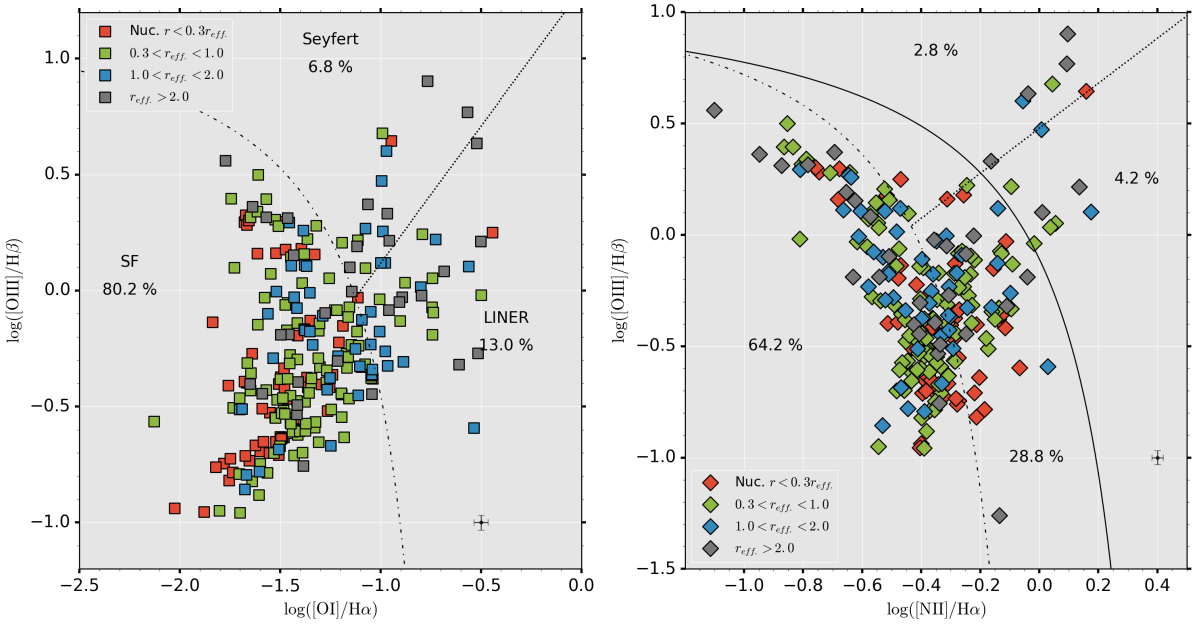

Figure D.10: BPT diagram of radial apertures grouped and colour-coded by Location. The two panels shows the two types of BPT diagram with the *left panel* showing ratios log([OI]/Hα) vs log($[OIII]/H\beta$) and the *right panel* showing the ratios of log([NII]/Hα) vs log($[OIII]/H\beta$). A typical error-bar is provided at (0.4, −1)

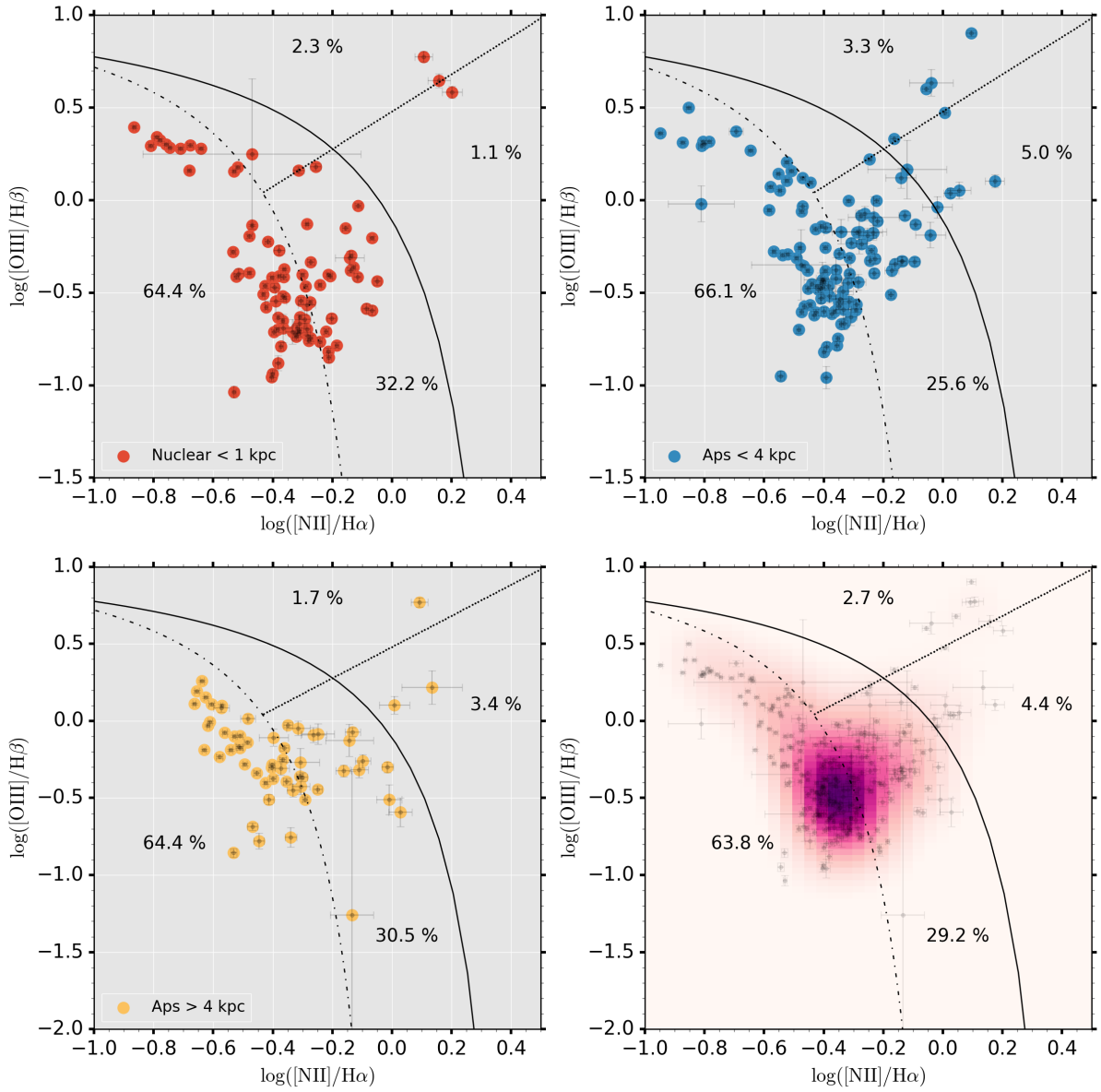

Figure D.11: The BPT diagrams for different areas of SUNBIRD galaxies. Same as Figure 5.11 but with Effective radius.

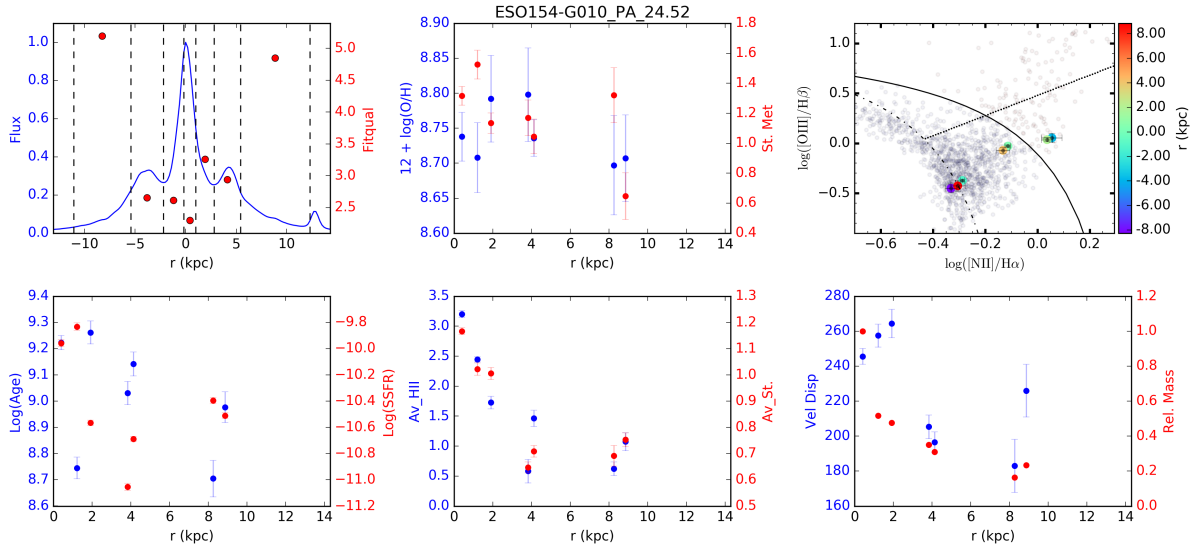

Figure D.12: Radial distribution of parameters for galaxy ESO154-G010, similar to Figure 5.3

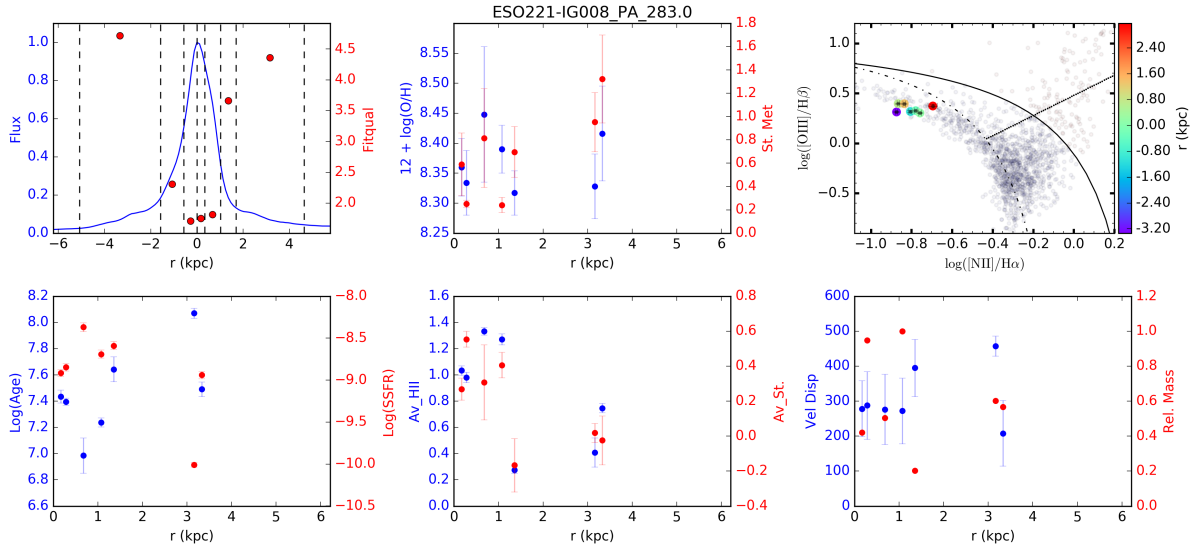

Figure D.13: Radial distribution of parameters for galaxy ESO221-IG008, similar to Figure 5.3

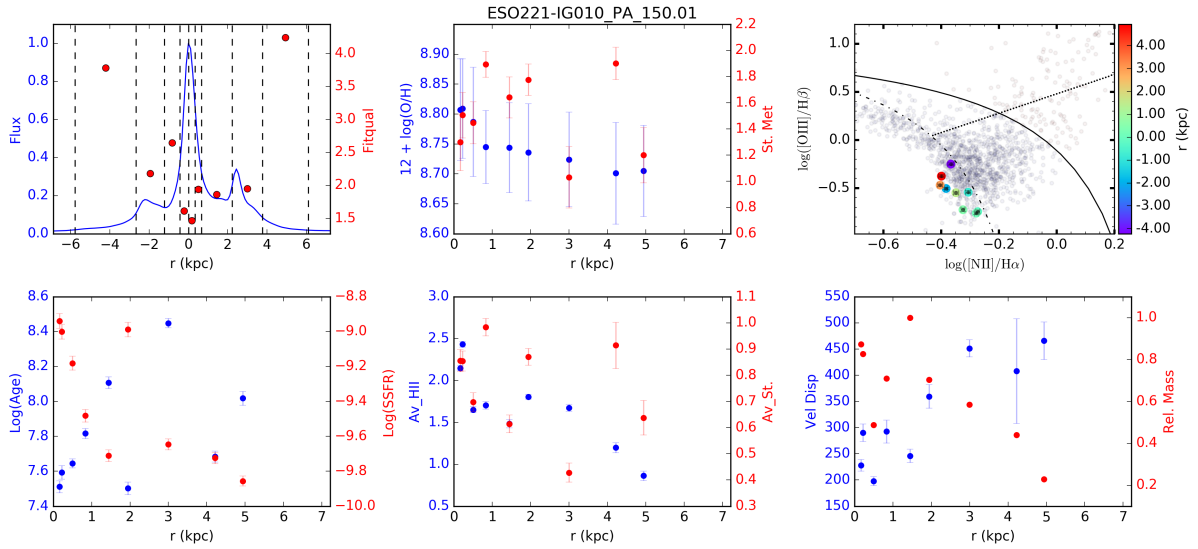

Figure D.14: Radial distribution of parameters for galaxy ESO221-IG010, similar to Figure 5.3

Bibliography

Adamo, A., Östlin, G., & Zackrisson, E. 2011, MNRAS, 417, 1904

Alexander, D. M., & Hickox, R. C. 2012, New A Rev., 56, 93

Allen, C. W. 1976, Astrophysical Quantities

Alloin, D., Collin-Souffrin, S., Joly, M., & Vigroux, L. 1979, A&A, 78, 200

Alongi, M., Bertelli, G., Bressan, A., et al. 1993, A&AS, 97, 851

Alonso-Herrero, A., García-Marín, M., Monreal-Ibero, A., et al. 2009, A&A, 506, 1541

Alonso-Herrero, A., García-Marín, M., Rodríguez Zaurín, J., et al. 2010, A&A, 522, A7

Alonso-Herrero, A., Pereira-Santaella, M., Rieke, G. H., & Rigopoulou, D. 2012, ApJ, 744, 2

Alton, P. D., Smith, R. J., & Lucey, J. R. 2017, MNRAS, 468, 1594

Aragón-Salamanca, A., Alonso-Herrero, A., Gallego, J., et al. 2003, in Astronomical Society of the Pacific Conference Series, Vol. 297, Star Formation Through Time, ed. E. Perez, R. M. Gonzalez Delgado, & G. Tenorio-Tagle, 191

Armus, L., Mazzarella, J. M., Evans, A. S., et al. 2009, PASP, 121, 559

Asari, N. V., Cid Fernandes, R., Stasińska, G., et al. 2007, MNRAS, 381, 263

Baldry, I. K., Glazebrook, K., Brinkmann, J., et al. 2004, ApJ, 600, 681

Baldwin, J. A., Phillips, M. M., & Terlevich, R. 1981, PASP, 93, 5

Balogh, M. L., Morris, S. L., Yee, H. K. C., Carlberg, R. G., & Ellingson, E. 1999, ApJ, 527, 54

Barnes, J. E., & Hernquist, L. 1996, ApJ, 471, 115

Barrera-Ballesteros, J. K., Sánchez, S. F., García-Lorenzo, B., et al. 2015, A&A, 579, A45

Bastian, N. 2008, MNRAS, 390, 759

Bastian, N., Covey, K. R., & Meyer, M. R. 2010, ARA&A, 48, 339

Bastian, N., & Goodwin, S. P. 2006, MNRAS, 369, L9

Bauer, A. E., Conselice, C. J., Pérez-González, P. G., et al. 2011, MNRAS, 417, 289

Baugh, C. M. 2006, Reports on Progress in Physics, 69, 3101

Behroozi, P. S., Wechsler, R. H., & Conroy, C. 2013, ApJ, 770, 57

Bekki, K., & Shioya, Y. 1999, ApJ, 513, 108

Bell, E. F., McIntosh, D. H., Katz, N., & Weinberg, M. D. 2003, ApJS, 149, 289

Bell, E. F., Wolf, C., Meisenheimer, K., et al. 2004, ApJ, 608, 752

Benson, A. J. 2010, Phys. Rep., 495, 33

Berentzen, I., Athanassoula, E., Heller, C. H., & Fricke, K. J. 2004, MNRAS, 347, 220

Bertelli, G., Bressan, A., Chiosi, C., Fagotto, F., & Nasi, E. 1994, A&AS, 106, 275

Bianco, F. B., Modjaz, M., Oh, S. M., et al. 2016, Astronomy and Computing, 16, 54

Bica, E., Arimoto, N., & Alloin, D. 1988, A&A, 202, 8

Bigiel, F., Leroy, A., Walter, F., et al. 2008, AJ, 136, 2846

Blanc, G. A., Kewley, L., Vogt, F. P. A., & Dopita, M. A. 2015, ApJ, 798, 99

Blumenthal, G. R., Faber, S. M., Primack, J. R., & Rees, M. J. 1984, Nature, 311, 517

Bolatto, A. D., Wolfire, M., & Leroy, A. K. 2013, ARA&A, 51, 207

Bolatto, A. D., Leroy, A. K., Jameson, K., et al. 2011, ApJ, 741, 12

Bournaud, F. 2011, in EAS Publications Series, Vol. 51, EAS Publications Series, ed. C. Charbonnel & T. Montmerle, 107–131

Bournaud, F., Duc, P.-A., & Emsellem, E. 2008, MNRAS, 389, L8

Bournaud, F., Jog, C. J., & Combes, F. 2005, A&A, 437, 69

Bressan, A., Fagotto, F., Bertelli, G., & Chiosi, C. 1993, A&AS, 100, 647

Brinchmann, J., & Ellis, R. S. 2000, ApJ, 536, L77

Bruzual, G., & Charlot, S. 2003, MNRAS, 344, 1000

Buckley, D. A. H., Swart, G. P., & Meiring, J. G. 2006, in Society of Photo-Optical Instrumentation Engineers (SPIE) Conference Series, Vol. 6267, Society of Photo-Optical Instrumentation Engineers (SPIE) Conference Series, 0

Bundy, K., Bershady, M. A., Law, D. R., et al. 2015, ApJ, 798, 7

Burgarella, D., Buat, V., & Iglesias-Páramo, J. 2005, MNRAS, 360, 1413

Burgh, E. B., Nordsieck, K. H., Kobulnicky, H. A., et al. 2003, in Society of Photo-Optical Instrumentation Engineers (SPIE) Conference Series, Vol. 4841, Instrument Design and Performance for Optical/Infrared Ground-based Telescopes, ed. M. Iye & A. F. M. Moorwood, 1463–1471

Burstein, D., Faber, S. M., Gaskell, C. M., & Krumm, N. 1984, ApJ, 287, 586

Buta, R. J., Sheth, K., Athanassoula, E., et al. 2015, ApJS, 217, 32

Calzetti, D., Armus, L., Bohlin, R. C., et al. 2000, ApJ, 533, 682

Calzetti, D., Kinney, A. L., & Storchi-Bergmann, T. 1994, ApJ, 429, 582

Cappellari, M., & Emsellem, E. 2004, PASP, 116, 138

Cappellari, M., Emsellem, E., Krajnović, D., et al. 2011, MNRAS, 413, 813

Caputi, K. I., Lagache, G., Yan, L., et al. 2007, ApJ, 660, 97

Cardelli, J. A., Clayton, G. C., & Mathis, J. S. 1989, ApJ, 345, 245

Cardiel, N., Gorgas, J., Sánchez-Blázquez, P., et al. 2003, A&A, 409, 511

Casado, J., Ascasibar, Y., Gavilán, M., et al. 2015, MNRAS, 451, 888

Cattaneo, A., Dekel, A., Faber, S. M., & Guiderdoni, B. 2008, MNRAS, 389, 567

Cazzoli, S., Arribas, S., Colina, L., et al. 2014, A&A, 569, A14

Chabrier, G. 2003, PASP, 115, 763

Charbonnel, C., Meynet, G., Maeder, A., & Schaerer, D. 1996, A&AS, 115, 339

Charlot, S., & Fall, S. M. 2000, ApJ, 539, 718

Chiaberge, M., Gilli, R., Lotz, J. M., & Norman, C. 2015, ApJ, 806, 147

Chiosi, C., Merlin, E., Piovan, L., & Tantalo, R. 2014, Galaxies, 2, 300

Cicone, C., Maiolino, R., Sturm, E., et al. 2014, A&A, 562, A21

Cid Fernandes, R. 2007, in IAU Symposium, Vol. 241, Stellar Populations as Building Blocks of Galaxies, ed. A. Vazdekis & R. Peletier, 461–469

Cid Fernandes, R., Gu, Q., Melnick, J., et al. 2004, MNRAS, 355, 273

Cid Fernandes, R., Mateus, A., Sodré, L., Stasińska, G., & Gomes, J. M. 2005, MNRAS, 358, 363

Cid Fernandes, R., Stasińska, G., Schlickmann, M. S., et al. 2010, MNRAS, 403, 1036

Cid Fernandes, R., Pérez, E., García Benito, R., et al. 2013, A&A, 557, A86

Cid Fernandes, R., González Delgado, R. M., García Benito, R., et al. 2014, A&A, 561, A130

Cirasuolo, M., McLure, R. J., Dunlop, J. S., et al. 2007, MNRAS, 380, 585

Clark, P. C., & Glover, S. C. O. 2015, MNRAS, 452, 2057

Cole, S., Aragon-Salamanca, A., Frenk, C. S., Navarro, J. F., & Zepf, S. E. 1994, MNRAS, 271, 781

Condon, J. J., & Yin, Q. F. 1990, ApJ, 357, 97

Conroy, C., Gunn, J. E., & White, M. 2009, ApJ, 699, 486

Cook, B. A., Conroy, C., Pillepich, A., Rodriguez-Gomez, V., & Hernquist, L. 2016, ApJ, 833, 158

Cortijo-Ferrero, C., González Delgado, R. M., Pérez, E., et al. 2017, MNRAS, 467, 3898

Cowie, L. L., Songaila, A., Hu, E. M., & Cohen, J. G. 1996, AJ, 112, 839

Cox, T. J., Jonsson, P., Somerville, R. S., Primack, J. R., & Dekel, A. 2008, MNRAS, 384, 386

Crause, L. A., Sharples, R. M., Bramall, D. G., et al. 2014, in Proc. SPIE, Vol. 9147, Ground-based and Airborne Instrumentation for Astronomy V, 91476T

Crawford, S. M., Still, M., Schellart, P., et al. 2010, in Proc. SPIE, Vol. 7737, Observatory Operations: Strategies, Processes, and Systems III, 773725

Cresci, G., Marconi, A., Zibetti, S., et al. 2015, A&A, 582, A63

Croom, S. M., Lawrence, J. S., Bland-Hawthorn, J., et al. 2012, MNRAS, 421, 872

da Cunha, E., Charlot, S., & Elbaz, D. 2008, MNRAS, 388, 1595

Daddi, E., Dickinson, M., Morrison, G., et al. 2007, ApJ, 670, 156

Daddi, E., Elbaz, D., Walter, F., et al. 2010, ApJ, 714, L118

de Vaucouleurs, G. 1948, Annales d'Astrophysique, 11, 247

—. 1959, Handbuch der Physik, 53, 275

Denicoló, G., Terlevich, R., & Terlevich, E. 2002, MNRAS, 330, 69

Díaz, A. I., & Pérez-Montero, E. 2000, MNRAS, 312, 130

Djorgovski, S., & Davis, M. 1987, ApJ, 313, 59

Dopita, M. A., Binette, L., & Schwartz, R. D. 1982, ApJ, 261, 183

Dopita, M. A., & Evans, I. N. 1986, ApJ, 307, 431

Dopita, M. A., & Sutherland, R. S. 1995, ApJ, 455, 468

Downes, D., & Solomon, P. M. 1998, ApJ, 507, 615

Edmunds, M. G., & Pagel, B. E. J. 1984, MNRAS, 211, 507

Eggen, O. J., Lynden-Bell, D., & Sandage, A. R. 1962, ApJ, 136, 748

Elbaz, D., Daddi, E., Le Borgne, D., et al. 2007, A&A, 468, 33

Elmegreen, D. M., Elmegreen, B. G., Ferguson, T., & Mullan, B. 2007, ApJ, 663, 734

Emsellem, E., Cappellari, M., Krajnović, D., et al. 2007, MNRAS, 379, 401

Erb, D. K., Shapley, A. E., Pettini, M., et al. 2006, ApJ, 644, 813

Faber, S. M., Friel, E. D., Burstein, D., & Gaskell, C. M. 1985, ApJS, 57, 711

Faber, S. M., Willmer, C. N. A., Wolf, C., et al. 2007, ApJ, 665, 265

Fagotto, F., Bressan, A., Bertelli, G., & Chiosi, C. 1994a, A&AS, 104

—. 1994b, A&AS, 105

—. 1994c, A&AS, 105

Ferland, G. J., Korista, K. T., Verner, D. A., et al. 1998, PASP, 110, 761

Ferland, G. J., Porter, R. L., van Hoof, P. A. M., et al. 2013, RMxAA, 49, 137

Ferrarese, L., & Merritt, D. 2000, ApJ, 539, L9

Ferrari, F., Pastoriza, M. G., Macchetto, F., & Caon, N. 1999, A&AS, 136, 269

Finlator, K., & Davé, R. 2008, MNRAS, 385, 2181

Fischera, J., Dopita, M. A., & Sutherland, R. S. 2003, ApJ, 599, L21

Fitzpatrick, E. L. 1999, PASP, 111, 63

Fontanot, F., De Lucia, G., Monaco, P., Somerville, R. S., & Santini, P. 2009, MNRAS, 397, 1776

Friedli, D. 1999, in Astronomical Society of the Pacific Conference Series, Vol. 187, The Evolution of Galaxies on Cosmological Timescales, ed. J. E. Beckman & T. J. Mahoney, 88–99

Fumagalli, M., Patel, S. G., Franx, M., et al. 2012, ApJ, 757, L22

Gallagher, J. S., Hunter, D. A., & Bushouse, H. 1989, AJ, 97, 700

Gallart, C., Stetson, P. B., Meschin, I. P., Pont, F., & Hardy, E. 2008, ApJ, 682, L89

Gallazzi, A., Charlot, S., Brinchmann, J., White, S. D. M., & Tremonti, C. A. 2005, MNRAS, 362, 41

García-Burillo, S., Combes, F., Usero, A., et al. 2014, A&A, 567, A125

Gebhardt, K., Bender, R., Bower, G., et al. 2000, ApJ, 539, L13

Geha, M., Blanton, M. R., Yan, R., & Tinker, J. L. 2012, ApJ, 757, 85

Gilbert, A. M., & Graham, J. R. 2007, ApJ, 668, 168

Girardi, L., Bressan, A., Chiosi, C., Bertelli, G., & Nasi, E. 1996, A&AS, 117, 113

González Delgado, R. M., Arribas, S., Pérez, E., & Heckman, T. 2002, ApJ, 579, 188

González Delgado, R. M., Cid Fernandes, R., Pérez, E., et al. 2004, ApJ, 605, 127

González Delgado, R. M., Pérez, E., Cid Fernandes, R., et al. 2014, A&A, 562, A47

González Delgado, R. M., García-Benito, R., Pérez, E., et al. 2015, A&A, 581, A103

Gordon, M. A., & Burton, W. B. 1976, ApJ, 208, 346

Groves, B. A., Dopita, M. A., & Sutherland, R. S. 2004, ApJS, 153, 9

Guo, K., Zheng, X. Z., & Fu, H. 2013, ApJ, 778, 23

Harwit, M., & Pacini, F. 1975, ApJ, 200, L127

Heavens, A., Panter, B., Jimenez, R., & Dunlop, J. 2004, Nature, 428, 625

Hernquist, L. 1989, Nature, 340, 687

Hernquist, L., & Mihos, J. C. 1995, ApJ, 448, 41

Hibbard, J. E., & Yun, M. S. 1999, AJ, 118, 162

Holtzman, J. A., Faber, S. M., Shaya, E. J., et al. 1992, AJ, 103, 691

Hopkins, A. M., & Beacom, J. F. 2006, ApJ, 651, 142

Hopkins, P. F., Cox, T. J., Hernquist, L., et al. 2013, MNRAS, 430, 1901

Hopkins, P. F., & Hernquist, L. 2009, ApJ, 694, 599

Hopkins, P. F., Hernquist, L., Cox, T. J., & Kereš, D. 2008, ApJS, 175, 356

Hopkins, P. F., Kereš, D., Oñorbe, J., et al. 2014, MNRAS, 445, 581

Hou, L. G., Han, J. L., Kong, M. Z., & Wu, X.-B. 2011, ApJ, 732, 72

Howell, J. H., Armus, L., Mazzarella, J. M., et al. 2010, ApJ, 715, 572

Hubble, E. P. 1926, ApJ, 64, doi:10.1086/143018

Iffrig, O., & Hennebelle, P. 2015, A&A, 576, A95

Israel, F. P., & Koornneef, J. 1979, ApJ, 230, 390

Izotov, Y. I., Guseva, N. G., Fricke, K. J., & Henkel, C. 2015, MNRAS, 451, 2251

Juneau, S., Glazebrook, K., Crampton, D., et al. 2005, ApJ, 619, L135

Kampakoglou, M., Trotta, R., & Silk, J. 2008, MNRAS, 384, 1414

Kauffmann, G., Heckman, T. M., White, S. D. M., et al. 2003a, MNRAS, 341, 33

Kauffmann, G., Heckman, T. M., Tremonti, C., et al. 2003b, MNRAS, 346, 1055

Kaviraj, S. 2014, MNRAS, 440, 2944

Keel, W. C. 2007, The road to galaxy formation (Praxis Publishing Ltd)

Kennicutt, Jr., R. C. 1983, ApJ, 272, 54

—. 1992a, ApJS, 79, 255

—. 1992b, ApJ, 388, 310

—. 1998a, ARA&A, 36, 189

—. 1998b, ApJ, 498, 541

Kennicutt, Jr., R. C., Hao, C.-N., Calzetti, D., et al. 2009, ApJ, 703, 1672

Kessler, M. F., Steinz, J. A., Anderegg, M. E., et al. 1996, A&A, 315, L27

Kewley, L. J., Dopita, M. A., Sutherland, R. S., Heisler, C. A., & Trevena, J. 2001, ApJ, 556, 121

Kewley, L. J., & Ellison, S. L. 2008, ApJ, 681, 1183

Kewley, L. J., Groves, B., Kauffmann, G., & Heckman, T. 2006, MNRAS, 372, 961

Kewley, L. J., Rupke, D., Zahid, H. J., Geller, M. J., & Barton, E. J. 2010, ApJ, 721, L48

Kleinmann, D. E., & Low, F. J. 1970, ApJ, 159, L165

Knapp, G. R., & Morris, M. 1976, ApJ, 206, 713

Kobayashi, C., Springel, V., & White, S. D. M. 2007, MNRAS, 376, 1465

Kobulnicky, H. A., Nordsieck, K. H., Burgh, E. B., et al. 2003, in Society of Photo-Optical Instrumentation Engineers (SPIE) Conference Series, Vol. 4841, Instrument Design and Performance for Optical/Infrared Ground-based Telescopes, ed. M. Iye & A. F. M. Moorwood, 1634–1644

Kobulnicky, H. A., & Zaritsky, D. 1999, ApJ, 511, 118

Koleva, M., Prugniel, P., Bouchard, A., & Wu, Y. 2009, A&A, 501, 1269

Koleva, M., Prugniel, P., Ocvirk, P., Le Borgne, D., & Soubiran, C. 2008, MNRAS, 385, 1998

Köppen, J., Weidner, C., & Kroupa, P. 2007, MNRAS, 375, 673

Kormendy, J., & Bender, R. 2012, ApJS, 198, 2

Kormendy, J., & Ho, L. C. 2013, ARA&A, 51, 511

Kormendy, J., & Kennicutt, Jr., R. C. 2004a, ARA&A, 42, 603

—. 2004b, ARA&A, 42, 603

Kormendy, J., & Sanders, D. B. 1992, ApJ, 390, L53

Korn, A. J., Maraston, C., & Thomas, D. 2005, A&A, 438, 685

Krabbe, A. C., Pastoriza, M. G., Winge, C., et al. 2011, MNRAS, 416, 38

Kriek, M., van der Wel, A., van Dokkum, P. G., Franx, M., & Illingworth, G. D. 2008, ApJ, 682, 896

Kroupa, P. 2001, MNRAS, 322, 231

—. 2002, Science, 295, 82

Kroupa, P., Tout, C. A., & Gilmore, G. 1993, MNRAS, 262, 545

Krumholz, M. R. 2014, Phys. Rep., 539, 49

Kurtz, M. J., & Mink, D. J. 1998, PASP, 110, 934

Lada, C. J., & Lada, E. A. 2003, ARA&A, 41, 57

Lagache, G., Puget, J.-L., & Dole, H. 2005, ARA&A, 43, 727

Lara-López, M. A., Cepa, J., Bongiovanni, A., et al. 2010, A&A, 521, L53

Larsen, S. S. 2002, AJ, 124, 1393

Larson, K. L., Sanders, D. B., Barnes, J. E., et al. 2016, ApJ, 825, 128

Le Borgne, J.-F., Bruzual, G., Pelló, R., et al. 2003, A&A, 402, 433

Leitherer, C. 2012, in Astronomical Society of India Conference Series, Vol. 6, Astronomical Society of India Conference Series, ed. P. Prugniel & H. P. Singh, 79

Leitherer, C., Ferguson, H. C., Heckman, T. M., & Lowenthal, J. D. 1995, ApJ, 454, L19

Leitherer, C., & Heckman, T. M. 1995, ApJS, 96, 9

Leitherer, C., Schaerer, D., Goldader, J. D., et al. 1999, ApJS, 123, 3

Lequeux, J., Maucherat-Joubert, M., Deharveng, J. M., & Kunth, D. 1981, A&A, 103, 305

Lequeux, J., Peimbert, M., Rayo, J. F., Serrano, A., & Torres-Peimbert, S. 1979, A&A, 80, 155

Leroy, A. K., Walter, F., Bigiel, F., et al. 2009, AJ, 137, 4670

Leroy, A. K., Walter, F., Sandstrom, K., et al. 2013, AJ, 146, 19

Liang, Y. C., Yin, S. Y., Hammer, F., et al. 2006, ApJ, 652, 257

Lilly, S. J., Le Fevre, O., Hammer, F., & Crampton, D. 1996, ApJ, 460, L1

Lonsdale, C. J., Farrah, D., & Smith, H. E. 2006, Ultraluminous Infrared Galaxies, ed. Mason, J. W. (Springer Verlag), 285–+

López Fernández, R., Cid Fernandes, R., González Delgado, R. M., et al. 2016, MNRAS, 458, 184

Loren, R. B., Vanden Bout, P. A., & Davis, J. H. 1973, ApJ, 185, L67

Lotz, J. M., Davis, M., Faber, S. M., et al. 2008, ApJ, 672, 177

Low, J., & Kleinmann, D. E. 1968, AJ, 73, 868

Lucero, D. M., Carignan, C., Elson, E. C., et al. 2015, MNRAS, 450, 3935

Ma, X., Hopkins, P. F., Faucher-Giguère, C.-A., et al. 2016, MNRAS, 456, 2140

Madau, P., & Dickinson, M. 2014, ARA&A, 52, 415

Madau, P., Ferguson, H. C., Dickinson, M. E., et al. 1996, MNRAS, 283, 1388

Magnani, L., & Onello, J. S. 1995, ApJ, 443, 169

Maiolino, R., Russell, H. R., Fabian, A. C., et al. 2017, Nature, 544, 202

Małek, K., Bankowicz, M., Pollo, A., et al. 2017, A&A, 598, A1

Mannucci, F., Cresci, G., Maiolino, R., Marconi, A., & Gnerucci, A. 2010, MNRAS, 408, 2115

Maraston, C. 2003, in Extragalactic Globular Cluster Systems, ed. M. Kissler-Patig, 237

Maraston, C. 2011, in IAU Symposium, Vol. 277, IAU Symposium, ed. C. Carignan, F. Combes, & K. C. Freeman, 158–165

Maraston, C. 2013, in IAU Symposium, Vol. 295, The Intriguing Life of Massive Galaxies, ed. D. Thomas, A. Pasquali, & I. Ferreras, 272–281

Marcillac, D., Elbaz, D., Charlot, S., et al. 2006, A&A, 458, 369

Marino, R. A., Rosales-Ortega, F. F., Sánchez, S. F., et al. 2013, A&A, 559, A114

Martin, C. L. 2005, ApJ, 621, 227

Martín-Navarro, I., La Barbera, F., Vazdekis, A., Falcón-Barroso, J., & Ferreras, I. 2015, MNRAS, 447, 1033

Martinez-Valpuesta, I., Aguerri, J. A. L., González-García, A. C., Dalla Vecchia, C., & Stringer, M. 2017, MNRAS, 464, 1502

Masters, K. L., Giovanelli, R., & Haynes, M. P. 2003, AJ, 126, 158

Matsuhara, H., Wada, T., Matsuura, S., et al. 2006, PASJ, 58, 673

McCall, M. L., Rybski, P. M., & Shields, G. A. 1985, ApJS, 57, 1

McGaugh, S. S. 1991, ApJ, 380, 140

McKee, C. F., & Ostriker, E. C. 2007, ARA&A, 45, 565

Meurer, G. R., Heckman, T. M., Leitherer, C., et al. 1995, AJ, 110, 2665

Mihos, J. C., & Hernquist, L. 1994, ApJ, 425, L13

—. 1996, ApJ, 464, 641

Miller, G. E., & Scalo, J. M. 1979, ApJS, 41, 513

Miralles-Caballero, D., Colina, L., & Arribas, S. 2012, A&A, 538, A61

Miralles-Caballero, D., Colina, L., Arribas, S., & Duc, P.-A. 2011, AJ, 142, 79

Miszalski, B., Manick, R., Mikołajewska, J., et al. 2018, MNRAS, 473, 2275

Mo, H., van den Bosch, F. C., & White, S. 2010, Galaxy Formation and Evolution

Monreal-Ibero, A., Arribas, S., Colina, L., et al. 2010, A&A, 517, A28

Moorwood, A. F. M. 1996, Space Sci. Rev., 77, 303

Morgan, W. W. 1958, PASP, 70, 364

Moustakas, J., Kennicutt, Jr., R. C., & Tremonti, C. A. 2006, ApJ, 642, 775

Moustakas, J., Kennicutt, Jr., R. C., Tremonti, C. A., et al. 2010, ApJS, 190, 233

Murphy, E. J., Bremseth, J., Mason, B. S., et al. 2012, ApJ, 761, 97

Nagao, T., Maiolino, R., & Marconi, A. 2006, A&A, 459, 85

Neininger, N., Guélin, M., Ungerechts, H., Lucas, R., & Wielebinski, R. 1998, Nature, 395, 871

Neistein, E., van den Bosch, F. C., & Dekel, A. 2006, MNRAS, 372, 933

Neugebauer, G., Habing, H. J., van Duinen, R., et al. 1984, ApJ, 278, L1

Noeske, K. G., Weiner, B. J., Faber, S. M., et al. 2007, ApJ, 660, L43

O'Connell, R. W. 1976, ApJ, 206, 370

—. 1980, ApJ, 236, 430

Ocvirk, P., Pichon, C., Lançon, A., & Thiébaut, E. 2006a, MNRAS, 365, 74

—. 2006b, MNRAS, 365, 46

O'Donoghue, D., Buckley, D. A. H., Balona, L. A., et al. 2006, MNRAS, 372, 151

Oemler, Jr., A., Abramson, L. E., Gladders, M. D., et al. 2017, ApJ, 844, 45

Ogando, R. L. C., Maia, M. A. G., Chiappini, C., et al. 2005, ApJ, 632, L61

Ohashi, N., Saigo, K., Aso, Y., et al. 2014, ApJ, 796, 131

Osterbrock, D. E. 1989, Astrophysics of gaseous nebulae and active galactic nuclei

Ostriker, J. P., & Tremaine, S. D. 1975, ApJ, 202, L113

Pagel, B. E. J. 2009, Nucleosynthesis and Chemical Evolution of Galaxies (Cambridge University Press), 484

Pagel, B. E. J., Edmunds, M. G., Blackwell, D. E., Chun, M. S., & Smith, G. 1979, MNRAS, 189, 95

Panter, B., Jimenez, R., Heavens, A. F., & Charlot, S. 2008, MNRAS, 391, 1117

Peletier, R. F. 2013, Stellar Populations, ed. J. Falcón-Barroso & J. H. Knapen, 353

Pereira-Santaella, M., Alonso-Herrero, A., Colina, L., et al. 2015, A&A, 577, A78

Pérez, E., Cid Fernandes, R., González Delgado, R. M., et al. 2013, ApJ, 764, L1

Pérez-González, P. G., Rieke, G. H., Villar, V., et al. 2008, ApJ, 675, 234

Petric, A. O., Armus, L., Howell, J., et al. 2011, ApJ, 730, 28

Pettini, M., & Pagel, B. E. J. 2004, MNRAS, 348, L59

Pilbratt, G. L., Riedinger, J. R., Passvogel, T., et al. 2010, A&A, 518, L1

Pilkington, K., Few, C. G., Gibson, B. K., et al. 2012, A&A, 540, A56

Pilyugin, L. S. 2001, A&A, 374, 412

Pilyugin, L. S., Lara-López, M. A., Grebel, E. K., et al. 2013, MNRAS, 432, 1217

Pilyugin, L. S., & Thuan, T. X. 2005, ApJ, 631, 231

Price, S. H., Kriek, M., Brammer, G. B., et al. 2014, ApJ, 788, 86

Randriamanakoto, Z., Escala, A., Väisänen, P., et al. 2013a, ApJ, 775, L38

Randriamanakoto, Z., Väisänen, P., Ryder, S., et al. 2013b, MNRAS, 431, 554

Recchi, S., & Kroupa, P. 2015, MNRAS, 446, 4168

Reddy, N. A., & Steidel, C. C. 2009, ApJ, 692, 778

Reddy, N. A., Steidel, C. C., Fadda, D., et al. 2006, ApJ, 644, 792

Regan, M. W., Thornley, M. D., Helfer, T. T., et al. 2001, ApJ, 561, 218

Rich, J. A., Kewley, L. J., & Dopita, M. A. 2014, The Astrophysical Journal Letters, 781, L12

Rich, J. A., Torrey, P., Kewley, L. J., Dopita, M. A., & Rupke, D. S. N. 2012, ApJ, 753, 5

Rieke, G. H., & Low, F. J. 1972, ApJ, 176, L95+

—. 1975, ApJ, 197, 17

Rodríguez Zaurín, J., Tadhunter, C. N., & González Delgado, R. M. 2009, MNRAS, 400, 1139

—. 2010, MNRAS, 403, 1317

Rosales-Ortega, F. F., Kennicutt, R. C., Sánchez, S. F., et al. 2010, MNRAS, 405, 735

Rothberg, B., & Joseph, R. D. 2006, AJ, 131, 185

Rupke, D. S., Veilleux, S., & Sanders, D. B. 2005, ApJS, 160, 115

Rupke, D. S. N., Veilleux, S., & Baker, A. J. 2008, ApJ, 674, 172

Salim, S., Rich, R. M., Charlot, S., et al. 2007, ApJS, 173, 267

Salimbeni, S., Giallongo, E., Menci, N., et al. 2008, A&A, 477, 763

Salpeter, E. E. 1955, ApJ, 121, 161

Sánchez, S. F., Kennicutt, R. C., Gil de Paz, A., et al. 2012, A&A, 538, A8

Sánchez, S. F., Rosales-Ortega, F. F., Jungwiert, B., et al. 2013, A&A, 554, A58

Sánchez, S. F., Rosales-Ortega, F. F., Iglesias-Páramo, J., et al. 2014, A&A, 563, A49

Sánchez-Blázquez, P., Gorgas, J., Cardiel, N., & González, J. J. 2006, A&A, 457, 787

Sandage, A., Sandage, M., & Kristian, J. 1975, Galaxies and the Universe

Sanders, D. B., Mazzarella, J. M., Kim, D., Surace, J. A., & Soifer, B. T. 2003, AJ, 126, 1607

Sanders, D. B., & Mirabel, I. F. 1996, ARA&A, 34, 749

Sanders, D. B., Soifer, B. T., Elias, J. H., et al. 1988, ApJ, 325, 74

Savaglio, S., Glazebrook, K., Le Borgne, D., et al. 2005, ApJ, 635, 260

Scalo, J. M. 1986, Fund. Cosmic Phys., 11, 1

Schaerer, D., Charbonnel, C., Meynet, G., Maeder, A., & Schaller, G. 1993, A&AS, 102, 339

Schaller, G., Schaerer, D., Meynet, G., & Maeder, A. 1992, A&AS, 96, 269

Schawinski, K., Urry, C. M., Simmons, B. D., et al. 2014, MNRAS, 440, 889

Schechter, P. 1976, ApJ, 203, 297

Schlafly, E. F., & Finkbeiner, D. P. 2011, ApJ, 737, 103

Schlegel, D. J., Finkbeiner, D. P., & Davis, M. 1998, ApJ, 500, 525

Schmidt, M. 1959, ApJ, 129, 243

Schruba, A., Leroy, A. K., Walter, F., et al. 2011, AJ, 142, 37

Sersic, J. L. 1968, Atlas de galaxias australes

Sheth, R. K., Mo, H. J., & Tormen, G. 2001, MNRAS, 323, 1

Singh, R., van de Ven, G., Jahnke, K., et al. 2013, A&A, 558, A43

Skrutskie, M. F., Cutri, R. M., Stiening, R., et al. 2006, AJ, 131, 1163

Smith, D. J. B., Dunne, L., da Cunha, E., et al. 2012, MNRAS, 427, 703

Soifer, B. T., Neugebauer, G., Helou, G., et al. 1984, ApJ, 283, L1

Somerville, R. S., & Davé, R. 2015, ARA&A, 53, 51

Sparke, L. S., & Gallagher, III, J. S. 2007, Galaxies in the Universe

Stasińska, G. 2002, ArXiv Astrophysics e-prints, astro-ph/0207500

Steidel, C. C., Adelberger, K. L., Giavalisco, M., Dickinson, M., & Pettini, M. 1999, ApJ, 519, 1

Steinmetz, M., & Navarro, J. F. 2002, NA, 7, 155

Storchi-Bergmann, T., Calzetti, D., & Kinney, A. L. 1994, ApJ, 429, 572

Strateva, I., Ivezić, Ž., Knapp, G. R., et al. 2001, AJ, 122, 1861

Sturm, E., González-Alfonso, E., Veilleux, S., et al. 2011, ApJ, 733, L16

Sutherland, R. S., & Dopita, M. A. 1993, ApJS, 88, 253

Taniguchi, Y. 1999, ApJ, 524, 65

Terlouw, J. P., & Vogelaar, M. G. R. 2015, Kapteyn Package, version 2.3, Kapteyn Astronomical Institute, Groningen, available from http://www.astro.rug.nl/software/kapteyn/

Thomas, D., Maraston, C., Bender, R., & Mendes de Oliveira, C. 2005, ApJ, 621, 673

Thomas, D., Maraston, C., Schawinski, K., Sarzi, M., & Silk, J. 2010, MNRAS, 404, 1775

Tohline, J. E. 1980, ApJ, 239, 417

Toomre, A. 1977, in Evolution of Galaxies and Stellar Populations, ed. B. M. Tinsley & R. B. Larson, 401–+

Toomre, A., & Toomre, J. 1972, ApJ, 178, 623

Trager, S. C., Faber, S. M., Worthey, G., & González, J. J. 2000, AJ, 119, 1645

Tran, K.-V. H., van Dokkum, P., Franx, M., et al. 2005, ApJ, 627, L25

Tremonti, C. A., Heckman, T. M., Kauffmann, G., et al. 2004, ApJ, 613, 898

Tully, R. B., & Fisher, J. R. 1977, A&A, 54, 661

Väisänen, P., Reunanen, J., Kotilainen, J., et al. 2017, MNRAS, 471, 2059

Väisänen, P., Mattila, S., Kniazev, A., et al. 2008, MNRAS, 384, 886

Väisänen, P., Randriamanakoto, Z., Escala, A., et al. 2014, in Massive Young Star Clusters Near and Far: From the Milky Way to Reionization, 185–189

van den Bergh, S. 1976, ApJ, 206, 883

van Dokkum, P. G. 2001, PASP, 113, 1420

van Dokkum, P. G., & Franx, M. 1995, AJ, 110, 2027

Vazdekis, A. 2011, LECTOR: Line-strengths in One-dimensional ASCII Spectra, Astrophysics Source Code Library, ascl:1104.006

Veilleux, S., Cecil, G., & Bland-Hawthorn, J. 2005, ARA&A, 43, 769

Veilleux, S., Kim, D.-C., & Sanders, D. B. 1999, ApJ, 522, 113

—. 2002, ApJS, 143, 315

Veilleux, S., & Osterbrock, D. E. 1987, ApJS, 63, 295

Veilleux, S., Rupke, D. S. N., Kim, D.-C., et al. 2009, ApJS, 182, 628

Walcher, J., Groves, B., Budavári, T., & Dale, D. 2011, Ap&SS, 331, 1

Walter, F., Brinks, E., de Blok, W. J. G., et al. 2008, AJ, 136, 2563

Weedman, D. W., Feldman, F. R., Balzano, V. A., et al. 1981, ApJ, 248, 105

Weidner, C., Kroupa, P., & Larsen, S. S. 2004, MNRAS, 350, 1503

Weiner, B. J., Coil, A. L., Prochaska, J. X., et al. 2009, ApJ, 692, 187

Werner, M. W., Roellig, T. L., Low, F. J., et al. 2004, ApJS, 154, 1

Whitaker, K. E., van Dokkum, P. G., Brammer, G., & Franx, M. 2012, ApJ, 754, L29

Whitaker, K. E., Labbé, I., van Dokkum, P. G., et al. 2011, ApJ, 735, 86

White, S. D. M., & Frenk, C. S. 1991, ApJ, 379, 52

White, S. D. M., & Rees, M. J. 1978, MNRAS, 183, 341

Whitmore, B. C. 2000, ArXiv Astrophysics e-prints, arXiv:astro-ph/0012546

Wild, V., Charlot, S., Brinchmann, J., et al. 2011, MNRAS, 417, 1760

Wilkins, S. M., Trentham, N., & Hopkins, A. M. 2008, MNRAS, 385, 687

Wilkinson, D. M., Maraston, C., Goddard, D., Thomas, D., & Parikh, T. 2017, MNRAS, 472, 4297

Wilman, D. J., & Erwin, P. 2012, ApJ, 746, 160

Wilson, A. S., Helfer, T. T., Haniff, C. A., & Ward, M. J. 1991, ApJ, 381, 79

Woodward, P. R. 1976, ApJ, 207, 484

Worthey, G. 1999, in Astronomical Society of the Pacific Conference Series, Vol. 192, Spectrophotometric Dating of Stars and Galaxies, ed. I. Hubeny, S. Heap, & R. Cornett, 283

Worthey, G., Faber, S. M., Gonzalez, J. J., & Burstein, D. 1994, ApJS, 94, 687

Worthey, G., & Ottaviani, D. L. 1997, ApJS, 111, 377

Wuyts, S., Förster Schreiber, N. M., van der Wel, A., et al. 2011, ApJ, 742, 96

York, D. G., Adelman, J., Anderson, Jr., J. E., et al. 2000, AJ, 120, 1579

Yuan, T.-T., Kewley, L. J., & Sanders, D. B. 2010, ApJ, 709, 884

Zahid, H. J., Dima, G. I., Kudritzki, R.-P., et al. 2014, ApJ, 791, 130

Zahid, H. J., Kewley, L. J., & Bresolin, F. 2011, ApJ, 730, 137

Zaritsky, D., Kennicutt, Jr., R. C., & Huchra, J. P. 1994, ApJ, 420, 87